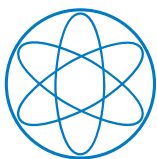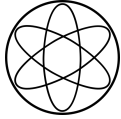# CONSTRAINING LOW-ENERGY MODELS OF QCD FROM FUNDAMENTAL INTERACTIONS

Paul Springer
October, 2016

Technische Universität München
Physik Department
Institut für Theoretische Physik T39

Constraining Low-Energy Models of QCD
from Fundamental Interactions

Paul Springer

Vollständiger Abdruck der von der Fakultät für Physik der Technischen Universität München zur Erlangung des akademischen Grades eines
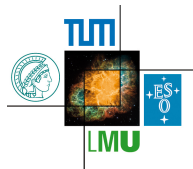
Doktors der Naturwissenschaften (Dr. rer. nat.)

genehmigten Dissertation.

Vorsitzende: Univ.-Prof. Dr. Laura Fabbietti

Prüfer der Dissertation: 1.   apl. Prof. Dr. Norbert Kaiser
                           2.   Univ.-Prof. Dr. Jens Braun

Die Dissertation wurde am 09.11.2016 bei der Technischen Universität München eingereicht und durch die Fakultät für Physik am 28.11.2016 angenommen.

ABSTRACT

In this work we investigate the phase transitions in quantum chromodynamics (QCD) at finite chemical potential. We analyze the fixed-point structure of four-fermion interactions in two-flavor QCD and show that there appears to be a mechanism which dynamically locks the chiral phase transition to the deconfinement phase transition, both at vanishing and at finite quark chemical potential. As a direct consequence, this observation suggests that the chiral phase transition and the deconfinement phase transition temperatures lie close to each other. Further, we propose to apply non-perturbative functional Renormalization Group methods (FRG) to QCD in order to determine constraints on the parameters used in low-energy QCD models. In particular, this includes a determination of the dependence of these parameters on temperature and quark chemical potential. The presented approach can be used to improve the predictive power of model calculations.

ZUSAMMENFASSUNG

In dieser Arbeit untersuchen wir die Phasenübergänge in Quantenchromodynamik (QCD) beim endlichen chemischen Potential von Quarks. Wir analysieren die Fixpunktstruktur von Vier-Fermionen-Wechselwirkung in zwei-Flavor QCD und beschreiben einen dynamischen Mechanismus, der den chiralen Phasenübergang erzwingt, falls das Farbconfinement realisiert ist. Dieser Mechanismus ist gültig sowohl für verschwindend kleine als auch für endliche Werte vom chemischen Potential von Quarks und führt zu einer Vermutung, dass der chirale Phasenübergang und der Deconfinementphasenübergang bei gleicher kritischer Temperatur stattfinden. Außerdem präsentieren wir eine Methode zur Einschätzung von Parametern der Niederenergiemodellen der QCD. Diese Methode basiert auf der nicht-perturbativen funktionalen Renormierungsgruppe (FRG). Unter anderem erlaubt diese Vorgehensweise die Bestimmung der Abhängigkeit der Modellparameter von der Temperatur und vom chemischen Potential von Quarks. Die präsentierte Methode kann benutzt werden, um die Vorhersagekraft aktueller Modelle zu steigern.

CONTENTS

INTRODUCTION

Quantum Chromodynamics (QCD) is a part of the modern Standard Model of Particle Physics and is universally accepted as the theory which describes the strong interaction [1, 2, 3, 4]. Originally introduced in order to explain the hadron spectrum, this non-Abelian gauge theory postulates the existence of quarks which are assumed to be the fundamental particles of strongly interacting matter. The quarks carry the so-called color charge. Since it is strongly believed that there are three different colors, the underlying symmetry group of QCD is SU(3). Exploiting the principle of local gauge invariance, QCD also postulates the existence of eight gauge bosons, so-called gluons, which carry different combinations of color and anti-color and act as mediators of the strong interaction between quarks. These massless particles are a kind of the QCD equivalent of photons in Quantum Electrodynamics (QED) but, in contrast to photons, they interact with each other. Among others, this property of gluons explains why the strong force has only a very short range.

A very characteristic feature of QCD is that no color charged particles, i.e., quarks and gluons can be observed in nature as isolated states. The quarks appear only as colorless bound states, namely hadrons which are either the quark-antiquark pairs (mesons) or are built up of three quarks (baryons). This phenomenon is called confinement and can be explained by the fact that at large distances the amount of energy needed to separate a quarks and an antiquark is proportional to the distance between them. At some critical distance it is even more favorable that a quark-antiquark pair is created and, thus, the final state are two mesons. Another type of possible colorless states are the so-called glueballs, particles consisting solely of gluons (and sea quarks). However, up to now such states have not been unambiguously identified in experiments. Confinement poses one of the main features of QCD and was observed in numerous studies [5, 6, 7, 8]. However, it is still not fully understood and needs more extensive research [9].

Even though confinement describes how hadrons are built up of quarks, it cannot explain some characteristic properties of the hadron spectrum. First, concerning the symmetries of QCD one would expect the so-called parity doubling, i.e., one would expect to observe an opposite-parity partner for any hadron in the QCD spectrum. However, from the experimental side there is no evidence for the existence of such parity partners [10]. Second, there is a large difference between the mass of pions, $m_\pi \approx 140$ MeV, and the typical masses of hadrons $m_H \gtrsim 1$ GeV. Even more, kaons and η-meson also have relatively small masses ~ 500 MeV. Both these observations suggest that the so-called chiral symmetry, which is approximately realized in QCD on the level of Lagrangian, is not respected by QCD ground state. Assuming a full realization of the chiral symmetry in QCD Lagrangian, one would say that the symmetry is spontaneously broken. Due to the Goldstone theorem [11], a spontaneous breaking of a continuous symmetry implies the existence of massless Nambu-Goldstone bosons. Since the chiral symmetry is only an approximate symmetry of QCD, these bosons remain massive but are still very light. These so-called pseudo
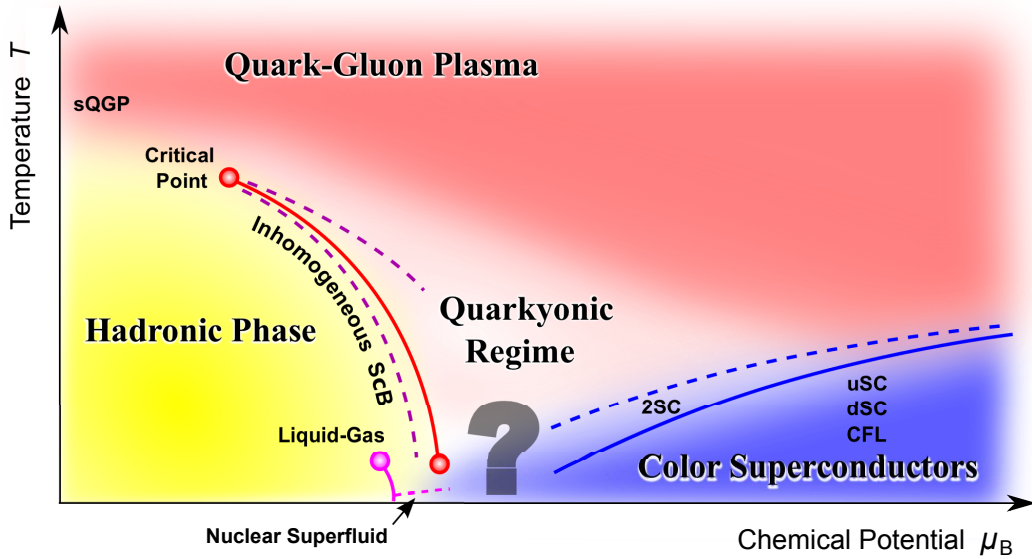
FIGURE 1.1: A sketch of conjectured QCD phase diagram taken from [28].

Nambu-Goldstone bosons can be indeed associated with pions, kaons and η-meson, see, e.g., [12].

Another very characteristic property of QCD is the so-called asymptotic freedom [13, 14] which means that the coupling strength in QCD decreases with increasing energy or, equivalently, with decreasing distances. It was shown that the origin of this behavior lies in the non-Abelian nature of QCD [15]. The asymptotic freedom implies that, at high energies, perturbation theory can be applied to QCD. However, it also implies that at low energies the coupling strength becomes larger. Consequently, if the coupling achieves values of the order of one, perturbation theory is no longer applicable and predicts its own breakdown. The scale where the perturbative coupling even diverges is called Landau pole Λ_{QCD} and depends on the used renormalization scheme. For the $\overline{\mathrm{MS}}$-scheme it was calculated to $\Lambda_{\mathrm{QCD}} \approx 200$ MeV [16]. Although perturbative QCD at high energies is well understood and shows very good agreement with experimental observations, spontaneous breaking of chiral symmetry as well as confinement are associated with scales where perturbation theory loses its applicability. Thus, to study this characteristic properties of QCD, one is restricted to non-perturbative methods. There are a lot of approaches developed to study low-energy QCD, such as lattice QCD [17, 18], effective field theories [19, 20, 21, 22, 23, 24] and non-perturbative functional continuum methods [25, 26, 27]. All these approaches are associated with a certain scope of validity and have their own advantages and weak points.

Asymptotic freedom, spontaneous breaking of chiral symmetry and confinement make the description of QCD quite challenging. However, it becomes even more involved if we include finite temperature T and finite quark chemical potential μ[1]. Inclusion of these external parameters leads to appearance of various phases of strongly interacting matter, see Fig. 1.1 and, e.g., [28] for review. The corresponding phase diagram is characterized by a rich structure and includes phenomena such as liquid-gas phase transition of nuclear matter [29, 30, 31, 32, 33], color superconductivity [34, 35, 36, 37, 38] and a transition between the phase where quarks and gluons are confined in hadrons (hadronic phase)

---

1 Quark chemical potential is given by $1/3$ of the baryon chemical potential μ_{B} which can be related to the baryon density.

and the so-called quark gluon plasma (QGP) – a phase of deconfined quarks and gluons [39, 40, 41, 42, 43]. The latter transition is of particular interest for this work. In fact, this transition involves not only the confinement-deconfinement phase transition but also the so-called chiral phase transition which is associated with the restoration of the chiral symmetry [11, 44, 45, 46, 47, 48]. The transition between the hadronic phase and QGP still raises a lot of questions and is the subject matter of intensive research: First, results from lattice QCD simulations indicate that for vanishing chemical potential the deconfinement and the chiral transition are realized as crossovers[2] and take place at approximately the same temperature [49, 50, 51, 52, 53]. It is not clear whether this statement is also valid for all values of chemical potential. The possible inequality of (pseudo-)critical temperatures at finite chemical potential has also given a rise to debates about existence of a new realization of QCD matter, the so-called quarkyonic matter [54, 55, 56, 57, 58]. This exotic phase describes confined quarks with restored chiral symmetry and can arise if the (pseudo-)critical temperature of the chiral phase transition T_χ is smaller than the (pseudo-)critical temperature of the deconfinement phase transition T_d. Further, following the chiral phase boundary, one expects to find the so-called critical point where the chiral crossover becomes a transition of first order. This point was observed in numerous calculations employing low-energy QCD models, see, e.g., [59, 60], but its existence is still under debate. The critical point is associated with enhanced fluctuations which lead to diverging behavior of susceptibilities. The resulting signatures are very distinct since they are nonmonotonic as a function of an experimental parameter such as the collision energy, centrality, rapidity or ion size [61, 62, 63]. Thus, the search for it is of great experimental interest. Furthermore, it is even possible that the first-order chiral phase transition ends at another critical point at very high μ and low T. This behavior was observed for three degenerate quark flavors and implies no clear phase boundary between superfluid nuclear matter and superconducting quark matter. This phenomenon is also called quark-hadron continuity, for details see, e.g., [28].

As sketched above, the theoretical investigation of QCD phase diagram is a quite complex task. However, its understanding is also of great importance for many areas of modern physics ranging from cosmology, e.g., the evolution of the early universe [64, 65], and astronomy, e.g., the neutron stars [66] throughout to heavy ion collision experiments [61, 62, 63, 67, 68].

The first part of this work is motivated by the fact that at $\mu = 0$ the pseudo-critical temperature of the chiral crossover is very similar to the pseudo-critical temperature of the deconfinement crossover as observed in lattice QCD. This similarity suggests that there could be a connection between the confinement and the chiral symmetry breaking. In addition, both these phenomena are driven by gauge dynamics: confinement appears also in pure Yang-Mills theory where only the gauge degrees of freedom are considered to be dynamic, and chiral symmetry breaking in full QCD is associated with strong quark self-interactions which are effectively generated via quark-gluon interactions. Thus, it seems to be reasonable to search for a mechanism connecting these two phenomena. And indeed, such a mechanism was already found and discussed in detail in [69, 70] for the case of

---

[2] A crossover is not a real phase transition since different phases are connected continuously. This circumstance leads to difficulties in defining critical temperature and one usually speaks about a pseudo-critical temperature. The chiral transition is a crossover because of the finite current quark masses which explicitly break the chiral symmetry. If one considers massless quarks (the so-called chiral limit), the chiral transition becomes a real phase transitions of second order. In contrast, the deconfinement crossover becomes a phase transition of first order if quarks are infinitely heavy.

zero chemical potential. More specifically, the authors have analyzed how the fixed-point structure of the fermionic self-interaction in the Polyakov-loop extended Nambu–Jona-Lasinio model (PNJL model) is affected by the order parameter of the deconfinement phase transition. For this purpose, they have employed a model with $N_{\mathrm{f}} = 2$ massless flavors and N_{c} colors which was investigated using the so-called functional renormalization group (FRG) approach. Further, the authors have partially resolved the momentum dependence of fermionic self-interaction by considering the so-called Polyakov-loop extended quark-meson model (PQM model). This has allowed them to study the phase diagram spanned by the pion decay constant f_{π} and temperature T and to get access to the physical low-energy observables. In the first part of this work we aim to extend this analysis to finite values of the chemical potential μ and beyond the chiral limit.

In the second part of this study we critically discuss approximations applied in common low-energy QCD models, such as (P)NJL and (P)QM models which are also used in this work. In short, the critique of modern low-energy QCD models involves the fine-tuning of model parameters and corresponding ambiguity in the choice of them, negligence of possible T- and μ-dependence of these parameters and not Fierz-complete interaction channels. We will see that all these approximations can be potentially improved by the use of QCD renormalization group (RG) flows [71, 72, 73]. Thereby, the main idea is to study effective quark self-interactions which are dynamically generated by gauge fields. Consideration of these effective interactions allows to study the mechanism of chiral symmetry breaking in QCD directly as it was shown in [71, 72, 73]. In this study, however, we use QCD RG flows in order to construct a low-energy QCD model. In particular, we introduce a Fierz-complete set of effective 4-quark interactions which can be also projected onto interaction channels commonly used in NJL models. Applying the FRG approach, we integrate out quantum fluctuations in QCD and, thus, generate the couplings of 4-quark interactions. At some particular momentum scale $k = \Lambda_{\mathrm{NJL}}$ we project our results from QCD RG flows onto an ansatz for an NJL model. In this way, we can derive a model with parameters which are not fine-tuned but are predicted by QCD RG flows. Even more, using this approach the model parameters can be calculated as functions of T and μ.

This work is organized as follows: In Chap. 2 we construct the QCD Lagrangian, briefly discuss its symmetries and introduce the concept of spontaneous symmetry breaking. Afterwards, we give a brief introduction to the FRG approach in Chap. 3. We start with the concept of the effective action and "upgrade" it to a scale-dependent quantity. Then, we derive the so-called Wetterich flow equation which is a standard FRG tool. Chap. 4 is assigned to a study of the mechanism connecting the chiral and the deconfinement phase transition which was found in Refs. [69, 70]. In the first place, we are interested in the extension of these studies to finite chemical potential. To this end, we first introduce the concept of the Polyakov loop and the ansatz for PNJL model. After that, we calculate the corresponding flow equation and discuss the fixed-point structure of the four-fermion interaction in the limit of infinite many colors $N_{\mathrm{c}} \to \infty$. We also present our numerical and analytical results for the physical case of $N_{\mathrm{c}} = 3$. In a further step, we partially resolve the momentum dependence of fermionic self-interaction by means of Hubbard-Stratonovich transformation, i.e., we introduce the PQM model. After derivation of the corresponding flow equations we study the phase diagram of PQM model spanned by the pion decay constant f_{π} and the temperature T. We consider both the chiral limit and the situation of explicitly broken chiral symmetry. In particular, we pay a close attention to the physical point in the (T, f_{π})-phase diagram. In Chap. 5 we present an idea how a low-energy QCD

model can be constructed starting from the QCD bare action by using QCD RG flows. First, we introduce our truncation scheme for dynamically generated effective interactions which includes a set of Fierz-complete 4-quark interactions. Then, we calculate the flows of corresponding couplings. In particular, we discuss the mechanism of chiral symmetry breaking in QCD. As we will see, a necessary condition for chiral symmetry breaking in the infrared regime is that the strong coupling g^2 (or, equivalently, $\alpha = g^2/(4\pi)$) should become sufficiently large. For our numerical calculation, we discuss a particular way how the strong coupling can be computed. As next, we project our results from QCD RG flows onto an ansatz for an NJL model. We obtain a model with T- and μ-dependent parameters predicted by QCD RG flow. The numerical output of this model, especially the phase diagram, is discussed. A summary of our major results and an outlook can be found in Chap. 6.

ASPECTS OF QCD

2.1 QCD LAGRANGIAN

In this section we briefly introduce the QCD Lagrangian and discuss some of its properties. To this end, we start with dynamical massive quarks which, however, do not interact. The corresponding Lagrangian in Euclidean spacetime[1] reads

$$\mathcal{L} = \mathrm{i}\bar{\psi}(\slashed{\partial} + m)\psi \ , \tag{2.1}$$

where ψ is a column vector in flavor and color space. We denote the number of flavors with N_f and the number of colors with N_c. The above Lagrangian is invariant under global $\mathrm{SU}(N_\mathrm{c})$ transformations[2]

$$\psi(x) \to \exp\left[\mathrm{i}\Theta^z t^z\right]\psi(x) \ , \tag{2.2}$$

where Θ^z are the real-valued parameters representing generalized rotating angles and t^z denotes generators of the underlying $\mathrm{SU}(N_\mathrm{c})$ group in the fundamental representation. In general, there are $N_\mathrm{c}^2 - 1$ generators t^z which are given in the physical case of $N_\mathrm{c} = 3$ by eight Gell-Mann matrices $t^z = \lambda^z/2$ ($z = 1, \ldots, 8$). The generators of a $\mathrm{SU}(N_\mathrm{c})$ group obey the following commutation relation:

$$[t^z, t^y] = t^z t^y - t^y t^z = \mathrm{i}f^{zyx}t^x \ , \tag{2.3}$$

with f^{zyx} the totally antisymmetric structure constants. For more details on properties of the $\mathrm{SU}(N_\mathrm{c})$ group, we refer the reader to App. C.

The Lagrangian (2.1) is only invariant under global $\mathrm{SU}(N_\mathrm{c})$ transformations. If a local gauge symmetry, i.e., $\Theta^z(x)$ is considered, then terms proportional to $\partial_\mu\Theta$ would appear. To make the Lagrangian (2.1) also invariant under the local $\mathrm{SU}(N_\mathrm{c})$ transformation, one has to replace the ordinary derivative ∂_μ by the covariant derivative D_μ which is defined as

$$D_\mu = \partial_\mu - \mathrm{i}\bar{g}A_\mu(x) \ , \tag{2.4}$$

with $A_\mu(x) = A_\mu^z(x)t^z$ and A_μ^z the auxiliary gauge fields or, in other words, the gluons. Since for the $\mathrm{SU}(N_\mathrm{c})$ group there are $N_\mathrm{c}^2 - 1$ generators t^z, there are also $N_\mathrm{c}^2 - 1$ gluons. The covariant derivative in Eq. (2.4) also introduces an interaction between gluons and quarks. The corresponding interaction strength is denoted by $\bar{g}$ which is usually called

---

1 For details on the relation between Minkowski and Euclidean spacetime, see App. A.2.
2 Global means that the transformation is independent of the spacetime coordinates.

the strong coupling. To ensure gauge invariance, the gauge fields have to transform in the following way:

$$A_\mu(x) \to U(x)(A_\mu(x) + \frac{\mathrm{i}}{g}\partial_\mu)U^\dagger(x) \qquad \text{with} \qquad U(x) = \exp\left[\mathrm{i}\Theta^z(x)t^z\right] , \qquad (2.5)$$

or for infinitesimal gauge transformations:

$$A_\mu^z(x) \to A_\mu^z(x) + \frac{1}{g}\partial_\mu\Theta^z(x) + f^{zyx}A_\mu^y(x)\Theta^x(x) . \qquad (2.6)$$

Altogether, we have obtained a Lagrangian which is invariant under the local gauge transformation:

$$\mathcal{L} = \mathrm{i}\bar{\psi}(\slashed{D} + m)\psi . \qquad (2.7)$$

In this Lagrangian we already have terms representing the interaction between quarks and gluons. However, to make gluons to the carriers of the strong interaction between quarks, we have to introduce a gluonic kinetic term. To this end, we consider the commutator of covariant derivatives:

$$[D_\mu, D_\nu]\psi = -\mathrm{i}\bar{g}F_{\mu\nu}\psi \qquad \text{with} \qquad F_{\mu\nu} = F_{\mu\nu}^z t^z. \qquad (2.8)$$

In the above equation, $F_{\mu\nu}^z$ is the so-called field strength tensor. This quantity poses a generalization of the usual field tensor in the quantum electrodynamics to the case of the non-Abelian gauge theories. Its explicit form is given by

$$F_{\mu\nu}^z = \partial_\mu A_\nu^z - \partial_\nu A_\mu^z + \bar{g}f^{zyx}A_\mu^y A_\nu^x . \qquad (2.9)$$

Note that the field strength tensor $F_{\mu\nu}^z$ itself is not a gauge invariant quantity since there are $N_c^2 - 1$ field strengths, i.e., for each gluon its own field strength. However, one notices that the quantity $F_{\mu\nu}$ transforms in the following way under the $\mathrm{SU}(N_c)$ gauge transformation

$$F_{\mu\nu} \to U(x)F_{\mu\nu}U^\dagger(x) . \qquad (2.10)$$

This observation allows us to construct a simplest kinetic term for gluons:

$$\mathcal{L}_{\mathrm{YM}} = \frac{1}{2}\mathrm{tr}[F_{\mu\nu}F_{\mu\nu}] = \frac{1}{4}F_{\mu\nu}^z F_{\mu\nu}^z . \qquad (2.11)$$

To derive this equation, we have used the normalization condition for the generators t^z:

$$\mathrm{tr}[t^z t^y] = \frac{1}{2}\delta^{zy} . \qquad (2.12)$$

The theory described by the Lagrangian (2.11) is the famous Yang-Mills theory. It deals with purely gluonic matter of massless bosons[3] and includes interactions between three and between four gluons. The classical action describing QCD can then be written by adding the matter-sector Lagrangian in Eq. (2.7) to the Yang-Mills Lagrangian in Eq. (2.11):

$$S_{\mathrm{QCD}} = \int \mathrm{d}^4x \left\{ \mathrm{i}\bar{\psi}(\slashed{D} + m)\psi + \frac{1}{4}F_{\mu\nu}^z F_{\mu\nu}^z \right\} . \qquad (2.13)$$

Up to now, we have considered QCD on the classical level. To be able to calculate observables, such as cross sections or scattering amplitudes, one has to quantize the theory. In the case of QCD, it is not a trivial task and involves the introduction of the so-called Faddeev-Popov ghost fields. A brief introduction to the quantization procedure in QCD can be found in App. D.

---

3 Please note that an additional mass term for gluons of the form $\propto m^2 A^2$ would violate the local gauge invariance.

2.2 SYMMETRIES OF QCD

The local gauge symmetry is not the only symmetry of QCD. Assuming the chiral limit, i.e., massless quarks and considering N_f flavors, QCD has an additional $U_V(N_f) \times U_A(N_f)$-symmetry which can be decomposed into $SU_V(N_f) \times SU_A(N_f) \times U_V(1) \times U_A(1)$. These symmetries are continuous and correspond on the classical level to conserved currents and charges by means of the Noether's theorem [74, 75]. However, not all of the above symmetries (and corresponding conserved quantities) are realized in nature since the invariance which is present on the classical level can be broken due to quantum effects. This is indeed the case for the $U_A(1)$ symmetry and is referred to as the axial anomaly [76, 77, 78]. In particular, the axial anomaly is responsible for the large mass of η'-meson. In contrast, the $U_V(1)$-symmetry is unbroken and the associated conserved charge is given by the baryon number:

$$B = \frac{1}{3} \int \mathrm{d}^3 x \, \psi^\dagger \psi \ .$$

Also the $SU_V(N_f)$-symmetry is realized in nature, at least as long as masses for different flavors are equal[4]. If one considers a theory with only the two lightest quarks, the $SU_V(2)$-symmetry is approximately realized even beyond the chiral limit, since the masses of up- and down-quarks are very similar. In this case the conserved quantity is the isospin.

The remaining $SU_A(N_f)$-symmetry is of particular importance for the present work. This so-called chiral symmetry is realized on the level of the Lagrangian as long as one considers the chiral limit and is approximately realized in the case of small current quark masses. However, the QCD vacuum does not preserve it and one says that the symmetry is spontaneously broken. This phenomenon is closely connected to the chiral phase transition at finite temperatures and chemical potentials which is the major topic of this work. In the following subsequent sections we introduce the concept of spontaneous symmetry breaking with the aid of the linear sigma-model and discuss how it is realized in QCD.

2.2.1 Chiral Symmetry and Its Spontaneous Breaking

Spontaneous Symmetry Breaking on Example of Linear Sigma-Model

In this section we take a brief look at the so-called linear sigma-model which is the simplest model with a manifestation of spontaneous chiral symmetry breaking. The model is defined by the following Lagrangian:

$$\mathcal{L} = \frac{1}{2}(\partial_\mu \bar{\varphi})^2 + \frac{1}{2}m^2 \bar{\varphi}^{\,2} + \frac{1}{4!}\lambda(\bar{\varphi}^{\,2})^2 \ , \tag{2.14}$$

where $\bar{\varphi} = (\sigma, \vec{\pi})^{\mathrm{T}}$ is a N-component vector of scalar fields and

$$V(\bar{\varphi}^{\,2}) = \frac{1}{2}m^2 \bar{\varphi}^{\,2} + \frac{1}{4!}\lambda(\bar{\varphi}^{\,2})^2 \tag{2.15}$$

is the potential of the model. Note that $\lambda > 0$. The above Lagrangian is invariant under continuous rotations of the field $\bar{\varphi}$ and, thus, shows the so-called $O(N)$ symmetry.

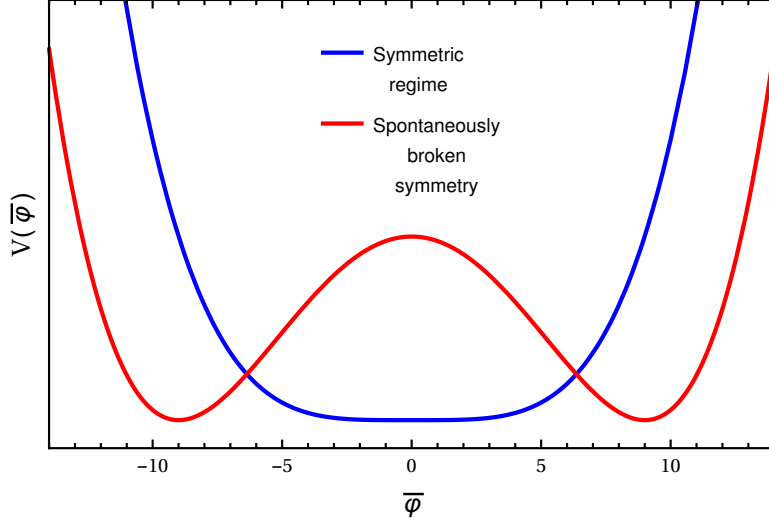4 This is, of course, always true in the chiral limit.

FIGURE 2.1: A sketch of the potential in Eq. (2.15) for the case of $N = 1$ and without explicit symmetry breaking. The symmetry of the model considered in this plot is the so-called discrete Z(2)-symmetry (alternative notation: O(1)-symmetry). The blue curve corresponds to the choice $m^2 > 0$ and, thus, to a symmetric ground state, $\langle \bar{\varphi} \rangle = 0$. The red curve was plotted with $m^2 < 0$ and visualizes the case of spontaneously broken symmetry. In this situation, there are a local maximum and two degenerated minimums. The potential itself still exhibits the Z(2)-symmetry. However, if one particular minimum is chosen, the ground state is not Z(2)-symmetric any more.

Now, let us discuss the ground state of this model. It is simply given by the global minimum of the potential V.

$$\left. \frac{\delta V}{\delta \bar{\varphi}_i} \right|_{\bar{\varphi} = \langle \bar{\varphi} \rangle \equiv \bar{\varphi}_0} = 0 \ . \tag{2.16}$$

Assuming that the coupling m^2 in Eq. (2.15) is positive, the only minimum of the potential corresponds to the vanishing vacuum expectation value of the fields $\bar{\varphi}_i$ (blue curve in the Fig. 2.1). Now, expanding the potential around its minimum $\bar{\varphi}_0 = 0$, one obtains the original expression in Eq. (2.15). Since after expansion the potential is still O(N) symmetric, the particular ground state $\bar{\varphi}_0 = 0$ is also invariant under the rotational transformations.

However, if the coupling m^2 becomes negative, the vacuum expectation value of the field $\bar{\varphi}$ obtains a finite value (red curve in the Fig. 2.1). Using an appropriate choice of coordinates, we can choose one particular ground state and write it as

$$\bar{\varphi}_0 = \left(\sqrt{-\frac{6m^2}{\lambda}}, \vec{0} \right)^{\mathrm{T}} \ . \tag{2.17}$$

Therefore, the field vector $\bar{\varphi}(x)$ can be now written as

$$\bar{\varphi}(x) = \left(\sqrt{-\frac{6m^2}{\lambda}} + \sigma(x), \vec{\pi}(x) \right)^{\mathrm{T}} \ . \tag{2.18}$$

If we again expand the potential around its new minimum, the Lagrangian takes the form

$$\mathcal{L} = \frac{1}{2}(\partial_\mu \sigma)^2 + \frac{1}{2}(\partial_\mu \vec{\pi})^2 - m^2 \sigma^2 + \sqrt{\frac{\lambda}{6}} \sqrt{-m^2} \sigma(\sigma^2 + \vec{\pi}^2) + \frac{\lambda}{4!}(\sigma^2 + \vec{\pi}^2)^2 \ . \tag{2.19}$$

This result is obviously not O(N)-symmetric and, thus, the symmetry is broken in the ground state. On the other hand, the potential itself is still O(N)-symmetric, even for $m^2 < 0$. In this situation one speaks about spontaneously broken symmetry. This kind of symmetry breaking appears because the system chooses one particular ground state. Further, in accordance with our choice of coordinates, the σ-field obtains a finite mass. The residual $N-1$ degrees of freedom, namely the fields $\vec{\pi}$, stay massless and degenerated. This indicates that the ground state has a residual O($N-1$)-symmetry. In the Fig. 2.1 we have visualized our above considerations for the case of $N = 1$ which is equivalent to the so-called Z(2)-symmetry. We observe that the massive σ-field corresponds to an oscillation in the radial direction. In a plot of a potential with spontaneously broken symmetry for a model with $N > 1$, the massless π-fields would correspond to oscillations in tangential directions.

In this section we have seen that the original O(N)-symmetry of the linear sigma-model can be spontaneously broken in the ground state. Such a symmetry breaking leads to the appearance of one massive and $N-1$ massless fields. Yet, this statement is valid not only for the linear sigma-model. The so-called Goldstone theorem states that if a generic continuous symmetry is spontaneously broken, the new massless scalar particles arise in the spectrum of possible excitations [11]. These particles are called Nambu-Goldstone bosons. Considering two-flavor QCD in the chiral limit, the Nambu-Goldstone bosons associated with the spontaneous chiral symmetry breaking are massless pions. Assuming three massless flavors, the Nambu-Goldstone bosons are pions, kaons and the η-meson. On the other hand, quarks (and mesons) are not massless in nature where the chiral symmetry is explicitly broken. However, since their masses are quite small, one can consider the chiral symmetry as approximately realized. Especially, it is the case for two-flavor QCD since the up- and down- quarks are very light. In order to get a feeling of how the (small) explicit symmetry breaking influences the spontaneous breaking of the chiral symmetry in QCD, we first discuss the same situation in the case of linear sigma-model.

Explicit Symmetry Breaking in the Linear Sigma-Model

We consider a situation when a symmetry is realized only approximately, i.e., the symmetry is explicitly broken but the strength of this breaking is small. Due the Goldstone theorem, the Nambu-Goldstone bosons appear also in this case. However, now they become massive, even though, their mass is small compared to the typical energy scale of the model[5]. To introduce the explicit symmetry breaking in the linear sigma-model, we add a new term $-c\sigma$ to the original potential in Eq. (2.15):

$$V(\sigma, \bar{\varphi}^{\,2}) = \frac{1}{2}m^2\bar{\varphi}^{\,2} + \frac{1}{4!}\lambda(\bar{\varphi}^{\,2})^2 - c\sigma \; . \tag{2.20}$$

Again, we distinguish between positive and negative m^2, see Fig. 2.2. Let us start with $m^2 > 0$. In order to minimize potential in the radial direction, one has to solve the following equation:

$$\frac{1}{3!}\lambda\sigma^3 + m^2\sigma - c = 0 \; . \tag{2.21}$$

---

5 This statement is indeed very well applicable to two-flavor QCD since the mass of pions is roughly 140 MeV and is small compared to the typical QCD scale ~ 1 GeV.
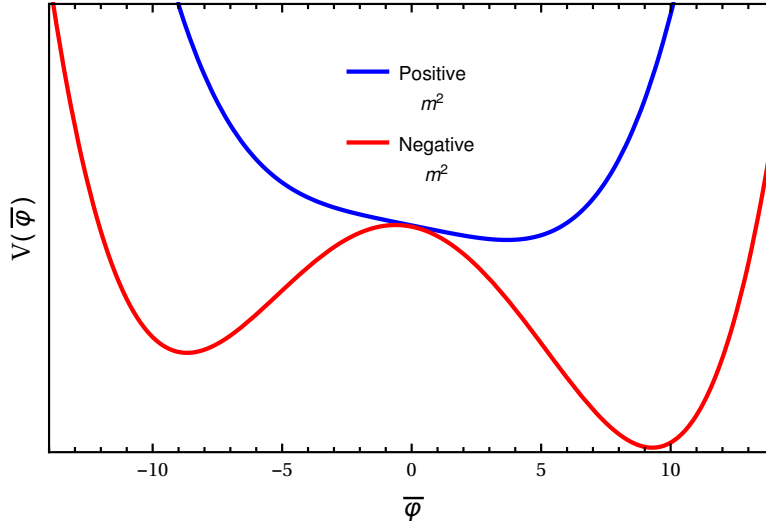
FIGURE 2.2: The potential in Eq. (2.20) for a Z(2)-symmetric model with additional explicit symmetry breaking. The blue curve represents the case of positive and the red one the case of negative m^2. The particular global minimum of the potential is strongly dependent on the choice of the sign of m^2.

Since we explicitly break symmetry only in the σ direction, the $\vec{\pi}$-sector is not interesting for our particular purpose. We assume that the symmetry is approximately realized and, thus, the parameter c is small. Therefore, we can expand the expectation value of the field σ in powers of c. Taking into account only the leading-order contribution, we find that

$$\sigma_0(c) = \langle \sigma \rangle = \frac{c}{m^2} \ . \tag{2.22}$$

Consequently, for $c \to 0$ we obtain $\sigma_0 = 0$. This is exactly what we have found in the previous section in the case of $m^2 > 0$.

Now, we study the case $m^2 < 0$. We again have to solve Eq. (2.21). But now, proceeding in the same way as described above, we find three real solutions: two of them correspond to the minima of potential $V(\sigma, \bar{\varphi}^{\,2})$ and one to a maximum. We find that the global minimum is given by

$$\sigma_0(c) = \sqrt{-\frac{6m^2}{\lambda}} - \frac{c}{2m} \ . \tag{2.23}$$

As one can see, the limit $c \to 0$ again reproduces our result from the previous section for the case of spontaneously broken symmetry.

Even though the ground state of our particular model does not respect the O(N) symmetry at all, we have illustrated above that the choice of the sign of m^2 leads to the different results for the particular value of σ_0. Thus, we have shown that the behavior of a system with approximate symmetry is strongly influenced by the behavior of this system in the limit of vanishing c where the symmetry is realized exactly.

Spontaneous chiral symmetry breaking is a necessary condition for the chiral phase transition in QCD in the chiral limit. However, due to the finite quark masses the chiral symmetry is explicitly broken and the real phase transition cannot appear. The behavior of such a system is called crossover. As we have seen above, as long as the explicit symmetry breaking is small, the crossover behavior is influenced by the behavior of the system in

the limit of vanishing explicit symmetry breaking. Therefore, if one aims to investigate the chiral crossover in QCD, it also makes sense to investigate the chiral limit in order to get a better understanding of the chiral nature of QCD.

Spontaneous Chiral Symmetry Breaking in QCD

We have seen above how spontaneous breaking of the chiral symmetry can take place in a linear sigma-model. Now, let us discuss how this phenomenon appears in QCD. Since we will consider two-flavor QCD throughout this work, we restrict our particular considerations to the case of $N_f = 2$. The chiral $\text{SU}_A(2)$-transformation is given by

$$\psi \to \exp[\frac{\mathrm{i}}{2} \vec{\Theta}_A \cdot \vec{\tau} \gamma_5] \, \psi \; , \tag{2.24}$$

where $\vec{\tau}$ is a vector containing Pauli matrices. The corresponding conserved current and the conserved charge read

$$\vec{j}_A^\mu = \frac{1}{2} \bar{\psi} \gamma^\mu \gamma_5 \vec{\tau} \psi \qquad \text{and} \qquad \vec{Q}_A = \frac{1}{2} \int \mathrm{d}^3 x \, \psi^\dagger \gamma_5 \vec{\tau} \psi \; . \tag{2.25}$$

The above symmetry is explicitly broken in QCD if the mass term for fermions is included in the action. However, since the current quark masses are very small, we restrict the following discussion to the chiral limit and consider the QCD Lagrangian to be $\text{SU}_A(2)$-invariant.

On the other hand, the theory "loses" chiral symmetry in the ground state if the quark mass is dynamically generated by loop corrections. This scenario corresponds to the appearance of a finite expectation value $\langle \bar{\psi}\psi \rangle$. This so-called chiral condensate can be calculated from the commutator of the chiral charge and the composite field $\bar{\psi}\mathrm{i}\gamma_5\vec{\tau}\psi$

$$\left\langle \left[\mathrm{i}Q_A^i, \bar{\psi}\mathrm{i}\gamma_5\tau^j\psi \right] \right\rangle = \delta^{ij} \langle \bar{\psi}\psi \rangle \; , \tag{2.26}$$

and was indeed measured in lattice simulations to be finite. In accordance with the Goldstone theorem, the composite fields $\bar{\psi}\mathrm{i}\gamma_5\tau^i\psi$ with $i = \{1, 2, 3\}$ correspond to three massless Nambu-Goldstone bosons. Since these states do not appear in the original QCD action, they must be bound states. Considering the more realistic case of finite (but small) explicit symmetry breaking due to the finite current quark masses, the fields $\bar{\psi}\mathrm{i}\gamma_5\tau^i\psi$ obtain some finite mass which is, however, small compared to the typical scale of QCD ~ 1 GeV. And indeed, there are bound states in the particle spectrum of QCD which have noticeable small masses, namely the pions: $m_\pi \approx 140$ MeV. Thus, the composite fields $\bar{\psi}\mathrm{i}\gamma_5\tau^i\psi$ are identified with pions in the spectrum of physical particles.

The chiral condensate $\langle \bar{\psi}\psi \rangle$ is used as the order parameter of the chiral phase transition. However, there is also another quantity which can be used in order to identify the spontaneous break down of chiral symmetry. To see it, let us first introduce an appropriately normalized one-pion state $|\pi_i(p)\rangle$ where p is the momentum and i denotes the isospin index. Then, since pions couple to the corresponding current, the state $j_A^{j,\mu}|0\rangle$ should have a non-vanishing overlap with the pionic fields:

$$\left\langle 0 \left| j_A^{j,\mu} \right| \pi_i(p) \right\rangle = -\mathrm{i}p^\mu f_\pi \delta^{ji} \mathrm{e}^{-\mathrm{i}px} \; , \tag{2.27}$$

where f_π is the so-called pion decay constant in the chiral limit[6] and the momentum dependence appears because of Lorentz symmetry. As next, we consider the divergence of the above relation evaluated on shell ($p^2 = m_\pi^2$):

$$\left\langle 0 \left| \partial_\mu j_A^{j,\mu} \right| \pi_i(p) \right\rangle = -m_\pi^2 f_\pi \delta^{ji} \mathrm{e}^{-ipx} \ . \tag{2.28}$$

This equation together with Eq. (2.27) implies that the axial current carried by pion can be written as

$$\vec{j}_{A,\pi}^\mu = f_\pi \partial^\mu \vec{\pi}(x) \ . \tag{2.29}$$

and, consequently,

$$\partial_\mu \vec{j}_{A,\pi}^\mu = f_\pi \partial^2 \vec{\pi}(x) \ . \tag{2.30}$$

On the other hand, we can assume that the total axial current

$$\vec{j}_A^\mu = \vec{j}_{A,\psi}^\mu + \vec{j}_{A,\pi}^\mu = \frac{1}{2} \bar{\psi} \gamma^\mu \gamma_5 \vec{\tau} \psi + f_\pi \partial^\mu \vec{\pi}(x) \ . \tag{2.31}$$

is still conserved, i.e., $\partial_\mu \vec{j}_A^\mu = 0$. Then, using the free Dirac equation, we find

$$\partial^2 \vec{\pi}(x) = -\mathrm{i} \frac{m_q}{f_\pi} \bar{\psi} \gamma_5 \vec{\tau} \psi \ , \tag{2.32}$$

where m_q is the constituent quark mass. The above relation is nothing but the Klein-Gordon equation for a massless pion and describes the coupling of the pions to the quark current. Such a coupling corresponds to the Yukawa-type interaction with the coupling strength h. Thus, we can state that

$$h = \frac{m_q}{f_\pi} \ . \tag{2.33}$$

This result is called Goldberger-Treiman relation[7] and relates the pion decay constant f_π and the constituent quark mass m_q. On the other hand, in the chiral limit, the constituent quark mass is zero if the chiral symmetry is restored and finite if the chiral symmetry is spontaneously broken. Thus, since the Yukawa coupling is finite, the pion decay constant f_π should also vanish in the chirally symmetric regime and should be finite in the chirally broken phase. Therefore, f_π can be seen as an alternative order parameter for the chiral phase transition.

2.2.2   *Center Symmetry*

In the previous sections concerning QCD symmetries we have considered either the chiral limit or the case of very small quark masses. Now, let us discuss the opposite case of

---

6 f_π was measured to $f_\pi = (92.21 \pm 0.01 \pm 0.14)$ MeV using $\pi^- \to \mu^- \bar{\nu}_\mu$ and $\pi^- \to \mu^- \bar{\nu}_\mu \gamma$ decays [79]. The errors are due to the uncertainty of $|V_{ud}|$ in the CKM-matrix and due to the higher-order corrections. In the chiral limit the value of the pion decay constant is slightly smaller, $f_\pi = 87$ MeV [80, 81].

7 This relation is formulated on the level of quarks. Originally, the Goldberger-Treiman relation was formulated for nucleons.

infinitely heavy quarks. This so-called quenched QCD[8] exhibits a global discrete $Z(N_c)$-symmetry. Using the imaginary-time formalism, one finds that gluons obey periodic boundary conditions in the Euclidean time direction

$$A_\mu(\tau + \beta, \vec{x}) = A_\mu(\tau, \vec{x}) \ . \tag{2.34}$$

Of course, the gauge transformed fields, Eq. (2.5), should also fulfill the above periodicity condition. It can by trivially achieved if the gauge transformations $U(x)$ are periodic in the Euclidean time direction by itself

$$U(\tau + \beta, \vec{x}) = U(\tau, \vec{x}) \ . \tag{2.35}$$

However, also some topologically non-trivial gauge transformations preserve the required boundary conditions for the transformed gluonic fields:

$$U(\tau + \beta, \vec{x}) = z\, U(\tau, \vec{x}) \qquad \text{with} \qquad z \in \text{SU}(N_c) \ , \tag{2.36}$$

see also [82, 83]. Obviously, z is not an arbitrary element of $\text{SU}(N_c)$. It can be straightforwardly seen from the gauge transformed field $A'(\tau + \beta, \vec{x})$:

$$\begin{aligned}
A'_\mu(\tau + \beta, \vec{x}) &= U(\tau + \beta, \vec{x})(A_\mu(\tau + \beta, \vec{x}) + \frac{\text{i}}{g}\partial_\mu)U^\dagger(\tau + \beta, \vec{x}) \\
&= z\, U(\tau, \vec{x})(A_\mu(\beta, \vec{x}) + \frac{\text{i}}{g}\partial_\mu)U^\dagger(\tau, \vec{x})\, z^\dagger = z\, A'_\mu(\tau, \vec{x})\, z^\dagger \ .
\end{aligned} \tag{2.37}$$

Consequently, z should be chosen in such a way that

$$z\, A'_\mu(\tau, \vec{x})\, z^\dagger = A'_\mu(\tau, \vec{x}) \tag{2.38}$$

This relation sets constraints on z. First, since $A_\mu = A^x_\mu\, t^x$, z should commute with all elements of the $\text{SU}(N_c)$ group. This property defines the so-called center of the group $Z(N_c)$ and gives rise to the name of the symmetry. Further, due to the Schur's Lemma, z should be a complex multiple of unity. Using the fact that $z \in \text{SU}(N_c)$ and, thus, $\det[z] = +1$, we can state that

$$z = \exp\left[\frac{2\pi\text{i}n}{N_c}\right] \mathbb{1} \qquad \text{with} \qquad n \in \{1, \dots, N_c\} \ , \tag{2.39}$$

with $\mathbb{1}$ being the N_c-dimensional identity matrix.

Altogether, we have seen that quenched QCD in Euclidean spacetime exhibits an additional $Z(N_c)$ center symmetry. This symmetry, however, is explicitly broken in the presence of dynamical quarks since the quark fields obey anti-periodic boundary conditions

$$\psi(\tau + \beta, \vec{x}) = -\psi(\tau, \vec{x}) \ , \tag{2.40}$$

and transform under the gauge transformation as

$$\psi'(\tau, \vec{x}) = U(\tau, \vec{x})\psi(\tau, \vec{x}) \ . \tag{2.41}$$

---

8 Quenched QCD is described by the Yang-Mills Lagrangian Eq. (2.11)

Using these relations, one finds

$$\psi'(\tau + \beta, \vec{x}) = -z\, \psi'(\tau, \vec{x}) \ . \tag{2.42}$$

This is only fulfilled for $z = 1$ and therefore the QCD Lagrangian is not invariant under the $Z(N_c)$ transformation anymore.

At this point we would like to emphasize that $Z(N_c)$ center symmetry is defined in Euclidean spacetime. Since the local $\mathrm{SU}(N_c)$ gauge symmetry is also a symmetry of the QCD Lagrangian in Minkowski spacetime, the $Z(N_c)$ symmetry should not be considered as a subgroup of $\mathrm{SU}(N_c)$. Consequently, even if the center symmetry is explicitly broken by the dynamical quarks, the QCD Lagrangian is still invariant under the $\mathrm{SU}(N_c)$ transformations.

An additional feature of the center symmetry is that it can be even broken spontaneously. This phenomenon is closely related to the so-called Polyakov loop and the deconfinement phase transition which we will discuss in Sec. 4.1.

EFFECTIVE ACTION AND FUNCTIONAL RENORMALIZATION GROUP APPROACH

As we have mentioned in Sec. 1, the QCD coupling becomes large in infrared regime and, therefore, the perturbation theory is no longer applicable. Additionally, due to the long-range fluctuations, perturbative calculations cannot be used to study the chiral phase transition. In this situation the correlation length becomes larger than the distance between the microscopic degrees of freedom and collective effects dominate the behavior of the system. Therefore, in order to investigate QCD phase transitions, we need an alternative non-perturbative treatment, e.g., the renormalization group approach (RG). The main idea of RG is the following: we start with some microscopic action S defined at a very high momentum scale and then we successively integrate out fluctuations down to a lower momentum scale, say k. As result we obtain an action defined at the scale k which already includes quantum corrections on the momentum scales $p^2 \gtrsim k^2$. The change of such a scale-dependent action with respect to the change of k is governed by continuous RG transformations. The major aim of such calculations is to obtain an action in the limit $k \to 0$ which should include all quantum fluctuations. We also mention that RG transformations do not always change the scale-dependent couplings appearing in the action. Sometimes, couplings approach constant values at some particular scale and remain unchanged by further application of RG transformations. In this case one says that RG flows have achieved a fixed point. Fixed points are very important in statistical and quantum field theories since they are closely related to the phenomenon of universality and to the critical behavior close to the phase transition. A very important advantage of the RG is that this approach allows to identify and to study the fixed point structure of a theory. For more introduction, see, e.g., [84].

In the following chapter we employ the so-called functional renormalization group approach (FRG) in its particular form given by Wetterich flow equation [85]. To this end we introduce the concept of effective action Γ and extend it to a scale-dependent effective action Γ_k.

3.1 EFFECTIVE ACTION

By introducing the effective action Γ we pursue essentially two objectives: First, we aim at a quantity which can be viewed as a quantum field theoretical analogon of the Gibbs free-energy in thermodynamics, i.e., Γ should give a geometrical interpretation of the preferred states in a quantum system. With other words, the minimum of Γ should correspond to the "most likely" state of the system which already includes quantum corrections. Additionally, by analogy with the Gibbs free-energy, Γ should be a function of the expectation value of the quantum field. Second, we want to have a generating functional of one-particle

irreducible diagrams (1PI). These diagrams cannot be separated into two disjoint diagrams by cutting one internal line and, therefore, represent a minimal basis for the connected Feynman graphs. As a consequence, using such a functional we can calculate all connected correlations of a given theory.

Here we briefly introduce the effective action and discuss its properties. More detailed discussion can be found in, e.g., Refs. [16, 86]. In order to derive the effective action, we start with the general definition of generating functional, Z, of a quantum field theory in Euclidean spacetime:

$$Z[J] = \int \mathcal{D}\phi \exp[-S[\phi] + (J, \phi)] = \langle 0|0 \rangle_J \; . \tag{3.1}$$

S represents the bare action and (J, ϕ) is the short-hand notation for $\int \mathrm{d}^4x \; J(x)^T \cdot \phi(x)$. The quantum field ϕ and the corresponding source J are considered as generalized vectors in field space:

$$\phi = \begin{pmatrix} \psi \\ \bar{\psi}^T \\ \varphi \\ \vdots \end{pmatrix} , \qquad J^T = (\bar{\eta}, \eta^T, j, \ldots) \; . \tag{3.2}$$

In this notation ψ denotes a Dirac spinor, φ a real scalar field and dots stand for other types of quantum fields like, e.g., gauge fields.

By taking functional derivatives of Z with respect to the source J we can calculate correlation functions (Green's functions) of the corresponding theory. However, it is not very useful to work with Z in practice since this functional "produces" all possible correlation functions including disconnected functions which do not contribute to the S-Matrix. Therefore, it is more convenient to use the so-called generating functional for connected correlation functions:

$$W[J] = \ln Z[J] \; . \tag{3.3}$$

We will discuss this functional in more details later in this section. At this point, however, we want to use it in order to define the so-called classical field Φ, which represents the normalized vacuum expectation value of the field ϕ in the presence of the source J:

$$\Phi_a(x) = \frac{\overrightarrow{\delta}}{\delta J_a^T(x)} W[J] = \frac{1}{Z} \int \mathcal{D}\phi \, \phi_a(x) \exp[-S[\phi] + (J, \phi)] = \frac{\langle 0|\phi_a(x)|0 \rangle_J}{\langle 0|0 \rangle_J} \; . \tag{3.4}$$

Since this new variable is given by the functional derivative of $W[J]$, we should treat Φ_a as a conjugate variable to J_a. Inspired by the Gibbs free-energy in thermodynamics, we can now define the effective action via the following Legendre transformation:

$$\Gamma[\Phi] = -W[J] + (J, \Phi) \; . \tag{3.5}$$

This new functional does not depend explicitly on the source J:

$$\frac{\overrightarrow{\delta}}{\delta J_a^T(x)} \Gamma[\Phi] = -\Phi_a(x) + \int \mathrm{d}^4y \, \Phi_a(y) \delta(x - y) = 0 \; . \tag{3.6}$$

So, the effective action depends only on the classical field Φ and all fluctuations have been already integrated out.

Taking the first derivative of $\Gamma[\Phi]$ with respect to the classical field, we find:

$$\Gamma[\Phi]\frac{\overleftarrow{\delta}}{\delta\Phi_a(x)} = J_a^T(x) \ . \tag{3.7}$$

This equation can be seen as the quantum mechanical analogon to the classical field equation. Moreover, in the absence of an external source J, solutions of this equation are those values of Φ which correspond to the stable quantum states. In conclusion, the effective action provide us a geometrical interpretation of the preferred state in a quantum system and already includes all quantum corrections.

An additional useful property of Γ is that this quantity is the generating functional of 1PI-correlation functions. To show this, we again consider the generating functional for connected correlation functions, W. The proof that W indeed generates only connected correlation functions is a straight-forward induction [16]. Here we show only the first step of this proof by induction. We consider the second derivative of $W[J^T]$:

$$\frac{\overrightarrow{\delta}}{\delta J_a^T(x)} \frac{\overrightarrow{\delta}}{\delta J_b(y)} W[J] = \frac{\langle 0|T\{\phi_a(x)\phi_b^T(y)\}|0\rangle_J}{\langle 0|0\rangle_J} - \frac{\langle 0|\phi_a(x)|0\rangle_J}{\langle 0|0\rangle_J} \frac{\langle 0|\phi_b^T(y)|0\rangle_J}{\langle 0|0\rangle_J} \ . \tag{3.8}$$

We see that it is given by the full two-point correlation minus its disconnected part, i.e., by the connected two-point function or, with other words, by the full propagator $G(x,y)$:

$$G_{ab}(x,y) \equiv \frac{\overrightarrow{\delta}}{\delta J_a^T(x)} \frac{\overrightarrow{\delta}}{\delta J_b(y)} W[J] \ . \tag{3.9}$$

Connected parts of the higher order correlation functions can be calculated in the same way by taking higher derivatives with respect to J.

One may realize immediately that connected higher order correlations produced by $W[J]$ are reducible, i.e., they do not represent a minimal basis of connected Feynman diagrams. Such a minimal basis, however, exists and is given by 1PI-correlation functions. These diagrams can be obtained by taking functional derivatives of the effective action $\Gamma[\Phi]$ with respect to the classical field Φ. Again, a rigorous proof can be done by induction [16]. Here we present only an idea how such a proof can be worked out. First, consider a functional derivative of the minimization condition (3.7) with respect to the source:

$$\frac{\overrightarrow{\delta}}{\delta J_a^T(x)}\Gamma[\Phi]\frac{\overleftarrow{\delta}}{\delta\Phi_b(y)} = \delta(x-y)\delta^{ab} = \int \mathrm{d}^4z\, G_{ac}(x,z) \left(\frac{\overrightarrow{\delta}}{\delta\Phi_c^T(z)}\Gamma[\Phi]\frac{\overleftarrow{\delta}}{\delta\Phi_b(y)}\right) \ . \tag{3.10}$$

Since the last expression is an operator identity, we have shown that:

$$\left(\frac{\overrightarrow{\delta}}{\delta\Phi_a^T(x)}\Gamma[\Phi]\frac{\overleftarrow{\delta}}{\delta\Phi_b(y)}\right) = G_{ab}(x,y)^{-1} \ . \tag{3.11}$$

From this crucial result we see that the second derivative of the effective action with respect to the classical field is the inverse dressed propagator. Further, we can use Eq. (3.11) to show that

$$G_{ab}(x,y) \cdot \left(\frac{\overrightarrow{\delta}}{\delta\Phi_b^T(y)}\Gamma[\Phi]\frac{\overleftarrow{\delta}}{\delta\Phi_e(u)}\right) \cdot G_{ed}(u,z) = G_{ad}(x,z) \ , \tag{3.12}$$

where dots mean

$$G_{ab}(x,y) \cdot \left(\frac{\overrightarrow{\delta}}{\delta \Phi_b^T(y)} \Gamma[\Phi] \frac{\overleftarrow{\delta}}{\delta \Phi_e(z)} \right) = \int \mathrm{d}^4 y \, G_{ac}(x,y) \left(\frac{\overrightarrow{\delta}}{\delta \Phi_c^T(y)} \Gamma[\Phi] \frac{\overleftarrow{\delta}}{\delta \Phi_b(z)} \right) \, . \quad (3.13)$$

The above equation means that two-point correlation can be calculated from 1PI two-point diagram by dressing external legs with the propagator. This result is general for any n-point correlations. To see it consider the following operator:

$$\frac{\overrightarrow{\delta}}{\delta J_a^T(x)} = \int \mathrm{d}^4 y \left(\frac{\overrightarrow{\delta}}{\delta J_a^T(x)} \Phi_b^T(y) \right) \frac{\overrightarrow{\delta}}{\delta \Phi_b^T(y)} = G_{ab}(x,y) \cdot \frac{\overrightarrow{\delta}}{\delta \Phi_b^T(y)} \, . \quad (3.14)$$

Now, we apply this operator on the second derivative of W, i.e., we calculate the three-point correlation:

$$\frac{\overrightarrow{\delta}}{\delta J_a^T(x)} \frac{\overrightarrow{\delta}}{\delta J_b^T(y)} \frac{\overrightarrow{\delta}}{\delta J_c(z)} W[J] = G_{ad}(x,u) \cdot \frac{\overrightarrow{\delta}}{\delta \Phi_d^T(u)} \left(\frac{\overrightarrow{\delta}}{\delta \Phi_b^T(y)} \Gamma[\Phi] \frac{\overleftarrow{\delta}}{\delta \Phi_c(z)} \right)^{-1}$$

$$= -G_{ad}(x,u) \cdot G_{be}(y,w) \cdot \left(\frac{\overrightarrow{\delta}}{\delta \Phi_d^T(u)} \frac{\overrightarrow{\delta}}{\delta \Phi_e^T(w)} \Gamma[\Phi] \frac{\overleftarrow{\delta}}{\delta \Phi_f(v)} \right) \cdot G_{fc}(v,z) \, . \quad (3.15)$$

Hence, we have confirmed our above statement also for three-point correlation. To proof it for the n-point correlation functions the procedure is straight forward: we have to apply the operator (3.14) on the $(n-1)$-point function.

The operator (3.14) also explains the difference between functional derivatives of $W[J^T]$ and functional derivatives of $\Gamma[\Phi]$: a derivative of W with respect to J adds an external line to a correlation function. A derivative of Γ with respect to Φ, however, not only adds an external line but also removes the propagator from this line simultaneously. This corresponds exactly to the procedure of generating the 1PI-diagrams.

Altogether, the effective action is an object which contains all information we need to provide the physical predictions for a given quantum field theory: it allows us to calculate all relevant correlations in a very handy manner and gives us a direct access to the ground state. Therefore, Γ is a convenient tool to study quantum field theories.

3.2   WETTERICH FLOW EQUATION

In this section we give a brief introduction to the Wetterich flow equation [85]. For a more detailed introduction as well as a discussion of different aspects of renormalization group approaches, see Refs. [87, 88, 89, 90, 91, 92, 93, 94, 95, 96, 97, 98, 99, 100, 101, 102, 103].

The Wetterich flow equation is a functional differential equation for the infrared regularized effective action Γ_k. This quantity depends on the momentum scale k and, in contrast to the conventional Γ, includes only the quantum corrections on scales $p^2 \gtrsim k^2$. In other words, the scale-dependent effective action represents an interpolation between micro- and macroscopic actions and satisfies following ultraviolet (UV) and infrared (IR) constrains:

$$\lim_{k \to 0} \Gamma_k = \Gamma \, ,$$
$$\lim_{k \to \Lambda} \Gamma_k = S \, , \text{ with } \Lambda \text{ an UV scale.} \quad (3.16)$$

Now, we pursue the following strategy: we start with a bare (microscopic) action S defined at a very large UV scale and then successively integrate out quantum fluctuations by lowering the momentum scale k. The way how to integrate out fluctuations is described by Wetterich equation. In the limit $k \to 0$ we obtain the macroscopic action Γ.

As the first step we extend the concept of the effective action to a scale-dependent Γ_k. For this purpose, we insert a scale-dependent infrared cutoff term $\Delta S_k[\phi]$ into the definition of $Z[J]$ in momentum space

$$Z_k[J] = \int \mathcal{D}\phi \exp[-S[\phi] + (J, \phi) - \Delta S_k[\phi]] = \exp[W_k[J]] \ , \tag{3.17}$$

Further, we apply a modified Legendre transformation to generating functional for connected correlations $W_k[J]$

$$\Gamma_k[\Phi] = -W_k[J] + (J, \Phi) - \Delta S_k[\Phi] \ . \tag{3.18}$$

Here, the field Φ is the classical field and is defined as usual

$$\Phi_a = \frac{\overrightarrow{\delta}}{\delta J_a^T} W_k[J] \ , \tag{3.19}$$

but is now a scale-dependent quantity. Since Γ_k should include only fluctuations on scales $p^2 \gtrsim k^2$, $\Delta S_k[\phi]$ has to cut off fluctuations with $p^2 < k^2$. Furthermore, $\Delta S_k[\phi]$ should be quadratic in the fields. This is required in order to obtain a one-loop flow equation. We choose the following form of $\Delta S_k[\phi]$:

$$\Delta S_k[\phi] = \frac{1}{2} \int \frac{d^d p}{(2\pi)^d} \phi_a^T(-p) R_k^{ab}(p^2) \phi_b(p) = \frac{1}{2} \phi_a^T \cdot R_k^{ab} \cdot \phi_b \ . \tag{3.20}$$

The function R_k is the so-called regulator function and needs to satisfy following relations:

$$\begin{aligned}
&\lim_{p^2/k^2 \to 0} R_k(p^2) > 0 \ , \\
&\lim_{k^2/p^2 \to 0} R_k(p^2) = 0 \ , \\
&\lim_{k \to \Lambda} R_k(p^2) \to \infty \ .
\end{aligned} \tag{3.21}$$

The first condition is necessary since $\Delta S_k[\phi]$ should regularize theory in the IR regime. The second and third conditions ensure that (3.16) is fulfilled and Γ_k has correct limiting behavior. Throughout this work we will use the linear form of cutoff functions. It means that, for fermions, R_k is given by

$$R_k^\psi(\not{p}) = Z_k^\psi \not{p} \, r_\psi\left(\frac{p^2}{k^2}\right) \ , \tag{3.22}$$

where $r_\psi(p^2/k^2)$ is a dimensionless regulator shape function. In contrast, the bosonic regulator has the following form:

$$R_k(p^2) = Z_k p^2 r\left(\frac{p^2}{k^2}\right) \ . \tag{3.23}$$

Here, Z_k^ψ and Z_k represent momentum-scale-dependent wave-function renormalizations of fermionic and bosonic fields respectively.

The regulator of bosonic fields from above is very well applicable to calculations with scalar degrees of freedom, however, the application of Eq. (3.23) to gauge theories needs some discussion: Due to the first condition in (3.21) the above regulator acts like a mass term in IR regime and therefore breaks gauge symmetry. So, we need to find a procedure to recover gauge invariance. To this end, one may find an inspiration in the conventional perturbative approach: in these calculations we always have to fix the gauge and any gauge-fixing procedure inevitably breaks gauge invariance. This problem is solved by applying Ward-Takahashi identities which allow to recover gauge-invariant results. Therefore, in the case of additional gauge-symmetry breaking coming from $R_k(p^2)$, we can introduce modified Ward-Takahashi identities [104, 105, 106, 107, 108, 109]. This procedure is very common nowadays but there are also two alternative methods: background-field formalism [86, 110] and the construction of manifestly gauge invariant and regularized renormalization flow equation [100, 111, 112]. We do not discuss details of these methods here since in this particular work we are interested in the fermionic flows. The influence of the gauge sector on the fermionic one, in particular the strong coupling α, is considered as input in this study. Thereby, we can use inputs calculated within any of mentioned methods.

The scale-dependent effective action Γ_k is now defined and we can show in analogy to Sec. 3.1 that it serves as a generator of 1PI-diagrams for the theory at the scale k. The major difference to calculations in the previous section is that we have to replace Γ by $\Gamma_k + \Delta S_k[\Phi]$. As a consequence, the inverse propagator is then given by:

$$\left(\frac{\overrightarrow{\delta}}{\delta \Phi_a^T} \Gamma_k[\Phi] \frac{\overleftarrow{\delta}}{\delta \Phi_b} \right) + R_k^{ab} = (G_k^{ab})^{-1} \ . \tag{3.24}$$

Further, we want to find how Γ_k changes if we change scale k. At this point, it is useful to introduce the dimensional scale variable t

$$t = \ln\left(\frac{k}{\Lambda}\right) \Rightarrow \partial_t = k\partial_k \ . \tag{3.25}$$

We consider the derivative of Γ_k with respect to this new scale and keep the classical field Φ fixed

$$\partial_t \Gamma_k[\Phi] \mid_\Phi = -\partial_t W_k[J] \mid_J -\partial_t \Delta S_k[\Phi] \mid_\Phi \ . \tag{3.26}$$
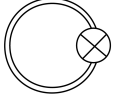
Now let us consider $\partial_t W_k[J] \mid_J$:

$$\begin{aligned} \partial_t W_k[J] \mid_J &= \exp(-W_k[J]) \, \partial_t Z_k[J] \\ &= -\frac{1}{2} \int \frac{d^d p}{(2\pi)^d} \, \partial_t R_k^{ab}(p^2) \exp(-W_k[J]) \, \frac{\overrightarrow{\delta}}{\delta J_a^T} \frac{\overrightarrow{\delta}}{\delta J_b} \exp(W_k[J]) \\ &= -\frac{1}{2} \mathrm{STr}\{G_k \, \partial_t R_k(p^2)\} - \partial_t \Delta S_k[\Phi] \mid_\Phi \ . \end{aligned} \tag{3.27}$$

Here the super-trace means summation over all possible quantum numbers of bosonic and fermionic degrees of freedom and includes integration over internal loop-momentum. We note that this trace will cause an additional minus sign in the fermionic sector. The flow equation for scale-dependent effective action is then given by:

$$\partial_t \Gamma_k[\Phi] \mid_\Phi = \frac{1}{2} \mathrm{STr} \left\{ \left(\partial_t R_k(p^2) \right) \left[\left(\frac{\overrightarrow{\delta}}{\delta \Phi^T} \Gamma_k[\Phi] \frac{\overleftarrow{\delta}}{\delta \Phi} \right) + R_k \right]^{-1} \right\} \ , \tag{3.28}$$

or, diagrammatically, by

$$\partial_t \Gamma_k[\Phi_k] = \frac{1}{2} \quad \bigcirc\!\!\!\bigotimes \quad .$$

The double line in the above representation stands for the dressed propagator of the theory at a particular momentum scale k. The circle with a cross represents an insertion of $\partial_t R_k(p^2)$ which specifies details of the momentum-shell integration.

Eq. (3.28) is known as the Wetterich equation. It is a nonlinear differential equation and has a simple one-loop structure. However, the Wetterich flow equation includes much more than the standard perturbative loop because it depends on the full dressed propagator. Indeed, one can show that integrating Eq. (3.28) leads to a summation of arbitrarily high loop orders [113].

The form of the right-hand side in Eq. (3.28) is convenient and allows a simple diagrammatic interpretation of $\partial_t \Gamma_k[\Phi]$. Nonetheless, for some particular problems it is useful to rewrite it in a bit different form:

$$\partial_t \Gamma_k[\Phi] = \frac{1}{2} \mathrm{STr}\, \tilde{\partial}_t \ln\left(\frac{\overrightarrow{\delta}}{\delta \Phi^T} \Gamma_k[\Phi] \frac{\overleftarrow{\delta}}{\delta \Phi} + R_k \right) \,, \tag{3.29}$$

where $\tilde{\partial}_t$ acts only on the regulator R_k. Here, we have dropped the index $|_\Phi$ for simplicity but we still evaluate $\Gamma_k[\Phi]$ at fixed Φ. Next, we decompose $\left(\frac{\overrightarrow{\delta}}{\delta \Phi^T} \Gamma_k[\Phi] \frac{\overleftarrow{\delta}}{\delta \Phi} + R_k \right)$ into a field-independent ($\mathcal{P}_k$) and a field-dependent ($\mathcal{F}_k$) part

$$\frac{\overrightarrow{\delta}}{\delta \Phi^T} \Gamma_k[\Phi] \frac{\overleftarrow{\delta}}{\delta \Phi} + R_k = \mathcal{P}_k + \mathcal{F}_k \,, \tag{3.30}$$

and expand Eq. (3.29) in powers of $\mathcal{F}_k / \mathcal{P}_k$:

$$\partial_t \Gamma_k[\Phi] = \frac{1}{2} \mathrm{STr}\left[\tilde{\partial}_k \left(\frac{\mathcal{F}_k}{\mathcal{P}_k} \right) \right] - \frac{1}{4} \mathrm{STr}\left[\tilde{\partial}_k \left(\frac{\mathcal{F}_k}{\mathcal{P}_k} \right)^2 \right] + \frac{1}{6} \mathrm{STr}\left[\tilde{\partial}_k \left(\frac{\mathcal{F}_k}{\mathcal{P}_k} \right)^3 \right] + \cdots \,. \tag{3.31}$$

In the above equation we have already dropped the term $\frac{1}{2} \mathrm{STr}\left[\tilde{\partial}_k \left(\mathcal{P}_k \right) \right]$ since it contributes only to the flow of the energy. The terms $(\mathcal{F}_k / \mathcal{P}_k)^n$ can be obtained by straight forward matrix multiplication and the flows for different couplings by comparing prefactors of given channels on the left hand-side with those on the right-hand side. The resulting differential equations are highly coupled. In general, there are infinitely many equations since couplings of n-point correlations depend on couplings of $(n + 1)$- and $(n + 2)$-correlations. Of course, such systems of equations are not solvable in the most cases. Therefore, we always have to restrict our calculations to some particular truncation. To find an appropriate truncation of a theory is often a quite difficult task. One possibility to check the reliability of a given truncation is to extend it to higher orders and compare results. However, such a procedure often increases the complexity of calculations dramatically and still does not ensure that taking into account even higher correlations would not change the outcome. This is due to the fact that in the expansion in Eq. (3.31) there is no small expansion parameter and we cannot neglect higher order contributions a priori. An alternative method to check the reliability of a truncation is to use the fact

that physical observables should be independent of the regularization scheme. Within the FRG approach, the regularization scheme is specified by the regulator function R_k. Therefore, we can try out different choices of R_k and compare the outcomes. If results are not sensitive to the specific choice of R_k, it indicates that the particular truncation is reliable. Also one may try to optimize the RG flow of a particular theory under a particular truncation. Thereby, one defines an optimization criterion and considers different choices of R_k. Then, those regulator functions R_k are optimized which match the given optimization criterion. There are different criteria on the market: for example one can study the gap induced in the effective propagator $\left(\left(\frac{\overrightarrow{\delta}}{\delta\Phi_a^T}\Gamma_k[\Phi]\frac{\overleftarrow{\delta}}{\delta\Phi_b}\right) + R_k^{ab}\right)^{-1}$, see Refs. [114, 115, 116]. The maximization of the gap corresponds in this procedure to the optimized choice of the regulator. As an alternative one can consider a given induced gap and compare the full theory at $k = 0$ with the regularized theory for different R_k [95]. The optimized R_k should then correspond to the regularized theory which is closest to the full one. In other words, this optimization criterion yields a shortest RG trajectory in the theory space connecting the theories at $k = \Lambda$ and at $k = 0$. For detailed discussions of the optimization of RG flows, we refer the reader to [95, 114, 115, 116].

As a concluding remark we stress that in the Wetterich equation, Eq. (3.28), we evaluate $\partial_t\Gamma_k$ at fixed Φ. Therefore, we do not take into account a possible contribution of the form $\sim \partial_t\Phi_k$. We mention here that the inclusion of this term allows to perform so-called continuous Hubbard-Stratonovich transformations in the RG flows. This technique provides a bridge between microscopic and macroscopic degrees of freedom, i.e., between quarks and gluons as fundamental microscopic particles and mesons as effective macroscopic degrees of freedom [117, 118, 119]. In this work we do not use this technique since we focus on the fermionic interactions. For more details concerning this powerful extension, we refer the reader to Refs. [91, 95, 117, 118, 119, 120, 121]. We also mention that these so-called dynamical hadronization technique was applied in numerous publications in order to study QCD and its phase diagram from first principles, see e.g. Refs. [122, 123, 124].

MODELS

As mentioned in Sec. 1, one can study the phase diagram of QCD using models which respect (some of) underlying symmetries of QCD but neglect the influence of the gluonic sector at low energy scales. One prominent example for such models is the so-called Nambu–Jona-Lasinio (NJL) model[1] [44, 45, 46, 125]. This model was originally introduced to study the phenomenon of superconductivity. However, since it includes strongly self-interacting chiral fermions, it is also very well applicable to describe the spontaneous breaking of the chiral symmetry (χSB) in QCD. In usual NJL calculations the quark self-interactions are considered as parameters which should be fitted to a given set of low-energy observables[2], see, e.g., [27, 126, 127, 128, 129, 130, 131, 132, 133, 134, 135, 136]. The simplest version of the NJL model includes only one interaction channel, the so-called scalar-pseudoscalar channel ((S−P)-channel), and is given by:

$$\mathcal{L}_{\mathrm{NJL}} = \bar{\psi}\mathrm{i}\slashed{\partial}\psi + \frac{\bar{\lambda}_\psi}{2}\left(\left(\bar{\psi}\psi\right)^2 - \left(\bar{\psi}\gamma_5\psi\right)^2\right) \; , \tag{4.1}$$

where the coupling $\bar{\lambda}_\psi$ represents the strength of the (S−P)-channel. Here, we have formulated this Lagrangian and the corresponding (S−P)-channel for only one massless quark flavor. The strength of the coupling $\bar{\lambda}_\psi$ is crucial for our discussion since if $\bar{\lambda}_\psi$ becomes strong enough, the chiral condensate is generated and we observe spontaneous chiral symmetry breaking.

4.1 POLYAKOV-LOOP EXTENDED NJL MODEL

4.1.1 *Polyakov Loop*

While the above NJL model already provides us with insights into the formation of the chiral condensate and into the dynamical generation of the constituent quark mass, it completely ignores the gluonic sector of QCD and, therefore, the deconfinement phase transition. Though, there are two observations which indicate that the gauge dynamics considerably influence the quark matter sector and, therefore, the chiral phase transition. First, the pseudo-critical temperatures for the chiral and the deconfinement phase transitions found in lattice QCD simulations at zero chemical potential are remarkably similar,

---

1 As alternative to the NJL model, one can use its bosonized version, the so-called quark-meson (QM) model. This model is derived from NJL Lagrangian using Hubbard-Stratonovich transformation and is introduced in Sec. 4.2.

2 The same is valid for Polyakov-loop extended version of NJL model, see also Sec. 4.1, and for (Polyakov-loop extended) QM model, see Sec. 4.2. In QM-type models, however, one fits bosonic interactions and Yukawa-type interactions.

$\langle \mathrm{P}\,[A_0]\rangle = 0$	confinement	center symmetric system
$\langle \mathrm{P}\,[A_0]\rangle \neq 0$	deconfinement	SSB of center symmetry

TABLE 4.1: An overview over the Polyakov loop.

see, e.g., Refs. [49, 50, 51, 52, 53]. Second, we expect that the quark self-interactions are dynamically generated by the gauge fields. This expectation was confirmed in numerous renormalization group (RG) studies [72, 73, 117, 123, 137, 138]. We present and discuss the corresponding mechanism in Sec. 5.2. These two facts already suggest a possible deeper relation between chiral and confining dynamics. Such a relation was already found and discussed in [69, 70] in detail for zero chemical potential, $\mu = 0$. In this chapter we will extend this analysis to finite values of μ.

A standard tool to incorporate some aspects of the gauge dynamics into the NJL/QM models is to introduce a background field $\langle A_0 \rangle$. This field is related to the Polyakov loop [139, 140] which is primarily used in lattice QCD as an order parameter for the deconfinement phase transition:

$$\mathrm{P}\,[A_0] = \mathrm{tr}_\mathrm{F}\,[L\,[A_0]] = \frac{1}{N_\mathrm{c}}\,\mathrm{tr}_\mathrm{F}\left[\mathcal{P}\exp\left(\mathrm{i}\bar{g}\int_0^\beta \mathrm{d}x_0 A_0(x)\right)\right]\,, \tag{4.2}$$

where N_c is the number of colors, β represents the inverse temperature, and $\mathcal{P}$ is the path ordering operator. The index F of the trace denotes that A_0 is in the fundamental representation. One can interpret the Polyakov loop as a world line of a infinite heavy (static) quark which propagates only in the periodic time direction. Hence, the negative logarithm of the expectation value of the Polyakov loop, $\langle \mathrm{P}\,[A_0]\rangle$, is proportional to the free energy of an isolated quark , see also Refs. [141, 142, 143]. In the case of confinement[3], all observed particles should be color-neutral and, therefore, the free energy of a single quark is infinite. Thus, $\langle \mathrm{P}\,[A_0]\rangle$ vanishes in the confined phase.

Further, one can show that in the absence of thermal quarks the Polyakov loop "measures" the center symmetry of the gauge theory, see, e.g., [142, 143] and Sec. 2.2.2. In short, the center symmetry means that the system is invariant under transformation $\mathrm{U} \to z\mathrm{U}$, with U being an element of the special unitary group $\mathrm{U} \in \mathrm{SU}(N_\mathrm{c})$ and $z \in Z(N_\mathrm{c})$ its center. Thereby, the center of a group defines the set of all elements which commute with all other elements of the group. Any gauge invariant action is also invariant under the central transformation $\mathrm{U} \to z\mathrm{U}$. However, the Polyakov loop is not: $\mathrm{P}\,[A_0] \to z\,\mathrm{P}\,[A_0]$. As a consequence, a finite expectation value of the Polyakov loop corresponds to the spontaneous breaking of the center symmetry. A summary on $\mathrm{P}\,[A_0]$ and its connection to the center symmetry and the deconfinement phase transition can be found in Tab. 4.1.

In the presence of dynamical quarks, there is no center symmetry and $\langle \mathrm{P}\,[A_0]\rangle \neq 0$. Thus, there is no spontaneous symmetry breaking and no phase transition. A possible explanation of this behavior is that the dynamic color sources generated by pair production screen the color of static external sources [144]. As a consequence, the infinite single-quark free energy is spoiled and there is no real color confinement. Nonetheless, there is still a

---

3 Considering the Polyakov loop as an order parameter for deconfinement phase transition, we always speak about color confinement (or deconfinement).
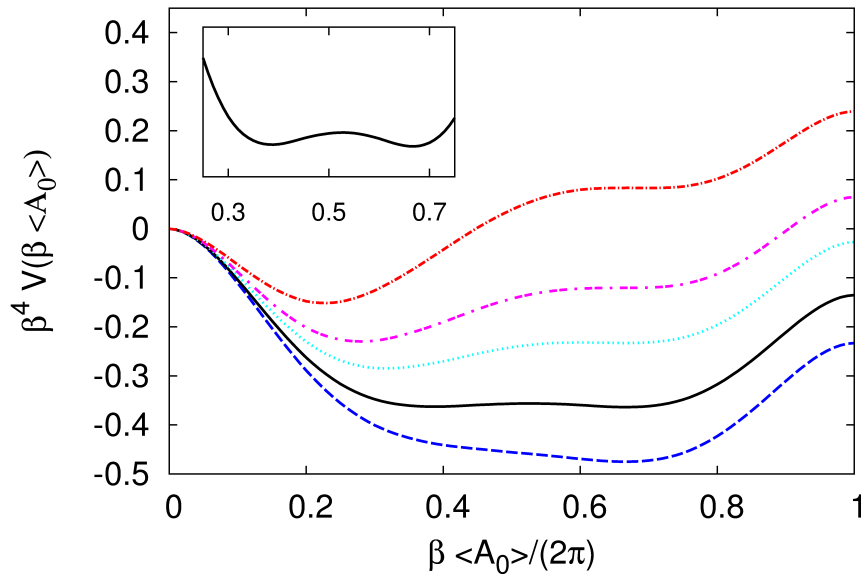
FIGURE 4.1: The normalized order-parameter potential obtained for a SU(3) Yang-Mills theory from a first-principle RG study [146]. For SU(3) Yang-Mills theory the Cartan subalgebra is two-dimensional. Here, only the relevant direction of the Cartan subalgebra is shown. The upper potential corresponds to $T = 310$ MeV and the lower one to $T = 285$ MeV. The phase transition takes place at $T_d \approx 290$ MeV and turns out to be a transition of first order.

crossover between confined and deconfined phases which turns out to be rather sharp, see, e.g., [27, 49, 131, 145]. Hence, $\langle \mathrm{P}\,[A_0] \rangle$ still serves as an approximate order parameter.

While in lattice QCD $\langle \mathrm{P}\,[A_0] \rangle$ can be calculated directly, in Polyakov-loop extended NJL model (PNJL) and Polyakov-loop extended QM model (PQM) one needs $\mathrm{P}\,[\langle A_0 \rangle]$ in order to define the effective Polyakov potential. These two quantities are related via the Jensen identity:

$$\mathrm{P}\,[\langle A_0 \rangle] \geq \langle \mathrm{P}\,[A_0] \rangle \;. \tag{4.3}$$

To fix the effective Polyakov potential in PNJL/PQM studies one applies an approximation

$$\mathrm{P}\,[\langle A_0 \rangle] = \langle \mathrm{P}\,[A_0] \rangle \quad \text{and} \quad \mathrm{tr}_{\mathrm{F}}\,[L\,[\langle A_0 \rangle]^n] = N_{\mathrm{c}} \left(\frac{\mathrm{P}\,[\langle A_0 \rangle]}{N_{\mathrm{c}}} \right)^n \;, \tag{4.4}$$

and fits the effective potential to results obtained from lattice QCD [27, 126, 127, 128, 129, 130, 131, 132, 133, 134, 135, 136]. Even though the parametrization of the effective Polyakov potential is not unique, the results for vanishing chemical potential are rather stable to variations of the parametrization. Also, in the case $\mu = 0$ it was found that the (pseudo-)critical temperatures of the deconfinement and the chiral phase transitions are very similar in PNJL/PQM models. This is in great agreement with results from lattice QCD, e.g., Ref. [49, 50, 51, 52, 53]. However, at finite values of the chemical potential the results from PNJL/PQM models seem to be quite sensitive to the choice of the parametrization of the effective potential, see, e.g., [147].

On the other hand, $\mathrm{P}\,[\langle A_0 \rangle]$ itself is an order parameter for the deconfinement phase transition as it was shown in [146, 148] for Polyakov-Landau-DeWitt gauge. Thereby, $\langle A_0 \rangle$ is an element of the Cartan subalgebra and is associated with the ground state of

the corresponding order-parameter potential. This potential was calculated in the first-principle RG studies in [146, 149], see also Fig. 4.1. Now, it seems to be very natural to use this result for $P\left[\langle A_0\rangle\right]$ to incorporate some aspects of the confinement in the PNJL/PQM models. Applying these strategy, we do not need to introduce the effective Polyakov potential fitted to lattice results and, therefore, omit the ambiguity in the parametrization.

4.1.2 *PNJL-Model Lagrangian*

The (scale-dependent) effective action of the PNJL model with only the (S−P)-channel is defined as:

$$\Gamma_k = \int \mathrm{d}^4 x \, \left\{ \bar{\psi}(\mathrm{i}Z_\psi \slashed{\partial} + Z_\psi \bar{g} \gamma_0 \langle A_0 \rangle + \mathrm{i}\gamma_0 \mu)\psi + \frac{\bar{\lambda}_\psi}{2} \left[(\bar{\psi}\psi)^2 - (\bar{\psi}\vec{\tau}\gamma_5\psi)^2 \right] \right\} \, . \qquad (4.5)$$

We consider a model with $N_\mathrm{f} = 2$ massless quark flavors and N_c colors at finite chemical potential μ and finite temperature T. The vector $\vec{\tau}$ contains the Pauli matrices and describes the coupling of spinors in flavor space. The coupling $\bar{\lambda}_\psi$ represents the strength of the effective quark self-interactions and is a scale-dependent quantity. In the above action, Z_ψ stands for the wave-function renormalization of quarks. In general, this quantity is also scale dependent and is linked to the quark anomalous dimension $\eta_\psi = -\partial_t \ln Z_\psi$. However, for vanishing background field $\langle A_0 \rangle$ this anomalous dimension has been find to be small [117, 123, 150, 151]. Therefore, we use $Z_\psi = 1$ in our further calculations.

In Eq. (4.5) we use only one interaction channel for quarks, the scalar-pseudoscalar channel. Such a simple ansatz suffers from a problem called Fierz ambiguity, see App. B.2. In general, this ambiguity comes from the fact that any $d \times d$-matrix M can be expanded in terms of a complete orthonormal set of $d \times d$-matrices. This transformation causes an algebraic reordering of the quark fields and, therefore, the emergence of additional interaction channels which preserve the underlying symmetries of the model. These new channels can be generated by quantum effects and can influence the phase diagram of (P)NJL model [57, 152, 153]. One simple example for a Fierz transformation can be found in App. B.2. Even though our ansatz suffers from the Fierz ambiguity, the major aim of this chapter is to understand the relation between the deconfinement and the chiral phase transition on a qualitative level. For more sophisticated ansatz for effective quark self-interactions, we refer the reader to Chap. 5.

In our particular calculations we consider the 4-quark coupling $\bar{\lambda}_\psi$ in the point-like limit, i.e., we drop a possible momentum dependence of this coupling: $\bar{\lambda}_\psi(|p| \ll k)$. Obviously, this approximation cannot be applied in the chirally broken regime since it does not give us access to the low-energy observables, such as the mesonic spectrum[4]. Nonetheless, for chirally symmetric regime the point-like limit seems to be a reasonable approximation which allows us to study how the system approaches the chiral phase boundary [73, 154, 123].

---

[4] Mesons (Goldstone bosons) correspond to momentum singularities in the 4-point functions.

In Sec. 4.2 we will partially resolve the momentum dependence of the 4-quark interaction by means of Hubbard-Stratonovich transformation, i.e, we will introduce the PQM model which is given by the following effective action:

$$
\Gamma_k = \int \mathrm{d}^4x \ \left\{ \bar{\psi}(\mathrm{i}Z_\psi \slashed{\partial} + Z_\psi \bar{g}\gamma_0 \langle A_0 \rangle + \mathrm{i}\gamma_0\mu)\psi \right.
$$
$$
\left. + \frac{1}{2} Z_\varphi (\partial_\mu \bar{\varphi})^2 + \mathrm{i}\bar{h}\bar{\psi}(\sigma + \mathrm{i}\vec{\tau}\cdot\vec{\pi}\gamma_5)\psi + U(\bar{\varphi}^2) \right\} \ ,
\tag{4.6}
$$

with $\bar{\varphi} = (\sigma, \vec{\pi})^T$ and

$$
\bar{\lambda}_\psi = \frac{\bar{h}^2}{\bar{m}^2} \ .
\tag{4.7}
$$

For more details, see Sec. 4.2. The PQM model will allow us to gain access to low-energy observables, e.g., mesonic and constituent quark masses. Also, it provides us with a condition for the spontaneous chiral symmetry breaking in PNJL model: Similarly to the linear sigma-model in Sec. 2.2.1, the chiral symmetry breaking in PQM model is triggered by $\bar{m}^2 = 0$. Consequently, due to the mapping identity (4.7), the chiral symmetry breaking in PNJL model takes place if $\bar{\lambda}_\psi \to \infty$. In this section we use this condition in order to identify the breaking of the chiral symmetry.

We also mention that in addition to the 4-quark coupling $\bar{\lambda}_\psi$, higher-order interactions, e.g., 8-quark interactions are generally allowed. However, the RG flow of $\bar{\lambda}_\psi$ is completely decoupled from higher-order channels as long one considers the chiral limit, the chirally symmetric regime and the point-like limit. So, since we do not aim to study the chirally broken regime in this section, we conclude that the truncation in Eq. (4.5) is sufficient for our purpose.

4.1.3 *Flow Equation for Coupling $\bar{\lambda}_\psi$ and RG Fixed-Point Analysis*

Starting with the action (4.5) and using the Wetterich equation (3.28), we can calculate the RG flow for the coupling $\bar{\lambda}_\psi$. Thereby, we use the expansion of the Wetterich equation presented in Eq. (3.31). We mention already at this point that since we have to project the right-hand side of the Wetterich equation onto the channel $\left[(\bar{\psi}\psi)^2 - (\bar{\psi}\vec{\tau}\gamma_5\psi)^2\right]$, all contributions relevant for the flow of $\bar{\lambda}_\psi$ are included in the term $-\frac{1}{4}\mathrm{STr}\left[\tilde{\partial}_k \left(\frac{\mathcal{F}_k}{\mathcal{P}_k}\right)^2\right]$.

Now, let us consider the second derivative of the effective action with respect to the fermionic fields:

$$
\frac{\overrightarrow{\delta}}{\delta\Phi^T}\Gamma_k[\Phi]\frac{\overleftarrow{\delta}}{\delta\Phi} = \begin{pmatrix} \overrightarrow{\delta}_{\psi^T_{-p}}\Gamma_k\overleftarrow{\delta}_{\psi_{p'}} & \overrightarrow{\delta}_{\psi^T_{-p}}\Gamma_k\overleftarrow{\delta}_{\bar{\psi}^T_{-p'}} \\ \overrightarrow{\delta}_{\bar{\psi}_p}\Gamma_k\overleftarrow{\delta}_{\psi_{p'}} & \overrightarrow{\delta}_{\bar{\psi}_p}\Gamma_k\overleftarrow{\delta}_{\bar{\psi}^T_{-p'}} \end{pmatrix} \ .
\tag{4.8}
$$

In our particular calculations we use homogeneous background fields $\bar{\Psi}$ and Ψ:

$$
\bar{\psi}_p = \bar{\Psi}(2\pi)^4\delta^{(4)}(p) \qquad \text{and} \qquad \psi_p = \Psi(2\pi)^{(4)}\delta^4(p) \ .
\tag{4.9}
$$

Using the linear cutoff function for fermions, Eq. (E.1), the field-dependent part of the inverse dressed propagator $\left(\frac{\overrightarrow{\delta}}{\delta\Phi^T}\Gamma_k[\Phi]\frac{\overleftarrow{\delta}}{\delta\Phi} + R_k\right)$ reads

$$
\mathcal{F}_k = -\bar{\lambda}_\psi \begin{pmatrix} \mathcal{F}_{11} & \mathcal{F}_{12} \\ \mathcal{F}_{21} & \mathcal{F}_{22} \end{pmatrix}(2\pi)^4\delta^{(4)}(p-p') \ ,
\tag{4.10}
$$

with

$$
\begin{aligned}
(\mathcal{F}_{11})_{ij}^{ab} &= \bar{\Psi}_{a,i}^T \bar{\Psi}_{b,j} - \tau_y^{ca} \gamma_5^T \bar{\Psi}_{c,i}^T \bar{\Psi}_{d,j} \gamma_5 \tau_y^{db} \ , \\
(\mathcal{F}_{22})_{ij}^{ab} &= \Psi_{a,i} \Psi_{b,j}^T - \tau_y^{ac} \gamma_5 \Psi_{c,i} \Psi_{d,j}^T \gamma_5^T \tau_y^{bd} \ , \\
(\mathcal{F}_{12})_{ij}^{ab} &= \Big[(\bar{\Psi}\Psi)(\mathbb{1}_{\mathrm{f}})^{ab}(\mathbb{1}_{\mathrm{c}})_{ij} + \Psi_{a,i} \bar{\Psi}_{b,j} \\
&\quad - (\bar{\Psi}\tau_y\gamma_5\Psi)\gamma_5\tau_y^{ab}(\mathbb{1}_{\mathrm{c}})_{ij} - \tau_y^{ac}\gamma_5\Psi_{c,i}\bar{\Psi}_{d,j}\gamma_5\tau_y^{db} \Big]^T = -(\mathcal{F}_{21}^T)_{ij}^{ab} \ ,
\end{aligned}
$$
(4.11)

where flavor and color indices are represented by $(a, b, \ldots)$ and $(i, j, \ldots)$ correspondingly. The index $y = \{1, 2, 3\}$ indicates a summation over the Pauli matrices.

The field-independent part, $\mathcal{P}_k$, assumes the form:

$$
\mathcal{P}_k = \begin{pmatrix} 0 & -\left(\slashed{p}^T (1 + r_\psi(y)) + \gamma_0^T \alpha_+ \right) \\ -(\slashed{p}(1 + r_\psi(y)) + \gamma_0 \, \alpha_-) & 0 \end{pmatrix} (2\pi)^4 \delta^{(4)}(p - p') \ ,
$$
(4.12)

where $\alpha_\pm = p_0 \pm (\bar{g} \langle A_0 \rangle + \mathrm{i}\mu)$ and $y = \vec{p}^{\,2}/k^2$. This matrix is used to calculate the propagator matrix $\mathcal{P}_k^{-1}$. For a detailed description of calculation of $\mathcal{P}_k^{-1}$, we refer the reader to [155, 156]. Here we only sketch the basic idea: First, we use the fact that the background field $\langle A_0 \rangle$ is an element of the Cartan subalgebra. Hence, we can parametrize it as follows:

$$
\bar{g} \langle A_0 \rangle = 2\pi T \sum_{t^z \in \text{Cartan}} t^z \phi^{(z)} = 2\pi T \sum_{t^z \in \text{Cartan}} t^z \nu^{(z)} |\phi| \ ,
$$
(4.13)

where t^z represent the $\mathrm{SU}(N_{\mathrm{c}})$ generators in fundamental representation, $\nu^{(z)}$ the unity vector and $\phi^{(z)}$ the coordinates of $\langle A_0 \rangle$. Note that the dimension of the Cartan subalgebra is $N_{\mathrm{c}} - 1$. From this transformation one clearly sees that the matrix $\mathcal{P}_k$ is not proportional to unity in the color space and its inversion becomes, in general, a non-trivial task. However, $\mathcal{P}_k^{-1}$ itself is an element of the Cartan subalgebra. So, it can by expanded using the complete orthogonal basis of the Cartan subalgebra given by the identity and the generators $t^z \in$ Cartan:

$$
\mathcal{P}_k^{-1} = \frac{1}{N_{\mathrm{c}}} \mathrm{tr}_{\mathrm{F}}[\mathcal{P}_k^{-1}] \mathbb{1}_{\mathrm{c}} + 2 \sum_{t^z \in \text{Cartan}} \mathrm{tr}_{\mathrm{F}}[\mathcal{P}_k^{-1} t^z] \, t^z \ ,
$$
(4.14)

where traces are taken in the fundamental representation. As a consequence any matrix contributing to the right-hand side of Eq. (3.31) is either proportional to $\mathbb{1}_{\mathrm{c}}$ or belongs to the Cartan subalgebra. Thus, all these matrices are commuting hermitian matrices and share the same set of eigenvectors. Therefore, they can be diagonalized simultaneously. In particular, this observation allows us to replace the color trace by a sum of the eigenvalues of the corresponding matrices. For this purpose, we introduce the eigenvalues ν_l of the matrix $t^z \nu^{(z)}$ from Eq. (4.13):

$$
\nu_l = \mathrm{spec}\{(t^z \nu^{(z)})_{ij} \mid \nu^2\} \ .
$$
(4.15)

Applying this technique we have calculated the relevant term of the expansion in Eq. (3.31), namely $-\frac{1}{4}\mathrm{STr}\left[\tilde{\partial}_k \left(\frac{\mathcal{F}_k}{\mathcal{P}_k} \right)^2 \right]$. Besides the color trace, this calculation also includes flavor
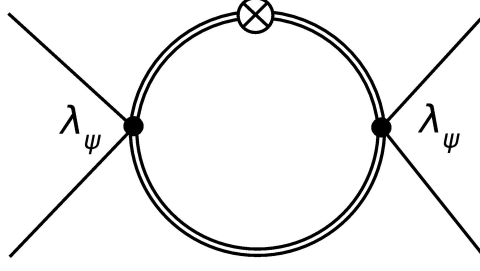
FIGURE 4.2: Graphical representation of the λ_ψ^2-term on the right-hand side of Eq. (4.18). The double lines denote fully dressed fermionic propagators. The white circle with a cross stands for $\partial_t R_k$.

and Dirac traces, integration over internal momenta and the appropriate projection onto the channel $\left[(\bar{\psi}\psi)^2 - (\bar{\psi}\vec{\tau}\gamma_5\psi)^2\right]$. As result we obtain:

$$\partial_t \bar{\lambda}_\psi = 4\left(2 + \frac{1}{N_c}\right)\bar{\lambda}_\psi^2 \sum_{l=1}^{N_c} \tilde{\partial}_t \int \frac{d^4 p}{(2\pi)^4} \sum_\pm \frac{1}{\vec{p}^2(1 + r_\psi)^2 + (p_0 \pm (2\pi T \nu_l|\phi| + i\mu))^2} \, ,$$

$$(4.16)$$

where $\tilde{\partial}_t$ acts only on the regulator shape function r_ψ and $\nu_l|\phi|$ represents the dimensionless coordinates of the background field $\langle A_0 \rangle$. Since we are interested in finite temperatures, we replace the zero component of the Euclidean momenta, p_0, by Matsubara frequencies:

$$p_0^2 \to \nu_n^2 \qquad \text{and} \qquad \int_{-\infty}^{\infty} \frac{dp_0}{(2\pi)} \cdots \overset{p_0^2 \to \nu_n^2}{\to} T\sum_n \cdots . \tag{4.17}$$

Since n runs over all integer values from $-\infty$ to $+\infty$, the difference between $\pm$-contributions disappears. Applying the optimized regulator shape function for fermions from Eq. (E.3) [157], we end with the following flow equation for the dimensionless coupling $\lambda_\psi = Z_\psi^{-2} k^2 \bar{\lambda}_\psi$:

$$\partial_t \lambda_\psi = 2\lambda_\psi - 16\, v_4 \left(2 + \frac{1}{N_c}\right)\sum_{l=1}^{N_c} l_1^{(\mathrm{F})}(\tau, \tilde{\mu} - i2\pi\tau\nu_l|\phi|, 0)\lambda_\psi^2 \, , \tag{4.18}$$

with $\tau = T/k$ the dimensionless temperature, $\tilde{\mu} = \mu/k$ the dimensionless chemical potential and v_4 a dimensional factor specified in App. E. We remind the reader that we use $Z_\psi = 1$ in this calculation. The threshold function $l_1^{(\mathrm{F})}$ in Eq (4.18) includes the temperature and chemical-potential dependence as well as the dependence on the input for $\nu_l|\phi|$ and on the regularization scheme. This function corresponds to the one-particle irreducible (1PI) diagram presented in Fig. 4.2 and can be calculated using the procedure described in App. E.

Now, let us discuss the fixed-point structure of the flow equation (4.18). Thereby, we proceed mainly as in Refs. [69, 70] but expand our analysis to finite values of chemical potential. The flow equation (4.18) has two fixed points which can be calculated setting $\partial_t \lambda_\psi = 0$. The first fixed point, $\lambda_\psi^G = 0$, is a trivial infrared (IR) attractive Gaussian fixed point. It corresponds to the interactionless theory. The second fixed point, $\lambda_\psi^*(\tau, \tilde{\mu} - i2\pi\tau\nu_l|\phi|, 0)$, is non-trivial and IR repulsive. Its particular value depends on the parameters τ and $\tilde{\mu}$ and on the coordinates $\nu_l|\phi|$ of the background field $\langle A_0 \rangle$. To understand the properties
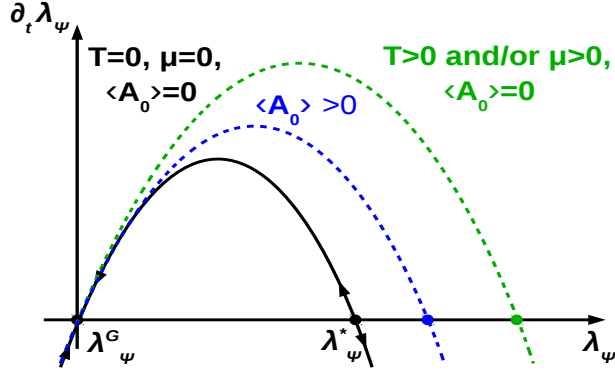
FIGURE 4.3: Sketch of the flow of the 4-quark coupling λ_ψ for different sets of parameters. The black solid line corresponds to $T = \mu = \langle A_0 \rangle = 0$, the green dashed one to finite temperature and chemical potential but vanishing $\langle A_0 \rangle$ (deconfined phase). The blue dashed line represents finite temperature, finite chemical potential and finite $\langle A_0 \rangle$ (confined phase). For $N_c \to \infty$, the blue and the black line coincide.

of the non-trivial fixed point, let us first start with the case of vanishing temperature and chemical potential as well as vanishing background field $\langle A_0 \rangle$, see also the black solid line in the Fig. 4.3. In this limit, one can show that $\lambda_\psi^*(\tau, \tilde{\mu} - \mathrm{i}2\pi\tau\nu_l|\phi|, 0)$ takes the form

$$\lambda_\psi^* \equiv \lambda_\psi^*(0,0,0) = \frac{1}{8\, v_4 (2N_c + 1) l_1^{(\mathrm{F})}(0,0,0)} = \frac{6\pi^2}{2N_c + 1} \ , \tag{4.19}$$

where we have used the limiting behavior of the function $l_1^{(\mathrm{F})}$ valid for our choice of regularization scheme, see App. E. At this point we would like to emphasize that even though the particular value of λ_ψ^* is regularization-scheme dependent, the very existence of the non-trivial fixed point is a universal property of our model.

Now, we would like to discuss how different initial values of coupling λ_ψ at the ultraviolet (UV) scale Λ_{UV} influence the model outcome. Choosing an initial value $\lambda_\psi^{\mathrm{UV}} < \lambda_\psi^*$ we find that the model is attracted by the Gaussian fixed point[5] and becomes chirally symmetric in the IR regime. In contrast, if $\lambda_\psi^{\mathrm{UV}} > \lambda_\psi^*$, then the coupling λ_ψ grows rapidly and even diverges at some finite scale k_{cr}. As we have seen above, the diverging behavior of the 4-quark coupling is associated with spontaneous breaking of the chiral symmetry. Thus, the value of the non-trivial fixed point λ_ψ^* separates regimes with broken and restored chiral symmetry in our approach.

The critical scale k_{cr} is related to the value of low-energy observables $\mathcal{O}$ as follows:

$$\mathcal{O} \sim k_{\mathrm{cr}}^{d_\mathcal{O}} \ , \tag{4.20}$$

with $d_\mathcal{O}$ the canonical mass dimension of the observable. The analytical expression for k_{cr} at vanishing T, μ and $\langle A_0 \rangle$ is given by

$$k_{\mathrm{cr}} = \Lambda_{\mathrm{UV}} \left(\frac{\lambda_\psi^{\mathrm{UV}} - \lambda_\psi^*}{\lambda_\psi^{\mathrm{UV}}} \right)^{1/2} \Theta\left(\lambda_\psi^{\mathrm{UV}} - \lambda_\psi^* \right) \ . \tag{4.21}$$

---

5 In Fig. 4.3 the direction of the RG flow towards IR regime is denoted by arrows.

This result shows that the value of the critical scale k_{cr}^2 is proportional to the distance of the initial value λ_ψ^{UV} from the value of the non-trivial fixed point λ_ψ^*. Consequently, increasing λ_ψ^{UV} leads to increasing k_{cr} and to an increase in the values of the low-energy observables, such as the pion decay constant f_π or the critical temperature of the chiral phase transition T_χ.

Since we are aiming at a model which is chirally broken in the limit $T \to 0$, $\mu \to 0$, we shall use some value $\lambda_\psi^{\text{UV}} > \lambda_\psi^*$. For calculations at finite temperature, chemical potential and background field, we keep this initial condition fixed. This approach ensures a proper study of effects caused by parameters variation. In Fig. 4.3 we sketch how different parameters influence the flow equation and the (pseudo-)fixed-point structure. First, let us discuss the impact of finite temperature. For increasing T we observe that the pseudo fixed point is shifted to larger values. Hence, at some critical value T_χ it passes the initial value λ_ψ^{UV} and the theory evolves in the direction of the Gaussian fixed point in the RG flow. Therefore, for $T > T_\chi$ our model is in the chirally symmetric regime. A similar effect is also caused by increasing chemical potential. Thereby, we observe that for any $0 \leq T < T_\chi$ there is a T-dependent finite value of chemical potential for which the pseudo fixed point is located at infinity. Consequently, there is only the Gaussian fixed point which attracts our model towards chirally symmetric regime. To illustrate this rather complex effect, let us consider the special case $T \to 0$. In this situation the threshold function $l_1^{(\text{F})}$ behaves as a Theta-function, see App. E.3:

$$\lim_{\tau \to 0} l_1^{(\text{F})}(\tau, \tilde{\mu}, 0) = \frac{1}{6} \frac{v_3}{v_4} \Theta(1 - \tilde{\mu}) \ . \tag{4.22}$$

Therefore, the fixed-point structure in this case is the same as for $T = 0$, $\mu = 0$ as long the RG scale $k > \mu$. For $k < \mu$, the right-hand side of Eq. (4.18) becomes linear in λ_ψ and has a positive slope. It means that the model is attracted by the Gaussian fixed point if we further integrate out fluctuations. Thus, if the value of chemical potential is large enough $\mu \geq \mu_\chi$, λ_ψ at $k \to 0$ becomes sufficiently small and no quark condensate can be produced. So, we observe restoration of the chiral symmetry.

As next, we discuss the influence of finite background field $\langle A_0 \rangle$ on the fixed-point structure. $\langle A_0 \rangle$ enters our discussion as an external input parameter and serves as the order parameter for the deconfinement phase transition. As we have already mentioned, the confined phase (or, equivalently, the center symmetric ground state of the model) is indicated by

$$\mathrm{P}\left[\langle A_0 \rangle\right] = \langle \mathrm{P}\left[A_0\right] \rangle = 0 \ . \tag{4.23}$$

Actually, in pure SU(N_{c}) Yang-Mills theory the trace of powers of the Polyakov variable $L\left[\langle A_0 \rangle\right]$ transforms in the similar way as the Polyakov loop under the center transformation:

$$\mathrm{tr}_{\text{F}}\left[L\left[\langle A_0 \rangle\right]^n\right] \quad \to \quad z^n \, \mathrm{tr}_{\text{F}}\left[L\left[\langle A_0 \rangle\right]^n\right] \ . \tag{4.24}$$

Therefore, one finds for the confined phase

$$\mathrm{tr}_{\text{F}}\left[L\left[\langle A_0 \rangle\right]^n\right] = 0 \ , \tag{4.25}$$

with $(n \bmod N_{\text{c}}) = 1, \ldots N_{\text{c}} - 1$. This condition uniquely determines[6] the position $\langle A_0 \rangle$ of the ground state in the confined regime [146, 149]. On the other hand, in the deep

---

6 Up to center transformations.

deconfined phase we have $\langle A_0 \rangle \to 0$ and $\mathrm{P}\,[\langle A_0 \rangle] \to 1$, see, e.g., Refs. [146, 148, 149, 158]. Consequently, for temperatures much higher than the critical temperature of the deconfinement phase transition, the background field $\langle A_0 \rangle$ does not change the pseudo fixed-point structure:

$$\lambda_\psi^*(\tau, \tilde{\mu} - \mathrm{i}2\pi\tau\nu_l|\phi|, 0) \to \lambda_\psi^*(\tau, \tilde{\mu}, 0) \quad \text{for} \quad T \gg T_d \,. \tag{4.26}$$

Reducing the temperature leads to confinement and to finite $\langle A_0 \rangle$. In this case, the pseudo fixed point $\lambda_\psi^*(\tau, \tilde{\mu} - \mathrm{i}2\pi\tau\nu_l|\phi|, 0)$ is computed to:

$$
\begin{aligned}
\lambda_\psi^*(\tau, \tilde{\mu} - \mathrm{i}2\pi\tau\nu_l|\phi|, 0) &= \left(8v_4 \left(2 + \frac{1}{N_\mathrm{c}} \right) \sum_{l=1}^{N_\mathrm{c}} l_1^{(\mathrm{F})}(\tau, \tilde{\mu} - \mathrm{i}2\pi\tau\nu_l|\phi|, 0) \right)^{-1} \\
&= \left\{ \frac{1}{\lambda_\psi^*} + \frac{1}{6\pi^2} \left(2 + \frac{1}{N_\mathrm{c}} \right) \sum_{n=1}^{\infty} (-N_\mathrm{c})^{-n} \left(1 + \frac{n}{\tau} \right) \right. \\
&\quad \left(\exp\left[-\frac{n(1+\tilde{\mu})}{\tau} \right] \mathrm{tr}_\mathrm{F}\left[L\,[\langle A_0 \rangle]^n \right] + \right. \\
&\quad \left. \left. \exp\left[-\frac{n(1-\tilde{\mu})}{\tau} \right] \mathrm{tr}_\mathrm{F}\left[L^\dagger\,[\langle A_0 \rangle]^n \right] \right) \right\}^{-1} \,.
\end{aligned}
\tag{4.27}
$$

To obtain this result, we have employed the regularization scheme described in App. E. Nonetheless, one can argue that the general form of this expression holds for any type of regulator functions [69]. We have also found that in the limit of vanishing chemical potential Eq. (4.27) coincides with the result which was already obtained in [69, 70]. The above result is important for our understanding of the limit of infinite many colors. For $N_\mathrm{c} \to \infty$, a trace of any power of the Polyakov variable vanishes in the confined phase, at least as long one considers a pure Yang-Mills theory[7]. Thus, we find

$$\lim_{N_\mathrm{c} \to \infty} \lambda_\psi^*(\tau, \tilde{\mu} - \mathrm{i}2\pi\tau\nu_l|\phi|, 0) \bigg|_{T \lesssim T_d} = \lambda_\psi^* \,. \tag{4.28}$$

Arguing in the same way, we find

$$\lim_{N_\mathrm{c} \to \infty} \partial_t \lambda_\psi(\tau, \tilde{\mu} - \mathrm{i}2\pi\tau\nu_l|\phi|, 0) \bigg|_{T \lesssim T_d} = \partial_t \lambda_\psi(0, 0, 0) \,. \tag{4.29}$$

This observation means that for infinite many colors the question of whether the spontaneous chiral symmetry breaking is realized or not is independent of temperature and chemical potential but is related only to the choice of $\lambda_\psi^{\mathrm{UV}}$ compared to λ_ψ^*. Even more, as long as the initial value of the coupling is chosen such that $\lambda_\psi^{\mathrm{UV}} \geq \lambda_\psi^*$, the appearance of the deconfinement phase transition automatically causes the chiral phase transition. Hence, we observe

$$T_\chi \geq T_d \,, \tag{4.30}$$

for $N_\mathrm{c} \to \infty$ and $\lambda_\psi^{\mathrm{UV}} \geq \lambda_\psi^*$, see also Ref. [126]. Thus, there is a dynamical locking mechanism which enforces the spontaneous breaking of the chiral symmetry in the matter

---

7 In our further considerations we assume that the presence of dynamical quarks does not impact the ground state value of $\langle A_0 \rangle$ obtained in the pure Yang-Mills theory. This assumption is based on the fact that for dynamical quarks we can still expect $\mathrm{P}\,[\langle A_0 \rangle] \ll 1$ in the confined phase.

sector if the gauge sector is confined [69]. One can think about this mechanism in terms of thermal quark-fields fluctuations. In general, they tend to restore the chiral symmetry but since they are directly linked to the background field $\langle A_0 \rangle$, they are suppressed in the confined phase.

The locking mechanism described above suggests that there is a window in the parameter space of $\lambda_\psi^{\mathrm{UV}}$ where critical temperatures are approximately equal. This window arises from the fact that there are values of $\lambda_\psi^{\mathrm{UV}}$ which would lead to $T_\chi < T_d$ if the background field $\langle A_0 \rangle$ is decoupled from the matter sector. However, due to the locking mechanism the chiral critical temperature is shifted to larger values such that $T_\chi \geq T_d$. Since $\lambda_\psi^{\mathrm{UV}}$ determines the values of low energy-observables, the window in the parameter space of $\lambda_\psi^{\mathrm{UV}}$ can be translated into a corresponding window in the values of low-energy observables. We will use this fact in our calculations in Sec. 4.2.

4.1.4 *Numerical Results*

Now, let us consider the physical number of colors, $N_{\mathrm{c}} = 3$. In this situation, the traces of powers of the Polyakov variable in Eq. (4.27) with ($n \bmod N_{\mathrm{c}}$) $= 0$ provide a finite contribution to the value of the pseudo fixed point. Even though the pseudo fixed point does not coincide with λ_ψ^* in the confined phase anymore, the finite value of the background field $\langle A_0 \rangle$ counteracts the effects of finite temperature and chemical potential on the fixed-point structure and we always observe

$$\lambda_\psi^* < \lambda_\psi^*(\tau, \tilde{\mu} - \mathrm{i}2\pi\tau\nu_l|\phi|, 0) < \lambda_\psi^*(\tau, \tilde{\mu}, 0) \; , \tag{4.31}$$

see also the blue dashed line in Fig. 4.3. Therefore, also for a finite number of colors, there should be a window in parameter space where the critical temperatures for deconfinement and chiral phase transitions are very close to each other. The fact that $\lambda_\psi^*(\tau, \tilde{\mu} - \mathrm{i}2\pi\tau\nu_l|\phi|, 0) > \lambda_\psi^*$ only implies that the lower end of the window in the parameter space is shifted to larger values of $\lambda_\psi^{\mathrm{UV}}$ compared to the case of infinite many colors.

For our $N_{\mathrm{c}} = 3$ numerical computations we employ the data from [146] as an input for the coordinates of the ground state $\langle A_0 \rangle$. These data were obtained for pure SU(3) Yang-Mills theory from the minimization of the corresponding order-parameter potential, see Fig. 4.1. In [146] the authors parametrize the background field $\langle A_0 \rangle$ as described in Eq. (4.13). For $N_{\mathrm{c}} = 3$ there are two generators of the Cartan subgroup which are chosen to be

$$t^3 = \mathrm{Diag}\{1/2, -1/2, 0\} \quad \text{and} \quad t^8 = 1/\sqrt{3} \cdot \mathrm{Diag}\{1/2, 1/2, -1\} \; . \tag{4.32}$$

A possible corresponding solution of Eq. (4.25) is then given by $(\phi^{(3)}, \phi^{(8)}) = (2/3, 0)$. In the left panel of Fig. 4.4 we visualize the result for $|\phi|$ from [146] as a function of T/T_d. Thereby, the critical temperature of the deconfinement phase transition was found to be $T_d \approx 290$ MeV.[8] From the non-continuous behavior of $|\phi|$ at $T = T_d$ we can see that the deconfinement phase transition is of the first order if one considers a pure SU(3) Yang-Mills theory. In the right panel of Fig. 4.4 we present the corresponding Polyakov loop $\mathrm{P}\left[\langle A_0 \rangle\right]$. As expected, it is zero at center symmetric phase and finite for $T > T_d$.

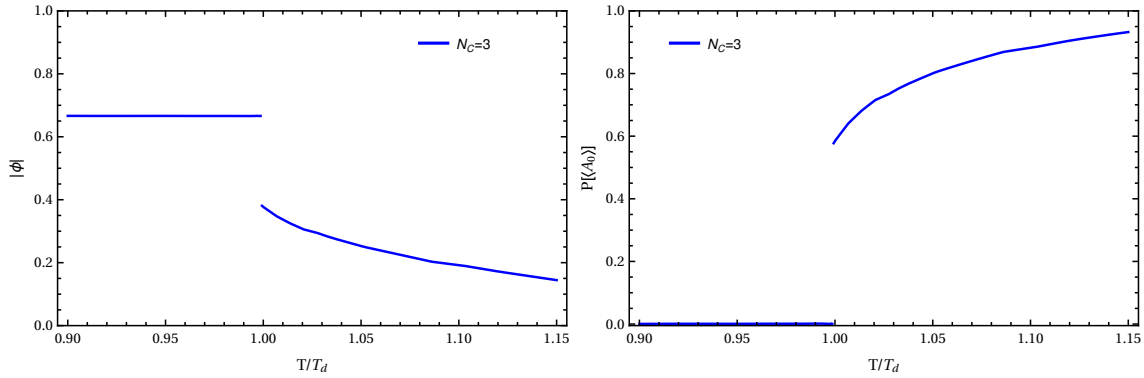8 The large value of T_d is due to the absence of dynamical quarks.

FIGURE 4.4: In this plot we present our input for the background field $\langle A_0 \rangle$ in the parametrization described in Eq. (4.13) (left panel) and the corresponding Polyakov Loop (right panel). Both quantities are plotted as function of T/T_d. The discontinuous behavior at $T = T_d$ signals the first order phase transition. The values for $\langle A_0 \rangle$ were taken from [146]. In this work the critical temperature was found to be $T_d \approx 290$ MeV.

In this particular work we set the UV cutoff scale of the model to $\Lambda_{\mathrm{UV}} = 1$ GeV and calculate the critical temperature of the chiral phase transition T_χ as a function of the initial condition $\lambda_\psi^{\mathrm{UV}}$ for different values of the chemical potential. Thereby, we define the critical temperature as the temperature where the 4-quark coupling λ_ψ diverges:

$$\frac{1}{\lambda_\psi} \to 0 \quad \text{for} \quad k \to 0 \ . \tag{4.33}$$

We mention that this definition provides only an upper boundary for T_χ since it only signals the formation of the chiral condensate but does not take into account that the chiral symmetry can be restored by Goldstone-bosons fluctuations in the deep IR, see [151] and Sec. 4.2. This feature is a direct consequence of the point-like limit we use here and can be improved using the PQM model, see Sec. 4.2.

Our results for $N_{\mathrm{c}} = 3$ are presented in Fig. 4.5. In this figure we plot T_χ/T_d as a function of $\lambda_\psi^{\mathrm{UV}}/\lambda_\psi^*$ for some chosen values of μ. For $\mu = 0$, our output shows the same behavior as results from [69, 70]. For all values of chemical potential μ we can basically distinguish between four different types of T_χ-behavior as function of $\lambda_\psi^{\mathrm{UV}}$: For small initial values of λ_ψ we observe $T_\chi = 0$. Thereby, the range of the corresponding $\lambda_\psi^{\mathrm{UV}}$-interval is going to zero for $\mu \to 0$ and increases with increasing μ. After this interval, T_χ starts to grow and approaches T_d. For even larger values of $\lambda_\psi^{\mathrm{UV}}$, we observe a window where the chiral phase transition is locked in by the deconfinement phase transition, i.e., $T_\chi \approx T_d$. This window is shifted to larger values in the parameter space if we increase the chemical potential. The range of this interval, however, seems to stay roughly the same. For even larger $\lambda_\psi^{\mathrm{UV}}$ we observe that $T_\chi > T_d$.

As already mentioned, our results for $\mu = 0$ reproduce those from [69, 70]. The major effect of the finite chemical potential is the shift of the phase diagram to larger values in the parameter space. This behavior also implies that for any pair of the initial value $\lambda_\psi^{\mathrm{UV}} > \lambda_\psi^*$ and the critical temperature with $T_\chi \lesssim T_d$, there is a certain critical value of the chemical potential μ_χ which separates the chirally symmetric and the chirally broken phase. Thus, for a model with fixed initial condition we observe the expected chiral symmetry restoration if we keep temperature constant and increase chemical potential.
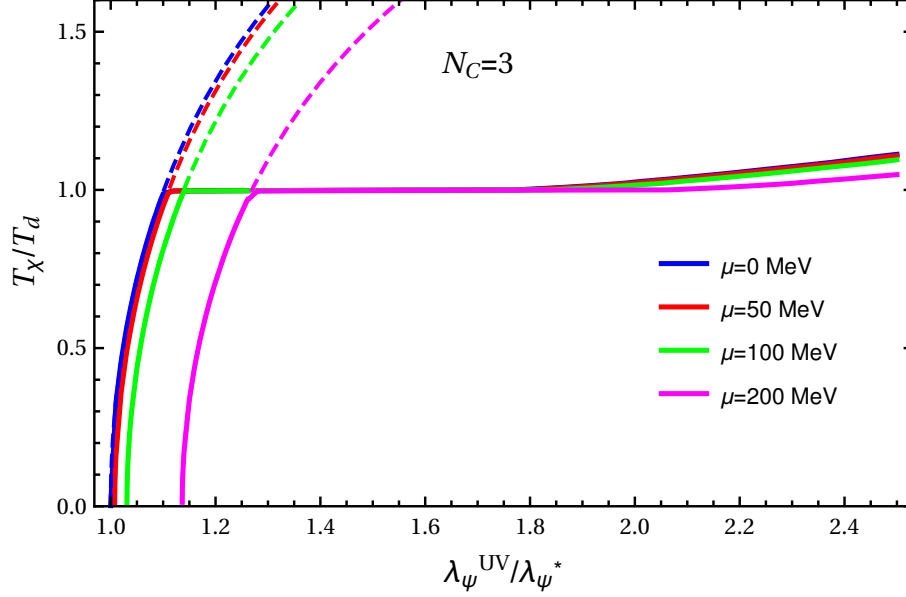
FIGURE 4.5: T_χ/T_d as a function of $\lambda_\psi^{\text{UV}}/\lambda_\psi^*$ for various values of μ. For all values of μ there are four different domains in the behavior of T_χ (from small to large λ_ψ^{UV}): $T_\chi = 0$, $T_\chi < T_d$, $T_\chi \approx T_d$ and $T_\chi > T_d$. The range of domain with $T_\chi = 0$ decreases with decreasing μ and approaches zero for $\mu \to 0$. Our current results are in agreement with [69, 70] and show that the finite μ basically shifts the phase diagram for $\mu = 0$ to larger values in the parameter space. The dashed lines correspond to analytical result presented in Eq. (4.38).

The observed behavior of the phase transition line can also be understood analytically, at least as long as critical temperature T_χ is assumed to be small. To show this, we start with the flow equation Eq. (4.18) and derive an implicit equation for T_χ using the definition in Eq. (4.33). We obtain

$$
\frac{N_c}{2}\left(1 - \frac{\lambda_\psi^*}{\lambda_\psi^{\text{UV}}}\right) = \sum_{l=1}^{N_c}\left\{3 - 3\frac{T_\chi}{\Lambda_{\text{UV}}}(\log[1 + G_+] + \log[1 + G_-])\right.
$$
$$
- (1 + G_+)^{-1} - (1 + G_-)^{-1}
$$
$$
+ 3\frac{T_\chi^2}{\Lambda_{\text{UV}}^2}\left[-\frac{\pi^2}{6} - \frac{1}{2}(\text{i}2\pi\nu_l|\phi| - \mu/T_\chi)^2\right.
$$
$$
\left.\left. - \text{Li}_2(-G_+) - \text{Li}_2(-G_-)\right]\right\}, \tag{4.34}
$$

where Li_2 means the dilogarithm and the functions $G_\pm$ are defined as

$$
G_\pm = \exp[\Lambda_{\text{UV}}/T_\chi \pm \text{i}2\pi\nu_l|\phi| \mp \mu/T_\chi]. \tag{4.35}
$$

From now on, we consider only temperatures which satisfy

$$
\frac{T}{\Lambda_{\text{UV}} \pm \mu} \ll 1. \tag{4.36}
$$

Under this assumption our result in Eq. (4.34) simplifies to

$$
\frac{N_c}{2}\left(1 - \frac{\lambda_\psi^*}{\lambda_\psi^{\text{UV}}}\right) = \sum_{l=1}^{N_c} 3\frac{T_\chi^2}{\Lambda_{\text{UV}}^2}\left[\frac{\pi^2}{6} + \frac{1}{2}(\text{i}2\pi\nu_l|\phi| - \mu/T_\chi)^2\right]. \tag{4.37}
$$

As next step we specify the number of colors, $N_c = 3$, and consider a system in the confined phase, i.e. $T_\chi < T_d$. These constrains further simplify our result:

$$0 < \frac{T_\chi^2}{\Lambda_{\mathrm{UV}}^2} = \frac{9}{\pi^2} \left[\left(1 - \frac{\lambda_\psi^*}{\lambda_\psi^{\mathrm{UV}}} \right) - 3 \frac{\mu^2}{\Lambda_{\mathrm{UV}}^2} \right] \Theta(\lambda_\psi^{\mathrm{UV}} - \lambda_\psi^*) . \tag{4.38}$$

We remind the reader that the chiral phase transition can appear in our model only for $\lambda_\psi^{\mathrm{UV}} > \lambda_\psi^*$. From the above result one can clearly see that for some specific value of the chemical potential μ, the critical temperature T_χ becomes zero and the chiral symmetry is restored. For even larger chemical potentials, there is no chiral phase transition anymore. Further, Eq. (4.38) shows once again that at finite μ the value of $\lambda_\psi^{\mathrm{UV}}/\lambda_\psi^*$ should be large enough in order to observe the finite T_χ. With other words, for any finite value of μ, there is an interval in the parameter space $1 \leq \lambda_\psi^{\mathrm{UV}}/\lambda_\psi^* \leq \lambda_{\psi,\chi}^{\mathrm{UV}}/\lambda_\psi^*$ where the chiral symmetry is always restored. this is exactly what we observe in our results in Fig. 4.5. To visualize our analytical result in Eq. (4.38), we have plotted it in Fig. 4.5 as dashed lines. Our analytical and numerical results perfectly agree in the regime where constraints needed to derive Eq. (4.38) are fulfilled, i.e, for $T_\chi \ll \Lambda_{\mathrm{UV}} \pm \mu$ and $T_\chi < T_d$.

Next, we use our results for the phase diagram in $(T_\chi/T_d, \lambda_\psi^{\mathrm{UV}}/\lambda_\psi^*)$-plane, see Fig. 4.5, in order to construct a phase diagram spanned by μ and T_χ/T_d. To this end, we have to specify the starting value $\lambda_\psi^{\mathrm{UV}}$. As discussed above, some particular value of $\lambda_\psi^{\mathrm{UV}}$ fixes the low-energy observables. However, since we cannot resolve momentum dependence of λ_ψ in our current approach, we cannot get access to the physical low-energy observables. Thus, we cannot find $\lambda_\psi^{\mathrm{UV}}$ reproducing the correct low-energy physics. However, we can use results from lattice simulations as motivation for our choice of $\lambda_\psi^{\mathrm{UV}}$. It is a very prominent fact that lattice simulations at zero chemical potential have shown very similar critical temperatures T_χ and T_d, e.g., Refs. [49, 50, 51, 52, 53]. Thus, we restrict our further calculations to the region in the parameter space where the locking window appears for $\mu = 0$. Our particular results show that the lower edge of the locking window at zero chemical potential corresponds to $\lambda_\psi^{\mathrm{UV}}/\lambda_\psi^* = 1.101$, see the upper left plot in Fig. 4.6. Using this value for $\lambda_\psi^{\mathrm{UV}}/\lambda_\psi^*$, one observes that the chiral and the deconfinement phase transition are equal only for $\mu = 0$. For larger chemical potentials we observe that the phase transitions are decoupled and $T_\chi < T_d$, see the upper right plot in Fig. 4.6. As alternative to the choice of $\lambda_\psi^{\mathrm{UV}}/\lambda_\psi^*$ at the lower boundary of the locking window, we can consider a larger value $\lambda_\psi^{\mathrm{UV}}/\lambda_\psi^* = 1.15$, see bottom panels of Fig. 4.6. For this choice of $\lambda_\psi^{\mathrm{UV}}/\lambda_\psi^*$ we observe that the the chiral phase transition is dynamically locked in due to the deconfinement transition and, thus, $T_\chi \approx T_d$. This behavior is realized for chemical potentials up to $\mu \approx 115$ MeV. For even larger μ the phase transitions are decoupled again.

At this point we should add a comment on the input for $\langle A_0 \rangle$ used in this work. We again stress that the data from [146] were calculated in the pure Yang-Mills theory. In full QCD, the ground state of the potential of the confinement order parameter is affected by contributions from Feynman diagrams with internal fermionic lines. The presence of dynamical quarks would also lead to smaller (pseudo-)critical temperature of the deconfinement phase transition. However, since our analytical findings for $N_c \to \infty$ are based on the very general properties of the confinement order parameter, we expect that they are not strongly affected by inclusion of quarks. Therefore, also for finite number of colors and in the presence of dynamical quarks, we can still expect the presence of a window in the parameter space where chiral and deconfinement critical temperatures lie close to each other. Assuming this scenario and that the choice of $\lambda_\psi^{\mathrm{UV}}/\lambda_\psi^*$ reproducing the correct
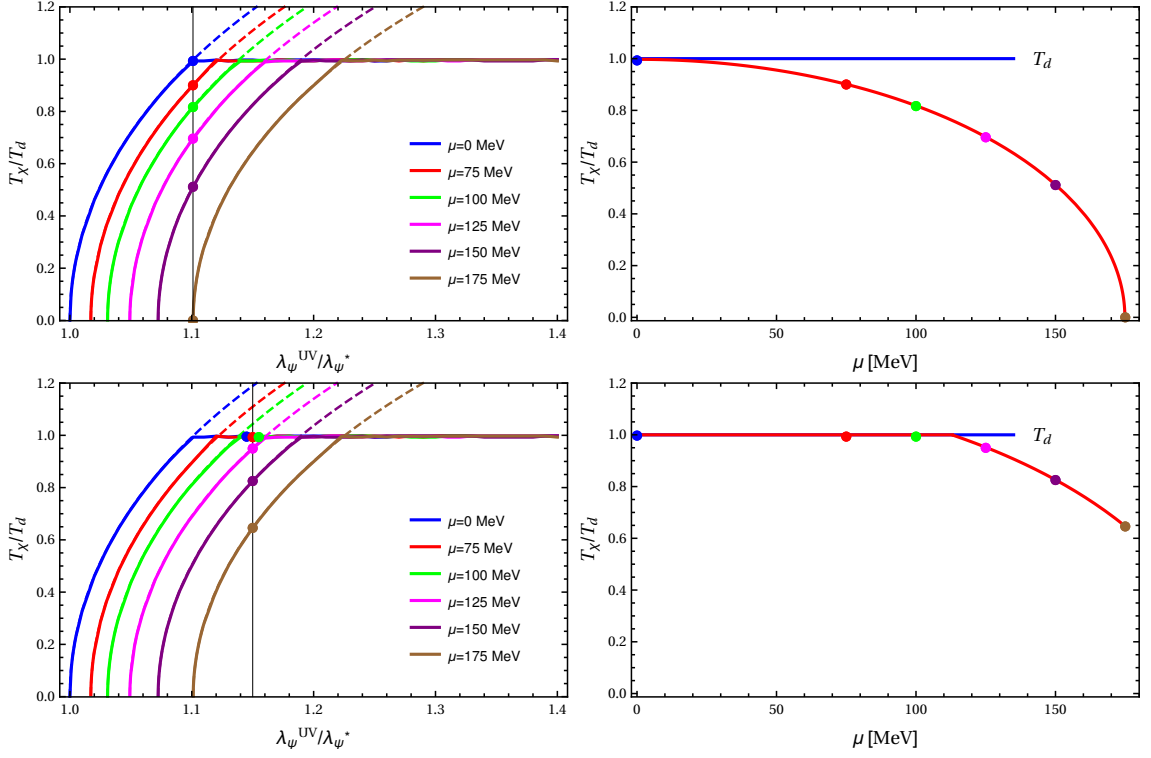
FIGURE 4.6: Here, we use our results partially presented in Fig. 4.5 in order to construct a phase diagram in $(T_\chi/T_d, \mu)$-plane. We consider two different values of the initial condition: $\lambda_\psi^{\mathrm{UV}}/\lambda_\psi^* = 1.101$ (upper plots) and $\lambda_\psi^{\mathrm{UV}}/\lambda_\psi^* = 1.15$ (lower plots). In the first case we observe a decoupling of phase boundaries of chiral and deconfinement phase transitions at finite chemical potentials. In the second case we observe $T_\chi \approx T_d$ for $\mu \lesssim 115$ MeV. The dashed lines in the left plots were obtained using our analytical result presented in Eq. (4.38). To obtain the phase boundaries with non-vanishing curvature (right plots), we also use this analytical expression. The points correspond to our numerical results. We can again state that our analytical result in Eq. (4.38) is in a very good agreement with numerics as long $T_\chi \lesssim T_d$.

low-energy observables is located inside of the locking window, one would observe that the chiral phase transition temperature is locked in to T_d. However, now it decreases with increasing μ since T_d is expected to decrease at finite quark chemical potential. In any case, we should keep in mind that our numerical results in Figs. 4.5 and 4.6 will considerably change on the quantitative level if we include dynamical quarks in calculation of $\langle A_0 \rangle$.

Our results in Figs. 4.5 and 4.6 can also be used in order to calculate the curvature κ of the QCD phase diagram spanned by μ and T at zero chemical potential. This quantity serves as an useful tool to compare different approaches which were developed to extend lattice QCD calculations to finite chemical potential. Even though lattice QCD is one of the most powerful techniques to study QCD at zero chemical potential, at finite μ these calculations are very involved because of the so-called sign problem: as many simulations of stochastic processes, the lattice QCD approach relies on the calculation technique called importance sampling. The later needs a properly defined probability measure which, in the case of lattice QCD, is given by the fermion determinant. At finite chemical potential, however, the fermion determinant becomes complex and, thus, cannot be used as a suitable probability measure. For more details see, e.g., [48, 159]. There are several methods which

aim to overcome this problem, e.g., the reweighting of the generated configurations or the analytic continuation to an imaginary chemical potential. However, all of the common methods are constrained to regime $\mu/T \lesssim 1$ [159, 160]. An alternative method is to Taylor-expand the observables in μ. This approach is quite useful since the coefficients of the Taylor series are computed at $\mu = 0$ [161]. Consequently, one can consider the chiral phase transition temperature T_χ as an expansion in the dimensionless quantity μ/T_χ. Up to second order it then reads:

$$T_\chi(\mu^2) \approx T_\chi(1 - \kappa \frac{\mu^2}{T_\chi^2}) \,, \tag{4.39}$$

where

$$\kappa = -T_\chi \left. \frac{\mathrm{d}T_\chi(\mu^2)}{\mathrm{d}\mu^2} \right|_{\mu=0} \qquad \text{and} \qquad T_\chi = T_\chi(0) \,. \tag{4.40}$$

In the above expansion there is no term of the first order. This is because the partition function Z is invariant under the charge conjugation and, thus, $Z(\mu) = Z(-\mu)$ [48, 160]. The coefficient κ in Eq. (4.40) is identical to the curvature of the phase diagram up to the factor $1/2$. As already mentioned above, κ is used in order to compare outcome of lattice QCD simulations at finite chemical potential which use different techniques to overcome the sign problem. The value of κ was measured, e.g., to 0.0032(1) in [162] and to 0.500(54) in [163]. These results differ quite strongly since they depend on the specific setup of each simulation. However, they can give us a feeling of the order of magnitude of κ. In any case, the curvature of the QCD phase boundary seems to be very small. In our particular calculations we also observe a strong dependence of κ on the specific configuration of the model: If we consider small values of $\lambda_\psi^{\mathrm{UV}}$ outside of the locking window, i.e., we consider the region with $T_\chi < T_d$ in Fig. 4.5, we can show analytically that $\kappa = 27/(2\pi^2) \approx 1.368$. It follows from Eq. (4.38). This value is clearly too large compared to the lattice outcome. On the other hand, once we consider the region in the parameter space where locking mechanism enforces $T_\chi \approx T_d$, the curvature vanishes completely, $\kappa = 0$. At this point we want to mention again that our input for $\langle A_0 \rangle$ was calculated neglecting any back-reaction of the quarks on the gauge sector. Including such back-reactions would lead to decrease of T_d with increasing μ. Thus, once we consider the locking window, it would mean that the curvature of the chiral phase transition is determined by the curvature of the deconfinement phase transition. This statement would then also be valid for some interval of finite μ.

To complete this section, we recapitulate a comment from [69] which relates our present study with assumptions typically made in PNJL/PQM studies. In contrast to our present work and studies in [69, 70], in usual PNJL/PQM calculations one assumes

$$\mathrm{P}\left[\langle A_0 \rangle\right] = \langle \mathrm{P}\left[A_0\right] \rangle \quad \text{and} \quad \mathrm{tr}_\mathrm{F}\left[L\left[\langle A_0 \rangle\right]^n\right] = N_\mathrm{c} \left(\frac{\mathrm{P}\left[\langle A_0 \rangle\right]}{N_\mathrm{c}}\right)^n \,, \tag{4.41}$$

see, e.g., [126]. These assumptions also implies that $N_\mathrm{c}^n \, \mathrm{tr}_\mathrm{F}\left[L\left[\langle A_0 \rangle\right]^n\right] = N_\mathrm{c} \langle \mathrm{P}\left[A_0\right] \rangle^n$. Consequently, a trace of any power of the Polyakov variable should vanish in the confined phase in this approximation. This statement is independent of number of colors. Along the lines of our discussion of Eq. (4.27) for $N_\mathrm{c} \to \infty$, one can easily show that this approximation leads to $T_\chi \geq T_d$ for any N_c. As we have shown above, such a behavior is associated with the limit $N_\mathrm{c} \to \infty$ if one does not use the approximation in Eq. (4.41).

Hence, we can conclude that the assumptions usually used in PNJL/PQM studies are related to large-N_c approximation in the coupling of the matter and the gauge sector. Following Ref. [69], we want to emphasize that this kind of large-N_c approximation should not be confused with large-N_c approximation sometimes used in the matter sector of PNJL/PQM models, such as neglecting pion fluctuations. In any case, from the point of view of our present analysis, the approximation $P\left[\langle A_0\rangle\right] = \langle P\left[A_0\right]\rangle$ affects the dynamics near the finite-temperature and finite-chemical-potential phase boundary and may also affect the PNJL/PQM-model predictions for the phase diagram spanned by T and μ.

Up to now, the initial value $\lambda_\psi^{\mathrm{UV}}$ of the 4-quark coupling was considered as a free parameter in our calculations. In full QCD, of course, $\lambda_\psi^{\mathrm{UV}}$ is not arbitrary and is generated by gluodynamics. Therefore, it can be related to the strong coupling α, see, e.g., [72, 73, 154, 123] and our study in Chap. 5. On the other hand, α determines all low-energy observables of QCD. Thus, in model calculations one usually fixes the value of $\lambda_\psi^{\mathrm{UV}}$ in such a way that one reproduces the physical low-energy observables, such as the pion decay constant, quark and boson masses. In our present study, however, we have employed the point-like-limit approximation and, therefore, we cannot access the low-energy observables. We solve this problem in the next section using the partial bosonization of action (4.5), i.e. we introduce a version of the Polyakov-loop extended quark-meson (PQM) model.

4.2 POLYAKOV-LOOP EXTENDED QM MODEL

4.2.1 *PQM-Model Lagrangian*

In previous section we have considered a low-energy model of QCD in a purely fermionic language. In such a model the spontaneous chiral symmetry breaking is associated with divergence in coupling λ_ψ. As already mentioned, this diverging behavior is an artifact of the point-like approximation and does not enable to get access to the physical low-energy observables. Additionally, T_χ calculated using this approach provides only an upper bound for the critical temperature of the chiral phase transition since bosonic fluctuations, which tend to restore chiral symmetry, are not included. These facts indicate the necessity to resolve, at least partially, the momentum dependence of λ_ψ.

To this end, we employ the convenient technique of partial bosonization by means of Hubbard-Stratonovich transformation [164, 165]. The basic idea of this transformation is to introduce new auxiliary fields $\bar\varphi = (\sigma, \vec\pi)^T$ into the generating functional of the model. These fields are assumed to be bound states of quarks:

$$\sigma \sim (\bar\psi\psi)$$
$$\vec\pi \sim (\bar\psi\vec\tau\gamma_5\psi) \,, \tag{4.42}$$

and, consequently, do not carry any internal charge, i.e., flavor and color. In order to (partially) resolve the momentum dependence of 4-quark coupling, i.e., to make σ and $\vec\pi$ to mediators of interaction between quarks, we have to make these new fields dynamical. This is achieved by introduction of corresponding kinetic term $\sim (\partial_\mu\bar\varphi)^2$. Eventually, we obtain the following effective action:

$$\Gamma_k = \int \mathrm{d}^4x \; \Big\{ \bar\psi(\mathrm{i}Z_\psi\slashed{\partial} + Z_\psi\bar g\gamma_0\langle A_0\rangle + \mathrm{i}\gamma_0\mu)\psi$$
$$+ \frac{1}{2}Z_\varphi(\partial_\mu\bar\varphi)^2 + \mathrm{i}\bar h\bar\psi(\sigma + \mathrm{i}\vec\tau\cdot\vec\pi\gamma_5)\psi + \frac{1}{2}\bar m^2\bar\varphi^2 + \frac{1}{8}\bar\lambda_\varphi\bar\varphi^4 \Big\} \,, \tag{4.43}$$

where $\bar{h}$ is a real-valued Yukawa coupling, Z_ψ and Z_φ are the wave-function renormalizations of quarks and bosons correspondingly, $\bar{m}$ is a bosonic mass parameter and $\bar{\lambda}_\varphi$ represents a 4-boson interaction. All this quantities are, in general, scale dependent. In order to insure that the effective action (4.43) represents the bosonized version of the action in Eq. (4.5) at the initial UV scale Λ_{UV}, one has to impose the following boundary conditions:

$$
\lim_{k \to \Lambda_{\mathrm{UV}}} Z_\varphi = 0 \;,
$$
$$
\lim_{k \to \Lambda_{\mathrm{UV}}} Z_\psi = 1 \;,
$$
$$
\lim_{k \to \Lambda_{\mathrm{UV}}} \bar{\lambda}_\varphi = 0 \;,
$$

(4.44)

and the identity

$$
\bar{\lambda}_\psi = \frac{\bar{h}^2}{\bar{m}^2} \;.
$$

(4.45)

The term $\sim \bar{\varphi}^4$ is not naturally resulting from Hubbard-Stratonovich transformation but was introduced by hand. The introduction of this term is essential for a study of the chiral phase transition since the coupling $\bar{\lambda}_\varphi$ is responsible for the mass difference between the σ and the pions. In the purely fermionic picture the term $\sim \bar{\varphi}^4$ corresponds to a 8-quark interaction. The last boundary condition in Eq. (4.44) insures that we do not have to adjust the parameter $\bar{\lambda}_\varphi$ by hand, i.e., it is not an additional parameter of the model. Thus, $\bar{\lambda}_\varphi$ is dynamically generated in the RG flow, see, e.g., [25, 117, 123, 150, 151].

In general, one can introduce bosonic interactions up to any order, $\bar{\varphi}^{2n}$. A bosonic term of n-th order corresponds then to a fermionic interaction between $4n$ quarks. Such a procedure is equivalent to the introduction of a general potential $U(\bar{\varphi}^2)$ for bosonic interactions which is then expanded up to desired order in $\bar{\varphi}^2$ around the particular minimum of $U(\bar{\varphi}^2)$. Our ansatz for the effective action in Eq. (4.43) corresponds to a potential $U(\bar{\varphi}^2)$ expanded around zero up to the second order. In the regime of broken chiral symmetry, however, this ansatz is not valid anymore: once chiral symmetry is broken, the quark condensate $\langle \bar{\psi}\psi \rangle$ appears and, therefore, we observe a finite expectation value of the field $\bar{\varphi}$ in the direction of σ:

$$
\langle \bar{\psi}\psi \rangle \neq 0 \quad \to \quad \bar{\varphi}_0 = \langle \bar{\varphi} \rangle = (\sigma_0, 0)^T \quad \text{with} \quad \sigma_0 \neq 0 \;.
$$

(4.46)

Then, the minimum of the potential $U(\bar{\varphi}^2)$ is given by finite $\bar{\varphi}_0$ and the appropriate second-order expansion reads

$$
U(\bar{\varphi}^2) = \frac{\bar{\lambda}_\varphi}{8} (\bar{\varphi}^2 - \bar{\varphi}_0^2)^2 \;.
$$

(4.47)

Connecting this expansion with our ansatz for $U(\bar{\varphi}^2)$ in the chirally symmetric regime, one finds

$$
\bar{\varphi}_0^2 = -\frac{2\bar{m}^2}{\bar{\lambda}_\varphi} \;.
$$

(4.48)

From this result it is clear that the coupling $\bar{m}^2$ becomes negative in the chirally broken regime and we can formulate a criterion for the chiral symmetry breaking/restoration in the RG flow: if $\bar{m}^2$ becomes zero, then the chiral phase transition takes place. Because of

Eq. (4.45), this condition is equivalent to $\bar{\lambda}_\psi \to \infty$ which triggers the onset of the chiral symmetry breaking in the purely fermionic description.

To summarize, throughout this work we use the following ansatz for the bosonic interactions:

$$U(\bar{\varphi}^2) = \begin{cases} \frac{1}{2}\bar{m}^2\bar{\varphi}^2 + \frac{1}{8}\bar{\lambda}_\varphi\bar{\varphi}^4 & \text{in the chirally symmetric regime,} \\ \frac{1}{8}\bar{\lambda}_\varphi(\bar{\varphi}^2 - \bar{\varphi}_0^2)^2 & \text{in the chirally broken regime.} \end{cases} \tag{4.49}$$

At this point we would like to add a comment about the number of free parameters in our study. Besides the input for the background field $\langle A_0 \rangle$ and the UV cutoff Λ_{UV}, we had only one free model parameter in our study of PNJL model, namely, $\bar{\lambda}_\psi^{\text{UV}}$. In the bosonized picture, $\bar{\lambda}_\psi^{\text{UV}}$ corresponds to $\bar{h}_{\text{UV}}^2/\bar{m}_{\text{UV}}^2$ and one could suggest that our particular model is completely determined by the choice of the value for this ratio. However, in 4 dimensions the Yukawa coupling is marginal and serves as an additional input parameter [151, 166]. Indeed, the ratio of low-energy observables, e.g., the ratio of the σ-mass and the constituent quark mass, depends on both $\bar{h}_{\text{UV}}$ and $\bar{m}_{\text{UV}}$ [166]. So, we treat the Yukawa coupling and the mass parameter for bosons as independent input parameters at the UV scale of the PQM model.

4.2.2 Flow Equations for PQM Model

Now, let us discuss the RG flows of couplings in PQM model. To this end, we introduce the dimensionless couplings:

$$\begin{aligned} m^2 &= \frac{\bar{m}^2}{Z_\varphi k^2} \ , \\ \lambda_\varphi &= \frac{\bar{\lambda}_\varphi}{Z_\varphi^2} \ , \\ h &= \frac{\bar{h}}{Z_\varphi^{1/2} Z_\psi} \ . \end{aligned} \tag{4.50}$$

In our study, we neglect the running of the fermionic and bosonic wave-function renormalizations, i.e., we use $Z_\psi = 1$ and $Z_\varphi = 1$. This approximation is justified by studies in Refs. [117, 123, 150] where the corresponding anomalous dimensions η_ψ and η_φ have been found to be small over a wide range of momentum scales. The negligence of the k-dependence of Z_ψ can also be motivated by the following argument: The RG flow of Z_ψ only includes contributions from 1PI diagrams with at least one internal bosonic and one internal fermionic line. In the chirally symmetric regime bosons are heavy and in the regime with broken symmetry the quarks acquire a large mass. Therefore, all contributions to the flow of Z_ψ are suppressed in both these regimes. However, we should mention that in the chiral limit and close to the phase boundary both the fermions and the mesons become massless. Hence, a study aiming at quantitatively correct description of the phase transition needs to include the RG running of Z_ψ. For details, see, e.g., Refs. [117, 123, 150]. For our qualitative study of locking mechanism, however, the approximation $Z_\psi = 1$ is reasonable.

In contrast to negligence of the running of Z_ψ, setting $Z_\varphi = 1$ needs a bit more discussion. This approximation violates the first boundary condition in Eq. (4.44) and results in the

fact that the model depends on two parameters instead of one. However, if we compare our numerical results at $\mu = 0$ with results in [70] where the running of mesonic wave-function renormalization was taken into account, we observe only an almost negligible impact of finite η_φ on the quantitative results for the critical temperature T_χ. Thus, we conclude that the approximation $Z_\varphi = 1$ seems to be reasonable for an explorative study of the locking mechanism. Nonetheless, we should keep in mind that the running of Z_φ is important for precise calculations, especially for computation of critical exponents.

Flow Equations in the Chirally Symmetric Regime

To calculate the flow equations for couplings in chirally symmetric regime, we follow the same strategy as in our calculations in purely fermionic picture in Sec. 4.1.3. The field-independent part of the inverse dressed propagator $\left(\frac{\overrightarrow{\delta}}{\delta\Phi^T} \Gamma_k[\Phi] \frac{\overleftarrow{\delta}}{\delta\Phi} + R_k \right)$ is calculated to:

$$\mathcal{P}_k = \begin{pmatrix} \mathcal{P}_{k,\text{bos.}} & 0 \\ 0 & \mathcal{P}_{k,\text{ferm.}} \end{pmatrix} (2\pi)^4 \delta^{(4)}(p - p') , \tag{4.51}$$

with bosonic contribution

$$\mathcal{P}_{k,\text{bos.}} = \left(\left(p_0^2 + (1 + r_{\text{B}}(y))\vec{p}^2 \right) + \bar{m}^2 \right) \mathbb{1}_4 , \tag{4.52}$$

and fermionic part

$$\mathcal{P}_{k,\text{ferm.}} = \begin{pmatrix} 0 & -\left(\slashed{p}^T(1 + r_\psi(y)) + \gamma_0^T \alpha_+ \right) \\ -(\slashed{p}(1 + r_\psi(y)) + \gamma_0 \alpha_-) & 0 \end{pmatrix} . \tag{4.53}$$

In analogy to Sec. 4.1.3, we have employed here the linear cutoff functions for both fermions and bosons, see Eq. (E.1) in App. E, and $y = \vec{p}^2/k^2$. The fermionic contribution $\mathcal{P}_{k,\text{ferm.}}$ is identical to our result in Eq. (4.12) for purely fermionic action, i.e., $\alpha_\pm = p_0 \pm (\bar{g} \langle A_0 \rangle + \mathrm{i}\mu)$.

Since $\mathcal{P}_k$ is a diagonal block matrix, we can calculate $\mathcal{P}_k^{-1}$ inverting bosonic and fermionic contributions separately. The inversion of $\mathcal{P}_{k,\text{bos.}}$ is trivial and for the inversion of $\mathcal{P}_{k,\text{ferm.}}$ we proceed along the lines of Sec. 4.1.3.

Let us now consider the field-dependent part of $\left(\frac{\overrightarrow{\delta}}{\delta\Phi^T} \Gamma_k[\Phi] \frac{\overleftarrow{\delta}}{\delta\Phi} + R_k \right)$. It reads

$$\mathcal{F}_k = \begin{pmatrix} \frac{\bar{\lambda}_\varphi}{2} \left(\varphi^2 \mathbb{1}_4 + 2\varphi\varphi^T \right) & & \mathrm{i}\bar{h}\bar{\psi} & -\mathrm{i}\bar{h}\psi^T \\ & & \mathrm{i}\bar{h}\bar{\psi}(\mathrm{i}\gamma_5\tau_i) & -\mathrm{i}\bar{h}\psi^T(\mathrm{i}\gamma_5\tau_i)^T \\ -\mathrm{i}\bar{h}\bar{\psi}^T & -\mathrm{i}\bar{h}(\mathrm{i}\gamma_5\tau_j)^T\bar{\psi}^T & 0 & -\mathrm{i}\bar{h}(\sigma + \mathrm{i}\gamma_5\vec{\pi}\cdot\vec{\tau})^T \\ \mathrm{i}\bar{h}\psi & \mathrm{i}\bar{h}(\mathrm{i}\gamma_5\tau_j)\psi & \mathrm{i}\bar{h}(\sigma + \mathrm{i}\gamma_5\vec{\pi}\cdot\vec{\tau})\mathrm{i} & 0 \end{pmatrix}$$
$$\times (2\pi)^4 \delta^{(4)}(p - p') . \tag{4.54}$$

The indices i and j label column entries of the vector $\vec{\tau}$ and row entries of the vector $\vec{\tau}^T$ respectively. Keep in mind that τ_j^T denote the transposition of the Pauli matrices itself. Already at this point one can see that in the expansion (3.31) following contributions are relevant: first and second order terms contribute to $\partial_t \bar{m}^2$, second and fourth order terms to $\partial_t \bar{\lambda}_\varphi$ and the third order term to $\partial_t \bar{h}$. In the language of 1PI Feynman diagrams these contributions then reads:

$$\partial_t \bar{m}^2 \quad \sim \qquad \text{} \qquad + \qquad \text{} \quad , \tag{4.55}$$

$$\partial_t \bar{\lambda}_\varphi \quad \sim \qquad\qquad + \qquad\qquad , \tag{4.56}$$

$$\partial_t \bar{h} \quad \sim \qquad\qquad + \qquad\qquad , \tag{4.57}$$

where quarks are denoted by full and mesons by dashed lines. The double lines label the corresponding fully dressed propagators and the big white circle with a cross stands for $\partial_t R_k$. The small circles denote vertices: the black one corresponds to the Yukawa interaction $\sim \bar{h}$ and the white one the to 4-meson interaction $\sim \bar{\lambda}_\varphi$.

Evaluating these diagrams, we find following flow equations for dimensionless couplings:

$$\partial_t m^2 = -2m^2 - 12 v_4 l_1^{(\mathrm{B})}(\tau, m^2) \lambda_\varphi + 32 v_4 \sum_{l=1}^{N_{\mathrm{c}}} l_1^{(\mathrm{F})}(\tau, \tilde{\mu} - \mathrm{i}2\pi\tau\nu_l|\phi|, 0) h^2 \ , \tag{4.58}$$

$$\partial_t \lambda_\varphi = 24 v_4 l_2^{(\mathrm{B})}(\tau, m^2) \lambda_\varphi^2 - 64 v_4 \sum_{l=1}^{N_{\mathrm{c}}} l_2^{(\mathrm{F})}(\tau, \tilde{\mu} - \mathrm{i}2\pi\tau\nu_l|\phi|, 0) h^4 \ , \tag{4.59}$$

$$\partial_t h^2 = -\frac{16}{N_{\mathrm{c}}} v_4 \sum_{l=1}^{N_{\mathrm{c}}} l_{1,1}^{(\mathrm{FB})}(\tau, \tilde{\mu} - \mathrm{i}2\pi\tau\nu_l|\phi|, 0, m^2) h^4 \ , \tag{4.60}$$

where the corresponding threshold functions $l_1^{(\mathrm{B})}(\tau, m^2)$, $l_2^{(\mathrm{B})}(\tau, m^2)$, $l_1^{(\mathrm{F})}(\tau, \tilde{\mu}-\mathrm{i}2\pi\tau\nu_l|\phi|, 0)$, $l_2^{(\mathrm{F})}(\tau, \tilde{\mu} - \mathrm{i}2\pi\tau\nu_l|\phi|, 0)$ and $l_{1,1}^{(\mathrm{FB})}(\tau, \tilde{\mu} - \mathrm{i}2\pi\tau\nu_l|\phi|, 0, m^2)$ are defined in App. E. Note that the zero in the argument of the threshold functions corresponds to $\omega_1 = m_q = 0$. This is because quarks are massless in the chirally symmetric regime.

Flow Equations in the Regime of Spontaneously Broken Chiral Symmetry

As already described above, in the chirally broken regime we use

$$U(\bar{\varphi}^2) = \frac{\bar{\lambda}_\varphi}{8}(\bar{\varphi}^2 - \bar{\varphi}_0^2)^2 \ , \tag{4.61}$$

as parametrization of the mesonic potential. Thus, we calculate the RG flow equations for $\bar{\lambda}_\varphi$ and $\bar{\varphi}_0^2$. To this end, we follow a different strategy as in our calculations for the chirally symmetric regime: In the beginning we do not specify a particular form of the potential and calculate the RG flow $\partial_t U(\bar{\varphi}^2)$ starting from the (non-expanded) Wetterich flow equation (3.28). After that, we expand the left- and right-hand side of the Wetterich equation around the ground state $\bar{\varphi}_0$ and compare the corresponding expansion

coefficients on both sides[9]. This approach implies that we have to invert the matrix $\left(\frac{\overrightarrow{\delta}}{\delta \Phi^T} \Gamma_k[\Phi] \frac{\overleftarrow{\delta}}{\delta \Phi} + R_k \right)$. Besides the subtleties appearing due to the presence of finite $\langle A_0 \rangle$, one should keep in mind that the mesonic mass matrix is no longer isotropic. Because of the finite expectation value $\bar{\varphi}_0$, the original O(4) symmetry of the bosonic sector is broken down to O(3) symmetry and we have to distinct in the mass matrix between the massive σ-direction and the massless $\vec{\pi}$-direction. However, these directions are orthogonal and we can split the mesonic mass matrix using the projectors

$$\bar{M}_\varphi^2 = \frac{\overrightarrow{\delta}}{\delta \bar{\varphi}^T} U[\bar{\varphi}^2] \frac{\overleftarrow{\delta}}{\delta \bar{\varphi}} = \bar{m}_\sigma^2(\bar{\varphi}^2) P_\varphi^\parallel + \bar{m}_\pi^2(\bar{\varphi}^2) P_\varphi^\perp \ , \tag{4.62}$$

where $P_\varphi^\parallel$ and $P_\varphi^\perp$ are longitudinal and transversal projector operators defined as

$$P_\varphi^\parallel = \frac{\bar{\varphi}_i \bar{\varphi}_j}{\bar{\varphi}^2} \quad \text{and} \quad P_\varphi^\perp = \delta_{ij} - P_\varphi^\parallel \ ,$$

$$\text{with} \quad \left(P_\varphi^\parallel \right)^2 = P_\varphi^\parallel \ , \quad \left(P_\varphi^\perp \right)^2 = P_\varphi^\perp \quad \text{and} \quad P_\varphi^\parallel P_\varphi^\perp = 0 \ . \tag{4.63}$$

Hence, $\bar{m}_\sigma^2(\bar{\varphi}^2)$ and $\bar{m}_\pi^2(\bar{\varphi}^2)$ denote the eigenvalues of the mass matrix and are given by

$$\bar{m}_\sigma^2(\bar{\varphi}^2) = 2 \, \partial_{\bar{\varphi}^2} U(\bar{\varphi}^2) + 4 \, \bar{\varphi}^2 \partial_{\bar{\varphi}^2}^2 U(\bar{\varphi}^2) \ , \tag{4.64}$$

and

$$\bar{m}_\pi^2(\bar{\varphi}^2) = 2 \, \partial_{\bar{\varphi}^2} U(\bar{\varphi}^2) \ . \tag{4.65}$$

Note that these eigenvalues are functions of $\bar{\varphi}^2$ and provides mesonic masses if we evaluate them at the ground state

$$\bar{m}_\sigma^2(\bar{\varphi}^2) \Big|_{\bar{\varphi}_0^2} = \bar{m}_\sigma^2 = \bar{\lambda}_\varphi \bar{\varphi}_0^2 \ ,$$

$$\bar{m}_\pi^2(\bar{\varphi}^2) \Big|_{\bar{\varphi}_0^2} = \bar{m}_\pi^2 = 0 \ . \tag{4.66}$$

Using above decomposition, we are now able to calculate the flow of the potential $U(\bar{\varphi}^2)$:

$$\partial_t U(\bar{\varphi}^2) = 2v_4 k^4 \Big[l_0^B(\tau, m_\sigma^2(\bar{\varphi}^2)) + 3 l_0^B(\tau, m_\pi^2(\bar{\varphi}^2))$$

$$- 8 \sum_{l=1}^{N_c} l_0^{(F)}(\tau, \tilde{\mu} - i2\pi\tau\nu_l|\phi|, m_q^2(\bar{\varphi}^2)) \Big] \ , \tag{4.67}$$

where the threshold functions $l_0^B(\tau, m_{\sigma/\pi}^2(\bar{\varphi}^2))$ and $l_0^{(F)}(\tau, \tilde{\mu} - i2\pi\tau\nu_l|\phi|, m_q^2(\bar{\varphi}^2))$ are defined in App. E. In the above equation we have introduced dimensionless mass parameters:

$$m_i^2(\bar{\varphi}^2) = \frac{\bar{m}_i^2(\bar{\varphi}^2)}{k^2} \ . \tag{4.68}$$

The constituent quark mass parameter $\bar{m}_q(\bar{\varphi}^2)$ is given in our model by $\bar{m}_q(\bar{\varphi}^2) = \bar{h}\bar{\varphi}$. This can be easily seen from the classical equation of motion for fermions calculated using the action in Eq. (4.43). As a consequence, the constituent quark mass is

$$\bar{m}_q^2(\bar{\varphi}^2) \Big|_{\bar{\varphi}_0^2} = \bar{m}_q^2 = \bar{h}^2 \bar{\varphi}_0^2 \ . \tag{4.69}$$

---

[9] This strategy can also be applied to the chirally symmetric regime whereat we should expand around zero. The resulting flow equations are then identical to those obtained by using expanded version of the Wetterich equation (3.31).

On the other hand, the Goldberger-Treiman relation, Eq. (2.33), states that $\bar{m}_q = \bar{h} f_\pi$. Hence, we can identify the expectation value $\bar{\varphi}_0$ with pion decay constant which is an measurable quantity.
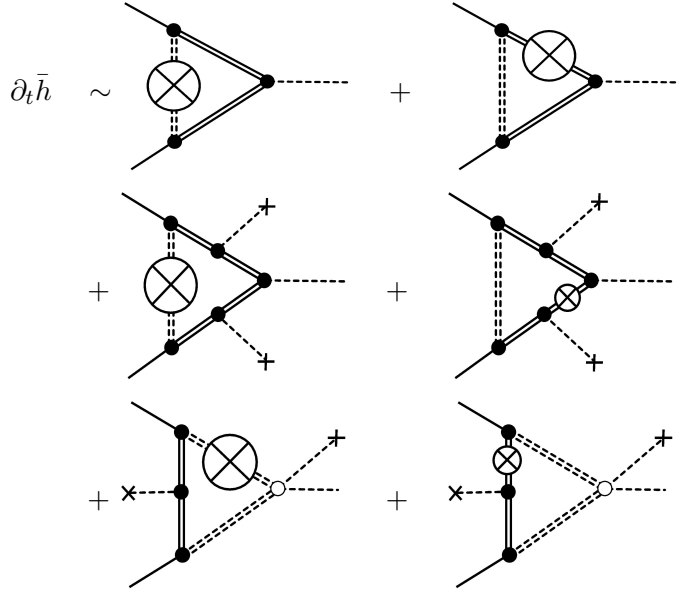
Now, we can expand the Eq. (4.67) in $\bar{\varphi}^2$ around $\bar{\varphi}_0^2$ on both left- and right-hand side. Through a comparison of the expansion coefficients we obtain the following flow equations:

$$\partial_t \varphi_0^2 = -2\varphi_0^2 + 12 v_4 l_1^B(\tau, m_\sigma^2) + 12 v_4 l_1^B(\tau, m_\pi^2)$$
$$- 64 v_4 \sum_{l=1}^{N_c} l_1^{(F)}(\tau, \tilde{\mu} - i2\pi\tau\nu_l|\phi|, m_q^2) \frac{h^2}{\lambda_\varphi} \,, \tag{4.70}$$

$$\partial_t \lambda_\varphi = 18 v_4 l_2^B(\tau, m_\sigma^2)\lambda_\varphi^2 + 6 l_2^B(\tau, m_\pi^2)\lambda_\varphi^2 - 64 v_4 \sum_{l=1}^{N_c} l_2^{(F)}(\tau, \tilde{\mu} - i2\pi\tau\nu_l|\phi|, m_q^2) h^4 \,, \tag{4.71}$$

where we have introduced the dimensionless pion decay constant $\varphi_0 = \bar{\varphi}_0/k$.

Finally, let us discuss the flow equation for the Yukawa coupling $\bar{h}$ in the regime of broken chiral symmetry. In general, we can proceed in the same way as in our calculations for the restored chiral symmetry. However, applying this procedure one has to be cautious. Proceeding in exactly the same way as in the previous subsection we would find that due to the finite expectation value of the field $\bar{\varphi}$, additional contributions to $\partial_t \bar{h}$ arise

$$\tag{4.72}$$

where the cross denotes $\bar{\varphi}_0$. The new diagrams in the second and third line, however, describe the scattering processes between three mesons and two quarks. This observation implies that a two-quark multi-meson interaction should be taken into account in order to obtain the proper flow of the Yukawa coupling. One can do it by introducing a field-dependent Yukawa coupling and expanding it around the particular value of $\bar{\varphi}_0$ [167]

$$\bar{h}(\bar{\varphi}^2) = \sum_{n=0}^{N_h} \frac{\bar{h}_n}{n!} (\bar{\varphi}^2 - \bar{\varphi}_0^2)^n \,. \tag{4.73}$$

Thereby, the expansion coefficients $\bar{h}_n$ are considered as scale-dependent couplings. In this expansion, the lowest-order coupling $\bar{h}_0$ corresponds to the coupling $\bar{h}$ used in our

truncation and the choice $N_h = 0$ would recover our ansatz for the Yukawa interaction in Eq. (4.43). Considering this more general ansatz for the Yukawa-type interactions, one can see that the new diagrams in Eq. (4.72) contribute to the flow of the coupling $\bar{h}_1$. As a consequence, in our particular truncation with only the lowest order of $\bar{h}(\bar{\varphi}^2)$ we should drop these new contributions. Therefore, we obtain

$$
\partial_t h^2 = -\frac{8}{N_c} v_4 \sum_{l=1}^{N_c} \Big[3\, l_{1,1}^{(\text{FB})}(\tau, \tilde{\mu} - \mathrm{i}2\pi\tau\nu_l|\phi|, m_\pi^2, m_q^2)
$$
$$
- l_{1,1}^{(\text{FB})}(\tau, \tilde{\mu} - \mathrm{i}2\pi\tau\nu_l|\phi|, m_\sigma^2, m_q^2)\Big] h^4 \ .
\tag{4.74}
$$

At this point we want to mention that even though our particular truncation covers only the lowest order of the general field-dependent Yukawa coupling, it is already sufficient for qualitative studies, such the present one. In Ref. [167] the authors have found that the inclusion of higher two-quark multi-meson interactions leads to only quantitative corrections and the results converge rapidly if one increases the order of the expansion.

In our numerical calculations we use the flow equations for the chirally symmetric regime, Eqs. (4.58)−(4.60), at high momentum scales where the chiral symmetry is assumed to be restored. As we will see in Sec. 4.2.3, integrating out fluctuations leads to a decrease of the bosonic mass parameter m in the RG-flow towards smaller scales. At sufficiently small temperatures this parameter becomes zero at some critical momentum scale k_{cr}. This behavior indicates the onset of the chiral symmetry breaking in the RG flow, and is associated with a diverging 4-fermion coupling $\bar{\lambda}_\psi$, see our discussion in Sec. 4.1.2. Thus, in order to integrate out fluctuations on the scales $k < k_{\text{cr}}$, we use the flow equations for the regime of spontaneously broken chiral symmetry, Eqs. (4.70), (4.71) and (4.74). At this point we have to mention that the appearance of the onset of chiral symmetry breaking at the critical scale k_{cr} does not necessarily mean that chiral symmetry is broken in the infrared, i.e., for $k \to 0$. This is because the mesonic fluctuations tend to restore the symmetry and, thus, tend to reduce the value of the pion decay constant in the RG flow in the chirally broken regime. Therefore, it is possible that for $k < k_{\text{cr}}$ the pion decay constant becomes zero again and the symmetry is restored in the RG flow, see also the right plot in Fig. 4.8 in Sec. 4.2.3. This fact implies that the appearance of the critical scale k_{cr} is a necessary but not sufficient condition for the chiral symmetry breaking [151]. Thus, our results from the purely fermionic calculation in the point-like limit, Sec. 4.1.4, should be considered as only an upper boundary for the critical temperature T_χ.

Flow Equations with Explicit Chiral Symmetry Breaking

In our above calculations we have considered the chiral limit, i.e., we have assumed that the current quarks are massless. In real QCD, however, the quark masses are finite, albeit small. This leads to an explicit breaking of the chiral symmetry. However, since the quark masses are rather small, the effect of explicit symmetry breaking is rather weak and chiral symmetry can be considered as an approximate symmetry of QCD.

To introduce a (small) explicit symmetry breaking in PQM model one has to slightly deform the potential $U(\bar{\varphi}^2)$. To this end, one introduce a new term $\bar{c}\sigma$ with $\bar{c} < 0$ which ensures that the minimum of potential and, consequently, the expectation value $\bar{\varphi}_0$ are finite at any scale. Using the definition of σ within the Hubbard-Stratonovich transformation, one can easily see that the term $\bar{c}\sigma$ corresponds to the finite quark mass in the PQM action in Eq. (4.43). The introduction of this new term also impacts the

expansion of the potential $U(\bar{\varphi}^2)$ in Eq. (4.61). In order to ensure that we expand around the true minimum, the potential expansion should be given by

$$U(\bar{\varphi}^2) = -\frac{\bar{c}}{2\bar{\varphi}_0}(\bar{\varphi}^2 - \bar{\varphi}_0^2) + \frac{\bar{\lambda}_\varphi}{8}(\bar{\varphi}^2 - \bar{\varphi}_0^2)^2 + \bar{c}\sigma \ . \tag{4.75}$$

Thereby, the parameter $\bar{c}$ is a scale independent quantity since it appears as a prefactor of a term linear in the bosonic field σ. Further, this new expansion of $U(\bar{\varphi}^2)$ does not influence the flow equations for couplings $\bar{\lambda}_\varphi$ and $\bar{h}$. Only the RG flow of $\bar{\varphi}_0^2$ becomes slightly modified

$$\begin{aligned}
\partial_t \varphi_0^2 = &- 2\varphi_0^2 + 12v_4 l_1^{\mathrm{B}}(\tau, m_\sigma^2)\frac{\lambda_\varphi}{\lambda_\varphi - c/\varphi_0^3} + 12v_4 l_1^{\mathrm{B}}(\tau, m_\pi^2)\frac{\lambda_\varphi}{\lambda_\varphi - c/\varphi_0^3} \\
&- 64v_4 \sum_{l=1}^{N_c} l_1^{(\mathrm{F})}(\tau, \tilde{\mu} - \mathrm{i}2\pi\tau\nu_l|\phi|, m_q^2)\frac{h^2}{\lambda_\varphi - c/\varphi_0^3} \ ,
\end{aligned} \tag{4.76}$$

where we have introduced the dimensionless explicit symmetry breaking parameter $c = \bar{c}/k^3$. The definitions of the eigenvalues of the bosonic mass matrix, Eqs. (4.64) and (4.65), do not change. However, if we evaluate them at the ground state, we obtain different bosonic masses compared to the chiral limit

$$\begin{aligned}
\bar{m}_\sigma^2 &= \bar{m}_\sigma^2(\bar{\varphi}^2)\big|_{\bar{\varphi}_0^2} = \bar{\lambda}_\varphi\bar{\varphi}_0^2 - \frac{\bar{c}}{\bar{\varphi}_0} \ , \\
\bar{m}_\pi^2 &= \bar{m}_\pi^2(\bar{\varphi}^2)\big|_{\bar{\varphi}_0^2} = -\frac{\bar{c}}{\bar{\varphi}_0} \ .
\end{aligned} \tag{4.77}$$

Note, especially, that the pions become massive. Setting c to zero, we recover our previous flow equations for the case of spontaneously broken chiral symmetry.

Since including explicit symmetry breaking means that the pion decay constant $\bar{\varphi}_0$ is finite at any scale, we only have to use the flow equations (4.76), (4.71) and (4.74) in our corresponding numerical calculations.

4.2.3 *Numerical Results*

In this section we present our numerical results for the phase diagram of the PQM model spanned by the temperature T and the pion decay constant f_π. We consider both the chiral limit and a model with finite explicit symmetry breaking. We also investigate the impact of the finite chemical potential on the phase diagram.

As first, we have to specify the parameters of the model. In present calculations we have used $\Lambda_{\mathrm{UV}} = 1$ GeV as the UV cutoff, as we have also done it in our considerations of the PNJL model. The next step is to fix the initial values of the dimensionless couplings at $k = \Lambda_{\mathrm{UV}}$. Thereby, we should chose the initial conditions in such a way that for $T = \mu = 0$ our calculations reproduce the low-energy observables in the IR limit $k \to 0$. In the case of the chiral limit we should fix the bosonic mass parameter m_{UV}^2 and the Yukawa coupling h_{UV}^2 to obtain the correct values of the pion decay constant f_π and the constituent quark mass $\bar{m}_q$. In the presence of the finite explicit symmetry breaking we additionally have to reproduce the correct pion mass $\bar{m}_\pi$. To this end, we fix the initial values of $\varphi_{0,\mathrm{UV}}$, h_{UV}^2 and c. Please note that c remains constant in the RG flow and the coupling λ_φ is chosen to be zero at $k = \Lambda_{\mathrm{UV}}$ in order to connect our current PQM ansatz to the ansatz for the

	UV parameters	low-energy observables
chiral limit	$m_{\mathrm{UV}}^2 = 0.445$ $h_{\mathrm{UV}}^2 = 5.889$	$f_\pi = 87$ MeV $\bar{m}_q = 280$ MeV
explicit symmetry breaking	$\varphi_{0,\mathrm{UV}} = 3.541 \cdot 10^{-3}$ $h_{\mathrm{UV}}^2 = 6.671$ $c = -1.771092 \cdot 10^{-3}$	$f_\pi = 93$ MeV $\bar{m}_q = 300$ MeV $\bar{m}_\pi = 138$ MeV

TABLE 4.2: Summary of the initial conditions for dimensionless couplings reproducing correct low-energy observables for $T = \mu = 0$. The UV scale was chosen to $\Lambda_{\mathrm{UV}} = 1$ GeV. In these calculations we consider a model in the chiral limit (upper part of the tabel) and a model with finite explicit symmetry breaking (lower part of the tabel).

PNJL model at the UV scale. We also mention that in the chiral limit the value of the pion decay constant and the value of the constituent quark mass are slightly different compared to the values measured in experiments [80, 81][10]. Additionally, the pion mass is zero in the chiral limit. Our choice of the initial couplings and the corresponding low-energy observables for both the chiral limit and the model with explicit symmetry breaking are presented in the Tab. 4.2. For completeness we mention that in the presence of finite c we have found the σ-mass to be $\bar{m}_\sigma = 467.1$ MeV. This result is in accordance with the value given in Ref. [10].[11]

In order to plot a phase diagram spanned by T and f_π, we have to consider different sets of initial conditions compared to the values given in Tab. 4.2. To this end, we vary the starting value of the parameter m_{UV}^2 in our chiral limit calculations and the starting value of $\varphi_{0,\mathrm{UV}}$ for the case of finite explicit symmetry breaking. Thereby, we keep other initial conditions fixed. Please note that such variations impact not only the value of the pion decay constant f_π but all low-energy observables. Our results for $N_{\mathrm{c}} = 3$ and $N_{\mathrm{f}} = 2$ and different values of the chemical potential μ are summarized in the left part of Fig. 4.7. The upper left plot corresponds to the case of the chiral limit and the lower left plot to a model with explicit chiral symmetry breaking. In both these plots the x-axis represents different values of the pion decay constant f_π and the y-axis the corresponding relation of the chiral phase transition temperature to the temperature of the deconfinement phase transition, T_χ/T_d. To implement the deconfinement phase transition numerically, we have again employed the data from [146] as input for the coordinates of the ground state $\langle A_0 \rangle$. The vertical lines in the left plots of Fig. 4.7 denote the corresponding "physical" values of the pion decay constant. Note once again that $f_\pi = 87$ MeV in the chiral limit and $f_\pi = 93$ MeV in the real QCD with finite quark masses. Please also note that we do not present our results for the shape of the phase boundary for very small values of f_π. The reason for that is the following: At finite but not too small chemical potential $\mu_{\mathrm{c}} < \mu \lesssim \bar{m}_q$ [12], the chiral phase transition turns out to be of the first order. This type of phase transition corresponds to the appearance of two minimums in the potential $U(\bar{\varphi}^2)$.

---

10 The value of the pion decay constant is measured using $\pi^- \to \mu^- \bar{\nu}_\mu$ and $\pi^- \to \mu^- \bar{\nu}_\mu \gamma$ decays and amounts to $f_\pi = (92.21 \pm 0.01 \pm 0.14)$ MeV [79]. The errors are due to the uncertainty of $|V_{ud}|$ in the CKM-matrix and due to the higher-order corrections.

11 In the real world, the σ-meson is not a particle but a broad resonance in the mesonic spectrum which is sometimes also called $f_0(500)$. The mass corresponding to this resonance is constrained to $m = 400 - 550$ MeV.

12 μ_{c} denotes the the value of the chemical potential corresponding to the critical endpoint which separates the regime of the second order phase transition (or crossover) and the regime of the first order phase
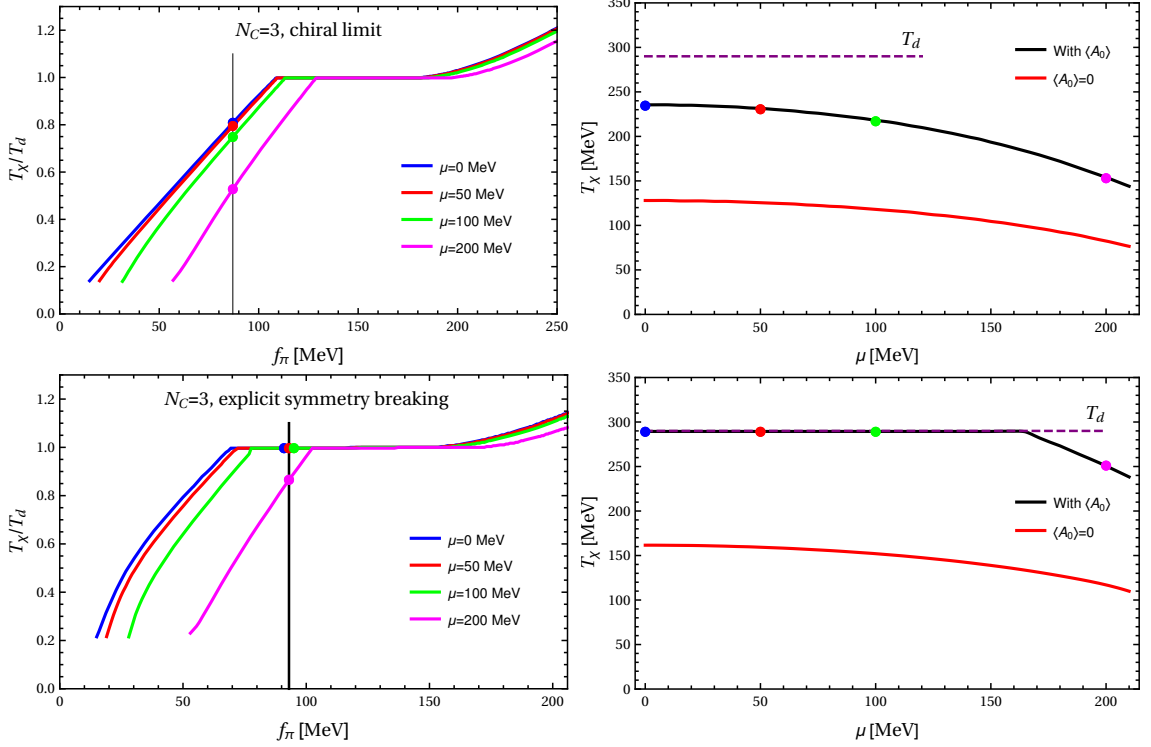
FIGURE 4.7: On the left: T_χ/T_d as a function of f_π for a PQM model in the chiral limit (upper plot) and with finite explicit symmetry breaking (lower plot) at selected values of chemical potential μ. In both cases we observe following regimes in the behavior of T_χ (from small to large f_π): $T_\chi < T_d$, $T_\chi \approx T_d$ and $T_\chi > T_d$. The impact of finite μ is basically a shift of the phase diagram for $\mu = 0$ to larger values in the parameter space. The vertical lines denote $f_\pi = 87$ MeV (chiral limit) and $f_\pi = 93$ MeV (explicit symmetry breaking) which correspond to the physical values of the pion decay constant in each case. The dots stand for T_χ/T_d at physical f_π for different μ. On the right: The phase diagrams spanned by μ and T_χ for the physical values of f_π (on the top: chiral limit, on the bottom: finite explicit symmetry breaking). Our results are denoted by black curves. For comparison we also plot the phase diagrams in the case of $\langle A_0 \rangle = 0$ (red line). Purple line represents the deconfinement transition temperature of our input $T_d \approx 290$ MeV [146].

In our particular calculations, however, we use the second order expansion in $\bar\varphi^2$ around $\bar\varphi_0^2$ as an ansatz for $U(\bar\varphi^2)$. Thus, we cannot properly capture the formation of the second minimum. Since very small values of f_π are associated with very small constituent quark mass $\bar m_q$, this effect already appears at relatively small values of μ and our formalism is not applicable to the corresponding region in the phase diagram.

Now, let us discuss the shape of the phase diagrams in the left panel of Fig. 4.7. We basically observe very similar results as in our calculations in purely fermionic picture in Sec. 4.1.3. It means that we again observe three different modes in the behavior of T_χ compared to the deconfinement critical temperature T_d: for small values of pion decay constant we have found that $T_\chi < T_d$, for large f_π that $T_\chi > T_d$ and for intermediate values of f_π we observe $T_\chi \approx T_d$. Thus, also in the bosonized picture we have found a window in parameter space given by f_π where the chiral phase transition is locked in by

---

transition in the phase diagram of QCD. For this particular discussion this point is not of interest. In Secs. 5.6 and 5.7 we present phase diagrams spanned by T and μ which include the critical endpoint.

	chiral limit, $\langle A_0 \rangle = 0$	chiral limit, $\langle A_0 \rangle \neq 0$	$c \neq 0$, $\langle A_0 \rangle = 0$	$c \neq 0$, $\langle A_0 \rangle \neq 0$
κ	0.125	0.394	0.147	0

TABLE 4.3: Our results for κ for different (P)QM models.

the gauge dynamics. Thereby, the inclusion of the finite chemical potential shifts the phase diagram to the larger values in the parameter space and almost does not change the size of the locking window. However, in contrast to our calculations in Sec. 4.1.3, we are now able to identify the "physical" point in the parameter space. Considering a model in the chiral limit, we find that the physical value of $f_\pi = 87$ MeV corresponds to a region where $T_\chi < T_d$. In contrast, if we include the finite explicit symmetry breaking, we find that the point in the parameter space corresponding to the value of $f_\pi = 93$ MeV is located inside of the locking window, at least as long as $\mu \lesssim 170$ MeV.

As next, we plot the phase diagrams spanned by μ and T_χ for the physical values of the pion decay constant. Our results are shown in the right part of Fig. 4.7. The upper plot corresponds to the chiral limit case and the lower to a model with finite explicit symmetry breaking. In both these plots the black lines denote our numerical results. For comparison we also plot the deconfinement phase transition temperature $T_d \approx 290$ MeV (purple dashed line) and colored dots which represent our results in the $(T_\chi/T_d, f_\pi)$-plane at the physical value of f_π. Further, we calculate the phase transition line also in the absence of the background field $\langle A_0 \rangle$ (QM model). This phase boundary is plotted as a red line. First, we consider the chiral limit (upper right plot in Fig. 4.7). One observes that the chiral phase transition boundary is decoupled from the deconfinement phase transition and $T_\chi < T_d$. However, it does not mean that the gauge dynamics do not influence the chiral symmetry breaking. And indeed, compared to the case of vanishing background field $\langle A_0 \rangle$, our calculations with finite $\langle A_0 \rangle$ lead to larger chiral phase transition temperature at all considered values of μ. Thus, even though we are out of the locking window, the confining dynamics tend to push the system into the phase with broken chiral symmetry. A different situation is realized if we consider the explicit symmetry breaking (lower right plot in Fig. 4.7). Here, the physical value of f_π lies in the locking region and we observe $T_\chi \approx T_d$ for $\mu \lesssim 170$ MeV. A model in the absence of $\langle A_0 \rangle$ produces also in the case of the finite explicit symmetry breaking considerably smaller T_χ.

Our results in the right part of Fig. 4.7 can also be used in order to calculate the curvature κ of the phase boundary, Eq. (4.40). To do this, we fit our data for the transition lines to an even polynomial of sixth degree. Our results are summarized in Tab. 4.3. In general, we observe that our (P)QM calculations always reproduce quite small κ as expected from Lattice QCD, e.g., $\kappa = 0.0032(1)$ in [162] and $\kappa = 0.500(54)$ in [163]. Especially in the case of finite explicit symmetry breaking and in the presence of the background field $\langle A_0 \rangle$ the curvature of the phase boundary is exactly zero. It is because in this case the chiral phase transition is locked in by the gauge dynamics and, thus, the curvature of the chiral phase transition is given by the curvature of the deconfinement phase boundary. However, we should mention that a constant $T_d(\mu)$ is an artifact of the input for $\langle A_0 \rangle$ where back-reactions from the matter sector on the gauge sector have been neglected. If such back-reactions are included, we expect to observe a finite κ for the deconfinement phase transition. Assuming that in this situation the chiral phase transition
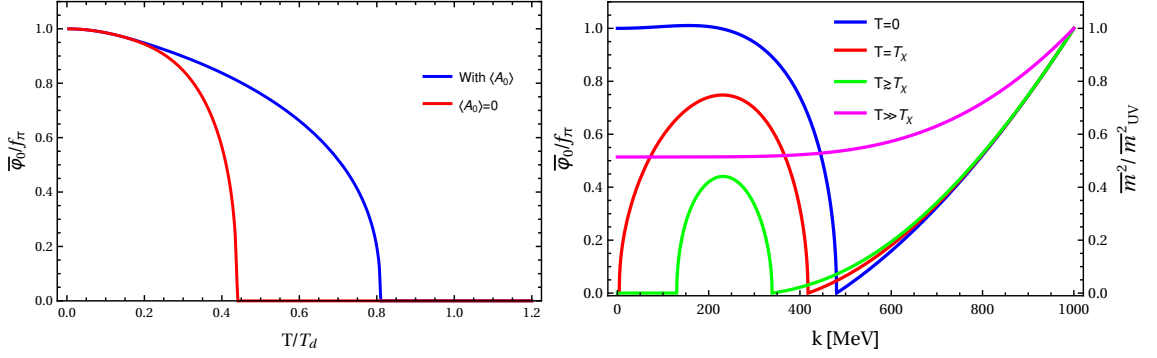
FIGURE 4.8: Here we present our results concerning the order parameter $\bar{\varphi}_0$ at $\mu = 0$ for a model in the chiral limit. On the left we plot the order parameter normalized by the physical value of the pion decay constant as a function of T/T_χ. We consider the model with finite and vanishing background field $\langle A_0 \rangle$. In both cases we observe a second order chiral phase transition. The presence of finite $\langle A_0 \rangle$ leads to higher critical temperature. On the right we present the flow of $\bar{\varphi}_0(k)/f_\pi$ at different temperatures. From this plot one can clearly see that the inclusion of bosonic fluctuations can lead to chiral symmetry restoration at small momentum scales even if the chiral symmetry was already broken in the RG-flow [151].

is still locked in by the gauge dynamics, the curvature of the chiral phase boundary would be the same as κ of the deconfinement transition line.

Further, we observe that the values of κ in the chiral limit and in the case of explicit symmetry breaking are very similar as long as the background field $\langle A_0 \rangle$ vanishes. In contrast, in the chiral limit the curvature seems to increase if one includes $\langle A_0 \rangle$. This is because the confining dynamics favor a ground state with broken chiral symmetry. This effect is opposite to the restoration of the chiral symmetry caused by thermal fluctuations at finite T. Therefore, as already mentioned above, for $\langle A_0 \rangle \neq 0$ we observe larger critical temperature T_χ. This, however, also means that in the region of (T, f_π)-phase diagram where $T_\chi < T_d$, the slope of the phase boundary becomes steeper compared to the case of vanishing $\langle A_0 \rangle$, consider Fig. 4.7. Consequently, if one increases the chemical potential and the phase diagram is shifted to larger values of f_π, the steeper slope leads to a larger curvature of the transition line in (T, μ)-plane.

Before we conclude this chapter, let us discuss some technical details of our numerical calculations with the (P)QM model. In Fig. 4.7 we have used different definitions of the chiral phase transition temperature T_χ for the case of the chiral limit and for the case of finite explicit symmetry breaking. While in the chiral limit the chirally restored phase is uniquely defined by vanishing expectation value $\bar{\varphi}_0$ at $k \to 0$, in a model with finite explicit symmetry breaking there is no real chiral phase transition and $\bar{\varphi}_0$ is always larger than zero. To define T_χ for this so-called crossover behavior, we have to look for an alternative procedure. Before we discuss this issue, let us discuss the behavior of the order parameter $\bar{\varphi}_0$ in the case of the chiral limit. In Fig. 4.8 we plot some of our results concerning the order parameter. In the left plot we present $\bar{\varphi}_0$ as function of T at $\mu = 0$. Thereby we compare the outcome of a PQM model (finite $\langle A_0 \rangle$) and of a QM model ($\langle A_0 \rangle = 0$). We observe a continuous behavior of the order parameter and $\bar{\varphi} = 0$ for $T \gtrsim T_\chi$. Thus, the observed phase transition is of the second order. In agreement with our discussion of Fig. 4.7, the chiral phase transition temperature T_χ is smaller than T_d. Also, the presence of the background field $\langle A_0 \rangle$ leads to larger T_χ. In the right plot of Fig. 4.8 we

present the RG flow of the mass parameter $m^2(k)$ in combination with $\bar{\varphi}(k)$ for different temperatures. Thereby, $\mu = 0$ and finite $\langle A_0 \rangle$ is included. At very high temperatures there is no chiral symmetry breaking and the mass parameter $\bar{m}^2(k)$ is always finite. However, if the temperature is small enough, $\bar{m}^2(k)$ becomes zero what indicates the onset of the chiral symmetry breaking in the RG-flow. We remind the reader that $\bar{m}^2 = 0$ is equivalent to $\bar{\lambda}_\psi \to \infty$ which we have used in our calculations with PNJL model as the indicator for the chiral phase transition. However, in the bosonic picture we have found that the onset of the chiral symmetry breaking in the RG flow does not necessarily mean that chiral symmetry is broken in the limit $k \to 0$. In the right panel of Fig. 4.8 the green curve shows that even the chiral symmetry becomes broken in the RG flow, it can be restored at smaller scales due to the bosonic fluctuations [151]. Thus, the condition $\bar{m}^2 = 0$ in the bosonic or, equivalently, $\bar{\lambda}_\psi \to \infty$ in the purely fermionic picture, represents only an upper bound for the critical temperature T_χ. For $T = T_\chi$ (red curve) the restoration of chiral symmetry due to the bosonic fluctuations happens exactly at $k = 0$. For even smaller temperatures the order parameter is finite in the limit $k \to 0$.

As next, we discuss how the pseudo-critical temperature of the chiral crossover in a model with explicit symmetry breaking can be determined. In our particular calculations we define the temperature T_χ using the maximum of the longitudinal susceptibility. In general, the susceptibility is defined as a derivative of the classical field with respect to the source

$$\chi_a = \frac{\overrightarrow{\delta}}{\delta J_a^T(x)} \Phi_a(x) = \frac{\overrightarrow{\delta}}{\delta J_a^T(x)} \frac{\overrightarrow{\delta}}{\delta J_a(x)} W[J] \ , \tag{4.78}$$

and, thus, is connected to the dressed propagator. Evaluating the susceptibility at the ground state and considering only the longitudinal part, i.e., only the σ-direction, we find

$$\chi_\sigma = V \frac{1}{\bar{m}_\sigma^2} \ , \tag{4.79}$$

where V denotes the $4d$ spacetime volume. In the chiral limit χ_σ diverges at $T = T_\chi$ since $\bar{m}_\sigma^2$ vanishes at the phase boundary. This diverging behavior can also be used in order to determine T_χ in the chiral limit and leads to exactly the same results as for the condition of a vanishing $\bar{\varphi}_0$ for $T \geq T_\chi$. In the case of a crossover, χ_σ does not diverge but still have a maximum which can be used to define T_χ. Since we work with infinite volumes, we use the maximum of $\chi_\sigma(T)/\chi_\sigma(T = 0)$ to measure T_χ.

Our results for the susceptibility $\chi_\sigma(T)$ normalized by $\chi_\sigma(T = 0)$ at $\mu = 0$ are presented in the left plot of Fig. 4.9. We distinguish between two cases: $\langle A_0 \rangle = 0$ and $\langle A_0 \rangle \neq 0$. In the first case, we observe a very typical behavior of the susceptibility for a model with a crossover, i.e., that $\chi_\sigma(T)/\chi_\sigma(T = 0)$ is continuous and has a maximum. We use this maximum in order to define T_χ for the corresponding phase boundary in the lower right plot of Fig. 4.7. However, if we include the background field $\langle A_0 \rangle$ in our calculations, the model at $\mu = 0$ is located inside of the locking window and T_χ is determined by T_d. Also the behavior of the susceptibility and the chiral order parameter $\bar{\varphi}_0$ is strongly influenced by the behavior of the background field $\langle A_0 \rangle = 0$. Therefore, since our input for $\langle A_0 \rangle$ was calculated for a pure SU(3) Yang-Mills theory and shows the first order deconfinement phase transition, we observe a jump in $\chi_\sigma(T)/\chi_\sigma(T = 0)$ for $T = T_d$. However, one should keep in mind that this is an artifact of our input for $\langle A_0 \rangle$. If the back-reaction of the matter sector on the gauge sector is included, $\langle A_0 \rangle$ would show a crossover behavior.
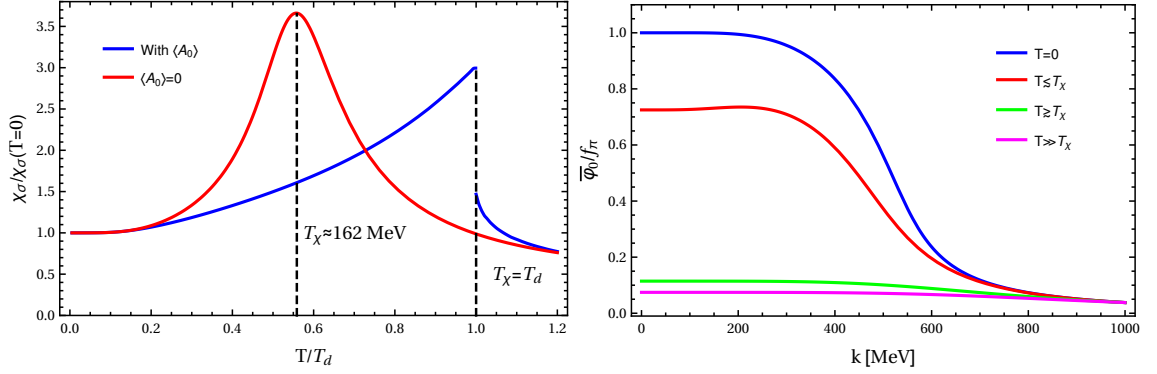
FIGURE 4.9: In the left plot we present our results for the normalized longitudinal susceptibility $\chi_\sigma(T)/\chi_\sigma(T = 0)$ at $\mu = 0$ for a model with explicit symmetry breaking. We consider two cases: finite and vanishing background field $\langle A_0 \rangle$. For $\langle A_0 \rangle = 0$ the susceptibility have a peak which is used to determine the pseudo-critical temperature of the chiral crossover. In the case of finite $\langle A_0 \rangle$, the chiral phase transition is locked in by the confining dynamics. Thus, we observe a transition of the first order indicated by a jump in $\chi_\sigma(T)/\chi_\sigma(T = 0)$. In the right plot we present the flow of $\bar{\varphi}_0(k)/f_\pi$ at different temperatures ($\langle A_0 \rangle \neq 0$). Since bosonic fluctuations, especially, pions are massive in the case of finite explicit symmetry breaking, their impact on the restoration of the chiral symmetry towards $k \to 0$ in the RG-flow is clearly suppressed compared to the chiral limit (see. the right plot in Fig. 4.8).

Additionally the expectation value of $\bar{\varphi}_0$ is finite for all temperatures. Thus, we should consider the observed chiral transition as a crossover and not as a transition of first order.

For the sake of completeness, we present in the right panel of Fig. 4.9, the flow of $\bar{\varphi}_0(k)/f_\pi(k = 0)$ for a model with finite explicit symmetry breaking and in presence of the background field $\langle A_0 \rangle \neq 0$, where we consider different temperatures. As already mentioned above, we observe that the order parameter is finite on all scales and for all temperatures. Thus, the chiral phase transition in the particular model is realized as a crossover. For low temperatures, we observe a strong increase of $\bar{\varphi}_0(k)/f_\pi$ towards $k \to 0$ which takes place at 400 MeV $\lesssim k \lesssim$ 600 MeV. Due to the choice of the initial conditions, for $T = 0$ and in the infrared, we observe the physical value of the pion decay constant, $\bar{\varphi}_0(k) = f_\pi = 93$ MeV. For temperatures $T > T_\chi$ the value of $\bar{\varphi}_0(k)/f_\pi$ does not increase considerably in the RG flow.

To conclude this chapter, we remind the reader that in our particular calculations we have observed an interval in the parameter space of low-energy QCD models where the chiral phase transition is locked in due to the gauge dynamics and, thus, $T_\chi \approx T_d$. This locking window appears both in purely fermionic picture (PNJL model) and in the partially bosonized model (PQM model). The inclusion of the finite chemical potential basically shifts the phase diagram and, thus, the locking window to the larger values in the parameter space. Whether the physical point is located inside of this window is strongly dependent on the details of the model. In particular a PQM model with finite explicit symmetry breaking and parameters adjusted to reproduce correct low-energy observables is located inside of the locking window in our study. Therefore, we can suggest that a comparable mechanism relating the chiral and the deconfinement phase transition could also be present in nature. This would explain why the critical temperatures of these phase transitions are so similar in the lattice QCD simulations, Refs. [49, 50, 51, 52, 53]. However, we should also keep in mind that the current models are based on some approxi-

mations, such as fine-tuning of the parameters, Fierz-incomplete interaction channels and negligence of the possible T- and μ-dependence of the initial model parameters. In the next chapter, we suggest an approach how these problems of the current model calculations can be improved by means of QCD RG flows. In particular, we apply this approach in order to derive an NJL model.

<div style="text-align: right">5</div>

QCD INSPIRED DETERMINATION OF NJL-MODEL PARAMETERS

As we have seen in the previous chapter, low-energy QCD models provide us with some guidance how the phase diagram of QCD could look like. However, in common model calculations one is restricted to some approximations which could influence the phase-diagram structure considerably:

1. Model parameters are fine-tuned:
   In model calculations one always has to fix the UV scale of the model and the values of model couplings at this scale, see, e.g., [27, 126, 127, 128, 129, 130, 131, 132, 133, 134, 135, 136]. A particular choice of these parameters is always justified post festum, i.e., it has to reproduce correct physical observables at zero temperature and zero chemical potential. However, different sets of starting parameters can reproduce the correct values of physical observables in the limit $T = \mu = 0$ equally well. Thereby, they would lead to different realizations of the phase diagram, i.e., to different critical temperatures, critical endpoints etc. In common model calculations there is no possibility to justify the exact values of starting parameters from the point of view of the underlying fundamental theory.

2. Model parameters do not depend on temperature T, and chemical potential μ:
   Once model parameters are fixed, one uses them also for finite T- and μ-studies. But, in general, these parameters will depend on T and μ. In common model studies there is no possibility to estimate T- and μ-dependence of the starting parameters. However, as we will see later in this chapter, this dependence can influence the phase diagram of a particular model significantly.

3. Fierz ambiguity:
   Often one uses only the phenomenologically important scalar-pseudoscalar interaction channel for quarks as we have done it in our NJL calculations above[1]. In general, there are much more channels which are allowed by Fierz ambiguity[2] [168, 169]. For details on the Fierz transformation, we refer the reader to App. B.2. In short, a Fierz transformation leads to an algebraic reordering of the fermionic fields in a given interaction channel and, thus, to the appearance of additional channels compatible with underlying symmetries of the model. These channels can be potentially generated by quantum effects. In different studies it was shown that taking into account additional

---

[1] The scalar-pseudoscalar channel in NJL model translates into the usual quark-meson model with one sigma and three pions by virtue of a Hubbard-Stratonovich transformation, see Sec. 4.2.1.

[2] Inclusion of additional channels in the NJL model would lead to additional mesons in the QM model.
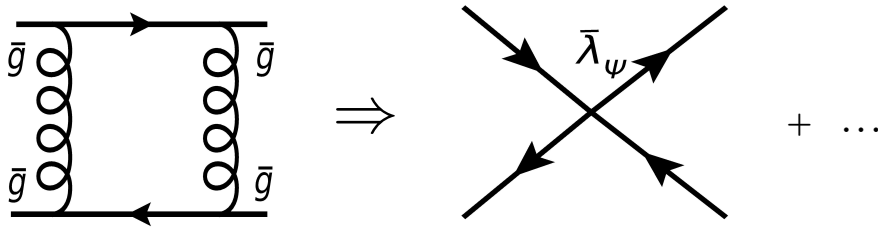
FIGURE 5.1: The effective quark self-interactions are generated by gauge dynamics and can be projected onto interaction channels used in model calculations.

interaction channels can change the phase structure of an NJL model quite strongly [57, 152, 153]. Even though the studies with more interaction channels are more sophisticated, the problem of parameter choice becomes here more pronounced since more parameters have to be fine-tuned. This leads to an even stronger ambiguity.

In the light of these problems we can see that predictive power of model calculations is constrained. Therefore, models require some improvement from the point of view of the underlying fundamental theory, namely QCD. Such an improvement can be achieved considering the QCD RG flows [71, 72, 73].

5.1   BASIC IDEA AND ANSATZ

To calculate QCD RG flows and to understand how they can improve model calculations let us first start with the usual QCD Lagrangian in Euclidean space:

$$\mathcal{L}_{\mathrm{QCD}} = \bar{\psi}(\mathrm{i}\slashed{\partial} + \bar{g}\slashed{A} + \mathrm{i}\gamma_0\mu)\psi + \frac{1}{4}F^z_{\mu\nu}F^z_{\mu\nu} \; . \tag{5.1}$$

Compared to Eq. (2.13), we consider QCD in the chiral limit, $\bar{m}_q = 0$, and introduce the finite chemical potential, μ. In this Lagrangian the interaction between quarks is mediated by gluons. Now, the idea is to calculate the flow equations for effective quark self-interactions which are generated by the gauge fields, see Fig. 5.1 [71, 72, 73]. These effective interactions allow to study mechanisms of chiral symmetry breaking in QCD directly. In [71, 72, 73] it was shown that very strong (or diverging) couplings of 4-quark interaction channels, $\bar{\lambda}_\psi$, trigger the chiral symmetry breaking. We sketch the corresponding mechanism in the next section.

In general there are infinite many effective quark self-interactions. However, the most interesting for us are the 4-fermion interactions since they can directly be related to order parameters. The strategy we pursue is as follows (see also Fig. 5.2): First, we consider a truncation of the scale-dependent effective action of QCD which includes Fierz-complete effective 4-quark interactions with corresponding couplings $\bar{\lambda}_i$. For $k = \Lambda_{\mathrm{UV,\,QCD}}$, we have

$$\Gamma_{k=\Lambda_{\mathrm{UV,\,QCD}}} = \int \mathrm{d}^4x\, \mathcal{L}_{\mathrm{QCD}} \; , \tag{5.2}$$

with $\mathcal{L}_{\mathrm{QCD}}$ from Eq. (5.1). It means that for $k = \Lambda_{\mathrm{UV,\,QCD}}$ the strength of effective quark self-interactions is zero and we start with the usual QCD action in the UV-regime. Then, we apply the FRG to integrate out fluctuations and, thus, generate effective quark
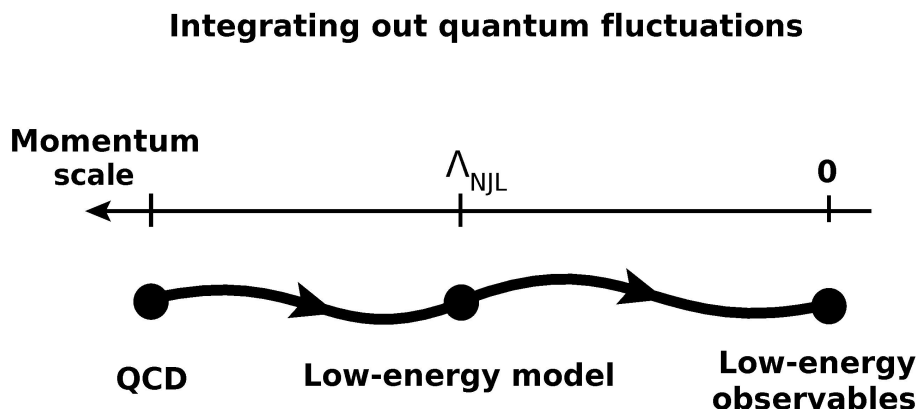
Integrating out quantum fluctuations

FIGURE 5.2: We start with QCD at very high momentum scale and successively integrate out fluctuations using FRG. Thereby, we generate effective quark self-interactions. At the scale $\Lambda_{\rm NJL}$ we project the results from QCD flows onto channels used in NJL calculations. For even smaller scales we apply FRG to resulting NJL model. $\Lambda_{\rm NJL}$ has to be fixed in such a way that correct low-energy observables are reproduced for $T \to 0$, $\mu \to 0$. The NJL couplings, $\bar{\lambda}_{i,\,{\rm NJL}}(\Lambda_{\rm NJL})$, are predicted by QCD flows and include T- and μ-dependence.

self-interactions. At some scale, $\Lambda_{\rm NJL}$, we project the 4-fermion interaction channels from QCD RG flows onto the channels commonly used in NJL studies. For $0 \lesssim k \leq \Lambda_{\rm NJL}$, we apply the FRG approach to the effective action of the resulting NJL model. In particular, $\Lambda_{\rm NJL}$ should be chosen in such a way that our model reproduces the correct low-energy observables in the limit $T \to 0$, $\mu \to 0$, i.e., it should reproduce the correct quark mass, $\bar{m}_q \simeq 300$ MeV (or alternatively the correct pion decay constant in the chiral limit, $f_\pi = 87$ MeV).

At this point we emphasize that, due to this strategy, in the left part of Fig. 5.2, we always deal with the chirally symmetric regime. Only after projection of our QCD flows onto the model channels and further integrating out fluctuations, right part of Fig. 5.2, we produce the breaking of the chiral symmetry in NJL model. In particular it means that for $k = \Lambda_{\rm NJL}$ the couplings of quark self-interactions, $\bar{\lambda}_\psi$, are not divergent.

The above strategy allows us to improve model calculations concerning at least some of the problems mentioned in the beginning of this chapter. First, as we will see later, in our present calculations we have only one parameter which should be fine-tuned, namely the UV cut-off of the model, $\Lambda_{\rm NJL}$. In contrast to the usual model calculations, the starting values for NJL couplings, $\bar{\lambda}_{i,\,{\rm NJL}}(\Lambda_{\rm NJL})$, are predicted by QCD RG flows[3]. Thereby, there is an one-to-one correspondence between an particular choice of $\Lambda_{\rm NJL}$ and resulting low-energy observables. Therefore, the ambiguity concerning the choice of the model parameters is much less present in our calculations. Our model is fully constrained by QCD RG flows and by physical low-energy observables. Second, after $\Lambda_{\rm NJL}$ is fixed at $T = 0$ and $\mu = 0$, we can keep $\Lambda_{\rm NJL}$ constant also for finite T and μ calculations. In contrast, the staring values of NJL couplings, $\bar{\lambda}_{i,\,{\rm NJL}}(\Lambda_{\rm NJL})$, become now functions of temperature and chemical potential. Thereby, the T- and μ-dependence of $\bar{\lambda}_{i,\,{\rm NJL}}(\Lambda_{\rm NJL})$ results from T- and μ-dependence of QCD RG flows. Third, we can use the Fierz-complete ansatz for 4-fermion interactions in the calculations with QCD RG flows in order to compare the relative strength of the NJL couplings at the UV cut-off of the model. This comparison

---

3 For more sophisticated models further parameters can be predicted as well.

can be used in order to estimate the importance of different channels in the NJL model.

Now, let us define our ansatz in a formal way. As we have explained above, we consider the standard gauge and fermionic sectors of QCD plus all effective 4-quark self-interactions compatible with $SU(N_c)$ gauge symmetry and $SU(N_f)_L \times SU(N_f)_R$ flavor symmetry. The inclusion of the ghost sector is tacitly assumed but is not relevant for our particular calculations. At this point we keep the number of colors N_c and number of flavors N_f as free parameters. Thus, our ansatz for effective scale-dependent action, Γ_k, in Euclidean spacetime is [71, 72, 73]:

$$
\begin{aligned}
\Gamma_k = \int \mathrm{d}^4x \ \bigg\{ & \bar{\psi}(\mathrm{i}Z_\psi \slashed{\partial} + Z_1 \bar{g}\slashed{A} + \mathrm{i}\gamma_0\mu)\psi + \frac{Z_A}{4}F^z_{\mu\nu}F^z_{\mu\nu} + \frac{(\partial_\mu A^z_\mu)^2}{2\xi} \\
& + \frac{1}{2}\Big[Z_-\bar{\lambda}_-(\mathrm{V}-\mathrm{A}) + Z_+\bar{\lambda}_+(\mathrm{V}+\mathrm{A}) + Z_\sigma\bar{\lambda}_\sigma(\mathrm{S}-\mathrm{P}) \\
& + Z_{\mathrm{VA}}\bar{\lambda}_{\mathrm{VA}}[2(\mathrm{V}-\mathrm{A})^{\mathrm{adj}} + 1/N_c(\mathrm{V}-\mathrm{A})]\Big]\bigg\} \ ,
\end{aligned}
\tag{5.3}
$$

where $A_\mu = A^z_\mu t^z$ with t^z generators of $SU(N_c)$ group in fundamental representation. The last term of the first line in action (5.3) is the so-called gauge fixing term which appears if one quantizes QCD, see. App. D.

In the above effective action, momentum-scale-dependent wave-function renormalizations Z_A and Z_ψ correspond to the kinetic terms of gauge and quark fields. The bare couplings $\bar{g}$, $\bar{\lambda}_-$, $\bar{\lambda}_+$, $\bar{\lambda}_\sigma$ and $\bar{\lambda}_{\mathrm{VA}}$ are accompanied by vertex renormalizations Z_1, Z_-, Z_+, Z_σ and Z_{VA} and are linked to dimensionless couplings via relations:

$$
g = \frac{\bar{g}Z_1}{Z_A^{1/2}Z_\psi} \ , \qquad \lambda_i = \frac{Z_i k^2 \bar{\lambda}_i}{Z_\psi^2} \ .
\tag{5.4}
$$

In this work we consider the Landau gauge, $\xi = 0$. The major reason to use this fixing condition is that Landau gauge is well known to be a fixed point of the renormalization group [105]. Additionally, the fermionic wave-function renormalization, Z_ψ, is not renormalized in the Landau gauge and in our truncation[4]. It means that Z_ψ becomes momentum-scale independent and we can use $Z_\psi = 1$ [16].

The first two 4-fermion channels appearing in Eq. (5.3) are given by:

$$
\begin{aligned}
(\mathrm{V}-\mathrm{A}) &= (\bar{\psi}\gamma_\mu\psi)^2 + (\bar{\psi}\gamma_\mu\gamma_5\psi)^2 \ , \\
(\mathrm{V}+\mathrm{A}) &= (\bar{\psi}\gamma_\mu\psi)^2 - (\bar{\psi}\gamma_\mu\gamma_5\psi)^2 \ ,
\end{aligned}
\tag{5.5}
$$

with color $(i, j, \ldots)$ and flavor $(a, b, \ldots)$ indices contracted pairwise. These two channels are color and flavor singlets. Channels with non-trivial color and flavor structure are:

$$
\begin{aligned}
(\mathrm{S}-\mathrm{P}) &= (\bar{\psi}^a\psi^b)^2 - (\bar{\psi}^a\gamma_5\psi^b)^2 \\
(\mathrm{V}-\mathrm{A})^{\mathrm{adj}} &= (\bar{\psi}\gamma_\mu t^z\psi)^2 + (\bar{\psi}\gamma_\mu\gamma_5 t^z\psi)^2 \ ,
\end{aligned}
\tag{5.6}
$$

where $(\bar{\psi}^a\psi^b)^2 = \bar{\psi}^a_i\psi^b_i\bar{\psi}^b_j\psi^a_j$ etc.

In the QCD part of our calculations, i.e., for $\Lambda_{\mathrm{NJL}} \leq k \leq \Lambda_{\mathrm{QCD, UV}}$ (left part of Fig. 5.2), we consider the 4-fermion couplings in the point-like limit, $\bar{\lambda}_i(|p| \ll k)$. This

---

4 In Landau gauge Z_ψ stays constant as long we do not resolve the momentum dependence of 4-fermion vertices [117].

approximation is not applicable in the regime with broken chiral symmetry. It is due to the fact that corresponding mesons (Goldstone bosons) manifest themselves as momentum singularities in the 4-fermion couplings. However, for the chirally symmetric regime the point-like limit serves as a reasonable approximation as it was quantitatively shown for the zero-temperature chiral phase transition in many flavor QCD in Ref. [72]. Also for finite temperatures this approximation was successfully applied in, e.g., [73]. Thereby, it was assumed that mechanisms which determine quark dynamics near the finite-T boundary and near the many-flavor phase boundary [170, 171, 172] are qualitatively similar.

We emphasize that the channels given in Eqs. (5.5) and (5.6) are different compared to the channels used in low-energy models, e.g. see Sec. 4.1. However, this set of quark self-interactions is Fierz-complete. It means that any other 4-fermion interaction compatible with $\mathrm{SU}(N_c)$ and $\mathrm{SU}(N_f)_L \times \mathrm{SU}(N_f)_R$ symmetries can be rewritten in terms of these interactions by means of the Fierz transformation, App. B.2. Therefore, it is possible to project the current set of interactions onto the common model channels, for details see Sec. 5.4. At this point we also want to mention two approximations we have used in our ansatz: First, we have neglected $\mathrm{U}_A(1)$-violating interactions since they are expected to become important only in the chirally broken regime or for small N_f [73]. In our numerical calculations we use $N_f = 2$ and consider the QCD flows only in the chirally symmetric regime. For $N_f = 2$ and for the case of restored chiral symmetry, the relative irrelevance of $\mathrm{U}_A(1)$-violating terms compared to channels used in this work was shown in [122]. Second, strictly speaking Eqs. (5.5) and (5.6) are Fierz-complete only for $T = 0$ and $\mu = 0$. For finite temperature and chemical potential additional channels would appear due to the presence of the heat bath. However, first attempts to include different runnings transversal and longitudinal to the heat bath for $N_f = 1$-theory suggest that the impact of such additional channels is rather small [151]. Nonetheless we aim to investigate this issue more properly in further works.

5.2 FLOW EQUATIONS FOR FERMIONIC INTERACTIONS

Using the ansatz in Eq. (5.3) and the Wetterich equation, Eq. (3.28), we can calculate β functions for the dimensionless 4-fermion couplings. Thereby, we proceed similarly to our calculations in Secs. 4.1.3 and 4.2.2. The major difference to our previous model calculations is that now we also have gauge bosons in our effective action (5.3). We obtain

$$
\begin{aligned}
\partial_t \lambda_- = {} & 2\lambda_- - 4 v_4 l_{1,1}^{(\mathrm{FB})}(\tau, \tilde{\mu}, 0, 0) \left[\frac{3}{N_c} g^2 \lambda_- - 3 g^2 \lambda_{\mathrm{VA}} \right] \\
& - \frac{1}{8} v_4 l_{1,2}^{(\mathrm{FB})}(\tau, \tilde{\mu}, 0, 0) \left[\frac{12 + 9 N_c^2}{N_c^2} g^4 \right] \\
& - 8 v_4 l_1^{(\mathrm{F})}(\tau, \tilde{\mu}, 0) \Big[-2(N_c + N_f)\lambda_- \lambda_{\mathrm{VA}} + N_f \lambda_\sigma \lambda_+ - N_c N_f (\lambda_+^2 + \lambda_-^2) \\
& \qquad\qquad + \lambda_-^2 + 2\lambda_{\mathrm{VA}}^2 \Big] \,,
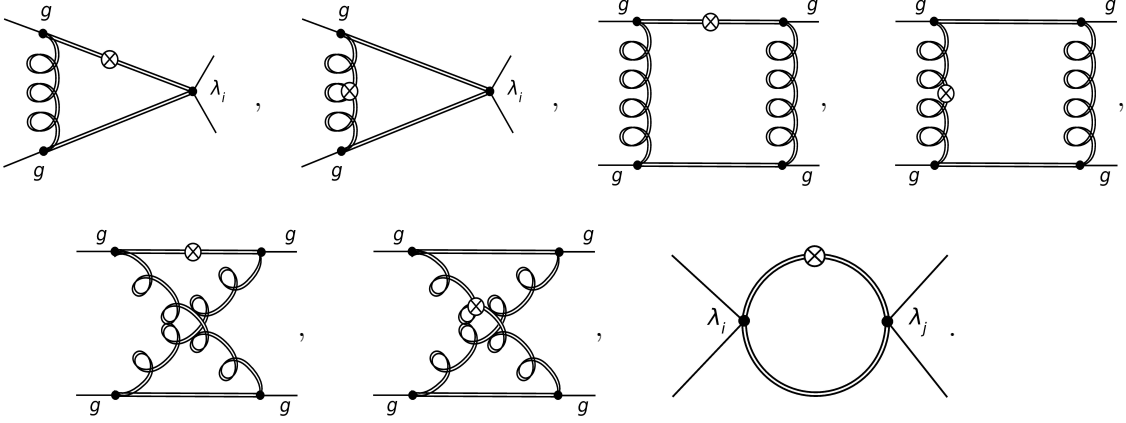\end{aligned}
$$

(5.7)

FIGURE 5.3: Graphical representation of different contributions to the RG flow equations for the quark self-interactions, Eqs. (5.7)–(5.10). The double lines correspond to the fully dressed fermionic and gluonic propagators, solid black dots to 4-fermion and quark-gluon vertices. The white circle with a cross represents the insertion of $\partial_t R_k$. λ_i and λ_j stay for λ_-, λ_+, λ_σ and λ_{VA}.

$$
\partial_t \lambda_+ = 2\lambda_+ - 4v_4 l_{1,1}^{(\mathrm{FB})}(\tau, \tilde{\mu}, 0, 0) \left[-\frac{3}{N_\mathrm{c}} g^2 \lambda_+ \right] - \frac{1}{8} v_4 l_{1,2}^{(\mathrm{FB})}(\tau, \tilde{\mu}, 0, 0) \left[-\frac{12 + 3N_\mathrm{c}^2}{N_\mathrm{c}^2} g^4 \right]
$$
$$
- 8v_4 l_1^{(\mathrm{F})}(\tau, \tilde{\mu}, 0) \Big[N_\mathrm{f} \lambda_\sigma \lambda_- + \lambda_\sigma \lambda_{\mathrm{VA}} - 2\lambda_+(\lambda_- + (N_\mathrm{c} + N_\mathrm{f})\lambda_{\mathrm{VA}})
$$
$$
- 2N_\mathrm{c} N_\mathrm{f} \lambda_+ \lambda_- - 3\lambda_+^2 + \frac{1}{4}\lambda_\sigma^2 \Big] ,
$$

$$(5.8)$$

$$
\partial_t \lambda_\sigma = 2\lambda_\sigma - 4v_4 l_{1,1}^{(\mathrm{FB})}(\tau, \tilde{\mu}, 0, 0) \left[6C_2(N_\mathrm{c}) g^2 \lambda_\sigma - 6g^2 \lambda_+ \right]
$$
$$
- \frac{1}{4} v_4 l_{1,2}^{(\mathrm{FB})}(\tau, \tilde{\mu}, 0, 0) \left[-\frac{24 - 9N_\mathrm{c}^2}{N_\mathrm{c}} g^4 \right]
$$
$$
- 8v_4 l_1^{(\mathrm{F})}(\tau, \tilde{\mu}, 0) \left[-2\lambda_\sigma \lambda_- - 2N_\mathrm{f} \lambda_\sigma \lambda_{\mathrm{VA}} - 6\lambda_+ \lambda_\sigma + 2N_\mathrm{c} \lambda_\sigma^2 \right] ,
$$

$$(5.9)$$

$$
\partial_t \lambda_{\mathrm{VA}} = 2\lambda_{\mathrm{VA}} - 4v_4 l_{1,1}^{(\mathrm{FB})}(\tau, \tilde{\mu}, 0, 0) \left[\frac{3}{N_\mathrm{c}} g^2 \lambda_{\mathrm{VA}} - 3g^2 \lambda_- \right]
$$
$$
- \frac{1}{8} v_4 l_{1,2}^{(\mathrm{FB})}(\tau, \tilde{\mu}, 0, 0) \left[-\frac{24 - 3N_\mathrm{c}^2}{N_\mathrm{c}} g^4 \right]
$$
$$
- 8v_4 l_1^{(\mathrm{F})}(\tau, \tilde{\mu}, 0) \left[-(N_\mathrm{c} + N_\mathrm{f})\lambda_{\mathrm{VA}}^2 - \frac{1}{4} N_\mathrm{f} \lambda_\sigma^2 + 4\lambda_- \lambda_{\mathrm{VA}} \right] .
$$

$$(5.10)$$

Here, $C_2(N_\mathrm{c}) = (N_\mathrm{c}^2 - 1)/(2N_\mathrm{c})$ is a Casimir operator of SU(N_c) group and $v_4 = 1/(32\pi^2)$. $\tau = T/k$ and $\tilde{\mu} = \mu/k$ represent the dimensionless temperature and the dimensionless chemical potential correspondingly. The threshold functions $l_1^{(\mathrm{F})}$, $l_{1,1}^{(\mathrm{FB})}$ and $l_{1,2}^{(\mathrm{FB})}$ include information about temperature and chemical potential dependence of the flow equations. Their particular shape also depends on the details of the regularization scheme. In this work we use the so-called $3d$ linear regulators for fermions and bosons [157]. These regulators and corresponding threshold functions are summarized and discussed in App. E.
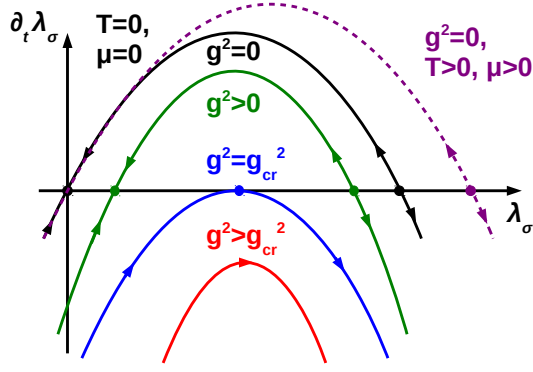
FIGURE 5.4: Sketch of a typical β-function for the coupling λ_σ. At $g^2 = 0$ (black solid line), there are two fixed points: an IR attractive Gaussian and an IR repulsive non-trivial fixed point. For small but finite g^2 (green solid line) the positions of the fixed points are shifted on the order of g^4. If the strong coupling reaches a critical value $g^2 = g_{cr}^2$, the fixed points melt together (blue solid line) and for even larger $g^2 > g_{cr}^2$, there are no fixed points (red solid line). In this case the strength of the quark self-interaction grows rapidly and signals the onset of the chiral symmetry breaking. For finite temperature and finite chemical potential (magenta dashed line), the parabolas become broader and higher. Thus, the critical value of the strong coupling, g_{cr}^2, grows and the chiral symmetry breaking scale, $k_{\chi SB}$, decreases. The flows of all other 4-fermion interactions can be analyzed in the same way.

The flow equations (5.7)–(5.10) are in agreement with results from [73], where also finite quark masses were introduced. In the zero temperature limit they also reproduce the results from [71] and [72].

Even though Eqs. (5.7)–(5.10) look quite complex, one may easily understand their structure if one thinks in terms of corresponding Feynman diagrams, see Fig. 5.3. From this figure, we can directly see that the change of 4-fermion couplings with a change of momentum scale k is given by all possible 1-loop contributions allowed by interactions encoded in Eq. (5.3). The 1-loop structure of the flow equations is a basic feature of the Wetterich flow equation.

A very remarkable point is that the flow equations (5.7)–(5.10) provide us a simple picture of the chiral dynamics in QCD [71, 72, 73]. To sketch it, we first consider the limit of vanishing T and μ. In this limit the threshold functions are simply given by some constants, see App. E. For simplicity, we look at only one 4-fermion coupling, e.g., λ_σ, and assume that all other couplings are zero. Thus, the flow of λ_σ is given by a simple equation

$$\partial_t \lambda_\sigma = 2\lambda_\sigma - c_1 g^2 \lambda_\sigma - c_2 g^4 - c_3 \lambda_\sigma^2 \, , \tag{5.11}$$

which is a function of λ_σ and g^2. The quantities c_1, c_2 and c_3 are constants in the limit $T \to 0$, $\mu \to 0$. Their particular absolute values are not of interest at this point. However, their signs are crucial for the fixed-point structure. Considering the flow of λ_σ, the constants c_1, c_2 and c_3 are positive as long as $N_c \geq 2$. Since in our numerical calculations we use the physical number of colors $N_c = 3$, in the following discussion, we consider the case that all constants in Eq. (5.11) are positive. Now let us consider the limit $g^2 \to 0$. In this case the flow $\partial_t \lambda_\sigma$ is a parable in λ_σ opened downwards (black solid line in Fig. 5.4) and has two zero points which correspond to the fixed points in

the RG flow. In Fig. 5.4 the arrows represent the direction of the RG-flow, or in other words, the direction of the change of $\partial_t \lambda_\sigma$ and λ_σ if we integrate out fluctuations. The two observed fixed points are an infrared attractive Gaussian and an infrared repulsive non-trivial fixed point. We emphasize that the Gaussian fixed point corresponds to a theory without any fermionic self-interactions. Of course, in QCD g^2 is not zero. However, for very high momenta the strong coupling g^2 is quite small (green solid curve). For finite but small coupling, the flow-parable is shifted down and the Gaussian fixed point becomes non-trivial. However, the value of this fixed point is on the order $\sim g^4$ and therefore very small[5]. In our calculations, we indeed start at very high momenta with the boundary conditions $\lambda_i = 0$. Thus, the coupling λ_σ grows if we apply the RG-transformation but is still bounded from above by a small value of the IR attractive non-trivial fixed point. In this regime of very weak quark self-interactions no quark condensate can be produced and we are in the regime of restored chiral symmetry.

For smaller k the coupling g^2 grows and the flow parabola is shifted more and more downwards. At some critical coupling, g_{cr}^2, both non-trivial fixed points melt together (blue solid line) and for $g^2 > g_{cr}^2$ they disappear (red solid line). In this situation the coupling λ_σ is not bounded from above and starts to grow rapidly. At some scale $k = k_{\chi SB}$ the quark self-interaction can even diverge. If this behavior appears, the chiral symmetry breaking takes place. We can see it immediately if we look at our considerations in Sec. 4.2.1 where bosonized version of PNJL model (PQM model) was introduced. In this section we have shown that $\bar{\lambda}_\psi \sim 1/\bar{m}^2$, and $\bar{m}^2 = 0$ indicates the chiral phase transition. Hence, the scale at which the 4-fermion interactions diverge in our truncation is a good measure for the chiral symmetry breaking scale $k_{\chi SB}$.

In general, for finite temperature and finite chemical potential the parabolas become broader and higher (for $g^2 = 0$ magenta dashed line). It leads to the larger values of g_{cr}^2 and therefore to smaller chiral symmetry breaking scale $k_{\chi SB}$. Hence, for some critical values of $T = T_\chi$ and $\mu = \mu_\chi$ there is no divergence in the 4-fermion coupling. So, if we increase temperature or/and chemical potential, the system becomes chirally symmetric, as it is expected.

Further, we would like to discuss the special case of $T \to 0$ but finite μ, which has never been discussed before in the context of QCD RG flows. In this limit, the β-function of the coupling λ_σ looks different compared to our above discussion. This results from the fact that the threshold function $l_1^{(F)}$ is proportional to $\Theta(k - \mu)$ in this limit as discussed in App. E.3. Consequently, if $\mu > k$, the flow of the 4-fermion coupling becomes linear as a function of λ_σ, see Eq. (5.9). In addition, the threshold functions $l_{1,1}^{(FB)}$ and $l_{1,2}^{(FB)}$ become negative for $\mu > k$, see App. E.3. Thus, the β-function is given by a straight line with positive slope, see Fig. 5.5. This function has only one fixed point which is non-trivial, IR attractive, and is located in the region $\lambda_\sigma \leq 0$. The second fixed point is shifted to infinity. In particular, this change in the fixed-point structure means that as long as the coupling λ_σ does not diverge at $k \geq \mu$, integrating out fluctuations at scales $k < \mu$ leads to a reduction of the coupling strength. Further, from our results for the threshold functions in the limit $T \to 0$ in App. E.3, one can see that if we integrate out fluctuations down to $k \to 0$, i.e, $\mu/k \to \infty$, then the non-trivial fixed point described above becomes a Gaussian one again and the coupling λ_σ is attracted towards zero. Thus, QCD remains in the chirally symmetric regime. This mechanism can take place only if the value of the

---

[5] The fact that the strength of the quark self-interaction generated in this way is on the order $\lambda_\sigma \sim g^4$ is in agreement with expectation for a perturbative 1PI scattering amplitude.
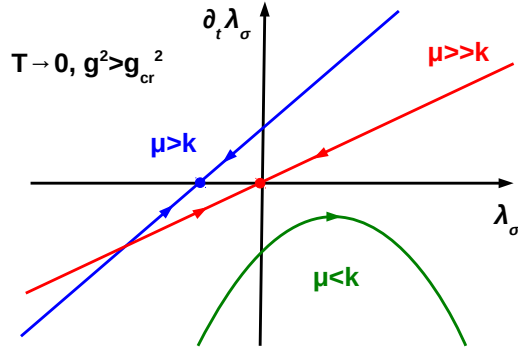
FIGURE 5.5: Sketch of the β-function for the coupling λ_σ in the limit $T \to 0$ and for $g^2 > g_{\mathrm{cr}}^2$. For $\mu < k$ (green line), the flow is given by a parabola and there are no fixed points. Thus, the coupling λ_σ grows rapidly in the RG flow. However, if μ becomes larger then k (blue line) the flow is given by a straight line with positive slop and there is a non-trivial IR attractive fixed point associated with negative value of λ_σ. This fixed point is shifted to $\lambda_\sigma = 0$ for $k \to 0$. Thus, if the β-function becomes a straight line, the coupling λ_σ cannot diverge and becomes zero for $k \to 0$. This behavior indicates chiral symmetry restoration.

chemical potential is at least as large as the chiral symmetry breaking scale $k_{\chi\mathrm{SB}}$. Of course, $k_{\chi\mathrm{SB}}$ itself is μ-dependent. From our analysis, we find that the critical value of the chemical potential μ_χ for $T \to 0$ above which QCD remains in the chirally symmetric regime is given by

$$\mu_\chi = \lim_{\epsilon \to 0} k_{\chi\mathrm{SB}}(\mu_\chi - \epsilon) \;. \tag{5.12}$$

In Sec. 5.4, we will show that for our particular truncation of the effective action and for the strong coupling calculated as described in Sec. 5.3, the critical value of the chemical potential at zero temperature is given by $\mu_\chi = 262$ MeV.

At this point we rush to add that the mechanism of chiral symmetry restoration at large μ and $T \to 0$ described above corresponds to a phase transition of the second order. It is to some extent in contrast to results observed in model calculations where, depending on the model parameters, the chiral phase transition at large μ was found to be first order phase transition. The fact that we observe a second order transition results from our truncation of the effective action: we consider only the effective 4-quark interactions. In order to resolve a first order phase transition, however, higher-order quark interactions need to be taken into account which corresponds to a calculation of the order parameter potential, see, e.g., our calculations in Secs. 5.5 and 5.6.

In our above discussion of the mechanisms of chiral symmetry breaking/restoration, we have considered an one-channel approximation of the QCD RG flows. The analysis of β-functions of λ_-, λ_+ and λ_{VA} can be performed in the same manner as for λ_σ. The behavior of these couplings is very similar to the behavior of λ_σ.

In this work we are not interested in the direct study of the chiral phase transition in QCD. Our major aim is to construct a low-energy model with starting parameters generated by the quark self-interaction flows in QCD. Therefore, we will not solve our set of flow equations down to $k_{\chi\mathrm{SB}}$. We will stop the QCD flows at $k = \Lambda_{\mathrm{NJL}} > k_{\chi\mathrm{SB}}$ in order to read off the strength of the couplings which are relevant for NJL-model calculations.

Thus, our calculations with QCD flows are restricted to the chirally symmetric phase. We also mention that in our particular numerical calculations we always have $\mu < \Lambda_{\mathrm{NJL}}$. In summary, the above discussion of the chiral dynamics in QCD already constrains the possible values of the projection scale at $T \to 0$ and $\mu \to 0$ to $k_{\chi\mathrm{SB}} < \Lambda_{\mathrm{NJL}} < k(g_{\mathrm{cr}}^2)$.

5.3 FLOW OF THE STRONG COUPLING

From the previous section one may immediately see that the quantitative behavior of 4-fermion interactions depends strongly on the behavior of the strong coupling. Unfortunately, this behavior is known exactly only for high momenta where perturbation theory is valid. Concerning quark self-interactions, however, the most interesting region is where the strong coupling grows fast so that $\alpha = g^2/(4\pi) \sim \mathcal{O}(1)$, i.e., becomes larger than $\alpha_{\mathrm{cr}} = g_{\mathrm{cr}}^2/(4\pi)$. For instance, at zero temperature and zero chemical potential, the SU(3) critical coupling is of the order $\alpha_{\mathrm{cr}} \approx 0.8$ [117], being almost independent of the number of flavors [72][6]. Thus, perturbation theory cannot be applied reliably. In this work we do not aim to calculate the strong coupling but consider it as an external input.

There are different non-perturbative methods to determine the flow of the strong coupling for low momenta: lattice QCD, FRG and the Dyson-Schwinger formalism. However, all of them depend on the choice of the gauge condition, renormalization scheme and particular definition of the strong coupling[7]. Since we treat the 4-fermion interactions using FRG and for Landau gauge fixing, it is self-evident to look for the strong coupling produced using the same method and the same gauge fixing condition. Additionally, we are interested in the temperature and chemical-potential dependence of quark self-interactions. Therefore, we would like to use a T- and μ-dependent input for α. Such data is indeed available [73]. In this work α was calculated as a function of k, N_{f} and T. Thereby, in order to preserve the gauge invariance, the background-field formalism was used, Refs. [86, 110]. We also discuss later how the dependence on the finite chemical potential can be included in this input. At this point we want to mention that α from [73] was calculated using the wave-function renormalization of gluons. In fact, it would be more consistent to use α from quark-gluon vertex in our calculations since the α- (or g-) dependence of the 4-fermion interactions arises from the quark-gluon vertex. Also, in [73] the $4d$ exponential regulator was used. This regulator is very convenient for the FRG approach. But in the present study of 4-fermion interactions we cannot use it since for finite μ it is not well-defined due to the presence of μ in the shape function[8]. Altogether, however, the results from [73] seems to be the most suitable input for our purpose.

In Sec. 5.7 we will also present calculations with another input for the strong coupling [122]. This FRG calculation in Landau gauge provides us with $\alpha(k)$ calculated from the quark-gluon vertex using a smooth approximation of the $4d$ linear regulator. The gauge invariance was preserved here by means of modified Slavnov-Taylor identities which are the non-Abelian generalization of Ward-Takahashi identities. The mayor disadvantage of this input compared to input from [73] is that it was calculated for $T = 0$ and $\mu = 0$. Nonethe-

---

6 This particular value of α_{cr} holds for the class of linear and exponential regulators in the FRG approach. For other renormalization schemes it can be different. In this work, however, we use only these very convenient types of regulators.

7 The strong coupling can be defined via quark-gluon, three-gluon, four-gluon or ghost-gluon vertices or via gluonic wave-function renormalization, see, e.g., Ref. [124].

8 This problem appears for all kinds of $4d$ regulators

less, it is useful to consider both inputs to study the influence of different definitions of α and different renormalization schemes on our results for the phase diagram.

Now, let us discuss how we can introduce the finite chemical potential in the data provided in Ref. [73]. Since in this paper the background-field formalism was used, the flow of the strong coupling α is determined by the anomalous dimension of the gauge fields, $\eta_{A,k}$, [110]:

$$\partial_t \alpha(k) = \eta_{A,k}\, \alpha(k) \ . \tag{5.13}$$

Thereby, $\eta_{A,k}$ contains gluonic and fermionic contributions and is a function of temperature:

$$\eta_{A,k}(T) = \eta_{A,k}^{\text{gluons}}(T) + \eta_{A,k}^{\text{quarks}}(T) \ . \tag{5.14}$$
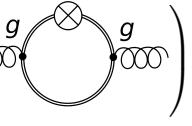
In [73], $\eta_{A,k}$ was calculated for different flavor numbers, including $N_{\text{f}} = 0$. As one would expect, the direct flavor-number dependence appears in the above equation only in the quark contribution to the gluon anomalous dimension, namely $\eta_{A,k}^{\text{quarks}} \propto N_{\text{f}}$. Therefore, for $N_{\text{f}} = 0$ one obtains

$$\eta_{A,k}(T) = \eta_{A,k}^{\text{YM}}(T) \ , \tag{5.15}$$

with $\eta_{A,k}^{\text{YM}}$ the gluon anomalous dimension of the pure Yang-Mills theory. Now, we can use a common approximation, see, e.g., Refs. [123, 124]:

$$\eta_{A,k}(T) = \eta_{A,k}^{\text{YM}}(T) + \Delta\eta_{A,k}(T,\mu) \ , \tag{5.16}$$

where $\Delta\eta_{A,k}$ is the vacuum polarization of the gluon calculated as:

$$\Delta\eta_{A,k} = \frac{Z_{A,k}^{-1}}{3(N_{\text{c}}^2 - 1)} \left(\frac{\partial}{\partial p^2} P_\perp^{\mu\nu}(p) \cdot \left. \vphantom{\frac{\partial}{\partial p^2}} \right. \right)\Bigg|_{p=0} . \tag{5.17}$$

In this equation p is the modulus of the external momentum and $P_\perp^{\mu\nu}(p)$ is the transversal projection operator, see App. E. The structure of Eq. (5.16) is basically the same as of Eq. (5.14). The difference is that in quark contribution (5.17) we consider only the leading term in the external-momentum expansion, whereas in [73] the expansion was done in a more sophisticated way. Nevertheless, our procedure has an import advantage – namely that we can incorporate the chemical potential dependence in $\Delta\eta_{A,k}$ in a straightforward manner[9]. Some details on our calculation of $\Delta\eta_{A,k}$ can be found in App. F. Here, we only present the result for $N_{\text{c}} = 3$ and $N_{\text{f}} = 2$ before evaluation of the Matsubara sum. The final result is also presented in App. F. Since we are considering the chiral limit, we also use zero quark mass. Additionally, since we work in Landau gauge, we have $\eta_\psi = 0$ in our truncation. We find:

$$\Delta\eta_{A,k}(T,\mu) = -\frac{g^2}{45\pi^2}\tau \sum_n \frac{33(\tilde{\nu}_n + \mathrm{i}\tilde{\mu})^4 + 2(\tilde{\nu}_n + \mathrm{i}\tilde{\mu})^2 - 55}{((\tilde{\nu}_n + \mathrm{i}\tilde{\mu})^2 + 1)^4} \ , \tag{5.18}$$

with $\tau = T/k$, $\tilde{\mu} = \mu/k$ and $\tilde{\nu}_n = (2n+1)\pi\tau$ the fermionic Matsubara frequencies. This result was obtained using the 3d linear regulator. For $\Delta\eta_{A,k}$ with a finite quark mass

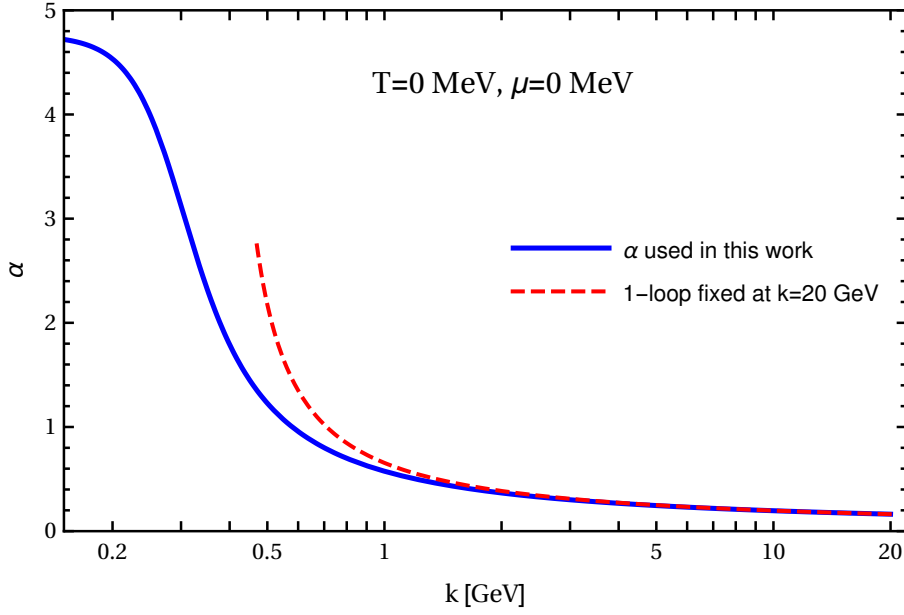9 There is no μ-dependence in $\eta_{A,k}^{\text{YM}}$ due to the absence of internal fermionic lines.

FIGURE 5.6: $\alpha(k)$ in the limit of $T \to 0$ and $\mu \to 0$. It was obtained by solving Eq. (5.13) using the ansatz in Eq. (5.16) and result for $\Delta\eta_{A,k}(T, \mu)$ from Eq. (5.18). $\eta_{A,k}^{\mathrm{YM}}(T)$ was taken from [73]. As boundary condition we use a perturbative result $\alpha(k = 20 \text{ GeV}) = 0.163$ [173]. We also plot a perturbative 1-loop $\alpha(k)$ fixed by the same boundary condition. We observe a perfect agreement in the UV-regime for $k \gtrsim 2$ GeV.

and finite quark anomalous dimension, we refer the reader to [124] where the $4d$ linear regulator and the limit of $T \to 0$ and $\mu \to 0$ were used. We also mention that in the limit of vanishing temperature and chemical potential Eq. (5.18) reduces to $\Delta\eta_{A,k} = g^2/(6\pi^2)$ which is a well-known result from one-loop perturbation theory.

Using our result for $\Delta\eta_{A,k}(T, \mu)$ and $\eta_{A,k}^{\mathrm{YM}}(T)$ from [73] we can calculate the strong coupling α. As UV scale we choose $\Lambda_{\mathrm{UV, \, QCD}} = 20$ GeV. The corresponding value of the strong coupling at this scale is well-known from perturbative calculations, $\alpha(\Lambda_{\mathrm{UV, \, QCD}}) = 0.163$, and is in line with experimental measurements [173]. Using these values, we solve Eq. (5.13) for $0.15 \text{ GeV} < k < 20 \text{ GeV}$. The choice of $\Lambda_{\mathrm{IR, \, QCD}} = 0.15$ GeV is small enough to obtain $\alpha > \alpha_{\mathrm{cr}}$ and, therefore, spontaneous chiral symmetry breaking in QCD. To achieve the limit $k \to 0$ is not of interest in this study. Our result for $\alpha(k)$ in the limit of vanishing T and μ is presented in the Fig. 5.6. As expected, in the UV-regime α remains very small but rapidly increases for $k \lesssim 1$ GeV. In the deep IR-regime α approaches a fixed point and remains constant[10]. The presence of such an IR fixed point in Yang-Mills theories is a very well-known phenomenon also in the Landau gauge [174, 175, 176, 177, 178, 179]. However, this observation is of less interest for our work. For a detailed discussion concerning this IR fixed point we refer the reader to Ref. [73]. In Fig. 5.6 we also present the perturbative 1-loop result for $\alpha(k)$ fixed by the same boundary condition $\alpha_{\text{1-loop}}(k = 20 \text{ GeV}) = 0.163$. We observe perfect agreement in the UV-regime for $k \gtrsim 2$ GeV. For smaller scales $\alpha_{\text{1-loop}}$ increases faster and diverges at $k \approx 370$ MeV. This observation justifies the validity of our calculations at UV scales.

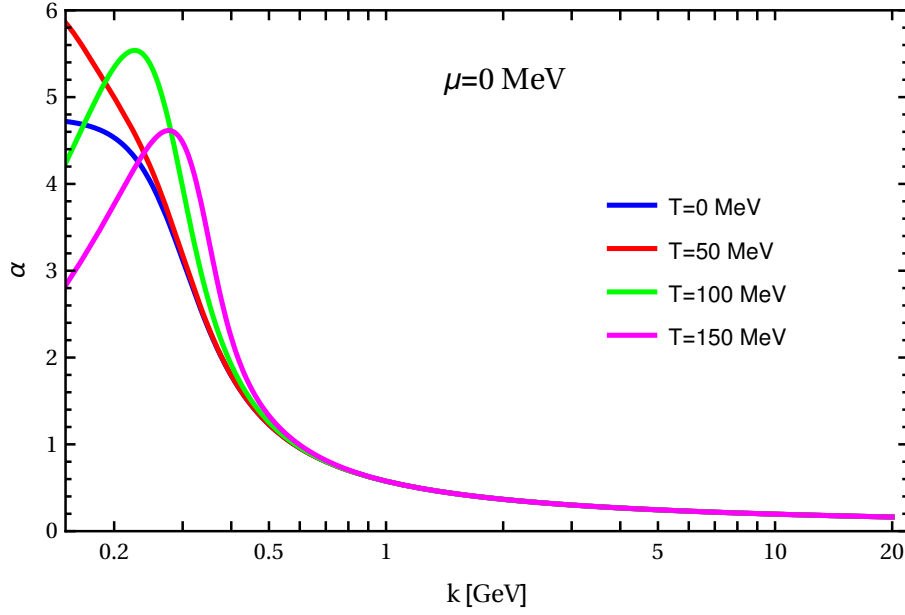
10 We have explicitly checked it also for $k < 0.15$ GeV

FIGURE 5.7: $\alpha(k)$ at $\mu = 0$ for different temperatures. For finite T we observe that $\alpha(k)$ increases stronger with decreasing k. It approaches a maximum at some scale and decreases for even smaller k. We have explicitly checked that for $k \to 0$ the strong coupling approaches zero for all finite temperatures presented in this plot. For explanation of this behavior see the main text.

The formalism we are working with allows us to take into account the T- and μ-dependence of the strong coupling. In Fig. 5.7 we present our results for finite temperature and zero chemical potential. We observe that inclusion of finite T leads to following modifications in the behavior of α: First, even though the flow of the strong coupling does not change for large momentum scale, at smaller scales α becomes stronger if we increase the temperature. Second, at some scale the strong coupling approaches a maximum and decreases for even smaller k. Thereby, for larger T the particular value of the maximum becomes smaller and the position of the maximum is shifted to higher scales. We have explicitly checked that in the limit $k \to 0$ the strong coupling approaches zero for all finite temperatures depicted in Fig. 5.7.

Let us first explain the stronger increasing α for increasing T: This behavior takes place due to the fact that fermions have only hard Matsubara modes or, with other words, no zero Matsubara mode. So, all Matsubara frequencies which contribute to the flow of α are proportional to $\pi T/k$. Therefore, for sufficiently large T/k the thermal Matsubara mass becomes large and quark contribution to the gluon anomalous dimension $\Delta\eta_{A,k}(T,\mu)$ becomes suppressed, see Eq. (5.18). As a consequence, the flow of the strong coupling is dominated by the Yang-Mills contribution. On the other hand, it is well-known fact that pure Yang-Mills theory has stronger α compared to the theories with finite flavor number. Therefore, we observe larger strong coupling for higher temperatures. Also, we mention that for higher T, quarks decouple already at larger k. This is also in agreement with above explanation. The line of arguments presented here is quite phenomenological but very intuitive. For a more formal explanation of the behavior of $\Delta\eta_{A,k}(T,\mu)$ at finite T and μ we refer the reader to our discussion of finite-μ influence on $\Delta\eta_{A,k}(T,\mu)$ below.
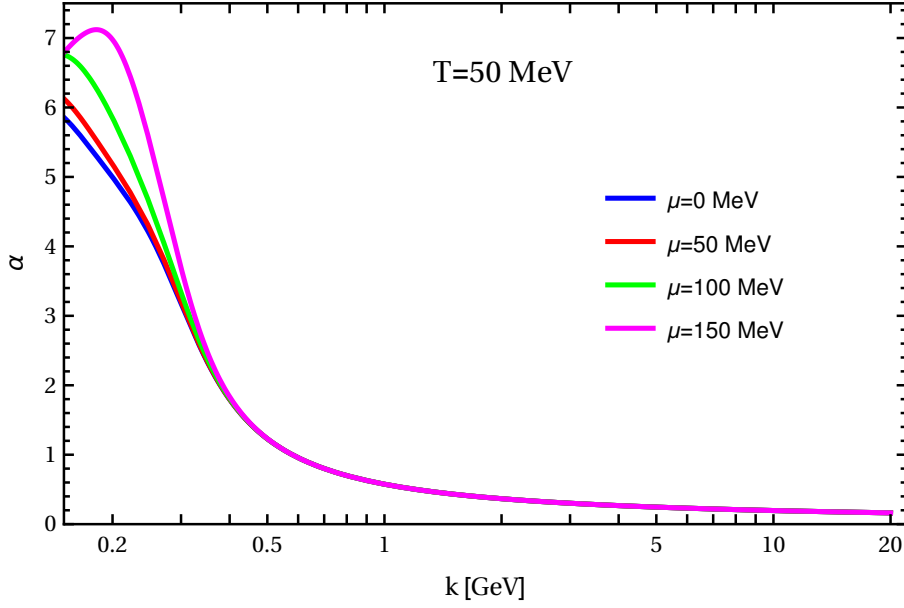
FIGURE 5.8: $\alpha(k)$ at $T = 50$ MeV for different values of chemical potential μ. For increasing μ we observe the same effect as for increasing T – namely that $\alpha(k)$ increases stronger with decreasing k. This behavior can be explained by analysis of $\Delta\eta_{A,k}$. In deep IR limit we observe effective dimensional reduction which is caused by the presence of finite T. For explanation of this behavior, see the corresponding parts in the main text.

The fact that the strong coupling becomes zero in the deep IR-regime is explained in the following way: For sufficiently small RG-scale, k, we take into account fluctuations with momentum $p^2 < T^2$. The wavelength of these modes is larger than the extent of the compactified Euclidean time direction and, therefore, these fluctuations become effectively 3-dimensional. This is also reflected in the limiting behavior of the strong coupling which is now governed by the dimensional reduced theory. In [73] it was shown that also in 3 dimensions there is a non-trivial IR fixed point in the flow of 3-dimensional strong coupling α_{3d}. The authors also provide a relation between 3- and 4-dimensional strong couplings:

$$\alpha = \frac{k}{T}\alpha_{3d} \ . \tag{5.19}$$

Thus, for $k/T \to 0$, the 4-dimensional coupling α has to approach zero. Thereby, the 3-dimensional coupling α_{3d} remains finite. We emphasize that it is really a finite-temperature effect and as long as we consider the limit $T \to 0$, no dimensional reduction can take place. Further, we mention that this interesting effect of decreasing α is not of interest for our particular study: We have explicitly checked that in our calculations we never "probe" the the region where α decreases with decreasing k.

Now, let us discuss the influence of the finite chemical potential on the strong coupling $\alpha(k)$. An example for $T = 50$ MeV and different μ is presented in Fig. 5.8. Basically, we observe the same effect of stronger $\alpha(k)$ as for finite T. To understand how this effect arises from inclusion of μ, we have to proceed in the following way: Since the μ-dependence of the strong coupling results in our calculations solely from $\Delta\eta_{A,k}(T,\mu)$, we should look
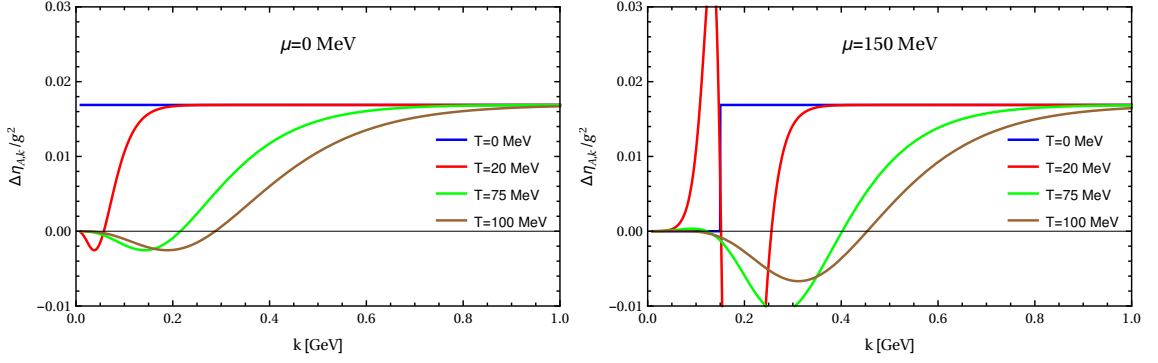
FIGURE 5.9: $\Delta\eta_{A,k}/g^2$ for different temperatures at $\mu = 0$ MeV (*left*) and $\mu = 150$ MeV (*right*). We observe that for vanishing temperature $\Delta\eta_{A,k}/g^2 \propto \Theta(k-\mu)$. For finite T there is an oscillating behavior. We also note that $\Delta\eta_{A,k}/g^2 \leq 1/(6\pi^2)$ for any T, μ and k as long as $k > \mu$. This is indeed the case in our present study since our IR cut-off of the QCD-flows is larger than the largest considered value of μ, see Secs. 5.5 and 5.6. The reduction of $\Delta\eta_{A,k}/g^2$ at finite temperature and chemical potential leads, in general, to stronger $\alpha(k)$ compared to the limit $T \to 0$, $\mu \to 0$.

at properties of this term. If we consider the limit $T/k \to 0$, $\Delta\eta_{A,k}(T,\mu)$ becomes a Θ-function, see App. F:

$$\Delta\eta_{A,k}(T,\mu)|_{\frac{T}{k}\to 0} = \frac{g^2}{6\pi^2}\Theta(k-\mu) \ . \tag{5.20}$$

Therefore, as long as $k > \mu$ we observe the same behavior as in the limit $T \to 0$, $\mu \to 0$. Indeed, in our present study the IR-scale of QCD-flows is always considerably larger than the value of the chemical potential, see Secs. 5.5 and 5.6. Thus, in the limit $T \to 0$, our results for the strong coupling are μ-independent. For finite temperatures the Θ-function in Eq. (5.20) becomes smeared, see Fig. 5.9 for examples. Thereby, we observe that $\Delta\eta_{A,k}/g^2 \leq 1/(6\pi^2)$ for any combination of T, μ and k as long as $k > \mu$. Sometimes, it can even become negative. As a consequence, $\Delta\eta_{A,k}$ is either suppressed compared to the case $T \to 0$, $\mu \to 0$ or even acts in the same direction as Yang-Mills contribution, i.e., it pushes α to larger values for decreasing k. The last case appears if $\Delta\eta_{A,k}/g^2 < 0$. A quantitative evaluation of the interplay between T- and μ-effects on $\Delta\eta_{A,k}$ seems to be rather complex. Nonetheless, one can conclude that finite temperature and chemical potential lead, in general, to stronger $\alpha(k)$. But one has to keep in mind that this statement is valid only as long as dimensional reduction of theory does not set in.

5.4 PROJECTION OF THE QCD RG FLOWS ONTO THE MODEL CHANNELS

Before we compute the 4-fermion interactions in QCD using the strong coupling discussed in Sec. 5.3, we mention once again that the interaction channels introduced in Eq. (5.3) are defined in a different way as channels used in model calculations, e.g., see Sec. 4.1. In order to project our original channels and corresponding flow equations from Sec. 5.2 onto channels conveniently used in model calculations, we start with the general Fierz-transformation, see also App. B.2:

$$M_{ad} = \sum_{j=1}^{n} O_{ad}^{(j)} \sum_{ef}(M_{ce}^{(2)}O_{ef}^{(j)}M_{fb}^{(1)}) \ , \tag{5.21}$$

where $(O^1, \ldots, O^n)$ is a complete orthogonalized basis of $(d \times d)$-matrices M with $M_{ad} = M_{ab}^{(1)} M_{cd}^{(2)}$. Applying this prescription on a product of two identities of an SU(N) group, we obtain:

$$\mathbb{1}_{ab}\mathbb{1}_{cd} = 2(\frac{1}{2N} - \frac{1}{4})\mathbb{1}_{ab}\mathbb{1}_{cd} + 2\sum_{\alpha=0}^{N^2-1} t_{ad}^\alpha t_{cb}^\alpha \ , \tag{5.22}$$

where t^α for $\alpha = 1, \ldots, N^2 - 1$ are the generators of SU(N) group and $t^0 = \frac{1}{2}\mathbb{1}$. Thus, t^α is a complete set of basis elements of SU(N) group.

We use this identity for $N = N_\mathrm{f} = 2$ and $N = N_\mathrm{c} = 3$ in order to rewrite our channels. We obtain following results:

$$
\begin{aligned}
(\mathrm{S} - \mathrm{P}) &= (\bar\psi^a\psi^b)^2 - (\bar\psi^a\gamma_5\psi^b)^2 \\
&= [(\bar\psi\psi)^2 - (\bar\psi\gamma_5\vec\tau\psi)^2] - [\det{}_\mathrm{f}\bar\psi(1 + \gamma_5)\psi + \det{}_\mathrm{f}\bar\psi(1 - \gamma_5)\psi] \ ,
\end{aligned}
\tag{5.23}
$$

$$
\begin{aligned}
(\mathrm{V} + \mathrm{A}) &= (\bar\psi\gamma_\mu\psi)^2 - (\bar\psi\gamma_\mu\gamma_5\psi)^2 \\
&= -\frac{2}{3}[(\bar\psi\psi)^2 - (\bar\psi\gamma_5\vec\tau\psi)^2] + \frac{2}{3}[\det{}_\mathrm{f}\bar\psi(1 + \gamma_5)\psi + \det{}_\mathrm{f}\bar\psi(1 - \gamma_5)\psi] \\
&\quad - \{[(\bar\psi\lambda^z\psi)^2 - (\bar\psi\gamma_5\lambda^z\vec\tau\psi)^2] \\
&\quad + [\det{}_\mathrm{f}\bar\psi(1 + \gamma_5)\lambda^z\psi + \det{}_\mathrm{f}\bar\psi(1 - \gamma_5)\lambda^z\psi]\} \ ,
\end{aligned}
\tag{5.24}
$$

$$(\mathrm{V} - \mathrm{A}) = [(\bar\psi\gamma_\mu\psi)^2 + (\bar\psi\gamma_\mu\gamma_5\psi)^2] \ , \tag{5.25}$$

$$
\begin{aligned}
2(\mathrm{V} - \mathrm{A})^{\mathrm{adj}} + \frac{1}{3}(\mathrm{V} - \mathrm{A}) &= 2[(\bar\psi\gamma_\mu t^z \psi)^2 - (\bar\psi\gamma_\mu\gamma_5 t^z \psi)^2] \\
&\quad + \frac{1}{3}[(\bar\psi\gamma_\mu\psi)^2 + (\bar\psi\gamma_\mu\gamma_5\psi)^2] \\
&= [(\bar\psi\gamma_\mu\psi)^2 + (\bar\psi\gamma_\mu\gamma_5\psi)^2] \\
&\quad - [\det{}_\mathrm{f}\bar\psi\gamma_\mu(1 + \gamma_5)\psi + \det{}_\mathrm{f}\bar\psi\gamma_\mu(1 - \gamma_5)\psi] \ ,
\end{aligned}
\tag{5.26}
$$

where $\vec\tau$ is a vector with Pauli matrices, λ^z the Gell-Mann matrices and determinants are performed in the flavor space. From this rewritten form, we can see that the usual scalar-pseudoscalar channel used in model calculations, $[(\bar\psi\psi)^2 - (\bar\psi\gamma_5\vec\tau\psi)^2]$, appears in our (S−P)- and (V + A)-channels, and the usual vector-axialvector channel, $[(\bar\psi\gamma_\mu\psi)^2 + (\bar\psi\gamma_\mu\gamma_5\psi)^2]$, in our (V − A)- and $2(\mathrm{V} - \mathrm{A})^{\mathrm{adj}} + \frac{1}{3}(\mathrm{V} - \mathrm{A})$-channels. In above equations we can also find $\mathrm{U_A}(1)$-symmetry breaking terms including the famous 't Hooft determinant. However, since we do not introduce separate couplings for these channels, the $\mathrm{U_A}(1)$-symmetry is preserved in our QCD calculations. Using Eqs. (5.23)–(5.26) we can redefine the basis of the Fierz-complete channels in such a way that all contributions to each typical model channel are combined together:

$$
\begin{aligned}
&\lambda_-(\mathrm{V} - \mathrm{A}) + \lambda_+(\mathrm{V} + \mathrm{A}) + \lambda_\sigma(\mathrm{S} - \mathrm{P}) + \lambda_{\mathrm{VA}}[2(\mathrm{V} - \mathrm{A})^{\mathrm{adj}} + 1/N_\mathrm{c}(\mathrm{V} - \mathrm{A})] = \\
&(\lambda_\sigma - \frac{2}{3}\lambda_+)(\mathrm{S} - \mathrm{P})_{\mathrm{NJL}} + \lambda_+\mathrm{Chn}_{2,\mathrm{NJL}} + (\lambda_- + \lambda_{\mathrm{VA}})(\mathrm{V} - \mathrm{A})_{\mathrm{NJL}} + \lambda_{\mathrm{VA}}\mathrm{Chn}_{4,\mathrm{NJL}} \ ,
\end{aligned}
\tag{5.27}
$$

with new channels

$$
\begin{aligned}
(\mathrm{S-P})_{\mathrm{NJL}} &= [(\bar{\psi}\psi)^2 - (\bar{\psi}\gamma_5\vec{\tau}\psi)^2] - [\det_{\mathrm{f}}\bar{\psi}(1+\gamma_5)\psi + \det_{\mathrm{f}}\bar{\psi}(1-\gamma_5)\psi] \;, \\
\mathrm{Chn}_{2,\,\mathrm{NJL}} &= -[(\bar{\psi}\lambda^z\psi)^2 - (\bar{\psi}\gamma_5\lambda^z\vec{\tau}\psi)^2] - [\det_{\mathrm{f}}\bar{\psi}(1+\gamma_5)\lambda^z\psi + \det_{\mathrm{f}}\bar{\psi}(1-\gamma_5)\lambda^z\psi] \;, \\
(\mathrm{V-A})_{\mathrm{NJL}} &= [(\bar{\psi}\gamma_\mu\psi)^2 + (\bar{\psi}\gamma_\mu\gamma_5\psi)^2] \;, \\
\mathrm{Chn}_{4,\mathrm{NJL}} &= -[\det_{\mathrm{f}}\bar{\psi}\gamma_\mu(1+\gamma_5)\psi + \det_{\mathrm{f}}\bar{\psi}\gamma_\mu(1-\gamma_5)\psi] \;,
\end{aligned}
\tag{5.28}
$$

where index NJL means that in this set of Fierz-complete channels each model channel appears only once. The first and the third channels in this basis correspond to the channels used in NJL models. The second and the fourth channels ensure that the current basis is Fierz-complete. The corresponding couplings are defined as

$$
\begin{aligned}
\lambda_{\sigma,\mathrm{NJL}} &= \lambda_\sigma - \frac{2}{3}\lambda_+ \;, \\
\lambda_{2,\mathrm{NJL}} &= \lambda_+ \;, \\
\lambda_{-,\mathrm{NJL}} &= \lambda_- + \lambda_{\mathrm{VA}} \;, \\
\lambda_{4,\mathrm{NJL}} &= \lambda_{\mathrm{VA}} \;,
\end{aligned}
\tag{5.29}
$$

The flow equations for these couplings can be calculated straightforwardly from our previous results in Eqs. (5.7)–(5.10). Here, we again use $N_{\mathrm{c}} = 3$ and $N_{\mathrm{f}} = 2$:

$$
\begin{aligned}
\partial_t \lambda_{\sigma,\mathrm{NJL}} =\;& 2\lambda_{\sigma,\mathrm{NJL}} - 32 v_4 l_{1,1}^{(\mathrm{FB})}(\tau,\tilde{\mu},0,0) g^2 \lambda_{\sigma,\mathrm{NJL}} - \frac{46}{9} v_4 l_{1,2}^{(\mathrm{FB})}(\tau,\tilde{\mu},0,0) g^4 \\
& - 8 v_4 l_1^{(\mathrm{F})}(\tau,\tilde{\mu},0)\Big[\frac{35}{6}\lambda_{\sigma,\mathrm{NJL}}^2 + \frac{16}{27}\lambda_{2,\mathrm{NJL}}^2 + \frac{16}{9}\lambda_{\sigma,\mathrm{NJL}}\lambda_{2,\mathrm{NJL}} \\
& - \frac{4}{3}\lambda_{\sigma,\mathrm{NJL}}\lambda_{4,\mathrm{NJL}} - \frac{10}{3}\lambda_{\sigma,\mathrm{NJL}}\lambda_{-,\mathrm{NJL}} + \frac{64}{9}\lambda_{2,\mathrm{NJL}}\lambda_{-,\mathrm{NJL}} \\
& - \frac{32}{9}\lambda_{2,\mathrm{NJL}}\lambda_{4,\mathrm{NJL}}\Big] \;,
\end{aligned}
\tag{5.30}
$$

$$
\begin{aligned}
\partial_t \lambda_{2,\mathrm{NJL}} =\;& 2\lambda_{2,\mathrm{NJL}} + 4 v_4 l_{1,1}^{(\mathrm{FB})}(\tau,\tilde{\mu},0,0) g^2 \lambda_{2,\mathrm{NJL}} + \frac{13}{24} v_4 l_{1,2}^{(\mathrm{FB})}(\tau,\tilde{\mu},0,0) g^4 \\
& - 8 v_4 l_1^{(\mathrm{F})}(\tau,\tilde{\mu},0)\Big[-\frac{26}{9}\lambda_{2,\mathrm{NJL}}^2 + \frac{1}{4}\lambda_{\sigma,\mathrm{NJL}}^2 - \frac{38}{3}\lambda_{2,\mathrm{NJL}}\lambda_{-,\mathrm{NJL}} \\
& + \frac{10}{3}\lambda_{2,\mathrm{NJL}}\lambda_{4,\mathrm{NJL}} + 2\lambda_{\sigma,\mathrm{NJL}}\lambda_{-,\mathrm{NJL}} - \lambda_{4,\mathrm{NJL}}\lambda_{\sigma,\mathrm{NJL}} + \frac{1}{3}\lambda_{\sigma,\mathrm{NJL}}\lambda_{2,\mathrm{NJL}}\Big] \;,
\end{aligned}
\tag{5.31}
$$

$$
\begin{aligned}
\partial_t \lambda_{-,\mathrm{NJL}} =\;& 2\lambda_{-,\mathrm{NJL}} + 8 v_4 l_{1,1}^{(\mathrm{FB})}(\tau,\tilde{\mu},0,0) g^2 \lambda_{-,\mathrm{NJL}} - \frac{17}{12} v_4 l_{1,2}^{(\mathrm{FB})}(\tau,\tilde{\mu},0,0) g^4 \\
& - 8 v_4 l_1^{(\mathrm{F})}(\tau,\tilde{\mu},0)\Big[-5\lambda_{-,\mathrm{NJL}}^2 - 2\lambda_{4,\mathrm{NJL}}^2 - \frac{44}{9}\lambda_{2,\mathrm{NJL}}^2 - \frac{1}{2}\lambda_{\sigma,\mathrm{NJL}}^2 \\
& + \frac{4}{3}\lambda_{\sigma,\mathrm{NJL}}\lambda_{2,\mathrm{NJL}} + 4\lambda_{4,\mathrm{NJL}}\lambda_{-,\mathrm{NJL}}\Big] \;,
\end{aligned}
\tag{5.32}
$$

$$
\begin{aligned}
\partial_t \lambda_{4,\mathrm{NJL}} =\;& 2\lambda_{4,\mathrm{NJL}} - 4 v_4 l_{1,1}^{(\mathrm{FB})}(\tau,\tilde{\mu},0,0) g^2 \Big[-3\lambda_{-,\mathrm{NJL}} + 4\lambda_{4,\mathrm{NJL}}\Big] \\
& - \frac{1}{8} v_4 l_{1,2}^{(\mathrm{FB})}(\tau,\tilde{\mu},0,0) g^4 - 8 v_4 l_1^{(\mathrm{F})}(\tau,\tilde{\mu},0)\Big[-9\lambda_{4,\mathrm{NJL}}^2 - \frac{1}{2}\lambda_{\sigma,\mathrm{NJL}}^2 - \frac{2}{9}\lambda_{2,\mathrm{NJL}}^2 \\
& + 4\lambda_{4,\mathrm{NJL}}\lambda_{-,\mathrm{NJL}} - \frac{2}{3}\lambda_{\sigma,\mathrm{NJL}}\lambda_{2,\mathrm{NJL}}\Big] \;.
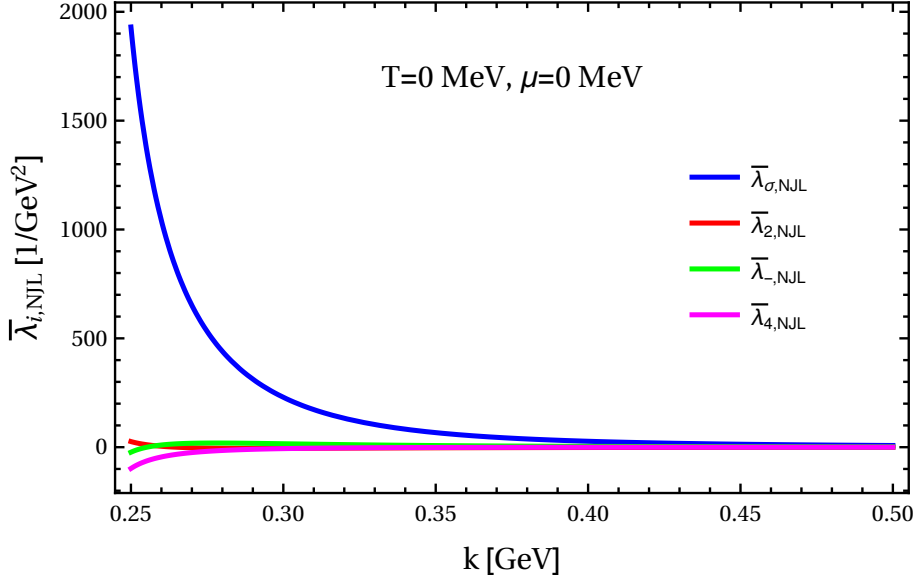\end{aligned}
\tag{5.33}
$$

FIGURE 5.10: Here, we present the dimensionful couplings $\bar{\lambda}_{i,\mathrm{NJL}}$ as functions of k at $T = 0$ and $\mu = 0$. We constrain this plot to $k < 500$ MeV since for larger momenta all couplings basically stay zero. Around $k \simeq 400$ MeV couplings start to grow and diverge at $k \simeq 233$ MeV. This behavior indicates the chiral symmetry breaking in QCD.

To use the basis in Eq. (5.28) and the corresponding couplings from Eq. (5.29) in the QCD part of our calculations has an important advantage – namely that we can easily read off the starting values for the NJL model couplings at the projection scale $k = \Lambda_{\mathrm{NJL}}$.

Now, we solve the set of differential equations (5.30)–(5.33) using the strong coupling from Sec. 5.3. We start at the scale $k = \Lambda_{\mathrm{UV, QCD}} = 20$ GeV with $\lambda_{i,\mathrm{NJL}}(\Lambda_{\mathrm{UV, QCD}}) = 0$. First, we do it for $T = 0$ and $\mu = 0$. Our results for dimensionful couplings $\bar{\lambda}_{i,\mathrm{NJL}}$ are shown in Fig. 5.10. Thereby, we have assumed that $Z_{i,\mathrm{NJL}} = 1$ for all 4-fermion vertex renormalizations so that corresponding anomalous dimensions $\eta_{i,\mathrm{NJL}} = -(\partial_t Z_{i,\mathrm{NJL}})/Z_{i,\mathrm{NJL}}$ vanish. We observe that, for momentum scales $k \gtrsim 400$ MeV, all couplings basically remain zero. It means that the critical value of the strong coupling is not achieved and the couplings $\bar{\lambda}_{i,\mathrm{NJL}}$ are bounded from above by the value of the slightly shifted IR-attractive Gaussian fixed point which is on order $\sim g^4$, see Sec. 5.2. At smaller scales all couplings start to grow. This observation indicates that the fixed points in the flows of quark self-interactions disappear. At $k \simeq 233$ MeV all 4-fermion couplings even diverge and it becomes impossible to solve the flows at smaller scales. As discussed in Sec. 5.2, this behavior indicates chiral symmetry breaking in QCD. For our purposes it means that the scale where we project the QCD flows results onto the model channels should be chosen in such a way that $\Lambda_{\mathrm{NJL}} > k_{\chi\mathrm{SB}} = 233$ MeV. We also observe that the coupling of the usual scalar-pseudoscalar channel, $\bar{\lambda}_{\sigma,\mathrm{NJL}}$, is clearly dominant. Therefore, it seems to be quite reasonable to use a model with only this channel in our further calculations.

However, before we start with model calculations, we would like to test numerically the mechanism of chiral symmetry restoration at large μ and $T \to 0$ which was found in Sec. 5.2. To this end, we now consider all four quark channels used in our truncation of the effective action. Our results for the flows of dimensionless effective couplings at $T \to 0$ and close to the critical chemical potential μ_χ are summarized in Fig. 5.11. We observe the
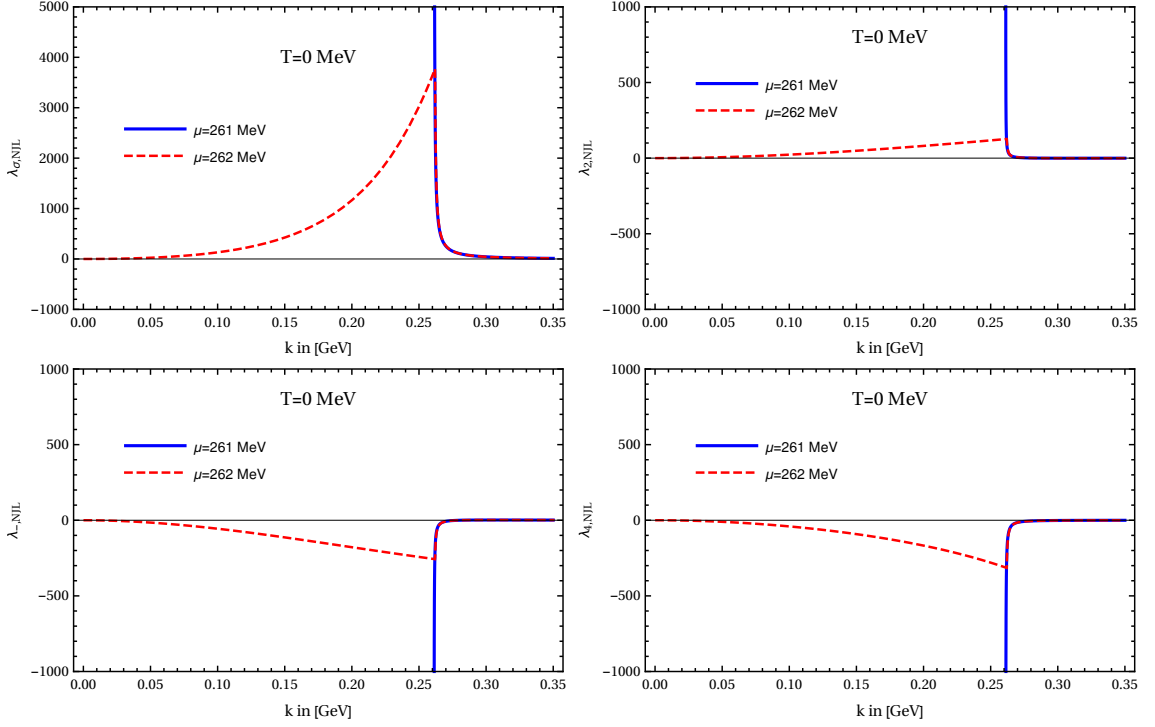
FIGURE 5.11: The flows of dimensionless couplings at $T \to 0$ and close to μ_χ. At $\mu = 261$ MeV all couplings diverges at the chiral symmetry breaking scale $k_{\chi\mathrm{SB}}(\mu) = 261.14$ MeV. This behavior indicates chiral symmetry breaking in QCD RG flows. For $\mu = 262$ MeV, the couplings are still increasing for $k \geq \mu$ but decrease for $k < \mu$ and become zero in the limit $k \to 0$. The system is then in the chirally symmetric regime. Therefore, the critical value of the chemical potential in the limit $T \to 0$ is given by $\mu_\chi \approx 262$ MeV in our approach.

following behavior: At $\mu = 261$ MeV all couplings grow rapidly close to the chiral symmetry breaking scale $k_{\chi\mathrm{SB}}(\mu) = 261.14$ MeV. Especially, λ_σ grows very fast. At $k = k_{\chi\mathrm{SB}}(\mu)$ all couplings even diverge and we observe chiral symmetry breaking in the QCD RG flows. However, if the value of the chemical potential is slightly increased, $\mu = 262$ MeV, the couplings do not diverge anymore. They still become large for $k \geq \mu = 262$ MeV but remain finite and decrease again for decreasing k. In fact, in the limit $k \to 0$, they even become zero and the system is clearly in the chirally symmetric regime. Thus, for our present QCD RG flows the critical value of the chemical potential in the limit $T \to 0$ is given by:

$$\mu_\chi \approx 262 \text{ MeV}. \tag{5.34}$$

This observation is in agreement with the mechanism of chiral symmetry restoration at large μ found in Sec. 5.2. The fact that the effective couplings become smaller for $k < \mu$ is the consequence of the existence of a non-trivial IR attractive fixed point for $\mu > k$ (and $T \to 0$). Since this point becomes a Gaussian fixed point for $k \to 0$, the couplings vanish if fluctuations are integrated out on all scales. In summary, we state that the mechanism described in Sec. 5.2 is validated in our numerical calculations and works also for truncations of the effective action beyond the one-channel approximation, which was used in Sec. 5.2 for the sake of simplicity.

5.5 LOW-ENERGY MODEL

As described above, in the high-energy region we consider the Fierz-complete set of 4-fermion interaction channels. However, we see that the scalar-pseudoscalar channel seems to be very dominant compared to other three channels. Therefore, in this very first study of QCD-inspired determination of NJL-model parameters we restrict our calculations to a model with only scalar-pseudoscalar channel. So, we use only the coupling $\bar{\lambda}_{\sigma,\mathrm{NJL}}$ in the momentum region $k \leq \Lambda_{\mathrm{NJL}}$.

The effective action of such an NJL model is similar to that of the PNJL model in Sec. 4.1:

$$\Gamma_k = \int \mathrm{d}^4 \mathrm{x} \left\{ \bar{\psi}(\mathrm{i}Z_\psi \slashed{\partial} + \mathrm{i}\gamma_0 \mu)\psi + \frac{\bar{\lambda}_{\sigma,\mathrm{NJL}}}{2}[(\bar{\psi}\psi)^2 - (\bar{\psi}\gamma_5\vec{\tau}\psi)^2] \right\} \, . \tag{5.35}$$

Here, however, we do not introduce the Polyakov-loop and, therefore, we cannot incorporate confinement in our calculations. Further, one may immediately notice that we have dropped the 't Hooft term which appears in the definition of the $(\mathrm{S} - \mathrm{P})_{\mathrm{NJL}}$-channel in our QCD calculations. This procedure corresponds to a maximal breaking of the $\mathrm{U}_\mathrm{A}(1)$-symmetry at the projection scale Λ_{NJL}. In summary, the effective action in Eq. (5.35) corresponds to the commonly used form of the NJL model.

In our calculation we use a bosonized version of NJL model:

$$\Gamma_k = \int \mathrm{d}^4 \mathrm{x} \; \bar{\psi}(\mathrm{i}Z_\psi \slashed{\partial} + \mathrm{i}\gamma_0 \mu)\psi + \frac{1}{2}Z_\varphi(\partial_\mu \bar{\varphi})^2 + \mathrm{i}\bar{h}\bar{\psi}(\sigma + \mathrm{i}\vec{\tau} \cdot \vec{\pi}\gamma_5)\psi + \frac{1}{2}\bar{m}^2\bar{\varphi}^2 \, , \tag{5.36}$$

with $\bar{\varphi} = (\sigma, \vec{\pi})^T$ and $\bar{h}$ a real valued Yukawa coupling. The boundary conditions of this model are

$$\lim_{k \to \Lambda_{\mathrm{NJL}}} Z_\varphi = 0 \, , \tag{5.37}$$

$$\lim_{k \to \Lambda_{\mathrm{NJL}}} Z_\psi = 1 \, , \tag{5.38}$$

and

$$\lim_{k \to \Lambda_{\mathrm{NJL}}} \frac{\bar{h}^2}{\bar{m}^2} = \bar{\lambda}_{\sigma,\mathrm{NJL}}(\Lambda_{\mathrm{NJL}}) \, . \tag{5.39}$$

The action in Eq. (5.36) can be derived from the action in Eq. (5.35) using Hubbard-Stratonovich transformation described in Sec. 4.2.1. In this study we again neglect the anomalous dimensions η_ψ and η_φ. So, we set $Z_\psi = 1$ and $Z_\varphi = 1$. For a detailed discussion concerning this approximations, we refer the reader to Sec. 4.2.2. In this first study we also ignore the possible running of the Yukawa coupling, $\bar{h}$, for the sake of simplicity. Therefore, $\bar{h}$ is simply a constant which can be obtained using low-energy observables in the limit $T \to 0$, $\mu \to 0$. Thereby, one uses the Goldberger-Treiman relation, Eq (2.33), and the low-energy values of the constituent quark mass, $\bar{m}_q \simeq 300$ MeV, and of the pion decay constant, $f_\pi \simeq 87$ MeV[11]. So, in our calculations the Yukawa coupling is given by $\bar{h} \simeq 3.448$.

---

11 This value is only valid in the chiral limit. The physical pion decay constant is measured to $f_\pi = (92.21 \pm 0.01 \pm 0.14)$ MeV [79].

In present work we restrict our calculations to the mean field level. It means that we use

$$\bar{\varphi} \equiv (\sigma, \vec{\pi})^T \stackrel{\text{mean field}}{=} (\sigma_0, 0)^T , \tag{5.40}$$

with $\sigma_0 = \bar{\varphi}_0$ being the expectation value of the field $\bar{\varphi}$. As we will see, this simplification provides us a very clear picture of how the projection of results from QCD-flows onto the model channels works. Inclusion of mesonic fluctuations will be covered in future work. From Wetterich flow equation (3.28) we can easily calculate the flow of potential U_k on the mean field level. For a model with $N_c = 3$, $N_f = 2$ and in the chiral limit we obtain the following expression for any $3d$-type regulator:

$$\partial_t U_k = -\frac{6}{\pi^2} k^3 T \sum_n \int_0^\infty dy \, y^{3/2} \frac{(\partial_t r_\psi(y))(1 + r_\psi(y))}{(\tilde{\nu}_n + i\tilde{\mu})^2 + y(1 + r_\psi(y))^2 + (\bar{m}_q/k)^2} , \tag{5.41}$$

with $\bar{m}_q = \bar{h}\sigma_0$ the constituent quark mass, $y = \vec{p}^2/k^2$ and $\tilde{\nu}_n = (2n+1)\pi T/k$ the Matsubara frequencies. In analogy to Sec. 4.2.2, we can identify the expectation value σ_0 with the pion decay constant f_π by means of the Goldberger-Treiman-relation, Eq. (2.33). $r_\psi(y)$ represents here the dimensionless regulator shape function for fermions and is specified for $3d$ linear regulator in App. E. In order to get the potential, we integrate the above flow equation:

$$U(k = 0) = \int_{\Lambda_{\text{NJL}}}^0 dk \, \frac{\partial_t U_k}{k} + U(k = \Lambda_{\text{NJL}}) . \tag{5.42}$$

Using

$$U(k = \Lambda_{\text{NJL}}) = \frac{1}{2}\bar{m}^2 \bar{\varphi}_0^2 = \frac{1}{2\bar{\lambda}_{\sigma,\text{M}}}\bar{m}_q^2 , \tag{5.43}$$

we obtain the following result for $3d$ linear regulator:

$$U(k = 0) = -\frac{2}{\pi^2} \int_{\Lambda_{\text{NJL}}}^0 dk \, \frac{k^3}{\sqrt{1 + (\bar{m}_q/k)^2}} (1 - n_{\text{F}}(\bar{m}_q/k, \tilde{\mu}) - n_{\text{F}}(\bar{m}_q/k, -\tilde{\mu}))$$
$$+ \frac{1}{2\bar{\lambda}_{\sigma,\text{M}}}\bar{m}_q^2 , \tag{5.44}$$

where n_{F} denotes the fermionic occupation number and is given by:

$$n_{\text{F}}(\bar{m}_q/k, \tilde{\mu}) = \frac{1}{\exp\left(\frac{\sqrt{1 + (\bar{m}_q/k)^2} + \tilde{\mu}}{\tau}\right) + 1} . \tag{5.45}$$

Now, we can use Eq. (5.44) in order to calculate the potential $U(k = 0)$ as a function of σ_0 for different values of temperature and chemical potential[12]. The minimum of this potential corresponds to the physical ground state and can be used as the order parameter for the chiral phase transition. Before we can perform such calculations for finite temperature and chemical potential, we have to fix the UV scale of the NJL model, Λ_{NJL}, in the limit of vanishing T and μ. Thereby, we should reproduce the correct low-energy observables.

---

12 As an alternative, one can calculate the potential $U(k = 0)$ as a function of $\bar{m}_q = \bar{h}\sigma_0$

In the chiral limit it means that we want to obtain $\sigma_0 = f_\pi = 87$ MeV. For this purpose Eq. (5.44) can be used. However, here we use the gap equation to fix Λ_{NJL} since this alternative method provides us a clear picture of how our previous results from the QCD RG flows lead to the construction of an NJL model.

For $3d$ linear regulator the gap equation for NJL model with two flavors, three colors and zero chemical potential is given by the following expression, see e.g. [103] or [70]:

$$
1 = 24\bar{\lambda}_{\sigma,\mathrm{NJL}}(\Lambda_{\mathrm{NJL}})T\sum_n \int_{-\infty}^{\infty} \frac{\mathrm{d}^3p}{(2\pi)^3} \left[\frac{1}{\nu_n^2 + \vec{p}^{\,2} + \bar{m}_q^2} - \frac{1}{\nu_n^2 + \Lambda_{\mathrm{NJL}}^2 + \bar{m}_q^2} \right]
$$
$$
\times \Theta(\Lambda_{\mathrm{NJL}}^2 - \vec{p}^{\,2}) \, ,
$$
(5.46)

with $\bar{\lambda}_{\sigma,\mathrm{NJL}}(\Lambda_{\mathrm{NJL}})$ being the starting value of the coupling at the UV cut-off of the model and $\bar{m}_q$ the constituent quark mass in the limit $k \to 0$. Considering $T \to 0$, we can replace the Matsubara sum by:

$$
T\sum_n \cdots \overset{\nu_n^2 \to p_0^2}{\to} \int_{-\infty}^{\infty} \frac{\mathrm{d}p_0}{(2\pi)} \cdots \, ,
$$
(5.47)

and then perform the integration over the zero component of the momentum:

$$
1 = \frac{6}{\pi^2}\bar{\lambda}_{\sigma,\mathrm{NJL}}(\Lambda_{\mathrm{NJL}}) \int_0^{\Lambda_{\mathrm{NJL}}} \mathrm{d}p\,p^2 \left[\frac{1}{\sqrt{\vec{p}^{\,2} + \bar{m}_q^2}} - \frac{1}{\sqrt{\Lambda_{\mathrm{NJL}}^2 + \bar{m}_q^2}} \right] \, .
$$
(5.48)

After an integration over the spatial momentum, we obtain the following relation:

$$
\bar{\lambda}_{\sigma,\mathrm{NJL}}(\Lambda_{\mathrm{NJL}}) = \frac{\pi^2}{3\Lambda_{\mathrm{NJL}}^2} \frac{1}{\gamma(\bar{m}_q/\Lambda_{\mathrm{NJL}})} \, ,
$$
(5.49)

where $\gamma(x)$ is given by:

$$
\gamma(x) = \sqrt{1 + x^2} + x^2 \ln\left[\frac{x}{1 + \sqrt{1 + x^2}} \right] - \frac{2}{3}\frac{1}{\sqrt{1 + x^2}} \, .
$$
(5.50)

Using this result, we can choose the desired value of $\bar{m}_q$ and calculate the starting value of the coupling $\bar{\lambda}_{\sigma,\mathrm{NJL}}(\Lambda_{\mathrm{NJL}})$ as a function of the UV scale Λ_{NJL}. Thereby, any pair of $\bar{\lambda}_{\sigma,\mathrm{NJL}}(\Lambda_{\mathrm{NJL}})$ and Λ_{NJL} solving Eq (5.49) would lead to one and the same value of $\bar{m}_q$. In Fig. 5.12 we plot our result for $\bar{\lambda}_{\sigma,\mathrm{NJL}}(\Lambda_{\mathrm{NJL}})$ from the gap equation for $\bar{m}_q = 300$ MeV ($f_\pi = 87$ MeV) as a red line. In this plot we also show our result for $\bar{\lambda}_{\sigma,\mathrm{NJL}}(k)$ obtained from QCD RG flows (blue line) which was already presented in Fig. 5.10. We observe that these two lines cross at some scale. It means that if we stop our QCD calculations at this k and use it together with corresponding value of $\bar{\lambda}_{\sigma,\mathrm{NJL}}(k)$ as starting parameters of NJL model for $T \to 0$ and $\mu \to 0$, then we reproduce correct low-energy observables. With other words, we just fixed the projection scale. For the particular input for the strong coupling it is given by:

$$
\Lambda_{\mathrm{NJL}} = 260 \text{ MeV.}
$$
(5.51)

We emphasize once more that this scale coincides with the IR scale of our QCD-flows calculation and with the UV scale of the model. One may notice that this scale is quite
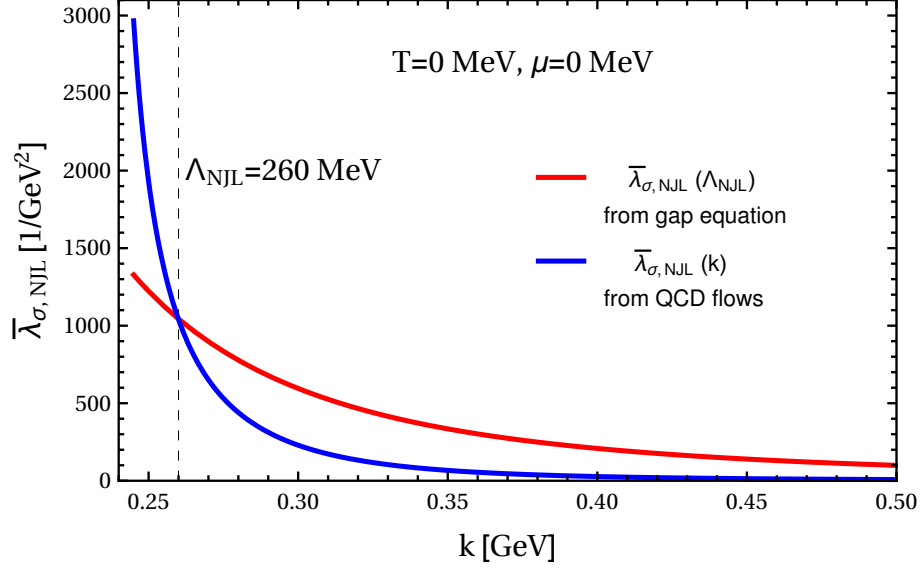
FIGURE 5.12: Our result for $\bar{\lambda}_{\sigma,\mathrm{NJL}}(\Lambda_{\mathrm{NJL}})$ from the gap equation for $f_\pi = 87$ MeV (red line) as well as $\bar{\lambda}_{\sigma,\mathrm{NJL}}(k)$ obtained from QCD flows using the strong coupling from [73] (blue line). Both lines were calculated in the limit $T \to 0$, $\mu \to 0$. We observe that they cross at $k \simeq 260$ MeV. It means that we have to project our results from QCD RG flows onto the NJL-model channel exact at this scale.

small compared to the UV scales usually used in NJL calculations. The typical NJL models are defined at UV scales between 500 MeV and 1 GeV. As we will see later, the small value of Λ_{NJL} in our calculation is a consequence of the particular choice of the input for the strong coupling. Different inputs for α would lead to very different results for Λ_{NJL}. Especially those inputs are of interest for us which provide stronger α at larger scales. Such inputs lead to stronger $\bar{\lambda}_{\sigma,\mathrm{NJL}}(k)$ and, consequently, the blue line in Fig. 5.12 would cross the red line at larger k. With other words, the observed projection scale would be larger. For an example of such an input, we refer the reader to Sec. 5.7.

Nonetheless, in the major part of our calculations we use the input from [73]. This input includes the temperature and, after manipulations described above, chemical-potential dependence of the strong coupling. So, it allows us to study the influence of T- and μ-dependent model parameters on the phase diagram in a more proper way.

5.6 PHASE DIAGRAM OF NJL MODEL

Since the UV scale of the model and the corresponding value of the 4-fermion coupling are fixed, we can calculate the phase diagram from our NJL model. Thereby, we can proceed in two different ways:

1. We can use Λ_{NJL} and $\bar{\lambda}_{\sigma,\mathrm{NJL}}(\Lambda_{\mathrm{NJL}})$ obtained for $T \to 0$, $\mu \to 0$ also for finite temperature and chemical potential calculations.

2. We can keep Λ_{NJL} fixed and calculate $\bar{\lambda}_{\sigma,\mathrm{NJL}}(\Lambda_{\mathrm{NJL}})$ as a function of T and μ from QCD RG flows.
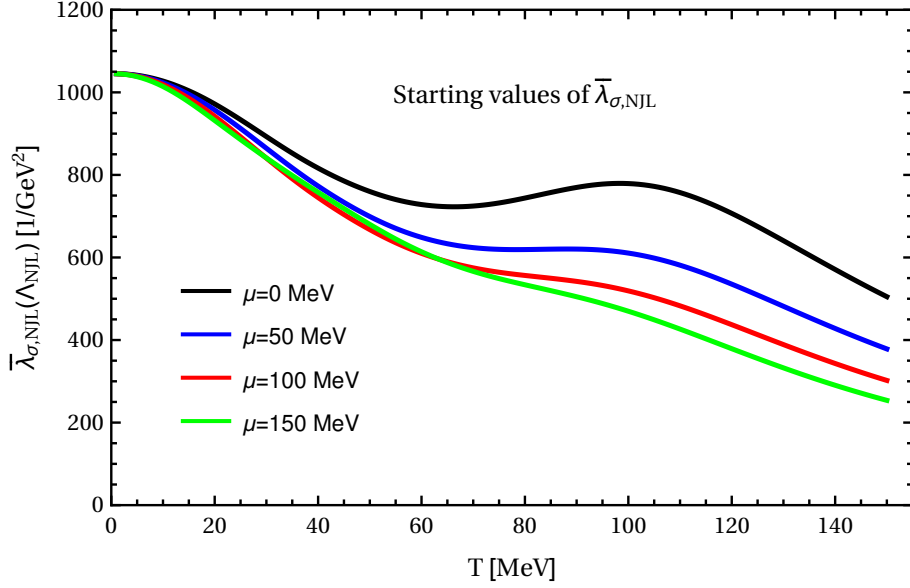
FIGURE 5.13: The starting values of $\bar{\lambda}_{\sigma,\mathrm{NJL}}(\Lambda_{\mathrm{NJL}})$ as a function of temperature for different values of chemical potential. We observe that $\bar{\lambda}_{\sigma,\mathrm{NJL}}(\Lambda_{\mathrm{NJL}})$ generally decreases with increasing T. It reflects the restoration of chiral symmetry in QCD and is consistent with our qualitative discussion in Sec. 5.2. However, for small μ we observe a non-monotonous behavior of $\bar{\lambda}_{\sigma,\mathrm{NJL}}(\Lambda_{\mathrm{NJL}})$. It appears due to the suppression of quark contribution to the strong coupling discussed in Sec. 5.3. This suppression leads to stronger α and, therefore, tends to produce stronger $\bar{\lambda}_{\sigma,\mathrm{NJL}}(\Lambda_{\mathrm{NJL}})$. This effect becomes less relevant with increasing chemical potential.

The first option basically corresponds to the standard procedure in NJL calculations and, therefore, will produce results which can be used as a reference for a typical NJL-model outcome. The second option represents an improvement of the typical NJL procedure and allows us to study the impact of T- and μ-dependence in the model parameters on the phase diagram.

Before we present phase diagrams for both cases mentioned above, it is useful to discuss the starting value of the coupling $\bar{\lambda}_{\sigma,\mathrm{NJL}}(\Lambda_{\mathrm{NJL}})$ as a function of T and μ, see Fig 5.13. In this figure we consider $\bar{\lambda}_{\sigma,\mathrm{NJL}}(\Lambda_{\mathrm{NJL}})$ as a function of temperature for different values of chemical potential. We observe that for $T \to 0$ the value of $\bar{\lambda}_{\sigma,\mathrm{NJL}}(\Lambda_{\mathrm{NJL}})$ is basically the same for all considered values of μ. This is due to the fact that $\Delta\eta_{A,k}$ behaves as a Θ-function and threshold functions of the fermionic flows have only a weak μ-dependence in the limit of zero temperature, see App. F and App. E.3 correspondingly. With increasing temperature $\bar{\lambda}_{\sigma,\mathrm{NJL}}(\Lambda_{\mathrm{NJL}})$ becomes generally smaller as one would expect it from the chiral symmetry restoration in QCD. However, for small values of μ we observe a non-monotonous behavior of $\bar{\lambda}_{\sigma,\mathrm{NJL}}(\Lambda_{\mathrm{NJL}})$: at intermediate temperatures it starts to grow and reaches a maximum. With further increase of T it decreases again. This unexpected behavior is a direct consequence of the thermal decoupling of quarks discussed in Sec. 5.3. In this section we have already argued that at finite temperatures the Yang-Mills contributions to the strong coupling are dominant and, therefore, α becomes stronger for increasing T. Therefore, neglecting the T- and μ-dependence of 4-fermion flows, one would expect that the 4-fermion couplings also become stronger. On the other hand, we have shown in Sec. 5.2 that for finite temperature and chemical potential the fermionic flows produce
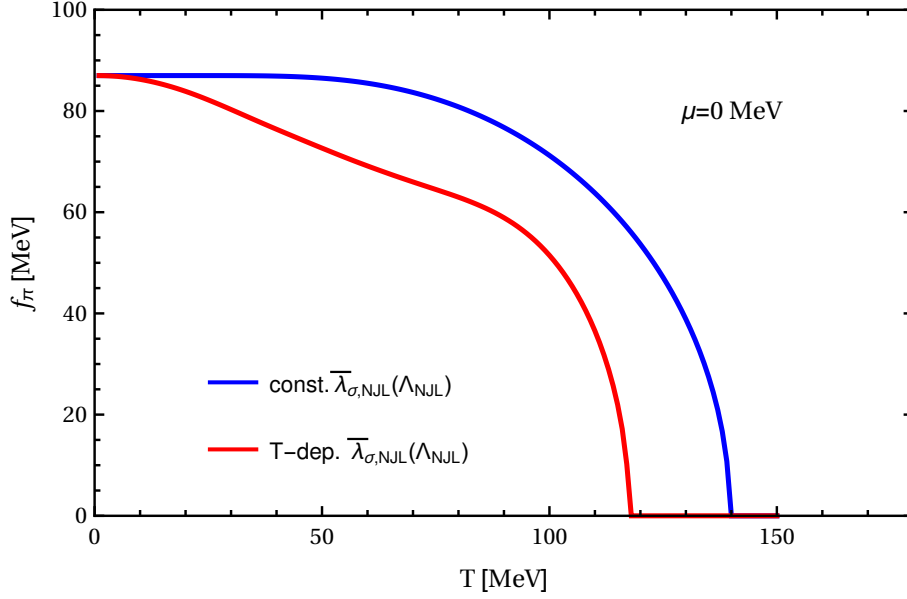
FIGURE 5.14: The order parameter f_π for $\mu = 0$ as function of temperature. We consider both the constant $\bar{\lambda}_{\sigma,\mathrm{NJL}}(\Lambda_{\mathrm{NJL}})$ (blue line) and μ-dependent $\bar{\lambda}_{\sigma,\mathrm{NJL}}(\Lambda_{\mathrm{NJL}})$ (red line). The resolution in temperature direction is 1 MeV. f_π calculated with T-dependent starting model parameter shows weak wave-like behavior which is reminiscent of the non-monotonous behavior of $\bar{\lambda}_{\sigma,\mathrm{NJL}}(\Lambda_{\mathrm{NJL}})$ as function of T and, therefore, of the thermal decoupling of quarks. We observe smaller T_χ in the case of temperature dependent $\bar{\lambda}_{\sigma,\mathrm{NJL}}(\Lambda_{\mathrm{NJL}})$. This is explained be the chiral restoration in QCD which is neglected in standard NJL procedure.

weaker couplings compared to the limit $T \to 0$, $\mu \to 0$. This mechanism reflects the restoration of chiral symmetry in QCD and acts contrary to the thermal decoupling of quarks, which leads to a stronger strong coupling and, therefore, favor the breaking of the chiral symmetry. The interplay of these two effects leads to the non-monotonous behavior of $\bar{\lambda}_{\sigma,\mathrm{NJL}}(\Lambda_{\mathrm{NJL}})$ for small μ. For larger chemical potential, however, the effect of the thermal decoupling of quarks appears to become subleading and $\bar{\lambda}_{\sigma,\mathrm{NJL}}(\Lambda_{\mathrm{NJL}})$ decreases monotonously with increasing T.

Now, we use these results to calculate the order parameter of the chiral phase transition. In Fig. 5.14 we present our results for f_π for vanishing chemical potential as function of T. In this plot we present f_π calculated with a temperature dependent starting value of the 4-fermion coupling (red line) as well as f_π obtained using the standard procedure of NJL calculations (blue line). Both curves indicate the second order phase transition as expected for an NJL model in the chiral limit and differ basically in two aspects: First, we observe a kind of weakly pronounced wave-like behavior of the order parameter if we use the temperature dependent starting parameter. This is a consequence of the non-monotonous behavior of $\bar{\lambda}_{\sigma,\mathrm{NJL}}(\Lambda_{\mathrm{NJL}})$ for small μ: larger values of $\bar{\lambda}_{\sigma,\mathrm{NJL}}(\Lambda_{\mathrm{NJL}})$ correspond to stronger breaking of the chiral symmetry and, therefore, push the order parameter to larger values. This behavior does not appear if we use constant $\bar{\lambda}_{\sigma,\mathrm{NJL}}(\Lambda_{\mathrm{NJL}})$ and seems to be rather unexpected. Nonetheless, it is in full agreement with the observation of the thermal decoupling of quarks from the gauge sector. We emphasize that the quantitative impact of this effect on the behavior of f_π strongly depends on the used input for α. For example, the strong coupling from [73] without modifications performed in this study and
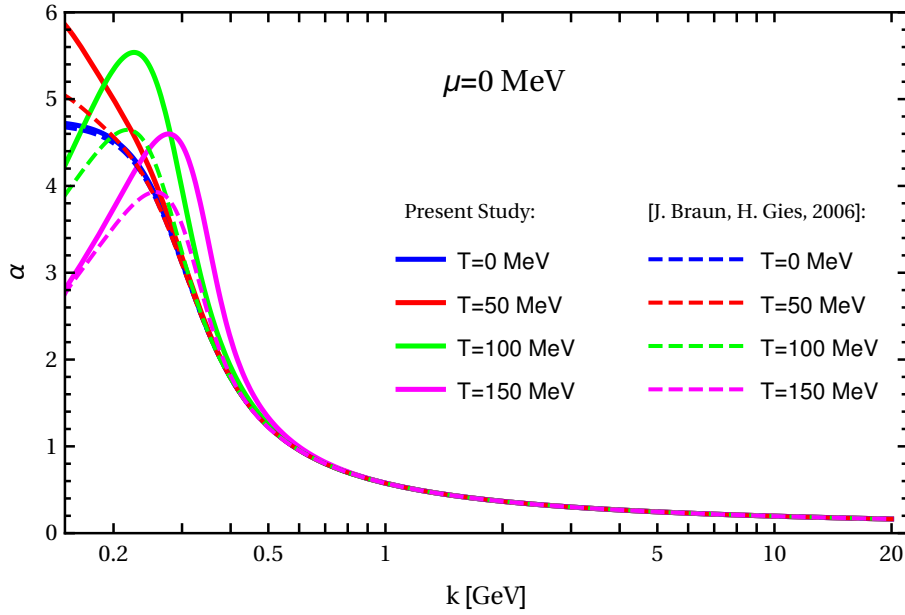
FIGURE 5.15: In this plot we compare our result from Fig. 5.7 with result from [73] for $N_f = 2$. Both results show the same qualitative behavior. However, the result from [73] exhibits much less pronounced effect of thermal decoupling of quarks. This is due to a more sophisticated ansatz for external-momentum expansion of $\eta_{A,k}^{\text{quarks}}(T)$ in [73].

for $N_f = 2$ shows a weaker increase of α with increasing T, see Fig. 5.15. According to this, the strong coupling from [73] would lead to less pronounced non-monotonous behavior of $\bar{\lambda}_{\sigma,\text{NJL}}(\Lambda_{\text{NJL}})$, and to less pronounced, or even negligible, wave-like behavior of f_π.

The second main aspect which distinguishes the red and blue curves in Fig. 5.14 is that the critical temperature, T_χ, is considerably smaller if we use T-dependent starting model parameter. It amounts to $T_\chi \approx 118$ MeV compared to $T_\chi \approx 141$ MeV for constant $\bar{\lambda}_{\sigma,\text{NJL}}(\Lambda_{\text{NJL}})$. Both these values are smaller than $T_\chi = (154 \pm 9)$ MeV measured in lattice QCD [180]. However, we emphasize that this is an effect of the rather small Λ_{NJL} and, consequently, of the particular input for the strong coupling used in this study. As we will see in the next section, other inputs can lead to more realistic values of T_χ. Nonetheless, the fact that the temperature dependent starting value of the model parameter leads to a reduction of the critical temperature of the NJL model is very remarkable. It is also in agreement with the chiral symmetry breaking mechanism described in [71, 72, 73] and in Sec. 5.2: The restoration of the chiral symmetry in QCD leads to smaller values of the starting parameter $\bar{\lambda}_{\sigma,\text{NJL}}(\Lambda_{\text{NJL}})$. On the other hand, smaller $\bar{\lambda}_{\sigma,\text{NJL}}(\Lambda_{\text{NJL}})$ lowers the order parameter and, therefore, the critical temperature. Even though this effect seems to be rather intuitive, to our knowledge, it was never incorporated in NJL calculations before. Typical critical temperatures observed up to date for NJL phase diagram seems to be too large since no chiral symmetry restoration in QCD itself was taken into account. In this calculation the critical temperature is lowered by $\sim 16\%$. This particular number can be different for models defined at higher UV scale or for different inputs of the strong coupling. Nonetheless, the major effect will remain the same and should be kept in mind if one interprets results from usual model calculations.
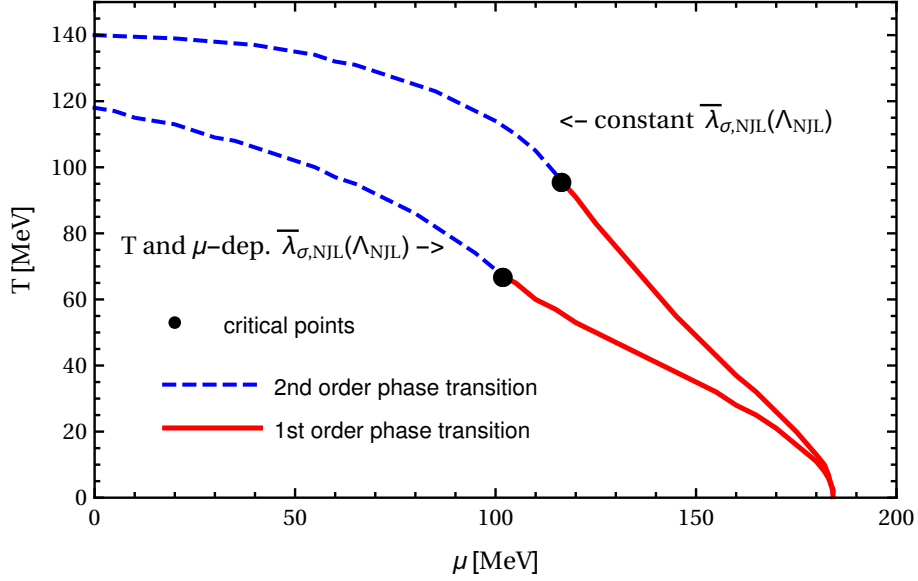
FIGURE 5.16: The phase diagram of our NJL model calculated using standard NJL-calculation procedure (upper line) and using T- and μ-dependent starting value of 4-fermion coupling (lower line). In both cases there is a phase transition of second order (dashed blue line) for smaller μ and a phase transition of first order (thick red line) for larger μ. These two regions are separated by critical endpoints. The critical temperature, T_χ, is continuously smaller for the case of T- and μ-dependent $\bar{\lambda}_{\sigma,\mathrm{NJL}}(\Lambda_{\mathrm{NJL}})$. The position of critical endpoint is also shifted to smaller values in this case. For $T \to 0$ both lines coincide. It is a consequence of absence of Silver Blaze problem in our calculations.

Further, we also consider finite chemical potential. The resulting phase diagram can be found in Fig. 5.16. The dashed blue line represents a phase transition of second order and the thick red line a phase transition of first order, the black dot represents the critical endpoint and separates transitions of different orders. The resolution in Fig. 5.16 is 1 MeV in T-direction and 5 MeV in μ-direction. We present two transition lines. The upper one corresponds to the result obtained using the standard NJL model, namely, keeping $\bar{\lambda}_{\sigma,\mathrm{NJL}}(\Lambda_{\mathrm{NJL}})$ constant. The lower transition line was calculated using temperature and chemical potential dependent starting values of the 4-fermion coupling. In both cases the structures of the corresponding phase diagrams are very similar and are in agreement with expectations for the chiral limit[13]. The main difference, thereby, are values of T_χ. One observes that also for finite μ the critical temperature lowers if one considers $\bar{\lambda}_{\sigma,\mathrm{NJL}}(\Lambda_{\mathrm{NJL}})$ as a function of T and μ as predicted from QCD flows. Also, the position of the critical endpoint is shifted to smaller values of $(T_{\mathrm{C}}, \mu_{\mathrm{C}})$.

An interesting observation is that for large μ and small T we observe that both transition lines basically coincide. This observation is remarkable in the context of the famous Silver-Blaze problem appearing in QCD at finite chemical potential, see, e.g., Ref [181][14]: In QCD the chemical potential appears in the functional determinant which is a product of eigenvalues of the Dirac operator. Therefore, any finite value of chemical potential should alter all of the eigenvalues and one would expect that all observables should change.

---

13 With finite explicit chiral symmetry breaking one would observe a crossover instead of a second order phase transition for small and intermediate μ.

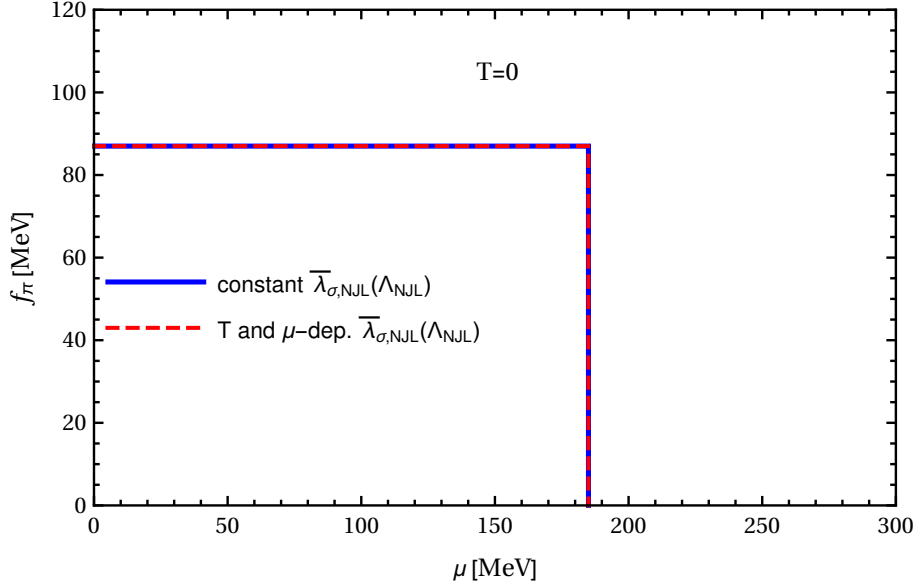14 For isospin chemical potential this problem also appears and was solved in [182].

FIGURE 5.17: The order parameter f_π for $T \to 0$ as function of chemical potential. We consider both the constant $\bar{\lambda}_{\sigma,\mathrm{NJL}}(\Lambda_{\mathrm{NJL}})$ (blue line) and temperature dependent $\bar{\lambda}_{\sigma,\mathrm{NJL}}(\Lambda_{\mathrm{NJL}})$ (red line). The resolution in μ-direction is 5 MeV. We observe that both lines coincide within resolution of our calculations. Also, in both cases f_π stays constant for $\mu \leq \mu_\chi$. This behavior indicates that no Silver-Blaze problem appear in our results.

However, from the phenomenological point of view we know that a physical system at vanishing temperature should stay unaffected by a chemical potential unless it exceeds some critical value. In the case of the (quark) chemical potential used in this work, the critical value of μ is bounded from above by $1/3$ of the nucleon mass. This problem does not appear in the NJL model. In particular, it means that the value of the order parameter does not change for $\mu \leq \mu_\chi$ at $T = 0$. In our present calculations we use QCD RG flows in order to calculate starting parameters of the NJL model in T- and μ-dependent way. Therefore, one could expect that the Silver Blaze problem may appear in our results. However, we observe that it is not the case, see Fig. 5.17. The absence of the Silver Blaze problem in our calculations can be explained by the behavior of $\bar{\lambda}_{\sigma,\mathrm{NJL}}(\Lambda_{\mathrm{NJL}})$ at small temperatures for all values of μ which we have discussed in Fig. 5.13. In the end, it is caused by the behavior of $\Delta\eta_{A,k}$ and of threshold functions for 4-fermion couplings in the corresponding limit. For more details, see App. F and App. E.3.

Altogether, we conclude that the temperature and chemical potential dependent starting parameters improve our understanding of NJL model. They considerably influence the phase transition diagram on the quantitative level and, in general, lower the critical temperature for all values of chemical potential. This happens because of the chiral symmetry restoration effects in the QCD RG flows. Even though our current model seems to be defined at too low UV scale, Λ_{NJL}[15], our conclusions are also valid for models defined at higher scales. To show this, we consider an alternative input for the strong coupling in the following section.

---

15 Too small Λ_{NJL} is also the reason for too small T_χ at $\mu \to 0$ and for too small μ_χ at $T \to 0$.

5.7 ALTERNATIVE INPUT FOR THE STRONG COUPLING

In this section we use an alternative input for the coupling α computed in Ref. [122]. The advantage of this FRG result in Landau gauge is that the strong coupling was calculated from the quark-gluon vertex which also enters in our 4-fermion flows. Moreover, in [122] a smooth approximation of the $4d$ linear regulator was used. Even though the dimensionality of this regulator is different compared to $3d$ linear regulator which was used in this work, both these regulators are from the same regulator class. A big disadvantage of the input from [122] is that it was obtained only in the limit $T \to 0$, $\mu \to 0$. Therefore, using this input, we partially lose information about T- and μ-dependence of 4-fermion flows. Another, rather technical, disadvantage is that $\eta_{A,k}^{\text{gluons}}$ is not explicitly given in the results from [122]. For our calculations, however, these quantity is quite important since it appears in threshold functions $l_{1,1}^{(\text{FB})}$ and $l_{1,2}^{(\text{FB})}$ of fermionic flows, see App. E. Hence, we cannot provide accurate calculations using this input. Nonetheless, we can consider two different approximations for $\eta_{A,k}^{\text{gluons}}$: First, we can simply neglect this contribution, i.e., we can set $\eta_{A,k}^{\text{gluons}} = 0$ in the threshold functions of 4-fermion flows. Second, we can consider $\eta_{A,k}^{\text{gluons}} \approx (\partial_t \alpha)/\alpha$ inspired by Eq. (5.13). In this approximation, $\eta_{A,k}^{\text{gluons}}$ includes much more than only contributions from the gluonic sector. It also includes quark contributions since in [122] the authors have used the dynamical-hadronization technique to calculate the strong coupling.

The authors of [122] have calculated the strong coupling α using the full tensor structure of the quark-gluon vertex. Thereby, they have considered different momentum configurations. In this work we consider only the data obtained from the classical tensor structure and with a momentum configuration where the momentum of the quark is zero and the momenta of antiquark and gluon are p. Further, in spirit of Wilsonian momentum-shell integration, we use the approximation $\alpha(k) = \alpha(k, p = k)$. The corresponding strong coupling can be found in Fig. 5.18. In this figure we also plot the perturbative 1-loop result for $\alpha(k)$ fixed at $k = 20$ GeV. However, in contrast to Sec. 5.3, we should use $\alpha(k = 20 \text{ GeV}) = 0.174$. It is the value obtained in [122] at $k = 20$ GeV and results from the fact that in [122] the quenched quarks were used. We observe that the result from [122] agrees with 1-loop α for $k \gtrsim 5$ GeV and starts to rapidly grow at much higher scales compared to our original input for α discussed in Sec. 5.3. For $k \lesssim 550$ MeV the strong coupling decreases and approaches zero for $k \to 0$ as it was already observed in lattice QCD calculations in the Landau gauge [183, 184]. However, as we will discuss below, this effect does not really play a role for our considerations.

Further, we proceed in the same way as described in Sec. 5.5 and Sec. 5.6. We obtain following projection scales Λ_{NJL}:

$$
\begin{aligned}
\eta_{A,k}^{\text{gluons}} &\approx 0 \Rightarrow \Lambda_{\text{NJL}} = 502 \text{ MeV}, \\
\eta_{A,k}^{\text{gluons}} &\approx (\partial_t \alpha)/\alpha \Rightarrow \Lambda_{\text{NJL}} = 557 \text{ MeV}.
\end{aligned}
\tag{5.52}
$$

In the first case, Λ_{NJL} is smaller than $k \approx 550$ MeV. It means that we define the model in the momentum region where α decreases with decreasing k due to the effective gluon mass. However, the value of α at $k = \Lambda_{\text{NJL}} = 502$ MeV differs from α at the position of the peak only by $\sim 1.6\%$ and is larger than the critical value of the strong coupling. In the case of $\eta_{A,k}^{\text{gluons}} \approx (\partial_t \alpha)/\alpha$, the projection scale is even larger than the scale corresponding
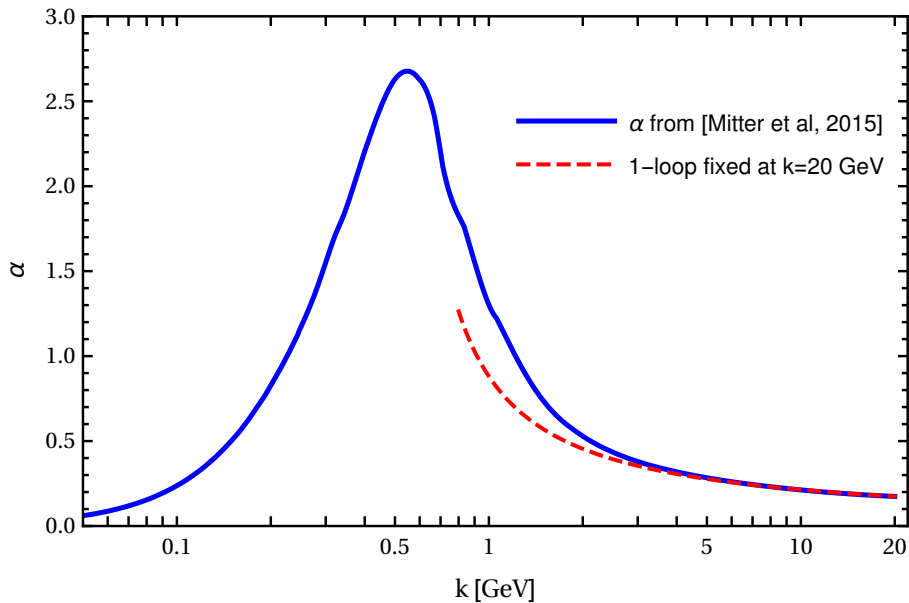
FIGURE 5.18: $\alpha(k)$ from [122] ($T \rightarrow 0$, $\mu \rightarrow 0$) as explained in the main text. We also plot a perturbative 1-loop $\alpha(k)$ fixed by $\alpha(k = 20 \text{ GeV}) = 0.174$. This is the value of the strong coupling obtained at $k = 20$ GeV in [122], where quenched quarks were used. We observe a very good agreement between these two couplings for $k \gtrsim 5$ GeV. We also observe that the coupling from [122] becomes large already at higher scales compared to the coupling in Sec. 5.3. For $k \lesssim 550$ MeV, $\alpha(k)$ from [122] decreases and approaches zero. This is due to the effective gluon mass.

to the peak in α. Therefore, the effect of decreasing α for $k \lesssim 550$ MeV is not relevant for our further considerations.

Both values in Eq. (5.52) are considerably larger than $\Lambda_{\text{NJL}} = 260$ MeV obtained for the strong-coupling input from [73]. They are also in agreement with common UV scales used in model calculations. Hence, we conclude that in general the formalism which we use in this study can produce models with usual boundary conditions. However, the particular values of the model parameters strongly depend on the input for the strong coupling α. We emphasize once again that the current input for α was calculated for zero temperature and zero chemical potential. Therefore, we lose some information about T- and μ-dependence in the behavior of 4-fermion flows. In particular, no quark decoupling described in Sec. 5.3 can take place. As a consequence, $\bar{\lambda}_{\sigma,\text{NJL}}(\Lambda_{\text{NJL}})$ is monotonously decreasing as a function of T for all values of μ and, therefore, the wave-like behavior of the order parameter does not appear (compare Sec. 5.6).

In Fig. 5.19 we present the phase diagrams for both approximations discussed above. To distinguish different cases we use the color scheme described in Tab. 5.1. The critical endpoints are represented by black dots. Further, the upper lines correspond to the case of the constant starting parameter $\bar{\lambda}_{\sigma,\text{NJL}}(\Lambda_{\text{NJL}})$ and the lower lines to the T- and μ-dependent $\bar{\lambda}_{\sigma,\text{NJL}}(\Lambda_{\text{NJL}})$. The qualitative structure of the phase diagrams is very usual for NJL model in the chiral limit and is basically the same as in our previous result, see
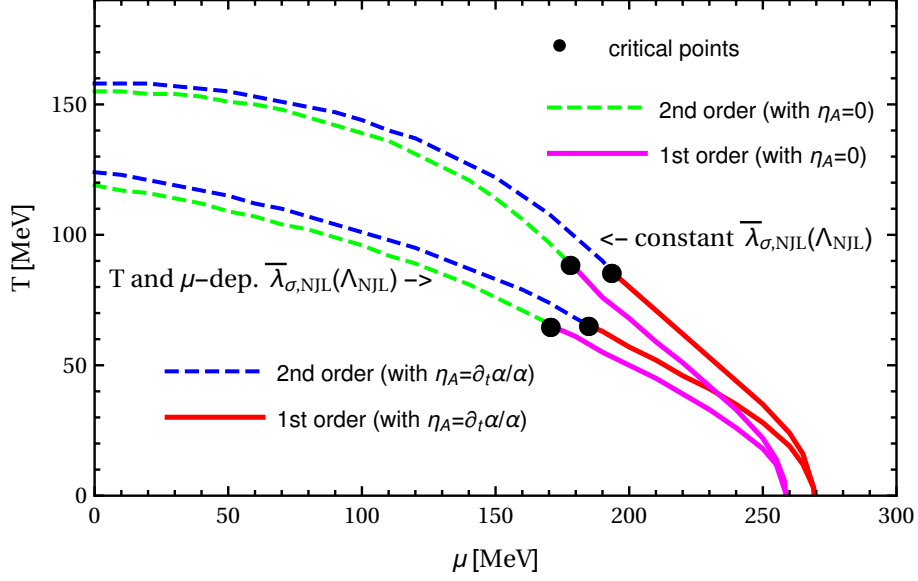
FIGURE 5.19: The phase diagrams for models derived using the input for $\alpha(k)$ from [122]. An explanation of the color scheme can be found in Tab. 5.1. The upper lines correspond to the case of constant $\bar{\lambda}_{\sigma,\mathrm{NJL}}(\Lambda_{\mathrm{NJL}})$ and lower lines to the case of T- and μ-dependent $\bar{\lambda}_{\sigma,\mathrm{NJL}}(\Lambda_{\mathrm{NJL}})$. We observe similar behavior as in Fig. 5.16 where the input from [73] was used: All diagrams exhibit the phase structure which is typical for the chiral limit (from left to right): second order phase transition, critical endpoint, first order phase transition. For T- and μ-dependent $\bar{\lambda}_{\sigma,\mathrm{NJL}}(\Lambda_{\mathrm{NJL}})$, we observe smaller T_χ for all values of μ. The positions of critical endpoints are shifted to smaller values in this case.

	second order phase transition	first order phase transition
$\eta_{A,k}^{\mathrm{gluons}} \approx 0$	green dashed line	magenta thick line
$\eta_{A,k}^{\mathrm{gluons}} \approx (\partial_t \alpha)/\alpha$	blue dashed line	red thick line

TABLE 5.1: Color scheme for Fig. 5.19.

Fig. 5.16. For constant $\bar{\lambda}_{\sigma,\mathrm{NJL}}(\Lambda_{\mathrm{NJL}})$ and for $\mu \to 0$ we observe the following critical temperatures:

$$\begin{aligned}
\eta_{A,k}^{\mathrm{gluons}} &\approx 0 \Rightarrow T_\chi = 155 \text{ MeV}, \\
\eta_{A,k}^{\mathrm{gluons}} &\approx (\partial_t \alpha)/\alpha \Rightarrow T_\chi = 158 \text{ MeV}.
\end{aligned} \tag{5.53}$$

These values are very similar and in perfect agreement with $T_\chi = (154 \pm 9)$ MeV measured in lattice QCD [180]. The critical values of μ for $T \to 0$ are in agreement with typical model predictions:

$$\begin{aligned}
\eta_{A,k}^{\mathrm{gluons}} &\approx 0 \Rightarrow \mu_\chi = 259 \text{ MeV}, \\
\eta_{A,k}^{\mathrm{gluons}} &\approx (\partial_t \alpha)/\alpha \Rightarrow \mu_\chi = 269 \text{ MeV}.
\end{aligned} \tag{5.54}$$

Now, let us discuss the influence of T- and μ-dependent $\bar{\lambda}_{\sigma,\mathrm{NJL}}(\Lambda_{\mathrm{NJL}})$. In general, we observe the same effects as already observed in Sec. 5.6: The critical temperatures become smaller compared to the case of constant starting parameters. This is valid for all values

of μ. For $\mu \to 0$, T_χ is lowered by $\sim 23\%$ for the case of $\eta_{A,k}^{\text{gluons}} \approx 0$ and by $\sim 21.5\%$ for $\eta_{A,k}^{\text{gluons}} \approx (\partial_t \alpha)/\alpha$. The positions of critical endpoints are also shifted to smaller values $(T_{\text{C}}, \mu_{\text{C}})$. We again observe that our formalism does not exhibit the Silver-Blaze problem.

To summarize, we have seen that QCD RG flows allows us to derive low-energy QCD models which are comparable with phenomenological models on both the qualitative as well as the quantitative level. However, the quantitative results strongly depends on the input for the strong coupling. The inclusion of T- and μ-dependent starting parameters in our calculations is a considerable improvement of the common model-calculations procedure. It takes into account not only the restoration of the chiral symmetry in the model but also chiral symmetry restoration effects in QCD. In particular, it leads to smaller critical temperatures.

SUMMARY AND OUTLOOK

This thesis was conducted with the aim to achieve a better understanding of the phase transitions in QCD at finite chemical potential, guided by two major goals: First, we sought a better understanding of the connection between the chiral and the deconfinement phase transition at finite chemical potential, which are both associated with very similar (pseudo-)critical temperatures at zero chemical potential as observed in lattice QCD simulations. Further, they both are driven by the gauge dynamics but their relation has not yet been fully understood, neither at zero chemical potential nor at finite chemical potential. Second, we intended to improve current low-energy QCD models which are based on several approximations and assumptions. To this end, we proposed an approach which makes use of QCD RG flows and allows to bring low-energy QCD models closer to QCD by taking into account the effects of QCD at high energy scales.

To achieve the first goal, we have studied the mechanism of dynamical locking which enforces the spontaneous breaking of the chiral symmetry if confinement takes place. This mechanism was first described in Refs. [69, 70] for zero chemical potential and was studied in this work at finite values of μ. To this end, we have employed a Polyakov-loop extended Nambu–Jona-Lasinio model with $N_f = 2$ massless flavors, N_c colors, and a scalar-pseudoscalar interaction channel. The confining dynamics was included by means of a temporal gluonic background field taken from [146]. Our analysis of the fixed-point structure of the four-fermion interaction in the limit of infinite many colors shows that all finite-temperature and finite chemical-potential corrections to the vacuum fixed point λ_ψ^* disappear as long as $T \leq T_d$. Consequently, for $N_c \to \infty$ all configurations of the model or, with other words, any choice of the starting value $\lambda_\psi^{\mathrm{UV}} \geq \lambda_\psi^*$ leads to chiral symmetry breaking such that $T_\chi \geq T_d$. In particular, it means that for all choices of $\lambda_\psi^{\mathrm{UV}}$ that would allow $T_\chi < T_d$, the chiral phase transition temperature is shifted such that $T_\chi \approx T_d$. Also, for the physical case $N_c = 3$ we have found a region in the parameter space of $\lambda_\psi^{\mathrm{UV}}$ where the locking window with $T_\chi \approx T_d$ is present. However, in contrast to the limit of infinite colors, there is a regime where $T_\chi < T_d$ which corresponds to small values of $\lambda_\psi^{\mathrm{UV}}$. Further, we have observed that the inclusion of finite chemical potential affects neither the existence nor the width of the locking window. The finite chemical potential solely shifts the locking window to larger values in the parameter space. This behavior also explains the shape of the chiral phase boundary in the phase diagram spanned by T and μ. Since our particular model did not allow to get access to physical observables, we were basically free in the choice of $\lambda_\psi^{\mathrm{UV}}$ as long as $\lambda_\psi^{\mathrm{UV}} \geq \lambda_\psi^*$. We have observed that this ambiguity significantly affects our results. In particular, the existence of the locking of the chiral and deconfinement phase transition in the (T, μ)-phase diagram as well as the curvature of the corresponding chiral phase transition line strongly depend on the specific configuration of the model.

In order to partially resolve the momentum dependence of fermionic self-interaction and to get access to the physical low-energy observables, we have introduced the Polyakov-loop extended quark-meson model. This procedure allowed us to study the phase diagram of PQM model spanned by the pion decay constant f_π and the temperature T. Thereby, we have considered both the chiral limit and the situation of explicitly broken chiral symmetry. In both cases we have found again a region where the chiral phase transition is locked in by the confining dynamics. Similar to our results in purely fermionic picture, we have observed that the locking window is shifted to the larger values of f_π if we increase the chemical potential μ. The width of this window is not significantly affected by finite values of μ. Further, we have payed a close attention to the behavior of the model with parameters adjusted to the correct low-energy observables. In the chiral limit we have found that the physical point corresponding to $f_\pi = 87$ MeV is located outside of the locking window. Consequently, we have observed that the critical temperatures of the chiral and deconfinement phase transitions do not coincide even for vanishing chemical potential. In contrast, once the explicit breaking of chiral symmetry is included, the chiral phase transition at the physical point $f_\pi = 93$ MeV is indeed locked in by the confining dynamics. We have found that the equality of the critical temperatures $T_\chi \approx T_d$ holds for $\mu \lesssim 170$ MeV. As a consequence, the curvature of the chiral phase transition line in the (T, μ)-plane at $\mu = 0$ is determined by the curvature of the deconfinement phase transition. Since the order parameter for the latter was calculated in pure Yang-Mills theory, it is μ-independent and, thus, the curvature of the chiral phase boundary is given by zero.

To conclude, we have shown that confinement can enforce the breaking of chiral symmetry both in the purely fermionic picture as well as in the partially bosonized model. This statement is valid for all considered values of the chemical potential μ. In our particular calculations the input for the background field $\langle A_0 \rangle$, which is used as the order parameter for the deconfinement phase transition, was calculated using pure Yang-Mills theory. Therefore, we actually miss the back-reaction of the quarks on the gauge sector. As a consequence, the deconfinement phase transition is μ-independent. Even though the inclusion of such a back-reaction is of great importance for quantitative studies, our particular calculations at finite chemical potential already provide an important qualitative understanding of the impact of confining dynamics in the gauge sector on the chiral phase transition in the matter sector. In particular, our analytical results in the limit $N_\mathrm{c} \to \infty$ may affect the interpretation of approximations made in common PNJL and PQM studies.

Working with PNJL and PQM model, we were confronted with commonly used approximations and assumptions. We have especially emphasized three of them: the Fierz-incomplete interaction channels, fine-tuning of model parameters and the corresponding ambiguity in their choice, and the negligence of the possible temperature and chemical-potential dependence of model parameters. We have presented an approach how these shortcomings of common models can be potentially improved by means of the QCD RG flows [71, 72, 73]. The main idea of this approach is to construct a low-energy QCD model using the flows of Fierz-complete effective 4-quark interactions which are generated by gluodynamics. We have calculated the flows of the effective couplings with the FRG approach and have recapitulated the mechanism of chiral symmetry breaking in QCD as it was shown in [71, 72, 73]. Thereby, we have seen the great importance of the strong coupling α for this mechanism.

In our numerical calculations we have considered the flow of the strong coupling to be given by the pure Yang-Mills contributions plus quark corrections. For Yang-Mills

contributions we have used the data from [73]. The quark corrections were calculated up to the leading order in the external-momentum expansion. Our procedure has allowed to calculate α as function of temperature and chemical potential. At vanishing T and μ we have observed a perfect agreement of our results and the perturbative 1-loop coupling at large momentum scales. For finite T and μ we have found two interesting effects: First, we have observed the thermal suppression of quark contributions. This effect implies the dominance of Yang-Mills contributions at high temperatures and leads to stronger α. Further, we have seen that for small momentum scales the dimensional reduction of the theory takes place. In particular, it causes a decrease of the strong coupling to zero for $k \to 0$. As we have seen, this behavior of the strong coupling in four dimensions does not mean that the theory becomes weakly interacting but only indicates the existence of a strong-coupling fixed-point in 3-dimensional Yang-Mills theory which governs the dynamic of the theory at high temperatures.

Using our results for α we have evaluated the flows of the effective 4-quark couplings. Our numerical results have shown that the scalar-pseudoscalar interaction channel is clearly the most dominant channel. Thus, in this first study, we have decided to construct an NJL model only with scalar-pseudoscalar channel. We have used the partially bosonized ansatz for the NJL model in the chiral limit which was evaluated on the mean-field level. In order to reproduce correct physical low-energy observables we have projected our results from QCD RG flows onto the model ansatz at $k = \Lambda_{\mathrm{NJL}} = 260$ MeV. Using our approach, we were able to calculate the corresponding starting value of the coupling $\bar{\lambda}_{\sigma,\mathrm{NJL}}(\Lambda_{\mathrm{NJL}})$ as function of T and μ. We have observed that the T- and μ-dependent $\bar{\lambda}_{\sigma,\mathrm{NJL}}(\Lambda_{\mathrm{NJL}})$ leads to smaller critical temperatures compared to the standard NJL procedure where $\bar{\lambda}_{\sigma,\mathrm{NJL}}(\Lambda_{\mathrm{NJL}})$ is assumed to be constant. This behavior reflects chiral symmetry restoration in QCD itself. Our numerical findings suggest that this effect is quite strong and should be taken into account in quantitative model studies. The observed UV cutoff of the model, $\Lambda_{\mathrm{NJL}} = 260$ MeV, is small compared to usual NJL calculations. The smallness of the UV cutoff also leads to a small critical temperature of the chiral phase transition compared to lattice QCD results. However, in our approach the particular value of the model UV cutoff is a direct consequence of the used input for the strong coupling. To show this, we have considered the zero-temperature coupling α computed in [122] and have repeated our analysis of the resulting model. This input was suitable to show that in the limit of $T \to 0$ and $\mu \to 0$ the resulting model has the UV cutoff $\Lambda_{\mathrm{NJL}} \sim 500 - 550$ MeV. These values are compatible with UV scales of common NJL calculations. Using the input from [122] for finite T and μ calculations we have observed again the effect of reduction of critical temperature due to the chiral symmetry restoration in QCD. We add that our approach seems to be not affected by Silver-Blaze problem.

We can conclude that the approach presented in this work can improve model calculations in many senses: First, it allows to estimate the relative strength of different channels allowed by Fierz ambiguity. Second, the initial values of model couplings at the UV scale of a model can be calculated as functions of temperature and chemical potential. This allows to take into account the effects of QCD at high energy scales which was completely ignored up to now. And last but not least, in the proposed approach there is only one set of model parameters which reproduces correct physical observables. Consequently, the ambiguity of the model parameter choice, which is present in the common model calculations, does not appear here. However, this set of model parameters depends strongly on the input for the strong coupling. Thus, improved RG flows calculations for the coupling

α as well as crosscheck against results from lattice QCD and Dyson-Schwinger formalism are needed. Further, for a quantitative check of our particular results one has to include the neglected interaction channels in the model ansatz. In addition, to go beyond the mean-field level posses a natural extension of our particular calculations since it would allow to study the effects of bosonic fluctuations. Moreover, the set of effective 4-quark interactions used in the present work is Fierz-complete only for $T \to 0$ and $\mu \to 0$. Considering finite temperature and chemical potential, new channels would appear, e.g., due to the presence of the heat bath. We will take into account these channels in the near-future works.

In summary, our findings concerning the locking of the chiral phase transition due to the confining dynamics at finite chemical potential and our approach to improve future model calculations will contribute fruitfully to the theoretical analysis of the QCD phase diagram and help to push our understanding of the QCD dynamics.

CONVENTIONS

A.1 UNITS

In this study we work with natural units commonly used in particle physics and cosmology:

$$\hbar = c = k_B = 1 \ , \tag{A.1}$$

where $\hbar$ is the reduced Planck constant, c the speed of light and k_B the Boltzmann constant. In this convention temperature is measured in the units of energy and length in the units of $\frac{1}{\text{energy}}$. The corresponding relations to the conventional SI units are given by:

$$1 \text{ m} \approx 5.1 \times 10^{12} \ \frac{1}{\text{MeV}} \qquad \text{and} \qquad 1 \text{ K} \approx 8.6 \times 10^{-11} \text{ MeV}. \tag{A.2}$$

Moreover, mass and momentum are also measured in the units of energy

$$1 \text{ kg} \approx 5.6 \times 10^{29} \text{ MeV} \qquad \text{and} \qquad 1 \text{ kg}\frac{\text{m}}{\text{s}} \approx 1.9 \times 10^{21} \text{ MeV}. \tag{A.3}$$

A.2 MINKOWSKI AND EUCLIDEAN SPACETIME

Throughout this study we work in four-dimensional Euclidean spacetime. It can be introduced starting with the Minkowski spacetime and applying following transformation:

$$x_{M,0} = -\mathrm{i}x_0 \ , \\ g_M^{\mu\nu} x_{M,\mu} x_{M,\nu} = x_{M,0}^2 - \vec{x}_M^2 = -x_0^2 - \vec{x}^2 = -g^{\mu\nu} x_\mu x_\nu = -x^2 \ . \tag{A.4}$$

The Minkowski metric in above equation is given by $g_M^{\mu\nu} = \mathrm{diag}(+,-,-,-)$ and the Euclidean metric by the Kronecker-delta, $g^{\mu\nu} = \delta^{\mu\nu}$.

A.3 FOURIER TRANSFORMATION

Applying Wetterich equation (3.28), we always use the momentum space. Our convention for Fourier transformation is given by:

$$\psi(x) = \int \frac{\mathrm{d}^4 p}{(2\pi)^4} \psi(p) \exp(\mathrm{i}p_\mu x_\mu) \ , \tag{A.5}$$

$$\bar{\psi}(x) = \int \frac{\mathrm{d}^4 p}{(2\pi)^4} \bar{\psi}(p) \exp(-\mathrm{i}p_\mu x_\mu) \ , \tag{A.6}$$

for fermionic fields and by:

$$\phi(x) = \int \frac{\mathrm{d}^4 p}{(2\pi)^4} \phi(p) \exp(\mathrm{i} p_\mu x_\mu) \; , \tag{A.7}$$

for bosonic fields. This choice of convention also implies that

$$\int \mathrm{d}^4 x \exp(-\mathrm{i} p_\mu x_\mu) = (2\pi)^4 \delta^4(p) \; . \tag{A.8}$$

Further, it leads to appearance of additional prefactor, $(2\pi)^4$, in the functional derivative of fields in momentum space:

$$\frac{\delta\phi(p)}{\delta\phi(q)} = (2\pi)^4 \delta^4(p-q) \; . \tag{A.9}$$

This is valid both for fermions and bosons.

DIRAC ALGEBRA AND FIERZ TRANSFORMATION

B.1 DIRAC ALGEBRA IN FOUR DIMENSIONS

Since we work in $4d$ Euclidean spacetime, we have to specify corresponding Dirac algebra which differs from those used in Minkowski space. Thus, the 4×4 Dirac matrices should satisfy following relations:

$$\{\gamma_\mu, \gamma_\nu\} = \gamma_\mu \gamma_\nu + \gamma_\nu \gamma_\mu = 2\delta_{\mu\nu} , \tag{B.1}$$

$$\gamma_\mu^\dagger = \gamma_\mu . \tag{B.2}$$

The fifth gamma matrix is defined as

$$\gamma_5 = \gamma_1 \gamma_2 \gamma_3 \gamma_0 , \tag{B.3}$$

and has usual properties:

$$\mathrm{tr}[\gamma_5] = 0 , \qquad \gamma_5^2 = \mathbb{1} , \qquad \{\gamma_5, \gamma_\mu\} = 0 . \tag{B.4}$$

We also need to specify the tensor $\sigma_{\mu\nu}$ which is given in the case of the Euclidean spacetime by

$$\sigma_{\mu\nu} = \frac{\mathrm{i}}{2}[\gamma_\mu, \gamma_\nu] = \frac{\mathrm{i}}{2}(\gamma_\mu \gamma_\nu - \gamma_\nu \gamma_\mu) . \tag{B.5}$$

The complete basis of the Dirac algebra is then given by sixteen elements $\gamma^{(A)}$:

$$\gamma^{(A)} = \left\{ \mathbb{1}, \gamma_\mu, \gamma_5, \mathrm{i}\gamma_\mu \gamma_5, \sigma_{01}, \sigma_{02}, \sigma_{03}, \sigma_{12}, \sigma_{13}, \sigma_{23} \right\} . \tag{B.6}$$

These elements obey

$$\mathrm{tr}[\gamma^{(A)} \gamma^{(B)}] = 4\delta_{AB} , \tag{B.7}$$

and the following completeness relation

$$\frac{1}{4} \sum_A \gamma_{ab}^{(A)} \gamma_{cd}^{(A)} = \delta_{ad}\delta_{bc} . \tag{B.8}$$

To understand where the ambiguity in representation of 4-fermion interactions comes from, we start with the generalized Fierz transformation which bases on the fact that any $d \times d$-matrix M can be expanded in terms of a complete orthonormal set of $d \times d$-matrices, $(O^1, \ldots, O^n)$:

$$M_{ab} = \sum_{j=1}^{n} O_{ab}^{(j)} \operatorname{tr}[O_j M] = \sum_{j=1}^{n} O_{ab}^{(j)} \sum_{cd} (O_{cd}^{(j)} M_{dc}^{(1)}) \ . \tag{B.9}$$

Rewriting the matrix M as a combination of two matrices $M_{ad} := M_{ab}^{(1)} M_{cd}^{(2)}$, we obtain for fixed b and c the following relation:

$$M_{ad} := M_{ab}^{(1)} M_{cd}^{(2)} = \sum_{j=1}^{n} O_{ad}^{(j)} \sum_{ef} (M_{ce}^{(2)} O_{ef}^{(j)} M_{fb}^{(1)}) \ . \tag{B.10}$$

Now, let us consider the particular case of the Dirac algebra which is spanned by elements $\gamma^{(A)}$ from Eq. (B.6). Applying the completeness relation from Eq. (B.8), we find:

$$M_{ab}^{(1)} M_{cd}^{(2)} = \frac{1}{4} \sum_{A} \gamma_{ad}^{A} \sum_{ef} (M_{ce}^{(2)} \gamma_{ef}^{(A)} M_{fb}^{(1)}) \ . \tag{B.11}$$

For further considerations we introduce the following notation:

$$O_{\mathrm{S}} = \mathbb{1} \ , \quad O_{\mathrm{V}} = \gamma_{\mu} \ , \quad O_{\mathrm{T}} = \frac{1}{\sqrt{2}} \sigma_{\mu\nu} \ , \quad O_{\mathrm{A}} = \gamma_{\mu} \gamma_5 \quad \text{and} \quad O_{\mathrm{P}} = \gamma_5 \ . \tag{B.12}$$

Now, we look at different combinations of 4-fermion channels $(\bar{\psi}_\alpha O_{\mathrm{X}} \psi_\beta)(\bar{\psi}_\gamma O_{\mathrm{X}} \psi_\delta)$ where Greek indices specify the quark species, i.e., color and flavor, and $\mathrm{X} = \mathrm{S, V, T, A, P}$. Applying transformation in Eq. (B.11) on the product $(O_{\mathrm{X}})_{ab}(O_{\mathrm{X}})_{cd}$ we find:

$$(\bar{\psi}_\alpha O_{\mathrm{X}} \psi_\beta)(\bar{\psi}_\gamma O_{\mathrm{X}} \psi_\delta) = \sum_{Y} C_{\mathrm{XY}} (\bar{\psi}_\alpha O_{\mathrm{Y}} \psi_\delta)(\bar{\psi}_\gamma O_{\mathrm{Y}} \psi_\beta) \ , \tag{B.13}$$

with

$$C_{\mathrm{XY}} = \frac{1}{4} \begin{pmatrix} -1 & -1 & -1 & 1 & -1 \\ -4 & 2 & 0 & 2 & 4 \\ -6 & 0 & 2 & 0 & -6 \\ 4 & 2 & 0 & 2 & -4 \\ -1 & 1 & -1 & -1 & -1 \end{pmatrix} \ . \tag{B.14}$$

Thus, the Fierz transformation can be seen as an algebraic reordering of fermionic fields which preserves the underlying symmetries of original channels.

To get feeling of how the Fierz ambiguity influences our understanding of 4-fermion interactions, let us provide a simple example. We consider a model at zero temperature with only one fermionic species and with interaction channel given by

$$(\bar{\psi} O_{\mathrm{S}} \psi)^2 - (\bar{\psi} O_{\mathrm{P}} \psi)^2 \ . \tag{B.15}$$

From Fierz transformation described above we find

$$(\bar{\psi} O_{\mathrm{S}} \psi)^2 - (\bar{\psi} O_{\mathrm{P}} \psi)^2 + \frac{1}{2}((\bar{\psi} O_{\mathrm{V}} \psi)^2 - (\bar{\psi} O_{\mathrm{A}} \psi)^2) = 0 \ , \tag{B.16}$$

so that the channel $(\bar{\psi}O_{\mathrm{V}}\psi)^2 - (\bar{\psi}O_{\mathrm{A}}\psi)^2$ can be completely transformed in $(\mathrm{S}-\mathrm{P})$-channel. As consequence this combination of vector and axial-vector channels can also contribute to the original $((\bar{\psi}O_{\mathrm{S}}\psi)^2 - (\bar{\psi}O_{\mathrm{P}}\psi)^2)$-channel. Therefore, even if we are mostly interested in the $(\mathrm{S}-\mathrm{P})$-channel, we also have to include the above combination of vector and axial-vector channels in the ansatz of our calculation.

<div style="text-align: right;">

C

</div>

SU(N) ALGEBRA

In this work we consider QCD with three colors and two flavors. In Chap. 5, in derivation of Eqs. (5.7)–(5.10) we actually keep the number of colors, N_c, and the number of flavors, N_f, arbitrary. The corresponding underlying group is SU(N) and is a group of unitary matrices U of rank N with determinant detU $= +1$. This group is generated by generators t^z with $z = 1, \ldots, N^2 - 1$ which obey following commutation relation:

$$[t^z, t^y] = t^z t^y - t^y t^z = \mathrm{i} f^{zyx} t^x \,, \tag{C.1}$$

with f^{zyx} the totally antisymmetric structure constants. The normalization condition for generators is

$$\mathrm{tr}\,[t^z t^y] = \frac{1}{2} \delta^{zy} \,. \tag{C.2}$$

Further, the contraction of two generators is proportional to identity and, therefore, is an invariant of the algebra. The corresponding proportionality factor is called quadratic Casimir operator, C_F, and is given by

$$t^z t^z = C_F \, \mathbb{1} = \frac{N^2 - 1}{2 N^2} \, \mathbb{1} \,. \tag{C.3}$$

Moreover, the generators fulfill two following (Fierz) completeness relations:

$$\sum_z (t^z)_{ab} (t^z)_{cd} = \frac{1}{2} \delta_{ad} \delta_{bc} - \frac{1}{2N} \delta_{ab} \delta_{cd} \,. \tag{C.4}$$

Here, the subspace spanned by the unity matrix is projected out since the generators are traceless. The second completeness relation reads to

$$\sum_z \{ (t^z)_{ab} (t^z)_{cd} + \frac{1}{N} (t^z)_{ad} (t^z)_{bc} \} = \frac{N^2 - 1}{2 N^2} \delta_{ad} \delta_{bc} \,. \tag{C.5}$$

In the case of SU(2), the generators t^z are basically given by the Pauli matrices, $t^z = \frac{1}{2} \tau^z$, in the case of SU(3) by the Gell-Mann matrices, $t^z = \frac{1}{2} \lambda^z$.

QUANTIZATION OF NON-ABELIAN GAUGE THEORIES

In this appendix, we discuss the quantization procedure for the classical QCD action in Eq. (2.13) using a method suggested by Faddeev and Popov. All the subtleties of quantization of QCD arise from the gauge sector, Eq. (2.11). Thus, we start with the pure Yang-Mills theory and consider the path integral:

$$Z = \int \mathcal{D}A_\mu \exp\left[-\int \mathrm{d}^4x \frac{1}{4}F_{\mu\nu}^z F_{\mu\nu}^z\right] = \int \mathcal{D}A_\mu \exp\left[-S_{\mathrm{YM}}\right] . \tag{D.1}$$

Now, one can see what kind of problem arises if one try to quantize Yang-Mills theory (or QCD): The above integral runs over all possible configurations of the gauge field. Consequently, all field configurations which are connected by means of a gauge transformation are repeatedly counted. These configurations cannot be distinct in the physical sense and the path integral in Eq. (D.1) loses any physical meaning. To overcome this problem, we can introduce the so-called orbits. This orbits include all gauge-field configurations which result by applying all possible gauge transformations to an arbitrarily chosen configuration. Thus, for all configurations inside an orbit the integrand in Eq. (D.1) is the same. Now, after the whole space of all gauge-field configurations is divided into orbits, we can pick up only one configuration from each orbit. Proceeding this way, the path integral runs only over physically distinct configurations and the generating functional Z becomes well-defined. The formal method to realize the above idea is known as the Faddeev-Popov trick. This trick includes an implementation of a gauge-fixing condition

$$\mathcal{F}^z[A_\mu] = 0 , \tag{D.2}$$

at each spacetime point by inserting the identity

$$1 = \int \mathcal{D}\Theta \, \delta\left(\mathcal{F}^z[A'_\mu]\right) \det\left(\frac{\delta\mathcal{F}^z[A'_\mu]}{\delta\Theta^y}\right) , \tag{D.3}$$

into the generating functional in Eq. (D.1). The prime denotes that the field A'_μ was obtained by applying the gauge transformation in Eq. (2.5) on the original field A_μ. Now, we have:

$$Z = \int \mathcal{D}\Theta \int \mathcal{D}A_\mu \exp\left[-S_{\mathrm{YM}}\right] \delta\left(\mathcal{F}^z[A'_\mu]\right) \det\left(\frac{\delta\mathcal{F}^z[A'_\mu]}{\delta\Theta^y}\right) . \tag{D.4}$$

The above path integral has some properties which make the calculations easier. First, as long as the gauge fixing condition $\mathcal{F}^z[A_\mu]$ is chosen to be linear, its functional derivative with respect to Θ^y is independent of Θ^y (see also the infinitesimal gauge transformation of the field A_μ^z in Eq. (2.6)). Second, the Yang-Mills action S_{YM} is invariant under the

gauge transformation $A_\mu \to A'_\mu$. On the other hand, since the gauge transformation contains basically a linear shift and a unitary rotation of various components of $A^z_\mu(x)$, the integration measures $\mathcal{D}A_\mu$ and $\mathcal{D}A'_\mu$ are absolutely the same. Thus, we can rewrite our partition function as

$$Z = N \int \mathcal{D}A_\mu \exp\left[-S_{\mathrm{YM}}\right] \delta\left(\mathcal{F}^z[A_\mu]\right) \det\left(\frac{\delta \mathcal{F}^z[A'_\mu]}{\delta \Theta^y}\right) . \tag{D.5}$$

Note that the integral over Θ is now factored out and results in a constant factor N which is not of relevance for calculation of the physical observables.

As next, we specify the gauge-fixing condition. We chose the generalized Lorentz gauge:

$$\mathcal{F}^z[A_\mu] = \partial_\mu A^z_\mu - \omega^a , \tag{D.6}$$

where ω^a is an arbitrary function. Since our result in Eq. (D.5) is independent of the choice of ω^a, we can integrate over the whole space of functions ω^a and weight each of them by, e.g., a Gaussian weighting function. This procedure also requires a properly chosen normalization constant which depends on the weighting function we use. However, since the constant prefactors in the partition function do not influence the results for physical observables, we don't have to specify the normalization constant.

$$Z = N(\xi) \int \mathcal{D}\omega \exp\left[-\int \mathrm{d}^4x \frac{(\omega^a)^2}{2\xi}\right] \times$$
$$\int \mathcal{D}A_\mu \exp\left[-S_{\mathrm{YM}}\right] \delta\left(\partial_\mu A^z_\mu - \omega^a\right) \det\left(\frac{\delta \mathcal{F}^z[A'_\mu]}{\delta \Theta^y}\right) . \tag{D.7}$$

The constant factor N obtained previously is included in $N(\xi)$. Performing integration over ω, we find

$$Z = N(\xi) \int \mathcal{D}A_\mu \exp\left[-S_{\mathrm{YM}}\right] \exp\left[-\int \mathrm{d}^4x \frac{(\partial_\mu A^z_\mu)^2}{2\xi}\right] \det\left(\frac{\delta \mathcal{F}^z[A'_\mu]}{\delta \Theta^y}\right) . \tag{D.8}$$

Now, let us calculate the determinant. Using the gauge-fixing condition in Eq. (D.6) and the infinitesimal gauge transformation of the field A^z_μ in Eq. (2.6), we can write the determinant as

$$\det\left(\frac{\delta \mathcal{F}^z[A'_\mu]}{\delta \Theta^y}\right) = \det\left(\frac{1}{\bar{g}}\delta^{zy}\partial^2 + f^{zxy}\partial_\mu A^x_\mu\right) . \tag{D.9}$$

one should have noticed that this result is not independent of the gauge field and, thus, cannot be factored out. However, to absorb the determinant into the Lagrangian, we can rewrite it as

$$\det\left(\frac{\delta \mathcal{F}^z[A'_\mu]}{\delta \Theta^y}\right) = N' \int \mathcal{D}\bar{c}\mathcal{D}c \exp\left[-\int \mathrm{d}^4x\, \bar{c}^z \left(\delta^{zy}\partial^2 + \bar{g}f^{zxy}\partial_\mu A^x_\mu\right)c^y\right] . \tag{D.10}$$

To obtain the above path-integral representation of determinant, we have introduced new fields $\bar{c}$ and c^1. Thereby, we have used the rules for fermionic functional integrals and, thus, $\bar{c}$ and c are anticommuting fields. On the other hand, the above expression shows

---

1 We have also absorbed the factor $1/\bar{g}$ into the normalization of the fields $\bar{c}$ and c

that $\bar{c}$ and c have to behave as scalars under the Lorentz transformation. Therefore, these so-called Faddeev-Popov ghosts are not physical and cannot appear as external lines in Feynman diagrams. However, they do appear in the loops.

Now, we are able to write the quantized version of the classical QCD action in Eq. (2.13). The corresponding Lagrangian includes the matter sector contribution $\mathcal{L}_{\text{Matter}}$, which is not affected by Faddeev-Popov trick described above, the Yang-Mills part $\mathcal{L}_{\text{YM}}$, the gauge fixing term $\mathcal{L}_{\text{GF}}$ and the ghost term $\mathcal{L}_{\text{Ghost}}$:

$$
\begin{aligned}
\mathcal{L} &= \mathcal{L}_{\text{Matter}} + \mathcal{L}_{\text{YM}} + \mathcal{L}_{\text{GF}} + \mathcal{L}_{\text{Ghost}} \\
&= \mathrm{i}\bar{\psi}(\slashed{D} + m)\psi + \frac{1}{4}F^z_{\mu\nu}F^z_{\mu\nu} + \frac{1}{2\xi}(\partial_\mu A^z_\mu)^2 + \bar{c}^z\left(\delta^{zy}\,\partial^2 + \bar{g}f^{zxy}\,\partial_\mu A^x_\mu\right)c^y \ .
\end{aligned}
\tag{D.11}
$$

With this Lagrangian it is possible to calculate observables of QCD. However, to perform such calculations one first has to fix the gauge parameter ξ. Throughout this work, we have used the so-called Landau gauge given by $\xi = 0$.

THRESHOLD FUNCTIONS

E.1 REGULATOR FUNCTIONS

Throughout this study we use the linear form of the cutoff functions. Since we investigate finite temperatures, we consider the $3d$ case:

$$
\begin{aligned}
R_k^\psi(\vec{p}^2) &= Z_\psi \vec{\slashed{p}}\, r_{\mathrm{F}}(\vec{p}^2/k^2) \ , \\
R_k^\varphi(\vec{p}^2) &= Z_\varphi \vec{p}^2 r_{\mathrm{B}}(\vec{p}^2/k^2) \ , \\
R_{k,zy}^{\mathrm{A},\mu\nu}(\vec{p}^2) &= Z_{\mathrm{A}} \vec{p}^2 r_{\mathrm{B}}(\vec{p}^2/k^2)(P_{\perp,zy}^{\mu\nu} + \frac{1}{\xi}P_{\|,zy}^{\mu\nu}) \ .
\end{aligned}
\tag{E.1}
$$

The first line represents the cut-off function for fermions in all our calculations, the second for bosons in quark-meson model and the third for gluons in QCD RG flows. In the last case, we have to consider longitudinal and transverse projections:

$$
P_{\|,zy}^{\mu\nu} = \frac{p^\mu p^\nu}{p^2}\delta^{zy}, \qquad P_{\perp,zy}^{\mu\nu} = \delta^{\mu\nu}\delta^{zy} - P_{\|,zy}^{\mu\nu} \ .
\tag{E.2}
$$

Note that in Landau gauge $\xi = 0$ and only the transverse projection survives. For regulator shapes $r_{\mathrm{F/B}}(y)$ we use optimized regulators [157]:

$$
\begin{aligned}
r_{\mathrm{F}}(y) &= \Big(\frac{1}{\sqrt{y}} - 1\Big)\Theta(1 - y) \ , \\
r_{\mathrm{B}}(y) &= \Big(\frac{1}{y} - 1\Big)\Theta(1 - y) \ .
\end{aligned}
\tag{E.3}
$$

E.2 THRESHOLD FUNCTIONS

All purely fermionic and purely bosonic threshold functions for $3d$ linear cut-off functions can by calculated by following prescription: first we define zero-threshold functions

$$
l_0^{(\mathrm{F})}(\tau, \tilde{\mu}, \omega) = \frac{v_3}{v_4}\tau \sum_n \int_0^\infty \mathrm{d}y\ y^{3/2}\frac{(\partial_t r_\psi(y))(1 + r_\psi(y))}{(\tilde{\nu}_n + \mathrm{i}\tilde{\mu})^2 + y(1 + r_\psi(y))^2 + \omega} \ ,
\tag{E.4}
$$

$$
l_0^{(\mathrm{B})}(\tau, \omega) = \frac{v_3}{v_4}\frac{\tau}{2}\sum_n \int_0^\infty \mathrm{d}y\ y^{3/2}\frac{\partial_t r_{\mathrm{B}}(y)}{\tilde{\omega}_n^2 + y(1 + r_{\mathrm{B}}(y)) + \omega} \ ,
\tag{E.5}
$$

where $\tilde{\nu}_n = (2n + 1)\pi\tau$ and $\tilde{\omega}_n = 2n\pi\tau$ represent the femionic and bosonic Matsubara frequencies correspondingly, $\tau = T/k$ and $\tilde{\mu} = \mu/k$ are the dimensionless temperature

and the dimensionless quark chemical potential, and y is defined as $y = \vec{p}^2/k^2$. The dimensional factors v_3 and v_4 can be calculated using:

$$v_d^{-1} = 2^{d+1}\pi^{d/2}\Gamma\left(\frac{d}{2}\right) . \tag{E.6}$$

At this point, we should mention that in our calculations we always assume that the wave-function renormalization of fermions, Z_ψ, and of bosons in quark-meson model, Z_φ, are constant. If one takes the running of Z_ψ and Z_φ into account, the threshold functions $l_0^{(\mathrm{F})}$ and $l_0^{(\mathrm{B})}$ have additional terms proportional to $\eta_\psi = -(\partial_t Z_\psi)/Z_\psi$ and to $\eta_\varphi = -(\partial_t Z_\varphi)/Z_\varphi$ correspondingly.

All higher threshold functions can be calculated by taking derivatives with respect to the mass parameter ω:

$$\frac{\partial}{\partial\omega}l_n^{(\mathrm{F})}(\tau,\tilde{\mu},\omega) = -(n+\delta_{n,0})l_{n+1}^{(\mathrm{F})}(\tau,\tilde{\mu},\omega) ,$$
$$\frac{\partial}{\partial\omega}l_n^{(\mathrm{B})}(\tau,\omega) = -(n+\delta_{n,0})l_{n+1}^{(\mathrm{B})}(\tau,\omega) . \tag{E.7}$$

For the optimized regulator shape [157] we obtain following zero threshold functions:

$$l_0^{(\mathrm{F})}(\tau,\tilde{\mu},\omega) = \frac{v_3}{v_4}\frac{1}{6}\frac{\tanh\left[\frac{\sqrt{1+\omega}-\tilde{\mu}}{2\tau}\right] + \tanh\left[\frac{\sqrt{1+\omega}+\tilde{\mu}}{2\tau}\right]}{\sqrt{1+\omega}} ,$$

$$l_0^{(\mathrm{B})}(\tau,\omega) = \frac{v_3}{v_4}\frac{1}{3}\frac{\coth\left[\frac{\sqrt{1+\omega}}{2\tau}\right]}{\sqrt{1+\omega}} , \tag{E.8}$$

and all higher threshold functions are obtained using prescription described above. In our calculations only the following pure fermionic/bosonic functions appear: $l_1^{(\mathrm{F})}$, $l_2^{(\mathrm{F})}$, $l_1^{(\mathrm{B})}$, $l_2^{(\mathrm{B})}$. The limiting behavior of these threshold functions is:

$$\lim_{\tau\to 0}l_1^{(\mathrm{F})}(\tau,0,0) = \lim_{\tau\to 0}l_1^{(\mathrm{B})}(\tau,0) = \frac{1}{6}\frac{v_3}{v_4} ,$$

$$\lim_{\tau\to 0}l_2^{(\mathrm{F})}(\tau,0,0) = \lim_{\tau\to 0}l_2^{(\mathrm{B})}(\tau,0) = \frac{1}{4}\frac{v_3}{v_4} . \tag{E.9}$$

In the flows of the effective 4-fermion couplings in QCD and in the flow of the Yukawa coupling in quark-meson model we have additional threshold functions of the form $l_{n_1,n_2}^{(\mathrm{FB})}(\tau,\tilde{\mu},\omega_1,\omega_2)$. They can be calculated using the following formula:

$$l_{n_1,n_2}^{(\mathrm{FB})}(\tau,\tilde{\mu},\omega_1,\omega_2) = \frac{v_3}{v_4}\tau\sum_n\int\limits_0^\infty dy\, y^{3/2}\frac{1}{[(\tilde{\nu}_n+i\tilde{\mu})^2 + y(1+r_\psi(y))^2 + \omega_1]^{n_1}}$$

$$\cdot\frac{1}{[\tilde{\omega}_n^2 + y(1+r_\mathrm{B}(y)) + \omega_2]^{n_2}}\left(n_1\frac{\partial_t r_\psi(y)(1+r_\psi(y))}{(\tilde{\nu}_n+i\tilde{\mu})^2 + y(1+r_\psi(y))^2 + \omega_1}\right.$$

$$\left.+\frac{n_2}{2}\frac{(\partial_t r_\mathrm{B}(y) - \eta_A r_\mathrm{B}(y))}{\tilde{\omega}_n^2 + y_\mathrm{B}(1+r_\mathrm{B}(y)) + \omega_2}\right) . \tag{E.10}$$

In the case of the running Yukawa coupling, η_A is replaced by η_φ. Since we assume that $Z_\varphi = 1$, the term proportional to η_φ disappears in this case. Further, $\omega_1 = m_q^2$, and ω_2 is

given either by the mass parameter m^2 in the chirally symmetric regime or by the masses of Goldstone bosons in the chirally broken phase: $\omega_2 = m_\sigma^2$ or $\omega_2 = m_\pi^2$.

In our QCD calculations $\eta_A = \eta_{A,k}^{\text{gluons}}$ is finite. It is equal to $\eta_{A,k}^{\text{YM}}$ for the strong-coupling input discussed in Sec. 5.3. In Sec. 5.7 we use two different approximations for $\eta_{A,k}^{\text{gluons}}$, namely, $\eta_{A,k}^{\text{gluons}} = 0$ and $\eta_{A,k}^{\text{gluons}} = (\partial_t \alpha)/\alpha$. In the case of QCD flows, the parameters ω_1 and ω_2 are both zero since we consider the chiral limit $\omega_1 = m_q^2 \to 0$ and gluons have no mass.

In particular, we should calculate functions $l_{1,1}^{(\text{FB})}$ and $l_{1,2}^{(\text{FB})}$. The analytical expressions for these functions are lengthy and we do not present them here. However, they can be calculated from Eq. (E.10) in a straight-forward way. Here, we only give the limiting behavior for these threshold functions:

$$
\begin{aligned}
\lim_{\tau \to 0} l_{1,1}^{(\text{FB})}(\tau, 0, 0, 0) &= \frac{v_3}{v_4} \left(\frac{1}{4} - \frac{\eta_A}{40} \right) , \\
\lim_{\tau \to 0} l_{1,2}^{(\text{FB})}(\tau, 0, 0, 0) &= \frac{v_3}{v_4} \left(\frac{5}{16} - \frac{\eta_A}{24} \right) .
\end{aligned}
\tag{E.11}
$$

E.3 THRESHOLD FUNCTIONS IN THE ZERO-TEMPERATURE LIMIT

In our calculations with QCD RG flows we have observed that our results do not exhibit the Silver-Blaze problem. One of the reasons for this observation is that the threshold functions $l_1^{(\text{F})}$, $l_{1,1}^{(\text{FB})}$ and $l_{1,2}^{(\text{FB})}$, which appear in the fermionic flows, show no or only a weak dependence on the chemical potential μ in the limit $T \to 0$. In this section, we will justify this statement.

Let us start with function $l_1^{(\text{F})}$:

$$
l_1^{(\text{F})}(\tau, \tilde{\mu}, 0) = -\frac{v_3}{v_4} \frac{\cosh\left[\frac{1+\tilde{\mu}}{2\tau}\right]^{-2} + \cosh\left[\frac{1-\tilde{\mu}}{2\tau}\right]^{-2} - 2\tau \left(\tanh\left[\frac{1-\tilde{\mu}}{2\tau}\right] + \tanh\left[\frac{1+\tilde{\mu}}{2\tau}\right]\right)}{24\tau} .
\tag{E.12}
$$

In the limit $\tau \to 0$, the terms proportional to $\cosh\left[\frac{1\pm\tilde{\mu}}{2\tau}\right]^{-2} \tau^{-1}$ are clearly zero. The limiting behavior of the sum of terms proportional to hyperbolic tangent depends on whether $k > \mu$ or $k < \mu$ and, therefore

$$
\lim_{\tau \to 0} l_1^{(\text{F})}(\tau, \tilde{\mu}, 0) = \frac{1}{6} \frac{v_3}{v_4} \Theta(1 - \tilde{\mu}) .
\tag{E.13}
$$

In our numerical calculations with QCD RG flows we always work in the regime with $k > \mu$ and, therefore, we obtain the limiting behavior which is also valid in the limit $T \to 0$, $\mu \to 0$, Eq. (E.9). Hence, the threshold functions $l_1^{(\text{F})}$ is $\tilde{\mu}$-independent in the limit $\tau \to 0$.

The explicit expressions for functions $l_{1,1}^{(\text{FB})}$ and $l_{1,2}^{(\text{FB})}$ are quite lengthy. So, we present here only the results for the limit $\tau \to 0$. Thereby, we have to consider two different cases: $k > \mu$ and $k < \mu$. The corresponding behavior of function $l_{1,1}^{(\text{FB})}$ is given by:

$$
\lim_{\tau \to 0} l_{1,1}^{(\text{FB})}(\tau, \tilde{\mu}, 0, 0) = \frac{v_3}{v_4} \left(l_{1,1}^{(\text{FB}),1}(\tilde{\mu}) - \frac{\eta_A}{5} l_{1,1}^{(\text{FB}),2}(\tilde{\mu}) \right) ,
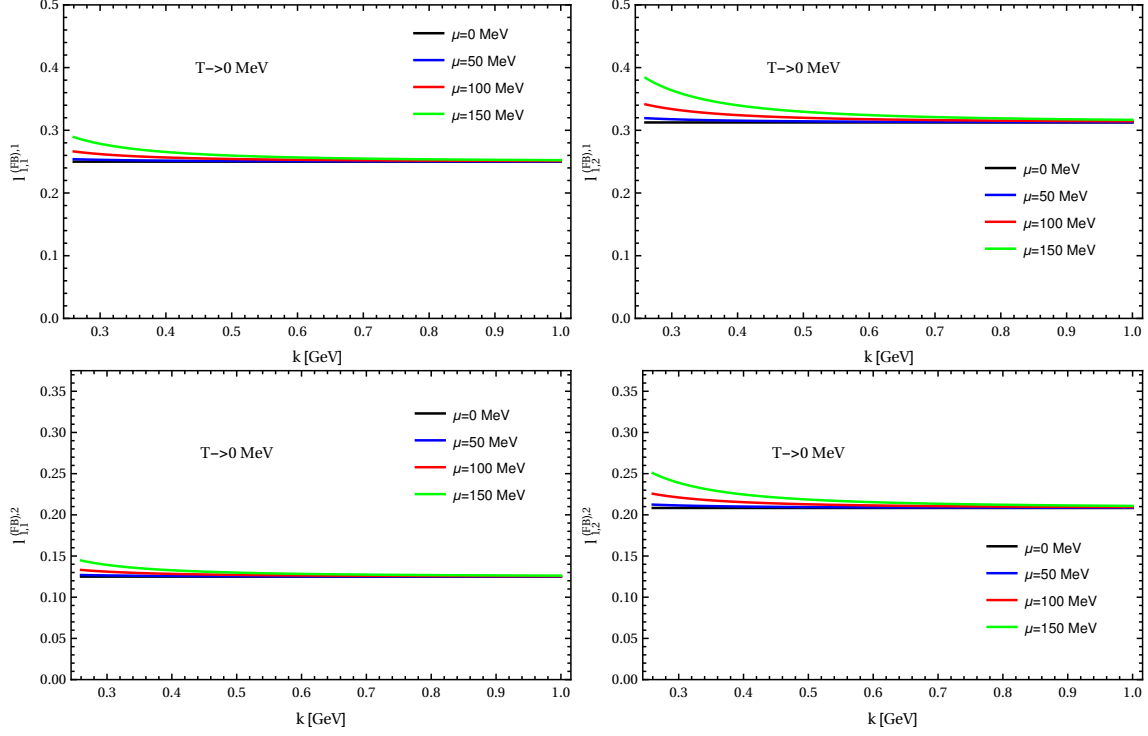\tag{E.14}
$$

FIGURE E.1: In this plot we consider $l_{1,1}^{(\text{FB}),1}$, $l_{1,1}^{(\text{FB}),2}$ (first column) and $l_{1,2}^{(\text{FB}),1}$, $l_{1,2}^{(\text{FB}),2}$ (second column) as functions of k for different values of μ. We always consider the case $k > \mu$. We observe a rather weak dependence on the chemical potential.

with

$$l_{1,1}^{(\text{FB}),1}(\tilde{\mu}) = \begin{cases} \frac{12-\tilde{\mu}^2}{3(\tilde{\mu}^2-4)^2} & \text{for } \mu < k \ , \\ -\frac{4+\tilde{\mu}^2}{6\tilde{\mu}(2+\tilde{\mu}^2)^2} & \text{for } \mu > k \ , \end{cases} \tag{E.15}$$

and

$$l_{1,1}^{(\text{FB}),2}(\tilde{\mu}) = \begin{cases} \frac{12-\tilde{\mu}^2}{6(\tilde{\mu}^2-4)^2} & \text{for } \mu < k \ , \\ -\frac{2+4\tilde{\mu}+\tilde{\mu}^2}{6\tilde{\mu}^2(2+\tilde{\mu})^2} & \text{for } \mu > k \ . \end{cases} \tag{E.16}$$

For $l_{1,2}^{(\text{FB})}$, we find:

$$\lim_{\tau \to 0} l_{1,2}^{(\text{FB})}(\tau, \tilde{\mu}, 0, 0) = \frac{v_3}{v_4} \left(l_{1,2}^{(\text{FB}),1}(\tilde{\mu}) - \frac{\eta_A}{5} l_{1,2}^{(\text{FB}),2}(\tilde{\mu}) \right) \ , \tag{E.17}$$

with

$$l_{1,2}^{(\text{FB}),1}(\tilde{\mu}) = \begin{cases} \frac{240-40\tilde{\mu}^2+3\tilde{\mu}^4}{12(4-\tilde{\mu}^2)^3} & \text{for } \mu < k \ , \\ -\frac{12+34\tilde{\mu}+18\tilde{\mu}^2+3\tilde{\mu}^3}{12\tilde{\mu}^2(2+\tilde{\mu})^3} & \text{for } \mu > k \ , \end{cases} \tag{E.18}$$

and

$$l_{1,2}^{(\text{FB}),2}(\tilde{\mu}) = \begin{cases} \frac{160-36\tilde{\mu}^2+3\tilde{\mu}^4}{12(4-\tilde{\mu}^2)^3} & \text{for } \mu < k \ , \\ -\frac{8+24\tilde{\mu}+36\tilde{\mu}^2+18\tilde{\mu}^3+3\tilde{\mu}^4}{12\tilde{\mu}^3(2+\tilde{\mu})^3} & \text{for } \mu > k \ . \end{cases} \tag{E.19}$$

From this expressions one can already see that the threshold functions $l_{1,1}^{(\mathrm{FB})}$ and $l_{1,2}^{(\mathrm{FB})}$ have rather weak μ-dependence. To visualize it, we plot $l_{1,1}^{(\mathrm{FB}),1}$, $l_{1,1}^{(\mathrm{FB}),2}$, $l_{1,2}^{(\mathrm{FB}),1}$ and $l_{1,2}^{(\mathrm{FB}),2}$ as functions of k for different values of μ, see Fig. E.1. Thereby, we always consider $k > \mu$ since it is the relevant case for our numerical calculations with QCD RG flows. In the first column we present our results for functions corresponding to $l_{1,1}^{(\mathrm{FB})}$, in the second column results corresponding to $l_{1,2}^{(\mathrm{FB})}$. We indeed observe that the μ-dependence of the threshold functions seems to be negligible. Only for large μ and small k, there are some finite-μ effects. However, these effects are still small and can contribute to the RG flow only at rather narrow scale interval.

As a concluding remark, we want to mention that in this study η_A has no μ-dependence: For calculations with the strong coupling from Sec. 5.3, we use $\eta_A = \eta_{A,k}^{\mathrm{YM}}$ and the results from the pure Yang-Mills theory cannot depend on μ per definition. The strong coupling from Sec. 5.7 was obtained only in the limit $T \to 0$, $\mu \to 0$.
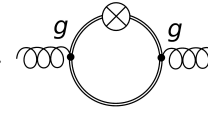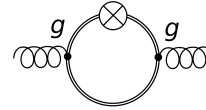
VACUUM POLARIZATION $\Delta\eta_{A,k}$

In this section we present some details of the calculation of $\Delta\eta_{A,k}$ which we have already defined in Eq. (5.17):

$$\Delta\eta_{A,k} = \frac{Z_{A,k}^{-1}}{3\,(N_c^2-1)}\left(\frac{\partial}{\partial p^2}P_\perp^{\mu\nu}(p)\cdot \text{⟨diagram⟩}\right)\Bigg|_{p=0} . \tag{F.1}$$

Here, p is the modulus of the external momentum and $P_\perp^{\mu\nu}(p)$ is the transversal projection operator defined in Appendix E. The three in the denominator is the number of spatial dimensions and corresponds to the normalization of the projection operator. $N_c = 3$ is, as usual, the number of colors. The graphical representation in the above equation corresponds to the expression:

$$\text{⟨diagram⟩} = \frac{-\delta^{xy}}{(2\pi)^4\delta(0)}\frac{\overrightarrow{\delta}}{\delta A_\mu^x(-p)}\left[\frac{1}{2}\text{STr}\frac{\partial R_k}{\Gamma_k^{(2)}+R_k}\right]\frac{\overleftarrow{\delta}}{\delta A_\nu^y(p)} , \tag{F.2}$$

where $\Gamma_k^{(2)}$ is the second derivative of the scale-dependent effective action with respect to the fermionic fields. To evaluate this quantity, we can use the expanded version of the Wetterich equation, Eq. (3.31). Thereby, the relevant term is

$$-\frac{1}{4}\text{STr}\left[\tilde{\partial}_k\left(\frac{\mathcal{F}_k}{\mathcal{P}_k}\right)^2\right] .$$

Since we are working at finite temperatures, we replace the $4d$ momentum projection by the projection onto the spatial momentum.

$$\frac{\partial}{\partial p^2} \quad \Rightarrow \quad \frac{\partial}{\partial\vec{p}^2} = \frac{1}{2}\frac{\partial^2}{\partial|\vec{p}|^2} . \tag{F.3}$$

Applying these prescriptions, we find

$$\begin{aligned}
\Delta\eta_{A,k} = \frac{N_f}{3}\,g^2 T\sum_n\sum_\pm\int\frac{\mathrm{d}^3 q}{(2\pi)^3}\frac{1}{2}\frac{\partial^2}{\partial|\vec{p}|^2}\tilde{\partial}_t\,[\,(\nu_n+i\mu)^2 \\
+(1+r_\psi(x))(1+r_\psi(x\pm y))\vec{q}^{\,2} \\
\pm 3(1+r_\psi(x))(1+r_\psi(x\pm y))|\vec{q}||\vec{p}|\cos\Theta \\
+2(1+r_\psi(x))(1+r_\psi(x\pm y))\vec{q}^{\,2}\cos^2\Theta] \\
\times[((\nu_n+i\mu)^2+(1+r_\psi(x))^2\vec{q}^{\,2})((\nu_n+i\mu)^2 \\
+(1+r_\psi(x\pm y))^2(\vec{q}^{\,2}+\vec{p}^{\,2}\pm 2|\vec{q}||\vec{p}|\cos\Theta))]^{-1}\,|_{|\vec{p}|=0} ,
\end{aligned} \tag{F.4}$$

where $\vec{q}$ is the momentum in the loop, $x = \vec{q}^{\,2}/k^2$, $y = \vec{p}^{\,2}/k^2$ and Θ the angle between vectors $\vec{q}$ and $\vec{p}$. The operator $\tilde{\partial}_t$ acts only on r_ψ and there is a sum over different signs. In the above equation we have already set the gluonic Matsubara frequencies ω_n to zero since we evaluate the vacuum polarization at $p = 0$.

Further calculations include application of the operator $\tilde{\partial}_t$, expansion in the modulus of the external spatial momentum $|\vec{p}|$, integration over the internal momentum $\vec{q}$ and summation over different signs. These calculations are quite lengthy but basically straightforward. The only one difficulty is that in these calculations the terms of the form $\Theta(y)\delta(y)$ appear in the limit of $|\vec{p}| \to 0$. They are not well defined since the Θ-function is not defined exactly at the point where δ-function has its support. To avoid this problem, we can introduce the smeared versions of these functions:

$$\lim_{\epsilon \to 0} \Theta_\epsilon(x) = \Theta(x) \ ,$$
$$\delta_\epsilon(x) = \partial_x \Theta_\epsilon(x) \ . \tag{F.5}$$

Now, we are allowed to exchange the $|\vec{p}| \to 0$ and $\epsilon \to 0$ limits and the problematic terms become $\lim_{\epsilon \to 0} \Theta_\epsilon(x)\delta_\epsilon(x)$. They are still not well defined but now we can use the following trick, see, e.g., Refs. [185, 186]:

$$\lim_{\epsilon \to 0} f\left(x, \Theta_\epsilon(x)\right)\delta_\epsilon(x) = \delta(x) \int_0^1 \mathrm{d}u f(0, u) \ . \tag{F.6}$$

Using this trick, we obtain for $N_\mathrm{f} = 2$ the result which we have already presented in Eq. (5.18)

$$\Delta\eta_{A,k}(T,\mu) = -\frac{g^2}{45\pi^2}\tau \sum_n \frac{33(\tilde{\nu}_n + \mathrm{i}\tilde{\mu})^4 + 2(\tilde{\nu}_n + \mathrm{i}\tilde{\mu})^2 - 55}{((\tilde{\nu}_n + \mathrm{i}\tilde{\mu})^2 + 1)^4} \ , \tag{F.7}$$

with $\tau = T/k$, $\tilde{\mu} = \mu/k$ and $\tilde{\nu}_n = (2n+1)\pi\tau$ the fermionic Matsubara frequencies. Performing Matsubara sum, we end with the following expression for the vacuum polarization:

$$\begin{aligned}
\Delta\eta_{A,k}(T,\mu) = \frac{g^2}{1440\pi^2\tau^3} \Bigg\{ & \frac{1}{\cosh\left[\frac{1-\tilde{\mu}}{2\tau}\right]^4} + \frac{1}{\cosh\left[\frac{1+\tilde{\mu}}{2\tau}\right]^4} \\
& - 4\frac{\tau}{\cosh\left[\frac{1-\tilde{\mu}}{2\tau}\right]^2}\left(15\tau + 11\tanh\left[\frac{1-\tilde{\mu}}{2\tau}\right]\right) \\
& - 4\frac{\tau}{\cosh\left[\frac{1+\tilde{\mu}}{2\tau}\right]^2}\left(15\tau + 11\tanh\left[\frac{1+\tilde{\mu}}{2\tau}\right]\right) \\
& - 32\left(\frac{\sinh\left[\frac{1-\tilde{\mu}}{2\tau}\right]^6}{\sinh\left[\frac{1-\tilde{\mu}}{\tau}\right]^4} + \frac{\sinh\left[\frac{1+\tilde{\mu}}{2\tau}\right]^6}{\sinh\left[\frac{1+\tilde{\mu}}{\tau}\right]^4}\right. \\
& \left.\left. - \frac{15}{4}\tau^3\left(\tanh\left[\frac{1-\tilde{\mu}}{2\tau}\right] + \tanh\left[\frac{1+\tilde{\mu}}{2\tau}\right]\right)\right)\right\} \ .
\end{aligned} \tag{F.8}$$

Using this result, it is easy to see how $\Delta\eta_{A,k}(T,\mu)$ behaves in the limit $T \to 0$. One see immediately that all term, except of the last two hyperbolic tangents, vanish for $T \to 0$.

The remaining terms amount to $g^2/(6\pi^2)$ for $k > \mu$ and to zero for $k < \mu$. Therefore, in the limit of vanishing temperature we obtain Eq. (5.20)

$$\Delta\eta_{A,k}(T,\mu)|_{\frac{T}{k}\to 0} = \frac{g^2}{6\pi^2}\Theta(k-\mu) \; . \tag{F.9}$$

This result is crucial for the fact that in our calculations no Silver-Blaze problem appears: Since in our calculations with QCD RG flows we are always working in the regime $k > \mu$, $\Delta\eta_{A,k}(T,\mu)$ is simply a constant as function of μ for $T \to 0$. This observation and the behavior of the threshold functions in this limit, see App. E.3, leads to the fact that our results do not depend on μ for $T \to 0$.

[1] H. Fritzsch, M. Gell-Mann, and H. Leutwyler, "Advantages of the Color Octet Gluon Picture," *Phys. Lett.* **B47** (1973) 365–368.

[2] Y. Nambu, "Strings, Monopoles and Gauge Fields," *Phys. Rev.* **D10** (1974) 4262.

[3] W. A. Bardeen and R. B. Pearson, "Local Gauge Invariance and the Bound State Nature of Hadrons," *Phys. Rev.* **D14** (1976) 547.

[4] O. W. Greenberg and C. A. Nelson, "Color Models of Hadrons," *Phys. Rept.* **32** (1977) 69–121.

[5] V. N. Gribov, "Quantization of Nonabelian Gauge Theories," *Nucl. Phys.* **B139** (1978) 1.

[6] J. B. Kogut and L. Susskind, "Vacuum Polarization and the Absence of Free Quarks in Four-Dimensions," *Phys. Rev.* **D9** (1974) 3501–3512.

[7] D. Zwanziger, "Renormalization in the Coulomb gauge and order parameter for confinement in QCD," *Nucl. Phys.* **B518** (1998) 237–272.

[8] R. Alkofer and J. Greensite, "Quark Confinement: The Hard Problem of Hadron Physics," *J. Phys.* **G34** (2007) S3, `arXiv:hep-ph/0610365 [hep-ph]`.

[9] J. Greensite, "An introduction to the confinement problem," *Lect. Notes Phys.* **821** (2011) 1–211.

[10] **Particle Data Group** Collaboration, K. A. Olive *et al.*, "Review of Particle Physics," *Chin. Phys.* **C38** (2014) 090001.

[11] J. Goldstone, A. Salam, and S. Weinberg, "Broken Symmetries," *Phys. Rev.* **127** (1962) 965–970.

[12] S. Weinberg, *The quantum theory of fields. Vol. 2: Modern applications.* Cambridge University Press, 2013.

[13] D. J. Gross and F. Wilczek, "Ultraviolet Behavior of Nonabelian Gauge Theories," *Phys. Rev. Lett.* **30** (1973) 1343–1346.

[14] H. D. Politzer, "Reliable Perturbative Results for Strong Interactions?," *Phys. Rev. Lett.* **30** (1973) 1346–1349.

[15] S. R. Coleman and D. J. Gross, "Price of asymptotic freedom," *Phys. Rev. Lett.* **31** (1973) 851–854.

[16] M. E. Peskin and D. V. Schroeder, *An Introduction to quantum field theory.* Addison-Wesley, Reading, USA, 1995. `http://www.slac.stanford.edu/spires/find/books/www?cl=QC174.45%3AP4`.

[17] I. Montvay and G. Munster, *Quantum fields on a lattice.* Cambridge University Press, 1997. http://www.cambridge.org/uk/catalogue/catalogue.asp?isbn=0521404320.

[18] W. Greiner, S. Schramm, and E. Stein, *Quantum chromodynamics.* Springer, Berlin, 2002.

[19] G. Ecker, "Effective field theories," arXiv:hep-ph/0507056 [hep-ph].

[20] C. P. Burgess, "Introduction to Effective Field Theory," *Ann. Rev. Nucl. Part. Sci.* **57** (2007) 329–362, arXiv:hep-th/0701053 [hep-th].

[21] V. Bernard, N. Kaiser, and U.-G. Meissner, "Chiral dynamics in nucleons and nuclei," *Int. J. Mod. Phys.* **E4** (1995) 193–346, arXiv:hep-ph/9501384 [hep-ph].

[22] S. Scherer and M. R. Schindler, *A primer for chiral perturbation theory.* Springer, Berlin, 2011.

[23] B. Grinstein, "Light Quark, Heavy Quark Systems: An Update," in *B physics at hadron accelerators. Proceedings, Workshop, Snowmass, USA, 1993*, pp. 109–120. 1993. arXiv:hep-ph/9310362 [hep-ph]. http://lss.fnal.gov/cgi-bin/find_paper.pl?other/ssc/sscl-preprint-514.

[24] N. Brambilla, A. Pineda, J. Soto, and A. Vairo, "Effective field theories for heavy quarkonium," *Rev. Mod. Phys.* **77** (2005) 1423, arXiv:hep-ph/0410047 [hep-ph].

[25] J. Braun, L. M. Haas, F. Marhauser, and J. M. Pawlowski, "Phase Structure of Two-Flavor QCD at Finite Chemical Potential," *Phys. Rev. Lett.* **106** (2011) 022002, arXiv:0908.0008 [hep-ph].

[26] J. M. Pawlowski, "The QCD phase diagram: Results and challenges," *AIP Conf. Proc.* **1343** (2011) 75–80, arXiv:1012.5075 [hep-ph].

[27] B.-J. Schaefer, J. M. Pawlowski, and J. Wambach, "The Phase Structure of the Polyakov–Quark-Meson Model," *Phys. Rev.* **D76** (2007) 074023, arXiv:0704.3234 [hep-ph].

[28] K. Fukushima and T. Hatsuda, "The phase diagram of dense QCD," *Rept. Prog. Phys.* **74** (2011) 014001, arXiv:1005.4814 [hep-ph].

[29] D. H. E. Gross, "Statistical decay of very hot nuclei: The Production of large clusters," *Rept. Prog. Phys.* **53** (1990) 605–658.

[30] J. Pochodzalla *et al.*, "Probing the nuclear liquid - gas phase transition," *Phys. Rev. Lett.* **75** (1995) 1040–1043.

[31] J. B. Natowitz, R. Wada, K. Hagel, T. Keutgen, M. Murray, Y. G. Ma, A. Makeev, L. Qin, P. Smith, and C. Hamilton, "Caloric curves and critical behavior in nuclei," *Phys. Rev.* **C65** (2002) 034618, arXiv:nucl-ex/0106016 [nucl-ex].

[32] S. Fiorilla, N. Kaiser, and W. Weise, "Chiral thermodynamics of nuclear matter," *Nucl. Phys.* **A880** (2012) 65–87, arXiv:1111.2791 [nucl-th].

[33] M. Drews, T. Hell, B. Klein, and W. Weise, "Thermodynamic phases and mesonic fluctuations in a chiral nucleon-meson model," *Phys. Rev.* **D88** no. 9, (2013) 096011, `arXiv:1308.5596 [hep-ph]`.

[34] B. C. Barrois, "Superconducting Quark Matter," *Nucl. Phys.* **B129** (1977) 390–396.

[35] D. Bailin and A. Love, "Superfluidity and Superconductivity in Relativistic Fermion Systems," *Phys. Rept.* **107** (1984) 325.

[36] K. Rajagopal and F. Wilczek, "The Condensed matter physics of QCD," `arXiv:hep-ph/0011333 [hep-ph]`.

[37] M. G. Alford, "Color superconducting quark matter," *Ann. Rev. Nucl. Part. Sci.* **51** (2001) 131–160, `arXiv:hep-ph/0102047 [hep-ph]`.

[38] M. Huang, "QCD Phase Diagram at High Temperature and Density," `arXiv:1001.3216 [hep-ph]`.

[39] E. V. Shuryak and I. Zahed, "Rethinking the properties of the quark gluon plasma at T approximately T(c)," *Phys. Rev.* **C70** (2004) 021901, `arXiv:hep-ph/0307267 [hep-ph]`.

[40] E. V. Shuryak, "What RHIC experiments and theory tell us about properties of quark-gluon plasma?," *Nucl. Phys.* **A750** (2005) 64–83, `arXiv:hep-ph/0405066 [hep-ph]`.

[41] **STAR** Collaboration, J. Adams *et al.*, "Experimental and theoretical challenges in the search for the quark gluon plasma: The STAR Collaboration's critical assessment of the evidence from RHIC collisions," *Nucl. Phys.* **A757** (2005) 102–183, `arXiv:nucl-ex/0501009 [nucl-ex]`.

[42] P. Braun-Munzinger and J. Wambach, "The Phase Diagram of Strongly-Interacting Matter," *Rev. Mod. Phys.* **81** (2009) 1031–1050, `arXiv:0801.4256 [hep-ph]`.

[43] Z. Fodor and S. D. Katz, "The Phase diagram of quantum chromodynamics," `arXiv:0908.3341 [hep-ph]`.

[44] Y. Nambu, "Axial vector current conservation in weak interactions," *Phys. Rev. Lett.* **4** (1960) 380–382.

[45] Y. Nambu and G. Jona-Lasinio, "Dynamical Model of Elementary Particles Based on an Analogy with Superconductivity. II," *Phys. Rev.* **124** (1961) 246–254.

[46] Y. Nambu and G. Jona-Lasinio, "Dynamical Model of Elementary Particles Based on an Analogy with Superconductivity. 1.," *Phys. Rev.* **122** (1961) 345–358.

[47] Y. Nambu, "Nobel Lecture: Spontaneous symmetry breaking in particle physics: A case of cross fertilization," *Int. J. Mod. Phys.* **A24** (2009) 2371–2377. [Rev. Mod. Phys.81,1015(2009)].

[48] O. Philipsen, "Lattice QCD at non-zero temperature and baryon density," in *Modern perspectives in lattice QCD: Quantum field theory and high performance computing. Proceedings, International School, 93rd Session, Les Houches, France, August 3-28, 2009*, pp. 273–330. 2010. `arXiv:1009.4089 [hep-lat]`. `https://inspirehep.net/record/870483/files/arXiv:1009.4089.pdf`.

[49] Y. Aoki, Z. Fodor, S. D. Katz, and K. K. Szabo, "The QCD transition temperature: Results with physical masses in the continuum limit," *Phys. Lett.* **B643** (2006) 46–54, `arXiv:hep-lat/0609068 [hep-lat]`.

[50] Y. Aoki, S. Borsanyi, S. Durr, Z. Fodor, S. D. Katz, S. Krieg, and K. K. Szabo, "The QCD transition temperature: results with physical masses in the continuum limit II.," *JHEP* **06** (2009) 088, `arXiv:0903.4155 [hep-lat]`.

[51] M. Cheng *et al.*, "Equation of State for physical quark masses," *Phys. Rev.* **D81** (2010) 054504, `arXiv:0911.2215 [hep-lat]`.

[52] S. Borsanyi, Z. Fodor, C. Hoelbling, S. D. Katz, S. Krieg, C. Ratti, and K. K. Szabó, "QCD transition temperature: full staggered result," *PoS* **Lattice2010** (2014) 185, `arXiv:1011.4230 [hep-lat]`.

[53] V. G. Bornyakov, R. Horsley, Y. Nakamura, M. I. Polikarpov, P. Rakow, and G. Schierholz, "Finite temperature phase transition with two flavors of improved Wilson fermions," *PoS* **Lattice2010** (2014) 170, `arXiv:1102.4461 [hep-lat]`.

[54] L. McLerran and R. D. Pisarski, "Phases of cold, dense quarks at large N(c)," *Nucl. Phys.* **A796** (2007) 83–100, `arXiv:0706.2191 [hep-ph]`.

[55] Y. Hidaka, L. D. McLerran, and R. D. Pisarski, "Baryons and the phase diagram for a large number of colors and flavors," *Nucl. Phys.* **A808** (2008) 117–123, `arXiv:0803.0279 [hep-ph]`.

[56] L. McLerran, K. Redlich, and C. Sasaki, "Quarkyonic Matter and Chiral Symmetry Breaking," *Nucl. Phys.* **A824** (2009) 86–100, `arXiv:0812.3585 [hep-ph]`.

[57] K. Fukushima, "Phase diagrams in the three-flavor Nambu-Jona-Lasinio model with the Polyakov loop," *Phys. Rev.* **D77** (2008) 114028, `arXiv:0803.3318 [hep-ph]`. [Erratum: Phys. Rev. D78, 039902 (2008)].

[58] L. Ya. Glozman and R. F. Wagenbrunn, "Chirally symmetric but confining dense and cold matter," *Phys. Rev.* **D77** (2008) 054027, `arXiv:0709.3080 [hep-ph]`.

[59] M. Asakawa and K. Yazaki, "Chiral Restoration at Finite Density and Temperature," *Nucl. Phys.* **A504** (1989) 668–684.

[60] J. Berges and K. Rajagopal, "Color superconductivity and chiral symmetry restoration at nonzero baryon density and temperature," *Nucl. Phys.* **B538** (1999) 215–232, `arXiv:hep-ph/9804233 [hep-ph]`.

[61] M. A. Stephanov, K. Rajagopal, and E. V. Shuryak, "Signatures of the tricritical point in QCD," *Phys. Rev. Lett.* **81** (1998) 4816–4819, `arXiv:hep-ph/9806219 [hep-ph]`.

[62] M. A. Stephanov, K. Rajagopal, and E. V. Shuryak, "Event-by-event fluctuations in heavy ion collisions and the QCD critical point," *Phys. Rev.* **D60** (1999) 114028, `arXiv:hep-ph/9903292 [hep-ph]`.

[63] **CBM** Collaboration, S. Chattopadhyay *et al.*, "Challenges in QCD matter physics - The Compressed Baryonic Matter experiment at FAIR," `arXiv:1607.01487 [nucl-ex]`.

[64] G. M. Fuller, G. J. Mathews, and C. R. Alcock, "The Quark - Hadron Phase Transition in the Early Universe: Isothermal Baryon Number Fluctuations and Primordial Nucleosynthesis," *Phys. Rev.* **D37** (1988) 1380.

[65] D. Boyanovsky, H. J. de Vega, and D. J. Schwarz, "Phase transitions in the early and the present universe," *Ann. Rev. Nucl. Part. Sci.* **56** (2006) 441–500, `arXiv:hep-ph/0602002 [hep-ph]`.

[66] F. Weber, "Strange quark matter and compact stars," *Prog. Part. Nucl. Phys.* **54** (2005) 193–288, `arXiv:astro-ph/0407155 [astro-ph]`.

[67] B. Muller and J. L. Nagle, "Results from the relativistic heavy ion collider," *Ann. Rev. Nucl. Part. Sci.* **56** (2006) 93–135, `arXiv:nucl-th/0602029 [nucl-th]`.

[68] U. A. Wiedemann, "Stepping outside the neighborhood of T(c) at LHC," *Nucl. Phys.* **A830** (2009) 74C–80C, `arXiv:0908.2294 [hep-ph]`.

[69] J. Braun and A. Janot, "Dynamical Locking of the Chiral and the Deconfinement Phase Transition in QCD," *Phys. Rev.* **D84** (2011) 114022, `arXiv:1102.4841 [hep-ph]`.

[70] J. Braun and T. K. Herbst, "On the Relation of the Deconfinement and the Chiral Phase Transition in Gauge Theories with Fundamental and Adjoint Matter," `arXiv:1205.0779 [hep-ph]`.

[71] H. Gies, J. Jaeckel, and C. Wetterich, "Towards a renormalizable standard model without fundamental Higgs scalar," *Phys. Rev.* **D69** (2004) 105008, `arXiv:hep-ph/0312034 [hep-ph]`.

[72] H. Gies and J. Jaeckel, "Chiral phase structure of QCD with many flavors," *Eur. Phys. J.* **C46** (2006) 433–438, `arXiv:hep-ph/0507171 [hep-ph]`.

[73] J. Braun and H. Gies, "Chiral phase boundary of QCD at finite temperature," *JHEP* **06** (2006) 024, `arXiv:hep-ph/0602226 [hep-ph]`.

[74] E. Noether, "Invariante variationsprobleme," *Nachrichten von der Gesellschaft der Wissenschaften zu Goettingen, Mathematisch-Physikalische Klasse* **1918** (1918) 235–257. `http://eudml.org/doc/59024`.

[75] E. Noether, "Invarianten beliebiger differentialausdrÃŒcke," *Nachrichten von der Gesellschaft der Wissenschaften zu Goettingen, Mathematisch-Physikalische Klasse* **1918** (1918) 37–44. `http://eudml.org/doc/59011`.

[76] J. S. Bell and R. Jackiw, "A PCAC puzzle: pi0 –> gamma gamma in the sigma model," *Nuovo Cim.* **A60** (1969) 47–61.

[77] S. L. Adler, "Axial vector vertex in spinor electrodynamics," *Phys. Rev.* **177** (1969) 2426–2438.

[78] K. Fujikawa, "Path Integral Measure for Gauge Invariant Fermion Theories," *Phys. Rev. Lett.* **42** (1979) 1195–1198.

[79] **Particle Data Group** Collaboration, J. Beringer *et al.*, "Review of Particle Physics (RPP)," *Phys. Rev.* **D86** (2012) 010001.

[80] V. Bernard and U.-G. Meissner, "Chiral perturbation theory," *Ann. Rev. Nucl. Part. Sci.* **57** (2007) 33–60, arXiv:hep-ph/0611231 [hep-ph].

[81] G. Colangelo and S. Durr, "The Pion mass in finite volume," *Eur. Phys. J.* **C33** (2004) 543–553, arXiv:hep-lat/0311023 [hep-lat].

[82] G. 't Hooft, "On the Phase Transition Towards Permanent Quark Confinement," *Nucl. Phys.* **B138** (1978) 1–25.

[83] G. 't Hooft, "A Property of Electric and Magnetic Flux in Nonabelian Gauge Theories," *Nucl. Phys.* **B153** (1979) 141–160.

[84] N. Goldenfeld, *Lectures On Phase Transitions And The Renormalization Group (Frontiers in Physics, 85)*. Westview Press, July, 1992. http://www.amazon.com/exec/obidos/redirect?tag=citeulike07-20&path=ASIN/0201554097.

[85] C. Wetterich, "Exact evolution equation for the effective potential," *Phys.Lett.* **B301** (1993) 90–94.

[86] L. F. Abbott, "Introduction to the Background Field Method," *Acta Phys. Polon.* **B13** (1982) 33.

[87] J. Berges, N. Tetradis, and C. Wetterich, "Nonperturbative renormalization flow in quantum field theory and statistical physics," *Phys.Rept.* **363** (2002) 223–386, arXiv:hep-ph/0005122 [hep-ph].

[88] D. F. Litim and J. M. Pawlowski, "On gauge invariant Wilsonian flows," in *The exact renormalization group. Proceedings, Workshop, Faro, Portugal, September 10-12, 1998*, pp. 168–185. 1998. arXiv:hep-th/9901063 [hep-th]. http://alice.cern.ch/format/showfull?sysnb=0302190.

[89] C. Bagnuls and C. Bervillier, "Exact renormalization group equations. An Introductory review," *Phys.Rept.* **348** (2001) 91, arXiv:hep-th/0002034 [hep-th].

[90] J. Polonyi, "Lectures on the functional renormalization group method," *Central Eur.J.Phys.* **1** (2003) 1–71, arXiv:hep-th/0110026 [hep-th].

[91] H. Gies, "Introduction to the functional RG and applications to gauge theories," *Lect.Notes Phys.* **852** (2012) 287–348, arXiv:hep-ph/0611146 [hep-ph].

[92] B.-J. Schaefer and J. Wambach, "Renormalization group approach towards the QCD phase diagram," *Phys.Part.Nucl.* **39** (2008) 1025–1032, arXiv:hep-ph/0611191 [hep-ph].

[93] B. Delamotte, "An Introduction to the nonperturbative renormalization group," *Lect.Notes Phys.* **852** (2012) 49–132, `arXiv:cond-mat/0702365 [COND-MAT]`.

[94] B. Delamotte, D. Mouhanna, and M. Tissier, "Nonperturbative renormalization group approach to frustrated magnets," *Phys.Rev.* **B69** (2004) 134413, `arXiv:cond-mat/0309101 [cond-mat]`.

[95] J. M. Pawlowski, "Aspects of the functional renormalisation group," *Annals Phys.* **322** (2007) 2831–2915, `arXiv:hep-th/0512261 [hep-th]`.

[96] R. Shankar, "Renormalization group approach to interacting fermions," *Rev. Mod. Phys.* **66** (1994) 129–192.

[97] M. Salmhofer, *Renormalization: An introduction.* Springer, Berlin, 1999.

[98] S. K. Bogner, T. T. S. Kuo, and A. Schwenk, "Model independent low momentum nucleon interaction from phase shift equivalence," *Phys. Rept.* **386** (2003) 1–27, `arXiv:nucl-th/0305035 [nucl-th]`.

[99] S. K. Bogner, R. J. Furnstahl, and A. Schwenk, "From low-momentum interactions to nuclear structure," *Prog. Part. Nucl. Phys.* **65** (2010) 94–147, `arXiv:0912.3688 [nucl-th]`.

[100] O. J. Rosten, "Fundamentals of the Exact Renormalization Group," *Phys. Rept.* **511** (2012) 177–272, `arXiv:1003.1366 [hep-th]`.

[101] P. Kopietz, L. Bartosch, and F. Schutz, "Introduction to the functional renormalization group," *Lect. Notes Phys.* **798** (2010) 1–380.

[102] W. Metzner, M. Salmhofer, C. Honerkamp, V. Meden, and K. Schönhammer, "Functional renormalization group approach to correlated fermion systems," *Rev. Mod. Phys.* **84** (Mar, 2012) 299–352. `http://link.aps.org/doi/10.1103/RevModPhys.84.299`.

[103] J. Braun, "Fermion Interactions and Universal Behavior in Strongly Interacting Theories," *J. Phys.* **G39** (2012) 033001, `arXiv:1108.4449 [hep-ph]`.

[104] U. Ellwanger, M. Hirsch, and A. Weber, "The Heavy quark potential from Wilson's exact renormalization group," *Eur. Phys. J.* **C1** (1998) 563–578, `arXiv:hep-ph/9606468 [hep-ph]`.

[105] U. Ellwanger, M. Hirsch, and A. Weber, "Flow equations for the relevant part of the pure Yang-Mills action," *Z. Phys.* **C69** (1996) 687–698, `arXiv:hep-th/9506019 [hep-th]`.

[106] M. Bonini, M. D'Attanasio, and G. Marchesini, "BRS symmetry for Yang-Mills theory with exact renormalization group," *Nucl. Phys.* **B437** (1995) 163–186, `arXiv:hep-th/9410138 [hep-th]`.

[107] M. Reuter, "Effective average actions and nonperturbative evolution equations," in *5th Hellenic School and Workshops on Elementary Particle Physics (CORFU 1995) Corfu, Greece, September 3-24, 1995.* 1996. `arXiv:hep-th/9602012 [hep-th]`.

[108] M. Reuter and C. Wetterich, "Gluon condensation in nonperturbative flow equations," *Phys. Rev.* **D56** (1997) 7893–7916, `arXiv:hep-th/9708051 [hep-th]`.

[109] F. Freire, D. F. Litim, and J. M. Pawlowski, "Gauge invariance and background field formalism in the exact renormalization group," *Phys. Lett.* **B495** (2000) 256–262, `arXiv:hep-th/0009110 [hep-th]`.

[110] L. F. Abbott, "The Background Field Method Beyond One Loop," *Nucl. Phys.* **B185** (1981) 189.

[111] T. R. Morris, "A Gauge invariant exact renormalization group. 2.," *JHEP* **12** (2000) 012, `arXiv:hep-th/0006064 [hep-th]`.

[112] S. Arnone, T. R. Morris, and O. J. Rosten, "A Generalised manifestly gauge invariant exact renormalisation group for SU(N) Yang-Mills," *Eur. Phys. J.* **C50** (2007) 467–504, `arXiv:hep-th/0507154 [hep-th]`.

[113] D. F. Litim and J. M. Pawlowski, "Completeness and consistency of renormalisation group flows," *Phys. Rev.* **D66** (2002) 025030, `arXiv:hep-th/0202188 [hep-th]`.

[114] D. F. Litim, "Mind the gap," *Int. J. Mod. Phys.* **A16** (2001) 2081–2088, `arXiv:hep-th/0104221 [hep-th]`.

[115] D. F. Litim, "Optimization of the exact renormalization group," *Phys. Lett.* **B486** (2000) 92–99, `arXiv:hep-th/0005245 [hep-th]`.

[116] D. F. Litim, "Optimized renormalization group flows," *Phys. Rev.* **D64** (2001) 105007, `arXiv:hep-th/0103195 [hep-th]`.

[117] H. Gies and C. Wetterich, "Universality of spontaneous chiral symmetry breaking in gauge theories," *Phys. Rev.* **D69** (2004) 025001, `arXiv:hep-th/0209183 [hep-th]`.

[118] H. Gies and C. Wetterich, "Renormalization flow of bound states," *Phys. Rev.* **D65** (2002) 065001, `arXiv:hep-th/0107221 [hep-th]`.

[119] H. Gies and C. Wetterich, "Renormalization flow from UV to IR degrees of freedom," *Acta Phys. Slov.* **52** (2002) 215–220, `arXiv:hep-ph/0205226 [hep-ph]`.

[120] S. Floerchinger and C. Wetterich, "Exact flow equation for composite operators," *Phys. Lett.* **B680** (2009) 371–376, `arXiv:0905.0915 [hep-th]`.

[121] S. Floerchinger, "Exact Flow Equation for Bound States," *Eur. Phys. J.* **C69** (2010) 119–132, `arXiv:1001.4497 [hep-th]`.

[122] M. Mitter, J. M. Pawlowski, and N. Strodthoff, "Chiral symmetry breaking in continuum QCD," *Phys. Rev.* **D91** (2015) 054035, `arXiv:1411.7978 [hep-ph]`.

[123] J. Braun, "The QCD Phase Boundary from Quark-Gluon Dynamics," *Eur. Phys. J.* **C64** (2009) 459–482, `arXiv:0810.1727 [hep-ph]`.

[124] J. Braun, L. Fister, J. M. Pawlowski, and F. Rennecke, "From Quarks and Gluons to Hadrons: Chiral Symmetry Breaking in Dynamical QCD," `arXiv:1412.1045 [hep-ph]`.

[125] Y. Nambu, "Quasiparticles and Gauge Invariance in the Theory of Superconductivity," *Phys. Rev.* **117** (1960) 648–663.

[126] P. N. Meisinger and M. C. Ogilvie, "Chiral symmetry restoration and Z(N) symmetry," *Phys. Lett.* **B379** (1996) 163–168, `arXiv:hep-lat/9512011 [hep-lat]`.

[127] R. D. Pisarski, "Quark gluon plasma as a condensate of SU(3) Wilson lines," *Phys. Rev.* **D62** (2000) 111501, `arXiv:hep-ph/0006205 [hep-ph]`.

[128] A. Mocsy, F. Sannino, and K. Tuominen, "Confinement versus chiral symmetry," *Phys. Rev. Lett.* **92** (2004) 182302, `arXiv:hep-ph/0308135 [hep-ph]`.

[129] K. Fukushima, "Chiral effective model with the Polyakov loop," *Phys. Lett.* **B591** (2004) 277–284, `arXiv:hep-ph/0310121 [hep-ph]`.

[130] E. Megias, E. Ruiz Arriola, and L. L. Salcedo, "Polyakov loop in chiral quark models at finite temperature," *Phys. Rev.* **D74** (2006) 065005, `arXiv:hep-ph/0412308 [hep-ph]`.

[131] C. Ratti, M. A. Thaler, and W. Weise, "Phases of QCD: Lattice thermodynamics and a field theoretical model," *Phys. Rev.* **D73** (2006) 014019, `arXiv:hep-ph/0506234 [hep-ph]`.

[132] C. Sasaki, B. Friman, and K. Redlich, "Susceptibilities and the Phase Structure of a Chiral Model with Polyakov Loops," *Phys. Rev.* **D75** (2007) 074013, `arXiv:hep-ph/0611147 [hep-ph]`.

[133] A. J. Mizher, M. N. Chernodub, and E. S. Fraga, "Phase diagram of hot QCD in an external magnetic field: possible splitting of deconfinement and chiral transitions," *Phys. Rev.* **D82** (2010) 105016, `arXiv:1004.2712 [hep-ph]`.

[134] V. Skokov, B. Stokic, B. Friman, and K. Redlich, "Meson fluctuations and thermodynamics of the Polyakov loop extended quark-meson model," *Phys. Rev.* **C82** (2010) 015206, `arXiv:1004.2665 [hep-ph]`.

[135] T. K. Herbst, J. M. Pawlowski, and B.-J. Schaefer, "The phase structure of the Polyakov-quark-meson model beyond mean field," *Phys. Lett.* **B696** (2011) 58–67, `arXiv:1008.0081 [hep-ph]`.

[136] V. Skokov, B. Friman, and K. Redlich, "Quark number fluctuations in the Polyakov loop-extended quark-meson model at finite baryon density," *Phys. Rev.* **C83** (2011) 054904, `arXiv:1008.4570 [hep-ph]`.

[137] J. Braun and H. Gies, "Scaling laws near the conformal window of many-flavor QCD," *JHEP* **05** (2010) 060, `arXiv:0912.4168 [hep-ph]`.

[138] J. Braun, C. S. Fischer, and H. Gies, "Beyond Miransky Scaling," *Phys. Rev.* **D84** (2011) 034045, `arXiv:1012.4279 [hep-ph]`.

[139] A. M. Polyakov, "Thermal Properties of Gauge Fields and Quark Liberation," *Phys. Lett.* **B72** (1978) 477–480.

[140] L. Susskind, "Lattice Models of Quark Confinement at High Temperature," *Phys. Rev.* **D20** (1979) 2610–2618.

[141] D. J. Gross, R. D. Pisarski, and L. G. Yaffe, "QCD and Instantons at Finite Temperature," *Rev. Mod. Phys.* **53** (1981) 43.

[142] B. Svetitsky, "Symmetry Aspects of Finite Temperature Confinement Transitions," *Phys. Rept.* **132** (1986) 1–53.

[143] J. Greensite, "The Confinement problem in lattice gauge theory," *Prog. Part. Nucl. Phys.* **51** (2003) 1, `arXiv:hep-lat/0301023 [hep-lat]`.

[144] N. Weiss, "The Wilson Line in Finite Temperature Gauge Theories," *Phys. Rev.* **D25** (1982) 2667.

[145] K. Szabo, *Dynamical fermions in lattice quantum chromodynamics*. PhD thesis, Wuppertal U., 2008. `arXiv:0801.0224 [hep-lat]`. `https://inspirehep.net/record/776627/files/arXiv:0801.0224.pdf`.

[146] J. Braun, H. Gies, and J. M. Pawlowski, "Quark Confinement from Color Confinement," *Phys. Lett.* **B684** (2010) 262–267, `arXiv:0708.2413 [hep-th]`.

[147] B.-J. Schaefer, M. Wagner, and J. Wambach, "Thermodynamics of (2+1)-flavor QCD: Confronting Models with Lattice Studies," *Phys. Rev.* **D81** (2010) 074013, `arXiv:0910.5628 [hep-ph]`.

[148] F. Marhauser and J. M. Pawlowski, "Confinement in Polyakov Gauge," `arXiv:0812.1144 [hep-ph]`.

[149] J. Braun, A. Eichhorn, H. Gies, and J. M. Pawlowski, "On the Nature of the Phase Transition in SU(N), Sp(2) and E(7) Yang-Mills theory," *Eur. Phys. J.* **C70** (2010) 689–702, `arXiv:1007.2619 [hep-ph]`.

[150] J. Berges, D. U. Jungnickel, and C. Wetterich, "Two flavor chiral phase transition from nonperturbative flow equations," *Phys. Rev.* **D59** (1999) 034010, `arXiv:hep-ph/9705474 [hep-ph]`.

[151] J. Braun, "Thermodynamics of QCD low-energy models and the derivative expansion of the effective action," *Phys. Rev.* **D81** (2010) 016008, `arXiv:0908.1543 [hep-ph]`.

[152] M. Kitazawa, T. Koide, T. Kunihiro, and Y. Nemoto, "Chiral and color superconducting phase transitions with vector interaction in a simple model," *Prog. Theor. Phys.* **108** (2002) 929–951, `arXiv:hep-ph/0207255 [hep-ph]`.

[153] N. M. Bratovic, T. Hatsuda, and W. Weise, "Role of Vector Interaction and Axial Anomaly in the PNJL Modeling of the QCD Phase Diagram," *Phys. Lett.* **B719** (2013) 131–135, `arXiv:1204.3788 [hep-ph]`.

[154] J. Braun and H. Gies, "Running coupling at finite temperature and chiral symmetry restoration in QCD," *Phys. Lett.* **B645** (2007) 53–58, `arXiv:hep-ph/0512085 [hep-ph]`.

[155] A. Janot, "The Impact of Confining Dynamics on Chiral Symmetry Breaking in QCD," Master's thesis, TU Darmstadt, 2011.

[156] M. Leonhardt, "On Confinement Effects on Chiral Dynamics," Master's thesis, TU Darmstadt, 2014.

[157] D. F. Litim and J. M. Pawlowski, "Non-perturbative thermal flows and resummations," *JHEP* **11** (2006) 026, `arXiv:hep-th/0609122 [hep-th]`.

[158] N. Weiss, "Introduction to Z(N) symmetry in SU(N) gauge theories at finite temperatures," in *3rd Workshop on Thermal Field Theories and their Applications Banff, Canada, August 15-27, 1993*. 1993. `arXiv:hep-ph/9311233 [hep-ph]`.

[159] O. Philipsen, "Status of the QCD Phase Diagram from Lattice Calculations," *Acta Phys. Polon. Supp.* **5** (2012) 825–835, `arXiv:1111.5370 [hep-ph]`.

[160] G. Endrodi, Z. Fodor, S. D. Katz, and K. K. Szabo, "The QCD phase diagram at nonzero quark density," *JHEP* **04** (2011) 001, `arXiv:1102.1356 [hep-lat]`.

[161] G. Endrodi, Z. Fodor, S. D. Katz, and K. K. Szabo, "The Curvature of the QCD phase transition line," *PoS* **LATTICE2008** (2008) 205, `arXiv:0901.3018 [hep-lat]`.

[162] Z. Fodor and S. D. Katz, "Critical point of QCD at finite T and mu, lattice results for physical quark masses," *JHEP* **04** (2004) 050, `arXiv:hep-lat/0402006 [hep-lat]`.

[163] P. de Forcrand and O. Philipsen, "The QCD phase diagram for small densities from imaginary chemical potential," *Nucl. Phys.* **B642** (2002) 290–306, `arXiv:hep-lat/0205016 [hep-lat]`.

[164] J. Hubbard, "Calculation of partition functions," *Phys. Rev. Lett.* **3** (1959) 77–80.

[165] R. Stratonovich *Dokl. Akad. Nauk.* **15** (1957) 1097.

[166] J. Braun, H. Gies, and D. D. Scherer, "Asymptotic safety: a simple example," *Phys. Rev.* **D83** (2011) 085012, `arXiv:1011.1456 [hep-th]`.

[167] J. M. Pawlowski and F. Rennecke, "Higher order quark-mesonic scattering processes and the phase structure of QCD," *Phys. Rev.* **D90** no. 7, (2014) 076002, `arXiv:1403.1179 [hep-ph]`.

[168] J. Jaeckel, *Effective actions for strongly interacting fermionic systems*. PhD thesis, Heidelberg U., 2003. `arXiv:hep-ph/0309090 [hep-ph]`.

[169] J. Jaeckel and C. Wetterich, "Flow equations without mean field ambiguity," *Phys. Rev.* **D68** (2003) 025020, `arXiv:hep-ph/0207094 [hep-ph]`.

[170] T. Banks and A. Zaks, "On the Phase Structure of Vector-Like Gauge Theories with Massless Fermions," *Nucl. Phys.* **B196** (1982) 189–204.

[171] V. A. Miransky and K. Yamawaki, "Conformal phase transition in gauge theories," *Phys. Rev.* **D55** (1997) 5051–5066, `arXiv:hep-th/9611142 [hep-th]`. [Erratum: Phys. Rev.D56,3768(1997)].

[172] T. Appelquist, J. Terning, and L. C. R. Wijewardhana, "The Zero temperature chiral phase transition in SU(N) gauge theories," *Phys. Rev. Lett.* **77** (1996) 1214–1217, `arXiv:hep-ph/9602385 [hep-ph]`.

[173] S. Bethke, "α_s 2002," *Nucl. Phys. Proc. Suppl.* **121** (2003) 74–81, `arXiv:hep-ex/0211012 [hep-ex]`. [,74(2002)].

[174] L. von Smekal, R. Alkofer, and A. Hauck, "The Infrared behavior of gluon and ghost propagators in Landau gauge QCD," *Phys. Rev. Lett.* **79** (1997) 3591–3594, `arXiv:hep-ph/9705242 [hep-ph]`.

[175] D. Atkinson and J. C. R. Bloch, "QCD in the infrared with exact angular integrations," *Mod. Phys. Lett.* **A13** (1998) 1055–1062, `arXiv:hep-ph/9802239 [hep-ph]`.

[176] C. Lerche and L. von Smekal, "On the infrared exponent for gluon and ghost propagation in Landau gauge QCD," *Phys. Rev.* **D65** (2002) 125006, `arXiv:hep-ph/0202194 [hep-ph]`.

[177] C. S. Fischer and R. Alkofer, "Infrared exponents and running coupling of SU(N) Yang-Mills theories," *Phys. Lett.* **B536** (2002) 177–184, `arXiv:hep-ph/0202202 [hep-ph]`.

[178] J. M. Pawlowski, D. F. Litim, S. Nedelko, and L. von Smekal, "Infrared behavior and fixed points in Landau gauge QCD," *Phys. Rev. Lett.* **93** (2004) 152002, `arXiv:hep-th/0312324 [hep-th]`.

[179] C. S. Fischer and H. Gies, "Renormalization flow of Yang-Mills propagators," *JHEP* **10** (2004) 048, `arXiv:hep-ph/0408089 [hep-ph]`.

[180] A. Bazavov *et al.*, "The chiral and deconfinement aspects of the QCD transition," *Phys. Rev.* **D85** (2012) 054503, `arXiv:1111.1710 [hep-lat]`.

[181] T. D. Cohen, "QCD functional integrals for systems with nonzero chemical potential," `arXiv:hep-ph/0405043 [hep-ph]`.

[182] T. D. . Cohen, "Functional integrals for QCD at nonzero chemical potential and zero density," *Phys. Rev. Lett.* **91** (2003) 222001, `arXiv:hep-ph/0307089 [hep-ph]`.

[183] P. O. Bowman, U. M. Heller, D. B. Leinweber, M. B. Parappilly, and A. G. Williams, "Unquenched gluon propagator in Landau gauge," *Phys. Rev.* **D70** (2004) 034509, `arXiv:hep-lat/0402032 [hep-lat]`.

[184] A. Sternbeck, E. M. Ilgenfritz, M. Muller-Preussker, A. Schiller, and I. L. Bogolubsky, "Lattice study of the infrared behavior of QCD Green's functions in Landau gauge," *PoS* **LAT2006** (2006) 076, `arXiv:hep-lat/0610053 [hep-lat]`.

[185] W. Metzner, M. Salmhofer, C. Honerkamp, V. Meden, and K. Schönhammer, "Functional renormalization group approach to correlated fermion systems," *Reviews of Modern Physics* **84** (Jan., 2012) 299–352, `arXiv:1105.5289 [cond-mat.str-el]`.

[186] T. R. Morris, "The Exact renormalization group and approximate solutions," *Int. J. Mod. Phys.* **A9** (1994) 2411–2450, `arXiv:hep-ph/9308265 [hep-ph]`.

ACKNOWLEDGMENTS